Faculty of Engineering and Science
Department of Mechanical Engineering

Heavy Vehicle Aerodynamics: Massively-Separated Turbulent Flow & a Bio-Inspired Device

Zachary S. MacChesney

0000-0002-4546-0364

This thesis is presented for the degree of
Doctor of Philosophy
of
Curtin University

June 2021

To the best of my knowledge and belief this thesis contains no material previously published by any other person except where due acknowledgement has been made. This thesis contains no material which has been accepted for the award of any other degree or diploma in any university.

Zachary S. MacChesney

24th July 2021

Heavy Vehicle Aerodynamics: Massively-Separated Turbulent Flow & A Bio-Inspired Device

Zachary S. MacChesney

Thesis Committee:

Principal Supervisor	Dr. Law Ming Chiat
Associate Supervisor	Dr. Vincent C. -C. Lee
Thesis Chair	A/Prof. Perumal Kumar

Ph.D. Thesis:
Department of Mechanical Engineering
Faculty of Engineering and Science
Curtin University
CDT 250, Miri, Sarawak 98009, Malaysia
Telephone +60 85 44 3939

"Big whirls have little whirls,
That feed on their velocity;
And little whirls have lesser whirls,
And so on to viscosity."
- Lewis Fry Richardson

Abstract

Road freight vehicles account for the second largest share of petroleum consumption after road transportation vehicles. This is despite the fact that their numbers are a fraction of that of road vehicles. Furthermore, at highway speeds, the majority of a heavy vehicle's power is consumed through overcoming aerodynamic drag. As such the development of drag reduction devices for heavy vehicles is an important endeavour. The state of the art features many drag reduction devices that are based on steady state analysis, however there are few devices that make use of unsteady phenomena. According to literature, a key area that is hindering the conception of such unsteady devices is the lack of understanding regarding the fundamental unsteady processes occurring in massively separated flows. Therefore the two key themes that are addressed in this thesis are A) improving fundamental understanding of unsteady massively separated flows, and B) the development of a drag reduction device that is based on unsteady phenomena. The studies are carried out on commercial CFD software Star CCM+ using facilities the Pawsey super-computing center solving using the $k-\omega$ and the Detatched Eddy Simulation turbulence models where appropriate. All studies are validated against experimental data with a 2.06% error in computation of drag coefficient for the truck study, and a precise fit of pressure coefficient for the fundamental study. For the drag reduction device , inspiration was taken from the geometry of a whisker of a harbour seal has been shown to reduce drag. The fundamental aspect of the work focused on turbulent flow over a backwards facing step. Through a novel flow decomposition method based on selective filtering the underlying structure of this type of flow was revealed. On top of the familiar Kelvin-Helmholtz instabilities that occur at the shear layer, larger convective patterns were discovered that alternate in polarity and move in a stream-wise direction. Taking inspiration from the famous doubly-periodic Couette flow these were hypothesised to be of centrifugal origin. A resulting analysis of centrifugal instability metrics confirmed conditions for such an instability were indeed present. Regarding the development of a drag reduction device a wavy geometry was found to reduce drag by up to 22%, comparable to other leading devices such as a boat tail, the benefit of the device is its nominally 2D geometry. An unsteady analysis showed it had an attenuating effect on wake vorticies. Furthermore, a significant contribution of the work is in understanding the fundamental mechanism of drag creation in the wake of a vehicle. A mathematical analysis of body forces in the wake of a vehicle highlighted the importance of recirculating flow in reducing drag.

Acknowledgements

The completion of this thesis wouldn't have been possible without the support of many parties involved. Firstly and foremost I would like to sincerely thank my supervisors Dr. Law Ming Chiat and Dr. Vincent C. C-. Lee for offering their patience and continual support and guidance. The project would not have been possible without resources provided by Curtin University under the Curtin Malaysia Post-Graduate Research Scholarship. Other staff from the university have been paramount in supporting the project with special thanks to Sheikh Zaffrullah for his assistance with software. I acknowledge the support granted by Pawsey Supercomputing Center in terms of computing time, and also the help from staff who work at the help desk in trouble shooting difficult technicalities. Many thanks is owed to Demetris Cleredis and his team at Siemens for their support with a Power-On-Demand license for Star CCM+ through their academic program. I would like to thank my friends and colleagues for their kinship and advice. Last but not least I would like to thank my family who have supported me throughout this endeavor.

Zachary MacChesney - Miri, Sarawak - June 2021

Contents

List of Figures

List of Tables

List of Symbols

Symbol	Description	Units
F_d	Drag Force	N
C_d	Drag Coefficient	-
ρ	Density	$kg.m^{-2}$
A	Area	m^2
v	Velocity	$m.s^{-1}$
Re	Reynolds Number	-
$\bar{C_d}$	Wind-Averaged Drag Coefficient	-
k/D	Surface Roughness Coefficient	-
St	Dimensionless Frequency (Strouhal Number)	-
h	Height	m
D_e	Equivalent Pipe Diameter	m
R_c	Radius of Curvature	m^{-1}
U_e	External Velocity	$m.s$
θ	Momentum Thickness	-
ν	Kinematic Viscosity	m^2s^{-1}
Φ	Characteristic Angular Velocity	rad.s^{-1}
R	Linear Dimension Perpendicular to the Rotation Axis	m
ρ_{heavy}	Density of Heavier Fluid	$kg.m^{-3}$
ρ_{light}	Density of Lighter Fluid	$kg.m^{-3}$
∇	Partial Derivative Operator	-
f	Frequency	Hz
P_crit	Critical Frequency	Hz
Re_i	Inner Cylinder Reynolds Number	-
Re_i	Outer Cylinder Reynolds Number	-
G_o	Gortler Number	-
U_∞	Freestream Velocity	$m.s^{-1}$
$\bar{x}$	Distance from leading edge	m

r	Radial Position	m
Γ	Circulation	$m^2.s^{-1}$
V	Tangential Velocity	$m.s^{-1}$
t	Time	s
u_i	Velocity Vector	$m.s^{-1}$
f_i	Body Forces	N
p	Pressure	Pa
τ_{ij}	Viscous Stress Tensor	$Pa.m^{-2}$
μ	Molecular Viscosity	$m^2.s^{-1}$
δ_{ij}	Kronecker Delta Function	-
E	Total Energy of Fluid	J
q_i	Heat Flux Vector	$W.m^{-2}$
k	Heat Transfer Coefficient	$W.m^{-2}.K^{-1}$
T	Temperature	K
$\boldsymbol{W}$	Vector of Conserved Variables	–
ϕ	Transport of Scalar Property	–
$\dot{m}_f$	Mass Flow Rate at Face	$kg.s^{-1}$
$\boldsymbol{s}_i$	Spacial Vector from Centroid of Adjacent Cells	m
D_f	Diffusive Flux	$kg.s^{-1}.m^{-2}$
Γ	Face Diffusivity	–
$\boldsymbol{a}$	Surface Area Vector	m^2
Γ_f	Harmonic Average of Face Diffusivity	–
$\bar{\phi}$	Mean Component of Property	–
ϕ'	Fluctuating Component of Property	–
k	Specific Energy of Fluctuations	$J.kg^{-1}$
R_t	Turbulent Reynolds Number $(k-\epsilon)$	–
R_ω	Turbulent Reynolds Number $(k-\omega)$	-
ϵ	Rate of Dissipation of Turbulent Kinetic Energy	s^{-1}
ν_t	Kinematic Eddy Viscosity	$m^2.s^{-1}$
ν	Molecular Viscosity	$m^2.s^{-1}$
$\tilde{\nu}$	Undamped Eddy Viscosity	$m^2.s^{-1}$
σ	Turbulent Prandtl Number	–
d	Wall Distance	m
d_t	Distance from Trip Point	m
ω_t	Vorticity at Trip Point	s^{-1}
Δx	Grid Spacing Along Wall at Trip Point	m
ω	k-Specific Dissipation Rate	s^{-1}

τ	Turbulent Time-Scale	s
C_μ	$k-\epsilon$ Model Coefficient	$-$
P	Production of Turbulence	$J.kg^{-1}.s^{-1}$
P_ω	Dissipation of Turbulence	$J.kg^{-1}.s^{-1}$
u^+	Non-Dimensionalised Flow Speed	$-$
y^+	Non-Dimensionalised Wall Distance	$-$
u^*	Reference Velocity	$m.s^{-1}$
G_k	Turbulent Production (k-$\omega Model$)	$J.kg^{-1}.s^{-1}$
Re_y	Wall-Distance Based Reynolds Number	$-$
$\boldsymbol{S}$	Mean Strain Rate	s^{-1}
S	Modulus of Mean Strain Rate	s^{-1}
u_t	Friction Velocity	$m.s^{-1}$
$\tilde{\boldsymbol{v}}$	Filtered Velocity	$m.s^{-1}$
$\tilde{p}$	Filtered Pressure	Pa
$\boldsymbol{I}$	Identity Tensor	$-$
$\boldsymbol{T}$	Stress Tensor	$N.m^{-2}$
$\boldsymbol{T}_t$	Turbulent Stress Tensor	$N.m^{-2}$
Δ	Length Scale	m
κ	Von-Karman Constant	$-$
f_v	Van Driest Damping Coefficient	$-$
$\boldsymbol{T}_t^{RANS}$	Reynolds-Stress Tensor	$N.m^{-2}$
$\boldsymbol{T}_t^{LES}$	LES Stress Tensor	$N.m^{-2}$
f	Free-Shear Modification Factor	$-$
f_e	Elevating Function	$-$
f_b	Blending Function	$-$
Re_H	Reynolds Number with Height as Characteristic Length	$-$
δ_{99}	Boundary-Layer Thickness	m
Re_θ	Momentum-Thickness Reynolds Number	$-$
H	Shape Factor	$-$
C_f	Skin Friction Coefficient	$-$
$\boldsymbol{S}$	Parameter Vector	$-$
$\boldsymbol{S'}$	Perturbation Vector	$-$
$\bar{\boldsymbol{S}}$	Mean Vector	$-$
$\hat{\mathbf{S}}'$	Filtered Vector	$-$
f_{cl}	Lower Cut-Off Frequency	Hz
f_{cu}	Upper Cut-Off Frequency	Hz
$\boldsymbol{\Omega}$	Vorticity Tensor	s^{-1}

$\boldsymbol{S}$	Rate of Strain Tensor	s^{-1}
$>$	Rational Operator	$-$
T	Vortex Strength Threshold	s^{-1}
σ	Standard Deviation	$-$
D_n	Dean Number	$-$
$\Re(V)$	Local Radius of Curvature	m^{-1}
$V(x, y)$	Velocity Vector Field	$m.s^{-1}$
W	Reference Width	m
p_∞	Pressure at Free-Stream	Pa
p_0	Stagnation Pressure	Pa
k	Wave Number	m^{-1}
τ_{yx}	Shear Stress in x Direction with respect to y axis	$N.m^-2$
τ_{zx}	Shear Stress in x Direction with respect to y axis	$N.m^-2$
σ_{xx}	Normal Stress Acting on the Base	$N.m^-2$
$_B$	Velocity Difference between Freestream and Wake at Base	$m.s^{-1}$
$_B$	Velocity Difference between Freestream and Wake at Probe	$m.s^{-1}$
x_b	x Distance to Base	m
x_p	x Distance to Probe	m
Q_B	Mass Flow Rate at Base	$kg.s^{-1}$
Q_P	Mass Flow Rate at Probe	$kg.s^{-1}$
$\bar{u}_B$	Mean Velocity at Base	$m.s^{-1}$
$\bar{u}_P$	Mean Velocity at Probe	$m.s^{-1}$
u_F	Freestream Velocity	$m.s^{-1}$
u_W	Wake Velocity	$m.s^{-1}$
$\bar{C}_d$	Time-Averaged Drag Coefficient	$-$
$\bar{F}$	Time-Averaged Force	N

1

Introduction

Heavy vehicles consume approximately 68% of all road vehicle fuel used, even though they account for a fraction of the commercial vehicle fleet. Moreover, fuel costs reportedly consume 33% of the total operating cost for the haulage business Hyams et al. (2011). These facts, coupled with increasingly stringent global regulations, continue to drive research into the improvement of heavy vehicle fuel economy. There are many approaches to improve fuel economy including engine improvements, weight improvement, mechanical improvements and aerodynamics. Aerodynamic improvement is usually brought on by the incorporation of devices that are added to the truck. Though forebody and underbody drag reduction devices are commonly applied, it is a rare sight to find a device that acts on the base (rear) of the vehicle. In accordance with this goal, Choi et al. (2014) suggested two key areas that require development A) developing a deeper understanding of vortex activity that occurs in the base of a heavy vehicle, and B) the development of passive drag reduction devices that are based on unsteady principles that operate in the base of the heavy vehicle.

The first section of this thesis concerns fundamental aspects of unsteady flow behind a backwards facing step; this can be considered to be the simplest analogy of the flow in the wake of a heavy vehicle. Through the literature review the state of the art was found to involve some confusion regarding the variety of unsteady processes that occur in this flow. Though the cause of shear-mode vortex shedding was firmly established as the Kelvin-Helmholtz instability, the cause of the lower frequency wake-mode shedding had been unclear. Moreover the relationship between the two was also not established. The chaotic motion of turbulence, and the high temporal and spacial fidelity required to accurately model makes the interpretation of turbulent flow behavior particularly challenging. Based on the idea that turbulent motion is mainly comprised of a superposition of simpler organised eddys (Cantwell, 1981), an original method of visualising individual motions was devised and is based on

band-pass filtering of the turbulent signals. This was combined with an original modification to the Q-Criterion vortex identification method in order to garner new insights into this class of flows. It was found that the wake-mode shedding is due to large vortices of centrifugal origin. This conclusion was drawn from the plotting of Deans number which confirmed that conditions for a centrifugal instability were ripe. Additionally, it was found that the wake-mode vortices and the well-known shear-mode vortices are related to one another with an overall flow structure; the shear-mode vortices reside within the wake-mode vorticies and may serve as an energy path for the dissipation of the wake-mode eddys.

The second section of this thesis concerns the development of a passive drag reduction device for heavy vehicles that is based on unsteady principles. The applicability of a wavy shape found in the natural world is investigated. The wavy shape is employed by animals such as a harbour seal in order to reduce Vortex-Induced-Vibrations (VIV) and improve the sensitivity of their vibrissa (whiskers); this allows them to sense disturbances caused by fleeing prey in turbid waters for example. Besides reducing vibrations, it was found to reduce drag on the whisker (Hanke et al., 2010), and other bodies it's been applied to such as a square-backed cylinder (Tombazis and Bearman, 1997). In this section, the geometry was incorporated into an original drag reduction device and tested using computational simulation of the flow around a heavy vehicle. The device was proven to have a significant drag reduction in the order of 21.56% compared to the baseline case with no device. This performance is in the range of the other best-performing base region devices such as the base flap. The design of the device has the added advantage that it is nominally two dimensional so may be easily incorporated to facilitate opening and closing of the rear doors. Further investigation into the unsteady properties of the device showed that the device had a stabilising effect on vortices from the rear of the vehicle and increased the base pressure which was the cause of drag reduction. From this an overall mechanism is proposed that gives a causal link between the shed vortices and the drag. Energetic vorticies cause high momentum transfer between the free-stream and the wake. This increases the shear force between the regions causing a greater 'pull' on the wake by the free-stream which is associated with a low pressure. This low pressure in the wake sucks the rear face of the truck backwards causing drag. Thereby through stabilisation of the wake vortices, the shear force is reduced and base pressure increases; resulting in a lower drag.

All studies in this work are simulation based and making use of commercial CFD code Star CCM+ in combination with resources granted by the Pawsey Supercom-

puter Facility in Perth, Australia. Wherever possible, the studies in this work have been based on published experimental data where validation of the models are possible.

2

Literature Review

Road freight vehicles perform a number of transportation roles that are critical to many industries and for this reason are vital to global economic activity. An essential role that we associate with road freight vehicles is the transportation of goods from their place of manufacture to the place of final sale. Apart from this, road freight is crucial to many other industries. For example it is used to transport: coal from mines to power stations; agricultural products from farms to markets; mail between distribution centers and to their final destinations. In fact, it is hard to think of a single industry that is not dependent on road freight in some way. In this chapter, several areas of the road freight industry are reviewed and the need for improved base drag reduction devices, and also the need for more understanding regarding their function is highlighted.

Also, in-line with the goal of improving fundamental understanding of unsteady flow in the wake of heavy vehicles, fundamental concepts of unsteady flow are covered. These include coverage of the fundamental laws of fluids and their applicability to computational fluid dynamic, and flow instabilities;

2.1 Global Heavy Vehicle Fuel Consumption

Recently, the International Energy Agency (IEA) released a comprehensive report entitled 'The Future of Trucks, implications for energy and the environment' (Teter et al., 2015). It represents a joint body of research by the IEA and its stakeholders which included truck manufacturers, energy companies, industry associations, governments and several other categories of contributors. The key facts derived from this report are as follows:

- Road freight transport accounts for the second-largest source of oil demand following passenger cars.

- Road freight transport accounts for 7% of global CO2 emissions, with the majority (65%) of CO2 growth from road freight vehicles deriving from large trucks.

- Road freight transport is a rapidly growing sector. Energy consumption has increased by over 50% over a 15 year period, from 23 exa-joules (x 10^{18}) in 2000, to 36 exa-joules in 2015. In energy equivalent barrels of oil, this is enough to cover the entire area of Singapore with a layer of oil 1.3m deep every year.

They summarised the report with recommendations. The first of which was improving vehicle efficiency. In a similar report by Diczfalusy et al. (2010), they highlighted the fact that Road freight is the second least efficient mode of transportation after aviation. These facts indicate that improving the fuel economy of road freight vehicles is a worthy pursuit that has a significant positive impact in both improving the profitability of businesses, and also reducing greenhouse gas emissions into the environment.

Sharpe and Muncrief (2015) compiled a white paper regarding heavy-duty vehicle (HDV) fuel consumption and green house gas emissions in the U.S., China, and E.U. From their extensive review they derived that tractor-trailer configuration of heavy vehicle represent the largest share of fuel use and green house gas emissions among commercial vehicles. This justifies the focus on the tractor-trailer geometry in this study. The data was sourced from several sources which included: national statistics such as fuel sales and activity rate surveys; company reports such as total fuel consumption and activity levels; on-road or closed track testing using ECM data, fuel flow meters, and fuel tank mass measurements. As these markets collectively represent 70% of global of heavy duty vehicle sales, the findings from this white-paper can be generalised to global heavy vehicle trends.

2.1.1 Market Attitudes and Challenges

Drag reduction devices play a large role in reducing the fuel consumption of heavy vehicles. However, there exist market barriers that prevent their incorporation into fleets. Ortega et al. (2013) conducted a survey of 256 trucking companies of various sizes to get their views on the matter. They found that 5% of companies used tractor-trailer gap devices and 4% used trailer skirts. 2-7% of the companies had been planning to use the devices and 27-30% would have considered using them. Importantly, the companies that were using drag reduction devices reported fuel savings in-line with expectations. They found that the purchase price was the main

barrier that prevented the adoption of the devices. Half of the companies were willing to spend $1000 on drag reduction devices. Additionally, half of the companies would have tolerated a payback period of one to two years while a third would have tolerated a three year payback. The survey had highlighted several concerns to truck operators. The lack of durability and maintenance facilities was a concern and was the main reason that companies discontinued using certain devices. The additional weight due add on-devices was a concern as vehicles needed to be kept under the maximum allowable weight. Half of companies were only willing to add 68 kg or less to their vehicles. Lastly, the design and deployment of the device presented a challenge to truck operators. Passive devices that did not require deployment being favoured over more complicated designs where there was a risk of human error or additional cost and complication due to automatic deployment. For this reason passive devices will be the focus of this work.

2.1.2 The Effect of Drag on Fuel Consumption

At highway speeds (65 mph), fuel consumption for heavy vehicles include: engine losses owing to thermal efficiency (60%), aerodynamic losses(21%), rolling resistance (13%) and other losses (5%) (Choi et al., 2008). The aerodynamic drag is governed by the drag equation

$$F_d = \frac{1}{2} C_d \rho A v^2 \tag{2.1}$$

where F_d is the drag force, C_d is a dimensionless coefficient known as the drag coefficient, ρ is the density, A is the frontal/reference area, and v is the velocity. From this it can be seen that drag force increases proportionally with the square of velocity. Thus drag reduction devices are most beneficial at high speeds. In a progress report on their research into heavy vehicle aerodynamic drag reduction, McCallen et al. (1999) considered a modern Class 8 tractor-trailer that possessed a wind averaged drag coefficient of $C_d = 0.60$ and weighed 80,000 pounds. They showed that at 70 mph, the aerodynamic drag represents about 65% of the total energy expenditure. Though the exact portion of energy consumed by drag may vary depending on conditions, it is certain that an improvement in the aerodynamic drag coefficient has a direct impact on the fuel consumption of freight vehicles. This ultimately improves the competitiveness of the business and also reduces emissions. In their review on the topic, Bradley (2010) stated that a 20% reduction in drag could be associated with a 10-15% reduction in fuel consumption for steady highway

travel.

2.2 Heavy Vehicle Drag Reduction Devices

The ill-optimised shape shared by most heavy vehicles is a result of the structure of regulations which often specify maximum dimensions in terms of width, length and height. Almost invariably the most economic option is to maximise cargo volume which results in a cuboidal shape. One of the important differentiators between the aerodynamics of heavy vehicles, as compared to other disciplines such as aeroplanes and cars, is the separated flow in the rear of the vehicle which has a significant impact on the force characteristics. As pressure drag has a much larger contribution than skin friction, the geometry is classified as a bluff body.

At highway speeds the flow speeds can be in excess of Re = 1,000,000. This means the that flow will always be turbulent. The instantaneous picture of the flow therefore exhibits a highly unsteady and turbulent nature. There are three main areas of focus within the tractor-trailer geometry. They include the forebody, underbody, and the base region. Each of the regions has it's own unique flow characteristics. This means that several designs of drag reduction devices exist within each category.

2.2.1 Forebody

The forebody of a heavy vehicle refers to the front-most portion of the vehicle goes by several names including the tractor, and 'cab' which is short for cabin. This part of the vehicle is the area where the majority of drag originates. Relevant locations within the forebody include the tractor-trailer gap, the shape of the leading portion of the vehicle, and devices that operate between the front of the vehicle and the road. According to Wood (2006) who conducted a literature review on the topic, 25% of drag originates from the front face, and 20% from the tractor-trailer gap. The earliest attempts to reduce drag from this region included rounding the edges of the geometry on trucks which at this time had typically been constructed in a faceted manner. Steers and Saltzman (1977) conducted full-scale fuel consumption and drag tests on cab-over-engine tractor-trailer configurations of the time, which were essentially a cuboidal tractor, and a cuboidal trailer. In the test they increased the radii of curvature on all front corners and edges of the tractor, and added a smooth fairing ontop of the tractor that extended to the trailer. They found a 20% to 24% reduction in fuel consumption, as well as a 0.43 reduction in drag coefficient from the baseline value of 1.17 at 88.5 km/hr. Following this, a plethora of drag reduction

devices were devised. Allan (1981) developed the vertical fence shown in Figure 2.1 (a), which when tested on a simplified 1/4 scale model failed to produce any drag reduction. The cab deflector shown in Figure 2.1 (b) is a rounded protrusion that sits above the cab. This device was tested at a 1/10 scale model in wind tunnel by Cooper and Leuschen (2005) at a speed of Re = 1.25×10^6 resulted in a 19.7 % reduction in drag. Malviya et al. (2009a) develop a novel rotating device placed on the leading edge of the trailer shown in Figure 2.1 (c). The device functions by imparting momentum on the near-wall flow, thereby improving flow attachment and reducing the reattachment length. Reductions in flow detachment are synonymous with improvement in drag due to reduced kinetic energy losses in turbulent regions. In their CFD based study they found that the moving surface contributed a 24% drag reduction from the baseline drag coefficient of 0.2593. Hyams et al. (2011) study the front spoiler which is a device that diverts flow from the underbody towards the sides of the vehicle, shown in Figure 2.1 (d). In their computational study based on the Generic Conventional Model geometry they find that the device actually increases the drag coefficient by 0.2%, though they note that in practice the device is expected to reduce drag because of the complex geometry found below real trucks, as opposed to the smooth geometry found in the test geometry.

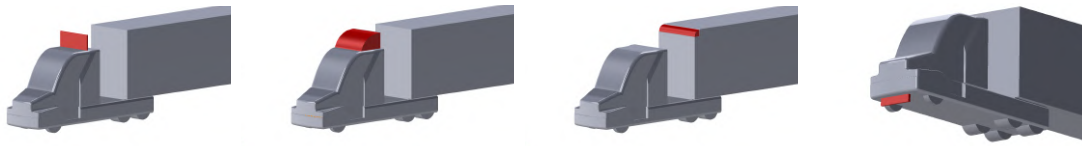

(a) Vertical Fence **(b)** Cab Deflector **(c)** Moving Surface **(d)** Front Spoiler

Figure 2.1: Tractor-based devices

Besides devices that modify the shape of the trailer, another major group of devices for forebody drag reduction acts on the tractor-trailer gap. Muirhead and Saltzman (1979) was among the first to try the gap enclosure shown in Figure 2.2 (a). They conducted their experiments on a 1/25 scale plastic toy in a wind tunnel at speeds up to $Re = 6.12 \times 10^5$. The gap enclosure contributed to a 19.7% reduction in drag from an original drag coefficient of 0.990. However In practice this device is impractical due to the inability of the tractor to articulate. A similar device which is commonly found on modern trucks is known as the side extender, and is shown in Figure 2.2 (b). Storms et al. (2004) studied this device in a wind tunnel on the Generic Conventional Model (GCM) in a 12 foot pressure wind tunnel at 1:8 scale. The flow speed was conducted over a Reynolds number of 500,000 - 6 million (equivalent to full-scale at 75 mph). They measured x, y and z forces and

also used Particle Image Velocimetry to visualise flow fields. They found that the side-extenders reduced drag by a considerable 27% relative to the baseline. They comment that the side extenders function by reducing gap-cross flow. The side extenders are probably the most commercially implemented gap-region device the almost complete closure of the gap, whilst still allowing articulation of the pivot and access to the space. Another device that limits cross flow is the tractor and trailer splitter plates shown in Figure 2.2 (c) and Figure 2.2 (e). Hyams et al. (2011) study the splitter plate at the rear of the tractor (Figure 2.2 (c)) using RANS at 1:8 scale and found no appreciable difference in drag coefficient, though Storms et al. (2004) mention success in the device reducing cross flow. Cooper (2003) research the splitter plate fitted on the front of the trailer that extends to the tractor known as a gap seal. At small yaw angles there is a slight decrease in drag, and at larger yaw angles the performance increases. Wood (2006) study the crossflow trap device through extensive operational fleet testing. The device shown in Figure 2.2 (d) comprises several plates on the front face of the trailer. The device functions by encouraging the formation of vortices within its baffles. Through this a low pressure is generated at the front face of the trailer that helps reduce drag. Moreover the effective narrowing of the cross-flow channel prevents the formation of significant flow separation on the rear of the tractor during cross-wind situations. When combined with side extenders, the authors found an overall 8% fuel savings which corresponds with a 20% drag reduction.

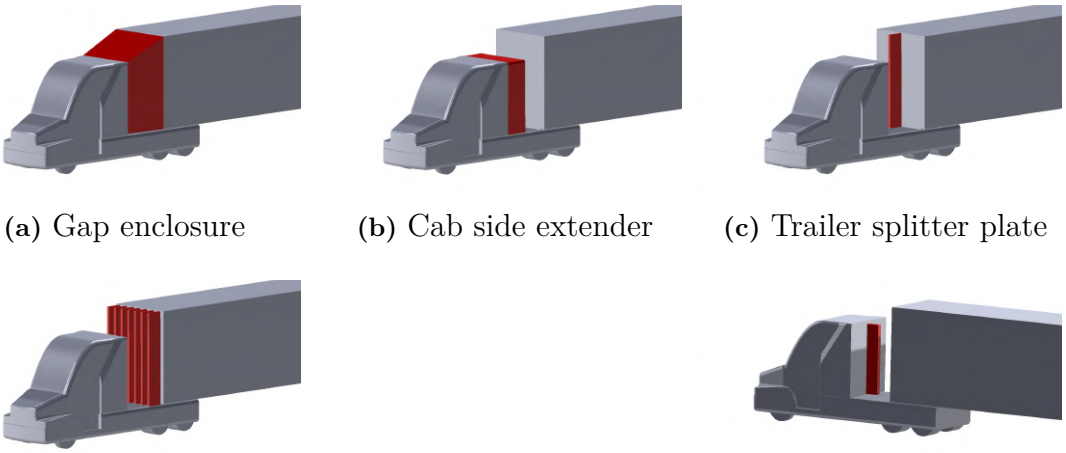

(a) Gap enclosure **(b)** Cab side extender **(c)** Trailer splitter plate

(d) Cross-flow trap device **(e)** Tractor splitter plate

Figure 2.2: Tractor-trailer gap devices

Fore-body modifications is regarded as a sufficiently optimised area as modern designs usually make use of both side-extenders and cab deflectors. Most improve-

ments would therefore come from small adjustments by the manufacturer rather than considering large scale changes to the design.

2.2.2 Underbody

The under-body is another major source of drag with some estimates at around 30% of total drag (Wood, 2006). Despite the major contribution to drag only a few devices exist in this area, which are the belly box (Storms et al., 2004; Ortega et al., 2004), undercarriage wedge skirt (Ortega et al., 2004; Cooper and Leuschen, 2005) and the side skirt (Buil and Herrer, 2009; Ortega et al., 2004; Cooper and Leuschen, 2005). During real-life operations a crosswind of some sort is almost always present. This means that the relative flow velocity almost never flows parallel to the direction of travel. This induces large flows across the underside of the geometry which result in large regions of separated flow. The primary objective of the side skirt is to reduce the flow through the undercarriage. Buil and Herrer (2009) studied a straight skirt device illustrated in Figure 2.3 (a), onto a cylindrical type liquid-holding trailer. In their computational study, they used the k-ϵ RANS turbulence model. The inlet flow velocity was set as 30 m/s (108 km/h) they found that the side skirt reduced the drag coefficient of the vehicle by 9.6%. Cooper and Leuschen (2005) also evaluated the side skirt, but on an experimental basis. They used a 1:10 scale model 40 foot truck inside a 2m x 3m wind tunnel at speeds of Re=1.25×10^{6} which previous research had shown gives full-scale-equivalent flow. The best performing version was the one with long side skirts that gave a drag reduction of 7.4%, which is based on the wind-averaged drag coefficient $\bar{C_d}$. The wind-averaged drag coefficient is the average drag coefficient throughout a range of yaw angles, in this case from 0° to 10°. The undercarriage wedge skirt shown in Figure 2.3 (b) and the belly box shown in Figure 2.3 (c) was also tested by Cooper and Leuschen (2005). The idea with these devices was to divert flow away from the wheel house thereby improving the 0° yaw performance by diverting flow around the wheel house. However in practice neither device showed any improvement over the side skirt with respective wind-averaged drag reductions of 4.4% and 4.2%; in fact the side skirt even outperformed these devices in the 0° case. In commercial operations the undercarriage serves important functions such as storage of spare tyres and other goods such as restrainers. It is vital that any device that operates in this area doesn't limit storage space and prohibit access to the area.

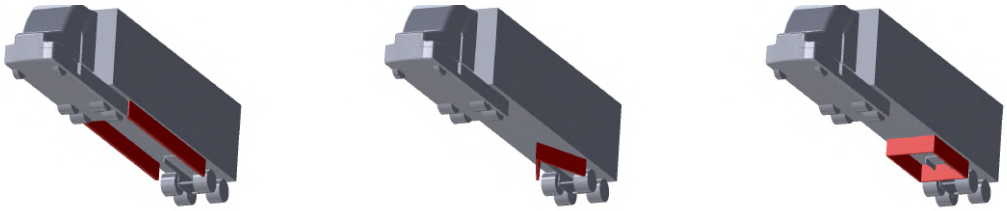

(a) Straight skirt **(b)** Wedge Skirt **(c)** Belly Box

Figure 2.3: Undercarriage devices

2.2.3 Base Region

The base region of the tractor-trailer refers to the rear-most portion where the doors usually are. This area is characterised by a large region of separated flow known as the wake bubble. The wake bubble has a low pressure that acts on the large back surface. Due to the bluff-body characteristic of heavy vehicles, the pressure drop at the base is large. According to some estimates, 25% of the drag originates from this area. Studies show that successful base drag reduction devices tend to make the wake bubble smaller (Balkanyi et al., 2002; Englar, 2001; Gilliéron and Kourta, 2010; Howell et al., 2003). The most effective and practical base drag reduction devices are boat tails and base cavities. A full boat tail is an inward-curving extension of the sides such that it forms a rounded tip at the rear of the vehicle. A base cavity on the other hand is a straight extension of the sides of the vehicle (Figure 2.4 a). A truncated boat tail is similar to a cavity, but it's walls are slanted inwards at an angle (Figure 2.4 b). Peterson (1981) showed that the truncated boat tail has a drag reduction that is comparable of that of a full boat tail. Kim et al. (2020) conducted a study on a sinusoidal variation of a boat-tail edge. The device was shown to reduce drag and side forces by 15.9% and 22.6% respectively with a yaw angle of 7° to the flow. The device was shown to reduce the formation of longitudinal vorticies and improve the streamwise flow. Choi et al. (2008) mention that there is a lack of practical base drag reduction devices, as compared to devices on other regions. He indicates that through a deeper understanding of the unsteady flow in the base region, better and more practical base drag reduction devices can be conceived. For its potential usefulness, and lack of understanding, the base region flow was the focus of this work.

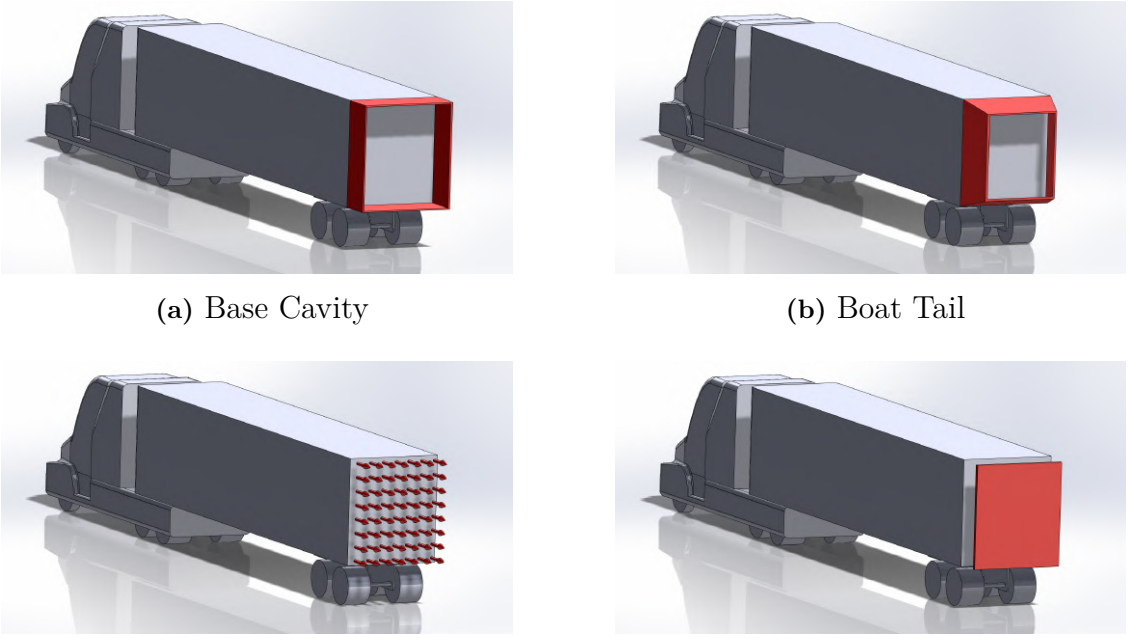

(a) Base Cavity

(b) Boat Tail

(c) Blowing

(d) Splitter Plate

Figure 2.4: Showing several of the most widely researched base-region drag reduction techniques

Flow Features

In square backed vehicles, flow separation occurs at the trailing edge of the vehicle causing a low pressure recirculation region at the rear that contributes significantly to drag. The control of this bubble is one of the main strategies to achieve drag reduction. The creation of the wake bubble starts with the formation a turbulent boundary layer over the sides of the trailer, when the boundary layer then separates from the trailer a free shear layer is formed from each side. These shear layers eventually converge to a point known as the free stagnation point. The area enclosed by these shear layers is known as the wake separation bubble and features a stationary vortex ring. Rouméas et al. (2009) showed that as the shear layers progress downstream, they expand and reduce in intensity. The wake region is found to fluctuate in shape and size. Duell and George (1999) made pressure measurements in the wake of a bus like body and report two periodic processes corresponding to the dimensionless frequencies at Strouhals numbers 0.069 and 1.16. They suggest that the lower frequency value derives from the interaction of the upper and lower sections of the vortex ring and the high frequency component is associated with a vortex shedding phenomena. The higher frequency component is associated with the shear layer vortex roll-up process, and the lower frequency is associated with the low fre-

quency growth and collapse of the wake region. This is known as bubble-pumping. Rouméas et al. (2009) conducted a 3D numerical simulation, and proposed the following mechanism behind the vortex shedding process. Small-scale eddies are first formed in the shear mixing layer near the separation point. As these eddies are fed vorticity provided by shear layer, they grow in size as they convect along the shear layer. When the vortex comes to the end of the wake bubble it draws the opposing shear layer and is released, causing a partial collapse. The stream-wise oscillation of the wake bubble is known as bubble pumping.

It has been established that the larger the wake bubble, the greater the drag. Evaluations of base drag reduction devices usually report the change in size of the wake bubble (Pointer et al., 2009; Storms et al., 2006). It is understood that a larger wake bubble is associated with a greater pressure drop. However, a some of the literature on the subject (Choi et al., 2008; Littlewood and Passmore, 2012) seems to be worded to imply that the size of the wake bubble is responsible for the reduction in pressure. There is little direct explanation for how the low pressure in the wake is formed in the first place, or how the vortex shedding affects this process. There is at least one instance of a contradiction to the proposed logic. Cai et al. (2008) conduct a DNS simulation of a drag reducing modification to a bluff cylinder. They find that despite the modification successfully reducing drag, the length of the recirculation region had actually increased. This contradiction in logic suggests that a more through understanding is required regarding the relationship between the flow dynamics and drag. More work is required in the fundamental aspects of base drag, with emphesis on the causality of drag.

The wake dynamics and flow topology of 3D bluff bodies is drastically different than that of nominally 2D geometries. 2D geometries which are frequently the subject of fundamental studies are characterised by the Karman vortex street. 3D axisymmetric bodies on the other hand, have a drastically different evolution. The first bifurcation of the flow occurs at low Reynolds numbers and entails the breakdown of the axial symmetry of the flow. Fabre et al. (2008) numerically study the instability in the wake of a circular disk and report several bifurcations in the following sequence: at $\mathrm{Re} \approx 115$, a pair of steady stream-wise vortices with reflectional symmetry about a longitudinal plane with arbitrary orientation, known as the steady-state (SS) mode. At $\mathrm{Re} \approx 121$, the flow undergoes a hopf bifurication and reflectional symmetry is lost. Pairs of vortices are now shed periodically. Though there is no actual symmetry, each shed vortex resembles a mirror image of the previous vortex pair. This mode is therefore refered to as a reflectional symmetry breaking (RSB)

mode. At Re $\approx$ 140 a third bifurcation occurs that restores symmetry to the flow. Interestingly the plane of symmetry in this case is found to be orthogonal to the original symmetry plane. This mode is referred to as the reflectional symmetry preserving (RSP) mode. This relates to base region aerodynamics as the flow behind a truck can be assumed to undergo similar transformations as it increases its speed. It should be noted that the Reynolds numbers of this study are orders of magnitudes lower than what would be expected in the wake of a vehicle.

Base Cavity

The base cavity is perhaps the most simple base region device and is interesting because it has a significant impact on drag in the range of 10-20% (Viswanath, 1996), but maintains the separation location. Nash et al. (1963) experimentally investigated the effect of a base cavity on the drag of a two dimensional body. They found that base pressure could be increased by up to 10%. They stated that according to steady-base-flow models, there is no mechanism by which the existence of a cavity at the base could influence the base pressure. For this reason they suggested that the cavity achieves drag reduction by virtue of its stabilising effect on eddies that form in the shear layer. Ormonde et al. (2018) studied the addition of an impermeable and perforated plate to the rear of a backwards facing step. They showed that the perforated plate changes the mean flow field by reducing the intensity of reverse flow close to the bottom wall. Khalighi et al. (2001) conducted a computational and numerical study to improve understanding on the drag reduction mechanisms of an inset cavity device. They measured pressure and velocity fluctuations, and obtained particle image velocimetry images of the base region. They reported that the device achieved a drag reduction that is caused by the deceleration of flow due to re-attachment on the device thereby increasing the pressure in the base region. This result eludes to the fact that turbulent flow prevents pressure recovery; the kinetic energy that would have been restored to pressure is instead dissipated as heat. The base cavity device reduces turbulence. Therefore more flow energy can be restored to pressure and the flow enjoys a better pressure recovery and reduced drag. Kruiswyk and Dutton (1990) experimentally studied a two dimensional body with a base cavity using the Schlieren technique to visualise the vortex shedding process. They also reported that the vortex shedding was weakened by the cavity and that this is associated with a higher base pressure. They reported that increasing the depth of the cavity beyond ½ base height does not have a significant effect on the drag reduction; the most dramatic changes occur just as a result of having a cavity in the first place up to ¼ base height. Their results contrast with the

hypothesis from Nash et al. (1963), that the drag reduction mechanism is related to a stabilisation of the vortex shedding process. Their imagery showed no evidence that the vortex shedding was modified by the cavity. Molezzi and Dutton (1995) studied the near-wake structure of a two dimensional base using particle image velocimetry to determine the fluid dynamic mechanisms associated with the drag reduction of a base cavity. They report that the vortex street is slightly weaker though not enough to account for the significant drag reduction. They suggested that the drag reduction is due to the displacement of the base surface further from the low pressure region associated with the vortex street. Viswanath (1996) experimentally evaluated several base drag reduction techniques. A key insight from that study is that the level of base drag reduction in axisymmetric geometries is comparable to two dimensional geometries. This is interesting because axisymmetric geometries tend not to produce any periodicity. So this is complementary to the finding by Kruiswyk and Dutton (1990) that the mechanism is not primarily involved with the Karman vortex street. They suggested that the increase in base pressure may be related to other effects. Martín-Alcántara et al. (2014) numerically studied the effect of a base cavity on a nominally 2D object using the Improved Delayed Detached Eddy Simulation (IDDES) methodology. They studied the effect of increasing the cavity depth and limit the cavity depth to a maximum of 0.3H citing practicality reasons. They found that the drag decreases monotonically before reaching an asymptotic value. They report that the inclusion of a 'multi-cavity' (i.e. more than one cavity in the base facilitated by the inclusion of an extra separating plate in the middle of the base) improves the drag reduction considerably. They found that the multi-cavity makes the flow less chaotic. Evrard et al. (2016a) numerically studied the effect of the base cavity on the instability known as the reflected symmetry breaking (RSB) mode. The RSB is an unstable horse-shoe shaped vortex that occurs in the rear of 3D bluff bodies. The crest of the horseshoe oscillates from one trailing edge to the other, with its toes facing the downstream direction. They found that the addition of the base cavity stabilises the wake by replacing the RSB with a stable toric rotation. Their findings complement our previously outlined hypothesis. The stabilisation of the wake leads to reduced fluid mixing between the freestream and the wake, therefore shear force is reduced leading to a higher base pressure.

In the context of heavy vehicles, the base cavity has been a well explored topic. Balkanyi et al. (2002) experimentally evaluated the effect of a base cavity of length ½ of the height on a square-back Ahmed model. They reported a 12% reduction in drag. Besides increasing the pressure recovery, they also found that the inclusion of

a cavity improved the homogeneity of pressure in the base region. Expectedly they found that the wake bubble is displaced in the stream wise direction by the length of the cavity. Through a vertical velocity probe in the centreline of the geometry at a position 1.5 model heights downstream of the base, they measured turbulence intensity. They found that the base cavity has a strong influence on the turbulence, most pronounced in the high turbulence regions such the shear layer. Khalighi et al. (2001) conducted a similar analysis on the Ahmed model, but they focused on the transient effects of the cavity. They compare an inset cavity to a standard square-back. They find the cavity has a very significant effect on the instability that occurs at St 0.07. In fact, by comparing spectral plots with and without the device, these instabilities seem to be completely attenuated.

2.3 Unsteady Heavy Vehicle Aerodynamics

In recent years, our understanding of unsteady characteristics of the flow around a heavy vehicle has developed. The research interest involves around developing a greater fundamental understanding as to develop better drag reduction strategies. The structure of the wake of square-back geometries is analogous to square back bluff-bodies with an aspect ratio between their height and width above unity (Castelain et al., 2018). Simulations by Krajnovic and Davidson (2003) and Rouméas et al. (2009) show that there is a toroidal structure that interacts with surrounding shear layers to form a pair of counter-rotating vortices downstream of the wake. Furthermore, Perry et al. (2016) confirmed their existence in an experimental study. The detailed characterisation of the dynamics of such wakes is still the subject of intense research with a greater emphasis on detailed elucidation of the behaviour. One research gap that has recently been explored is the effect of more realistic geometries compared to the simplified geometries that had been explored in the past. Haff (2015) measured on-road base pressure measurements and performed particle image velocimetry (PIV) measurements in the wake of a full-scale truck at a Reynolds number of 4×10^6. They show a large scale vortex in the lower part of the vehicles plane of symmetry which is similar to the vortex found in the simplified geometries.

A phenomenon that has been widely reported involves the instability modes in the wake. Earlier works include Duell and George (1999) who studied the wake of an extruded rectangular square-backed body with rounded leading edges in proximity to a moving ground plane. Two unsteady motions were identified and named bubble pumping and the shear-layer vortex shedding respectively. The former is

characterised as a quasi-periodic vortex emission from the wake at a frequency of St = 0.069. At this frequency the pressure peaks at the top and bottom of the base are approximately 180 degrees out of phase which implies an interaction between the upper and lower parts of the ring vortex. The shear-layer instability is characterised by a higher frequency of St $\approx$ 1.157 is associated with the well-understood vortex roll-up and discharge process that occurs in the shear layer. Littlewood and Passmore (2010) experimentally studied the Windsor model using PIV and described the vortex shedding process in the upper shear layer as a Markov chain which implies that shedding may occur for a number of cycles before being interrupted and being absent for some time. Subsequent findings from Varon et al. (2017) suggest that the low-frequency dynamics may be considered as a weak chaotic process with two attractors.

McArthur et al. (2021) experimentally studied a detailed tractor trailer model with the objective of discerning the differences in flow characteristics that more detailed geometries provide. They report a similar pumping mode of St $\approx$ 0.07 and also a lateral von Karman-like shedding at St $\approx$ 0.2. They found that models fitted with devices such as boat tails demonstrated a significant restructuring of wake flow topology. The addition of a boat tail resulted in the upper portion of the wake becoming steady whereas strong low-frequency oscillations were present downstream of the wheels. Recently, our understanding of the wake behavior of a heavy vehicle has advanced to include a mode known as the bi-stable mode. First reported in a 26mm Ahmed model at a low-speed hydrodynamic facility, Grandemange et al. (2012a) showed the existence of a permanent reflectional symmetry breaking state for the wake. The wake begins with a symmetrical shape (torroidal vortex). The first bifurcation from this occurred at ReH = 340 where the flow adopted a steady breaking state with reflectional symmetry. At the higher speed of $Re_H = 410$ the flow develops into a bi-stable behaviour via an imperfect supercritical bifurcation. This behaviour has been demonstrated at Reynolds numbers of up to ReH = 10^7 (Grandemange et al., 2015). The same trend has been captured in the large eddy simulations performed by Evstafyeva et al. (2017). In further studies, Grandemange et al. (2013a) showed that the well-known symmetrical bubble in steady state studies is actually the result of the left/right bi-stable behaviour of the flow. In other words while the time-averaged wake profile was found to be statistically symmetrical, the instantaneous flow fluctuated around one of the two asymmetric states. The two phases are mutually symmetric and switch randomly on a long time scale of the order of $10^3 \cdot H/V_\infty$. In the same work, coherent oscillations were found in both the

lateral and vertical directions in the wake behind the recirculation bubble. Their oscillation frequencies are close to St ≈ 0.17 which is coherent with results of Khalighi et al. (2012). This behavior has been shown to induce instantaneous pressure losses of about 25% (Volpe et al., 2014). Volpe et al. (2015) found evidence that the previously reported pumping mode exists simultaneously with the later reported bi-stable mode at a Reynolds number of ReH $= 5.1\times10^5$ and $Re_H = 7.7\times10^5$. The wake pumping, with a normalised frequency of $St_H = 0.08$, was found to be predominant in the shear layer of the recirculation bubble. In experimental studies with long time-spans this phenomenon is referred to as bi-stability, which is characterised by the random occurrence of the bi-stable states (Rao et al., 2018). In numerical solutions on the other hand only one of the two possible flow states are usually observed. While the bi-stable states observed in the wake of the squareback Ahmed body occur in the lateral midplane, the two flow states in the Generic Transport System (GTS) wake are observed in the vertical mid-plane. Flow state I was observed in numerical simulations by McArthur et al. (2016) and Gunes (2010), and flow state II in Schmidt et al. (2018),Rao et al. (2018), Ortega et al. (2004) and Unaune et al. (2005). Grandemange et al. (2013a) further characterised this bi-stable behaviour through testing the Ahmed body in a 3/4 open jet wind tunnel at $Re_H = 9.2 \times 10^4$. They found that the characteristic time between switches can be estimated as T_l $10^3 H/V_\infty$. In Grandemange et al. (2013a), it is shown that this long periodic motion yields an unsteady side-force that must be responsible for part of the drag. A shorter time-scale Ts $5H/V_\infty$ was also observed and was attributed to weak coherent oscillations of the wake in the vertical and lateral directions, associated with the interaction of top-bottom and lateral shear layers. No evidence of bubble pumping was found . This behaviour has been found to occur independently of the frontal shape of the bluff body and any planar symmetry that the body may possess Rao et al. (2018), conversely it has been found to be sensitive to other parameters such as aspect ratio, ground clearance Grandemange et al. (2013b) and the yaw angle (Cadot et al., 2015; Volpe et al., 2015). Studying the effect of base aspect ratio on the bi-stable mode away from the ground plane, Grandemange et al. (2013b) revealed that with a wide aspect ratio (W>H) the preferred direction of the bi-stable mode was laterally. Similarly for a tall aspect ratio (H>W) the preferred direction was vertically. In other words the wake orientation generally switches between the two further apart edges. In geometries that have axisymmetric properties such as spheres (Chrust et al., 2013; Grandemange et al., 2014), and cylinders with a sharp trailing edge (Rigas et al., 2015; Gentile et al., 2016), the instability doesn't exhibit a preferred direction since there is an infinite number of azimuthal symmetry planes.

Also considering an axisymmetric body, Grandemange et al. (2013a) showed that when the wake is forced to be symmetric in the lateral direction then the asymmetry is expressed in the vertical direction. Curiously the number of preferred positions on axisymmetric body such as a sphere (Grandemange et al., 2014) or cylinder Grandemange et al. (2012a) can be reduced to two by applying a pertubation to the base with an azimuthal wave number of m=2; thus a bi-stable behaviour is produced as with the square-backed geometries.

The effect of a mild yaw angle of +-1° was experimentally studied by Volpe et al. (2014). They found that the essential structure of the bi-stable mode remained in-tact however the probability distribution of the two wake states varied with yaw angle. For yaw angles > 1° only one of the flow regimes was stable and the wake became permanently asymmetric. Also present were dynamics that occured at higher frequencies than the bi-stable modes of St = 0.13 and 0.19 which were attributed to von Karman shedding between the vertical and horizontal edges of the base respectively. Simultaneously a low frequency peak was found at St = 0.07-0.08 which is associated with the bubble pumping dynamics (Khalighi et al., 2001, 2012; Duell and George, 1999). Ground clearance can vary depending on the practical use of the vehicle. The ground clearance affects the flow blockage in the underbody and results in different wake topologies. When clearance G > 0.14 H, the bulk underbody flow is close to the free-stream velocity (Croll et al. (1995); Gutierrez et al. (1995); Islam et al. (2017); Storms et al. (2004); Van Raemdonck and Van Tooren). The near-wake is then composed of a re-circulation bubble that is detached from the ground, not dissimilar from the wake topology of the Ahmed body (Ahmed et al., 1984) , Windsor (Littlewood and Passmore, 2012) or ASMO models (Tsubokura et al., 2010). For full-scale trucks on the other hand the under-body bulk velocity ranges from 10-40% of the freestream velocity. This results in a wake that hugs the ground due to limited momentum flux from the underbody flow (Castelain et al., 2018). Kowata et al. (2009) added a slanted underbody geometry to the square-backed Ahmed body. Varying the angle would result in a change of underbody velocity which has drag reducing properties. Perry and Passmore (2013) studied the effect of roughness on under-body velocity which led to a change in underbody velocity through induced pressure losses. The effect of a moving versus stationary ground plane can also affect the underbody bulk velocity. Garry (1996) measured the base pressure of bluff bodies with aspect ratio H/W >1. They varies the ground plane velocities ranging from zero to the free-stream velocity. Krajnović and Davidson (2005) showed that the influence of the motion of the ground on the wake topology

is qualitatively limited to the wake region near the ground. The effect of changes in ground clearence on square-back bodies with different aspect ratios was studied by Grandemange et al. (2013b) . Base pressure and ground clearance were found to exhibit a non-trivial relationship. The minimum base pressure was found at a ground clearance of G/H=0.045. This critical ground clearance is identified as the transition from a backwards facing step topology to a common wake topology of a simplified vehicle. McArthur et al. (2016) varied the ground clearance of the GTS model and characterised the wake from G/H = 0.14 to G/H = 0.03 by use of PIV. Reducing ground clearence was found to cause significant changes in both steady state and transient wake topology, with the wake becoming fully attached to the ground plane and the main upper vortex transitioning to an almost quasi-steady state. Castelain et al. (2018) experimentally studied the near wake of a simplified truck model with an aspect ratio H:W greater than one. They classify four different classes of flow. In the first class, high levels of transverse velocity flucuations are reported along with a re-circulation bubble that that remains in the upper part of the wake. The second class is characterised by high values of vertical base pressure gradient and high mean base pressure together with back-flow of the under-body into the general wake. The third class has a high back-flow intensity which induces a large increase in the streamline pressure gradient directed towards the model base. Furthermore the stagnation point is close to the top of the wake and a new wake structure comprising a recirculating bubble located near the ground is observed. Finally the fourth class is characterised by the presence of two counter-rotating bubbles detached from the ground as in previous studies of Ahmed body or GTS. These classes are in qualitative agreement with the classes identified by McArthur et al. (2016) in which only ground clearance was changed. The aspect ratio (L/W) of a separated wake is known to have a significant effect on bluff-body drag (Roshko, 1955). Bearman (1965) found an approximately linear correlation between base suction and the reciprocal of vortex formation length. Furthering the vortex core formation area from the base results in less suction on the rear surface and therefore reduced drag. Furthermore it has been shown that thicker seperating boundary layers results in an increased base pressure due to less momentum from the free-stream being entrained into the wake as describer by Hoerner (1965) and Mariotti and Buresti (2013).

The addition of devices can have profound effects on the reflectional symmetry breaking mode. Evrard et al. (2016b) found that the strength of the vortex system associated with the reflectional symmetry breaking mode decreased as cavity depth was increased, yielding a reduction in drag until a saturation depth was reached at

d>0.24H. They also proposed a new topology for each reflectional symmetry breaking state, comprising a horseshoe vortical structure. According to this explanation, the toroidal vortex usually reported (Krajnovic and Davidson, 2003; Rouméas et al., 2009); is the result of the temporal average of these asymmetric structures. In the same study suppression of the St = 0.069 pumping mode by adding the base cavity is achieved which resulted in an increase of up to 11% of base pressure and reduction in pressure fluctuations. Khalighi et al. (2001) report similar results using a different square-backed geometry with an aspect ratio of 1.4. The behavior of the bi-stable mode can be achieved through passive or active means to have a tangible effect on drag. Through placement of a small vertical control cylinder in the symmetry plane of the wake at a distance of 0.7 H downstream of the base, the two bi-stable phases were no longer observed by Grandemange et al. (2014) and the flow instead oscillated around a symmetrical topology. The result of suppressing the asymmetry was an increase in the mean recirculation length together with a drag reduction of 5.8%. It has recently been shown that the large-scale oscillations behave like a high-dimensional chaotic system with a well defined strange attractor Varon et al. (2017). Through the analysis of the evolution in time of the pressure center of the base, they demonstrated that the global dynamics of a turbulent 3D wake can be reduced to a simple dynamic system charaterised by a set of two variables. Faranda et al. (2017) found similar results in turbulent swirling flow. If such a simplification is possible, then the application of a simple forcing may be sufficient to control the dynamics of the wake. Active flow control devices shows promise as a means of base-pressure recovery without increasing vehicle length or decreasing cargo capacity. One class of modern active flow control devices aims to reduce the effect of low pressure wake vorticies on the base surface. Bruneau et al. (2010) used targeted blowing to move vortex cores away from the vehicle base wheras Pastoor et al. (2008), Parkin et al. (2014), Parkin et al. (2015) and Phersson et al. (2014) used constant frequency pressure oscillations to force synchronous vortex shedding from both sides of the body. This had the effect of delaying the formation of large-scale vorticies further downstream. A feedback control system with the aim of symmetrising the bi-modal dynamics of a bluff body was proposed by Li et al. (2016). The flow was controlled by two lateral slit jets and pressure sensors acted as the closed-loop feedback. A 2% increase in base pressure was achieved through stabilisation of the unstable symmetric state observed during the transition between bi-stable states. Brackston et al. (2016) employed a more efficient actuating system with moving flaps. The feedback control system employed a nonlinear Langevin equation consisting of a deterministic part, describing the evolution of the large-scale structures, and a stochastic term,

capturing the effects of the turbulent forcing.

2.4 Bluff Body Drag Reduction Techniques

The overarching strategy with this research project is to identify a drag reduction technology that has been tested fundamentally, but has not been attempted on a heavy vehicle. Therefore in this section flow control methods for bluff bodies are reviewed. Control of drag behind bluff bodies remains of consistent interest as the subject has implications in a wide variety of problems. Cylinders oriented in a span-wise direction are the frequent subject of fundamental bluff body research. Their two-dimensionality reduces the complexity of flow to allow the effect of certain devices and modifications to be discerned adequately. Furthermore the flows and effects of devices are often analogous with three dimensional flows which make the research applicable to practical situations. Other popular geometries include the sphere which is the simplest three-dimensional body. Bluff-body flow control can broadly be divided into three categories. Listed with respect of increasing complexity they are passive control, active open-loop control, and active closed-loop control. Passive control methods rely on non-actuated components. At most basic these are static structures that modify the flow, or in other cases are dynamic and flexible membranes that move as a result of the flow. Active flow control refers to actuation of some type, open loop representing a fixed instruction to the actuator, whereas in a closed-loop system the actuators may respond to sensors. The range of mechanisms may further be divided by whether they are two-dimensional forcing, or three-dimensional forcing; and also whether they control the incoming boundary layer thus reducing flow separation, or control the wake characteristics directly.

Passive devices are viewed as being the most practicable devices due to their inherent simplicity. To revisit some of the significant works in this area, Shih et al. (1993) studied the effect of surface roughness on a circular cylinder oriented in a span-wise direction to the flow in a 12 foot wind tunnel. They tested roughness of roughness values (k/D = roughness scale/cylinder diameter) of k/D = 0.0003, k/D = 0.0012, and k/D = 0.0101. They found that at high speeds, the roughness increased the span-wise coherence of the vortices, and also the intensity of the fluctuating forces, when compared with smooth cylinders at Reynolds numbers in the range of 5×10^5 to 100×10^5. The drag coefficient of the roughest cylinder showed greater Reynolds number independence across the range, and there was a 16% decrease in drag at $Re = 10^6$. Choi et al. (2006) studied the mechanism by which dimples on

a sphere reduce drag by way of an experimental study featuring flow visualisation and hot wire probes for velocity profile measurements. They tested at speeds of $Re = 0.5 \times 10^5$ to $Re = 2.8 \times 10^5$. The well-known cause of drag reduction in dimpled surfaces is related to turbulence being generated in the near-wall boundary layer. The mechanism they discovered is that the flow separation that occurs as the flow passes over a dimple, causes local shear layer instabilities which have the effect of increasing momentum transfer to the near-wall flow; this provides enough momentum for the flow to reattach to the sphere on the downstream side of the dimple. Lim and Lee (2002) studied the application of longitudinal grooved surfaces to circular cylinders experimentally. They measured drag force, mean velocity, and turbulence intensity profiles of the wake behind the bluff body. They used particle tracer techniques to qualitatively visualise the flow. They studied flow in the range of $Re = 8 \times 10^3$ to $Re = 1.4 \times 10^5$. A U-shaped groove had the effect of reducing drag coefficient by 18.6 %. Flow visualisation results showed that the grooves had the effect of breaking up the vortex shedding which usually has a high coherence in the stream-wise direction. Anderson and Szewczyk (1997) studied the effect of incorporating a plate aligned in the stream-wise direction in the wake of a circular cylinder experimentally. They used a lead precipitation flow visualization technique which particles were incorporated into the flow at the separation point. This technique allows for clear discernment of the vortices in the shear layer. They found that the incorporation of the splitter plate reduced the level of three-dimensionality of vortices in the wake by stabilising the flapping behaviour of the flow; in most cases greater the intensity of vortex shedding, the higher the drag. In a review of various means to suppress vortex shedding, Zdravkovich (1981) concludes that the most important factor in successful vortex suppression is how far the region where vortices are formed (formation region) has been moved down-stream. Further formation regions are associated with less intensity, and also less adverse interaction with the body. Rodriguez (1991) study the effect of a segmented trailing edge of a thick plate in a water tunnel. Through heating the plate, they are able to use Schlieren imaging in order to image the density variations that are influenced by vortex activity. Through this they find that the vortex shedding which is usually span-wise coherent, is broken up into sections that correspond with the sections of serration. They propose that the geometry creates transverse flow into the spaces created by the serrations that contribute to the longitudinal part of the 'U' shaped vortices that shed. This effect is illustrated in Figure 2.5 where clockwise vortices are shed from the top surface, and anti-clockwise from the bottom; also visible are the longitudinal components of the shed vortices which may contribute to the

stablilization of the vortex shedding through mitigating the unstable span-wise interaction that is characteristic of Karman vortices. There is a class of bluff body drag reduction devices that are similar in result that utilise a wavy profile that are reviewed in more detail in the next section.

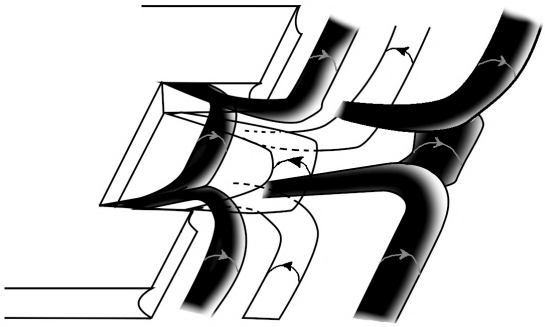

Figure 2.5: Illustration of how a serated trailing edge results in U shaped vorticies that terminate at the serations, as per Rodriguez (1991).

2.4.1 Wavy Geometry Bluff Body Drag Reduction

Found in Nature

A number of natural species make use of a waviness in geometry that they use in to a variety of advantages. Harbour seals have the ability to hunt pray even in conditions that far surpass the range of hearing and vision. To do this they rely on sensing small disturbances in the water with their whiskers. Their whiskers are sensitive enough to detect displacements of 1 μm. Remarkably, they can recognise their pray through the characteristics of the disturbences in the trail. The hydrodynamic design of the whisker plays a large role in the sensitivity of the whisker. The whisker is elliptical in cross section and has a wavy morphology such that the ratio of major to minor axis changes with length (Figure 2.6). Hanke et al. (2010) conducted an experimental and numerical study on the seals and their whiskers respectively. They find that the dynamic forces on the whisker of a harbor seal is at least one order of magnitude lower than that of the sea lion which does not share the undulated structure. They find that the wavy pattern suppresses vortex shedding (Figure 2.7) and reduces drag by up to 47% as long as the plane of waviness was parallel to the flow.

The humpback whale is another animal that makes use of this wavy geometry. The leading of the flippers have around 10 to 11 large protuberances across it's span such that it forms an irregular wavy pattern. It is believed that these turbacles assist the

Figure 2.6: A close-up sketch of the undulating shape of a Harbour Seal vibrissa.

whale to perform tight maneuvers while hunting. In their review of the topic, Fish et al. (2008) explain that the turbacles induce vorticity in the flow. The enhanced mixing of the flow provides the near-wall flow with the kinetic energy required to overcome the adverse pressure gradient. As a result, flow-separation is prevented. The principle of operation is similar of that as vortex generators found on the roof of sedan cars near the rear windshield which prevent flow separation and therefore reduce drag.

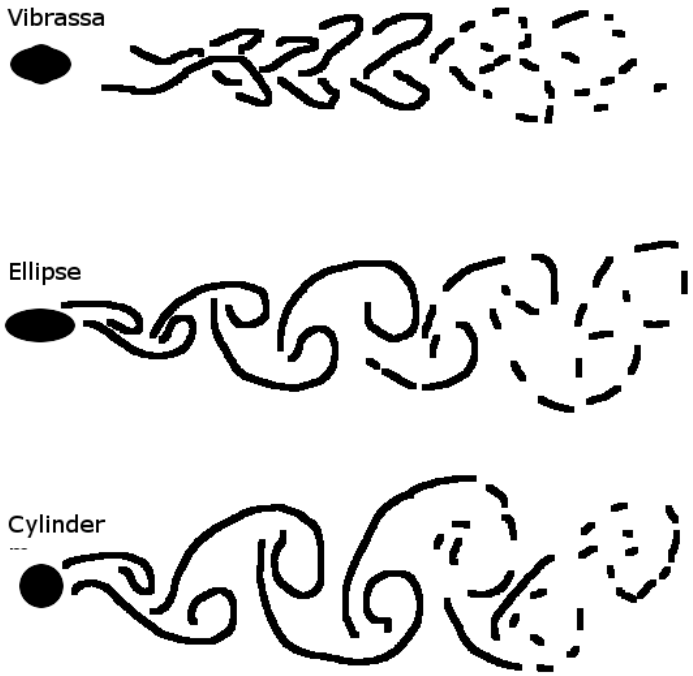

Figure 2.7: A illustration comparing vortex shedding characteristics behind a cylinder, an elliptical cylinder, and the wavy cylinder. (Hanke et al., 2010)

Fundamental Studies of Wavy Device

In a similar vein, there exist a range of planar drag reduction devices that are based on modifying the geometry of the trailing edge through the incorperation of a wavy trailing edge. Tombazis and Bearman (1997) experimentally studied a wavy trailing

edge geometry on a nominally 2D half-ellipse geometry that is oriented with its major axis in line with the flow. They tested a variety of steepness' and found the greatest reduction in base suction was achieved with the most steep wave. This led them to suggest that the steeper the wave, the greater the drag reduction. Through a flow visualization technique they were able to determine that the wavy geometry introduced vortex dislocations. They propose that the mechanism of drag reduction is related to the break up of otherwise coherent vorticies, similar to the mechanism described previously and shown in Figure 2.5. This idea of breaking up coherent vorticies is supported by a study by Park et al. (2006) in which they add small tabs on the trailing edge, which are oriented normal to the flow direction. They also report a drag reduction in the time-averaged drag coefficient that is attributed to the break-up of the Karman vortex street. Bearman and OWen (1998), conducted further work on implementing the wavy feature on the stagnation face of a square cylinder and showed that it was able to suppress the Karman vortex street with only a relatively small wave steepness of 0.09. Cai et al. (2008) extended this work with a Direct Numerical Simulation (DNS) study. They used a fairly shallow waviness amplitude of 1/2 a height while varying the wavelength of the waviness from 3 heights to 7 heights. They found that the waviness of 5h performs best, achieving a drag reduction of greater than 30%. Through analysing a time series of drag coefficient they make some important findings. The time-series of drag coefficient of the straight edge geometry can be seen to vary with time between the drag coefficients of approximately 0.3 - 0.6. Through inspection of correlated vortex identification visualisations, the periods of high drag are correlated with long and coherent span-wise vorticies. Periods of low drag are correlated with broken, U-shaped vorticies that resemble those formed with the modification. Moreover, the moving average drag coefficient for all of the tested models fall within the upper and lower bounds of the time-varying drag coefficient of the straight edged case. This implies that the wavy geometry seems to lock the shedding mode to the U-shaped vorticies that are associated with lower drag. Furthermore a possible lower bound to the drag reduction is suggested by looking at the minimum drag coefficient value of the straight-edged geometry. Kim and Choi (2019) studied the effect of spanwise length to perturbation length and found that in geometries where the pertubation length λ equals to the domain width, the drag reduction of devices is exaggerated. The majority of studies on this shape involve nominally 2D geometries for which the Karman vortex street is a dominant mechanism. The breakup of this vortex street is commonly cited as the drag reduction mechanism. However, the vortex street is not a prominent feature of 3D geometries such as that of a truck. For this reason it

is unclear to what extent the geometry could be beneficial for a commercial tractor-trailer. This point highlights the interest in applying this geometry to a truck.

2.5 Fundamentals of Massively Separated Flows

When investigating a complex phenomena it is natural to study the simplest form which exhibits similar properties. In the case of massively seperated flow in the wake of a truck, the Backwards-Facing Step (BFS) is a frequent choice as it shares many of the fundamental features of these flows (illustrated in Figure 2.8 and outlined in Table 2.1). Flow features include a fixed point of separation, a free shear layer, flow reattachment, several modes of instability, and turbulence. Due to the simplicity of the geometry and the pervasiveness of its features in other engineering flows, there has been continual interest in this geometry through the years. Typical control parameters of this flow include step height, expansion ratio, boundary layer properties at the step and Reynolds number.

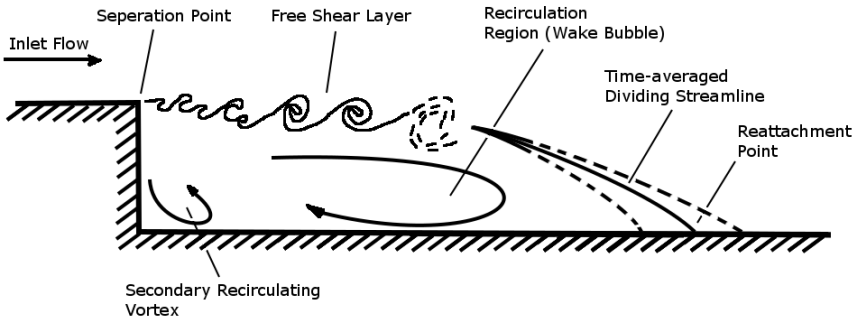

Figure 2.8: An illustration showing the general flow features of massively separated flow.

In the classical picture of the backward-facing step (Armaly et al., 1983; Eaton and Johnston, 1982; Driver et al., 1987), the flow begins with the development of a boundary layer upstream of the step. When the flow reaches the step, it separates from the surface and forms a free shear layer that curves downwards towards the lower surface. The flow, in general, is known to be three-dimensional (Bandyopadhyay, 1991; Friedrich and Arnal, 1990; Fureby, 1999; Furuichi and Kumada, 2002; Neto et al., 1993). This originates from coherent vortex structures that are recognised to play an important role (Troutt et al., 1984). Historically, the mainstream fluid-dynamic community had recognised two periodic processes, shear layer vortex

Table 2.1: A summary of phenomena within massively seperated flows (Eaton and Johnston, 1982)

Phenomenon	Location	Description
Flow Seperation	Trailing edge of step	Phenomena whereby flow field lines become detached from the surface at a gradual or sudden drop in pressure
Wake Bubble	Beyond and below the step	Low pressure region in the wake of the flow
Shear Layer	Interface between wake bubble and main flow	Characterised by span-wise shear-driven vorticies known as Kelvin-Helmholtz vorticies
Flow Instability	Found anywhere, typically downstream of a disturbance	An organised fluid motion driven by an underlying imbalance of forces
Turbulence	Within boundary layer and down-stream of step	A pattern of fluid motion characterised by chaotic changes in velocity and pressure

shedding and also the periodic oscillation of the reattachment point known as flapping. The frequencies of flapping and vortex roll-up correspond to St $\approx$ 0.06 and 0.23 respectively (Schäfer et al., 2009). The roll-up process was well understood, though the source of the flapping motion was an item of debate. To give an example of contrasting views, Eaton and Johnston (1982) proposed that an imbalance between shear layer entrainment and a re-injection of fluid near the reattachment point causes the volume of fluid in the recirculation to fluctuate. Whereas Driver et al. (1987) suggested that the phenomena is related to an escaping vortical structure from the recirculation zone. Spazzini et al. (2001) report that most authors did not directly observe a flapping motion; they only detected a low-frequency oscillation in either velocity or pressure fluctuations. To this day the source of the flapping behaviour remains elusive.

In another branch of fluids, the application of stability theory into describing fluid behaviour was finding success at explaining fluid behaviour. One early such example is the description of Tollmien-Schlichting wave packets in the boundary layer (Gaster, 1975). During the nineties, the popularisation of the application of stability theory into fluidic processes by Huerre and Monkewitz (1990) and others led to the formation of theoretical frameworks that can concisely describe seemingly complex flows. To recount the main themes, local instabilities relate to specific areas in the flow that cause intrinsic disturbances to amplify. These are further categorised into two groups. Local convective instabilities only amplify as they ad-

vect downstream; whereas local absolute instabilities may propagate upstream from their point of inception. The well-known Kelvin-Helmholtz instability in the shear layer is therefore categorised as a local convective instability. Global absolute instabilities (or sometimes just global or absolute instabilities), on the other hand, relate to dynamic effects that are intrinsic to the entire flow field. A growing body of evidence shows the existence of a global mode that is related to Taylor-Görtler and Taylor-Couette instabilities in backward-facing step flows. This has been shown in a stability analysis by Barkley et al. (2002) and an experimental study by Beaudoin et al. (2004). These are three-dimensional convective flow patterns that result from centrifugal effects. For this reason, the curvature of the flow beyond the step is suspected as the probable source. One of the earliest observations was that the onset of the longitudinal vortices seemed to coincide with the formation of the secondary recirculation region on the upper wall (Armaly et al., 1983). They explain that the formation of upper vortex subjects the main flow to a destabilising concave curvature. However, linear stability computations from Barkley et al. (2002) rule this hypothesis out. Nevertheless, they still maintain that it is a centrifugal effect but give evidence that attributes it to the curvature of the flow around the recirculation region. Moreover, the span-wise infinite nature of their computations shows that the three-dimensionality is inherent to the flow [also reported by Armaly et al. (1983), Kaiktsis et al. (1996)], rather than being exclusively an artefact of side-wall interactions. This is therefore classified as a global absolute instability. The generation of turbulence is caused by a causal sequence of instabilities that successively decrease in scale. Energy from large-scale disturbances is passed through the chain of instabilities until they reach the Kolmogorov microscale where the energy is dissipated as heat through viscous action. This is the mechanism for the well-known energy cascade and also for the emergence of turbulence. Less clear is what the secondary interactions look like, and how they reciprocate with one another. Kostas et al. (2005) mention that despite the importance of these interactions in the generation of turbulent stresses and turbulent kinetic energy, the area has received little attention. These interactions are thought to bring about enhanced heat transfer properties that has also been recently studied [Zhao et al. (2018), Xie et al. (2017)].

2.6 Instabilities

In the following section we will review in greater depth some other types of instabilities and where they are found. This is in an attempt to establish a greater understanding of the instability phenomenon from different sources. The impor-

Table 2.2: A summary of fluid instabilities (Swinney and Gollub, 1981)

Instability	Conditions	Forces	Stabilised by	Non-dimensional Number
Dean	Channel flow around a curve	Centrifugal, Pressure	Viscosity	$DeanNumber = \frac{\sqrt{\frac{1}{2}(inertial forces)(centripital forces)}}{viscous forces} = R_e\sqrt{\frac{D_e}{2R_c}}$
Taylor-Gortler	Boundary layer over a curved surface	Centrifugal, Pressure	Viscosity	$GortlerNumber = \frac{U_e\theta}{\nu}\frac{\theta}{R_c}^{1/2}$
Taylor-Couette	Closed parallel rotational system	Centrifugal, Pressure	Viscosity	$TaylorNumber = \frac{4\Omega^2 R_c^4}{\nu^2}$
Rayleigh–Taylor	Density interfaces	Buoyancy, Weight	Surface Tension	$AtwoodNumber = \frac{\rho_{heavy}-\rho_{light}}{\rho_{heavy}+\rho_{light}}$
Kelvin–Helmholtz	Shearing flows	Pressure	Surface Tension, Viscosity	$RichardsonNumber = \frac{Buoyancyterm}{ShearTerm} = \frac{\nabla\rho}{\rho(\nabla u)^2}$

tance of an understanding of instabilities is that they are thought to be the source of turbulence. The phenomena of fluid instabilities are generally associated with parallel shear flows (Lin, 1955; Drazin and Reid, 2004) though a range of other sources exist. They are fundamentally caused by competing forces in the system. Table 2.2 lists the most well-known instabilities.

2.6.1 Classification of Instabilities

Instabilities are broadly categorised depending on their behaviour with respect to the streamlines in the flow. An instability that grows beyond the disturbance streamline to eventually affect the entire flow-field is known as a global instability. Conversely, an instability that remains bounded within the streamlines where the disturbance took place is known as a local instability. Furthermore, a local instability that only affects flow downstream is known as a local convective instability, whereas if disturbances propagate upstream this is known as a local absolute instability (Huerre and Monkewitz, 1990).

Neutral Stability Curve

Instabilities begin as small disturbances and either amplify or dissipate. A higher the Reynolds number will often encourage the disturbance to amplify. Another important factor is the forcing frequency which is sometimes converted into spacial terms as wave-number with the units m^{-1}. The system often responds better to one particular frequency than any other. Assuming a variety of small perturbations within the system, as you increase Reynolds number, disturbances will first appear at the critical frequency. With higher Reynolds numbers, the system is unstable to a greater range of frequencies. The neutral stability curve shown in Figure 2.9 show a typical response of a system to Reynolds number and forcing frequency. Below a certain Reynolds number the flow remains stable. In real-turbulent flows the forcing frequency can thought to be a spectrum due to the many non-linear interactions that occur. At a certain Reynolds number, the flow will show unstable behaviour at a specific frequency known as the known as the critical point. As Reynolds

number increases further the range of frequencies present develop to encompass a large spectrum of frequencies.

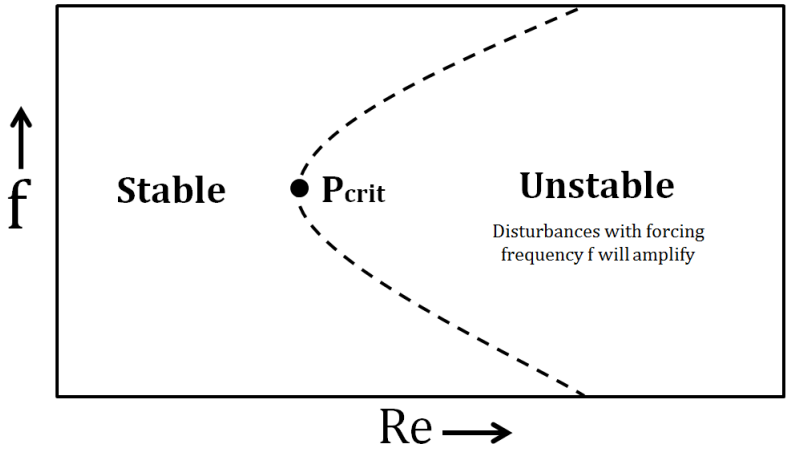

Figure 2.9: An illustration showing the general response of an unstable flow problem to disturbance frequency and Reynolds number.

2.6.2 Kelvin-Helmholtz Instabilities

The Kelvin-Helmholtz (K-H) instability is a fluid instability that occurs when fluids are in relative motion. The discontinuity in velocity introduces vorticity at the interface. As a result of this the vortex sheet rolls up into a number of parallel vortices. The instability is ubiquitous in a range of natural phenomena. These include within cloud formations, between ocean currents, and even in outer space such as the interaction of the earth's magnetopause with solar winds (Ong and Roderick, 1972), or the motion of interstellar clouds (Vietri et al., 1997).

The basic condition for the evolution of this instability is a velocity shear. The effects of surface tension, density, and viscosity may alter the characteristics of the instability but are not involved in the fundamental development of the force imbalance. The mechanism for the development of the Kelvin-Helmholtz instability is described in Figure 2.10. Through this mechanism fluid within a small disturbance is exposed to low pressure in the opposing flow as a result of the normal velocity continuity condition and the pressure continuous condition (Matsuoka, 2014). In some theoretical potential-flow based treatments of the problem a lighter fluid is superposed onto a heavier flow in Drazin (1970). There are two related instabilities known as the Rayleigh-Taylor Instability where a heavier fluid is superposed on a lighter one (Chandrasekhar, 1960); and the Richtmyer-Meshkov Instability (Richtmyer, 1960) which occurs in density stratified flows. The characteristic differences

between these types of instability is related to their growth rate at the linear stage of their development. Once the formation of the vortex roll-up occurs and complex interfacial motion occurs, the non-linear stage has been reached where the distinction between the three instabilities is no longer present. In such a point in time, the vortex-roll up behaviour is frequently discussed as simply a Kelvin-Helmholtz instability (Matsuoka, 2014).

Besides the extensive theoretical literature, the Kelvin-Helmholtz is discussed in a range of practical applications, and is ubiquitous in massively separated flows. Perhaps first noted by Lee and Mateescu (1998) in the backwards-facing step geometry. In their experimental and numerical study of the backwards-facing step they attributed the instability that exists between the separation and wake bubble to 'Helmholtz' instabilities. Since then a number of authors who study the backwards facing step also identify the Kelvin-Helmholtz instability within the shear layer. Kaltenbach and Janke (2000) conducted a numerical study of the backward-facing step and through spectral analysis observed the emergence of a single dominant frequency, and also the roll-up of vortices within the shear layer. They identify these characteristics as markers that are characteristic of the Kelvin-Helmholtz instability. Scarano and Riethmuller (2000) experimentally studied the temporal evolution of Kelvin-Helmholtz instabilities using a water flume and Particle-Image Velocimetry (PIV) particle tracking techniques. They algorithmically identify Kelvin-Helmholtz instabilities by looking for vortices with high span-wise coherency. the shear layer through an algorithm that identifies and tracks vortices that are span-wise coherent. Through this study they found that the vortices prefer to remain within the shear layer rather than convect along the time-averaged streamline towards the reattachment location.

2.6.3 Centrifugal Instabilities

Centrifugal instabilities are a fluidic process associated with an inherent centrifugal force within a fluid. Usually the source of the centrifugal force is associated with the existence of a curved fluid path. The result is pairs of counter-rotating vortices that significantly change the flow pattern, boundary-layer structure, and the transition to turbulence. An improved understanding of this phenomena may have profound impacts in a wide variety of areas where streamlines are curved.

Centrifugal instabilties are classified as Taylor, Gortler or Dean instabilities which are respectively defined as occurring in closed and parallel systems, open and non-

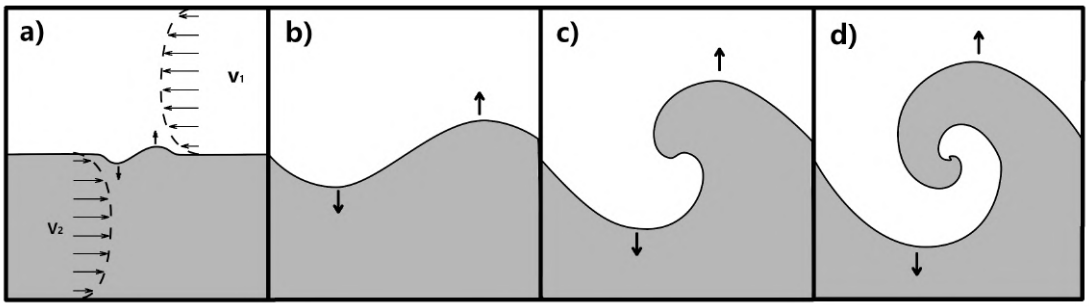

Figure 2.10: An illustrating showing the mechanism of a Kelvin-Helmholtz instability developing in a shearing flow. a) small perturbation is exposed to low pressure in oncoming flow b) due to increasing flow velocity further into opposing flow, pertubation grows in size c) under the shearing effect of oncoming flow perturbation distorts d) distortion leads to roll-up of interface sheet resulting in a vortex

parallel systems, open and parallel systems. More colloquially this means Taylor, Gortler and Dean vorticies respectively occur within rotating concentric cylinders, curved boundary layers, and curved pipe flows.

Taylor-Couette Instability

The interesting flow pictured in Figure 2.11 is produced by a simple apparatus. A fluid is confined between two cylinders, with a rotating inner cylinder as a necessary condition for the appearance of the cellular flow. This flow was discovered and mathematically modelled by Taylor (1923). Couette (1890) who is credited as the one of the founders of rheology, had previously devised this apparatus set up in his doctoral thesis, hence the combined name of the flow. This is a type of flow that has been considered by many of the greats in science. The flow was first discussed by Newton (1687) in his discussion of fluid dynamics. Many years before it's naming, George Stokes (Stokes, 2009), considered the Taylor-Couette flow. He was the first to have the intuition that such a flow would arise in instabilities mentioning that "if the inner one were made to revolve too fast, the fluid near it would have a tendancy to fly outwards in consequence of the centrifugal force, and eddies would be produced.". Taylor (1923) presented a landmark paper that analysed the linear stability theory for the general case of viscous flow within this geometry. When comparing calculations with ink dye experiments, there was a remarkable precision in the prediction of the on-set of instability. Linear instability theory may only predict the onset of instability, and not what occurs beyond that when non-linearity

plays a large role. With this in mind Taylor (1923) reported on their observations of the surprising complex flow regimes at higher speeds whereby the once stream-wise tubes take on a cellular form. Furthering this work in what is now a classic paper, Andereck et al. (1986) present a study of the effects of inner cylinder speed Re_i and outer cylinder speed Re_o against flow regime. They find and name a multitude of regimes including Couette flow, Taylor vortex flow, wavy vortex flow, modulated waves, turbulent Taylor vortices, spirals, wavy spirals, interpenetrating spirals, spiral turbulence, corkscrew wavelets, and featureless turbulence. They plot these phenomena in a phase diagram against Re_i and Re_o and demonstrate the richness of the phenomena. One their important findings was the path-dependant nature of these formations; that is to say that even though the Re_i and Re_o may be the same in two experiments, they may not share the same flow structure unless the same speed increments were followed.

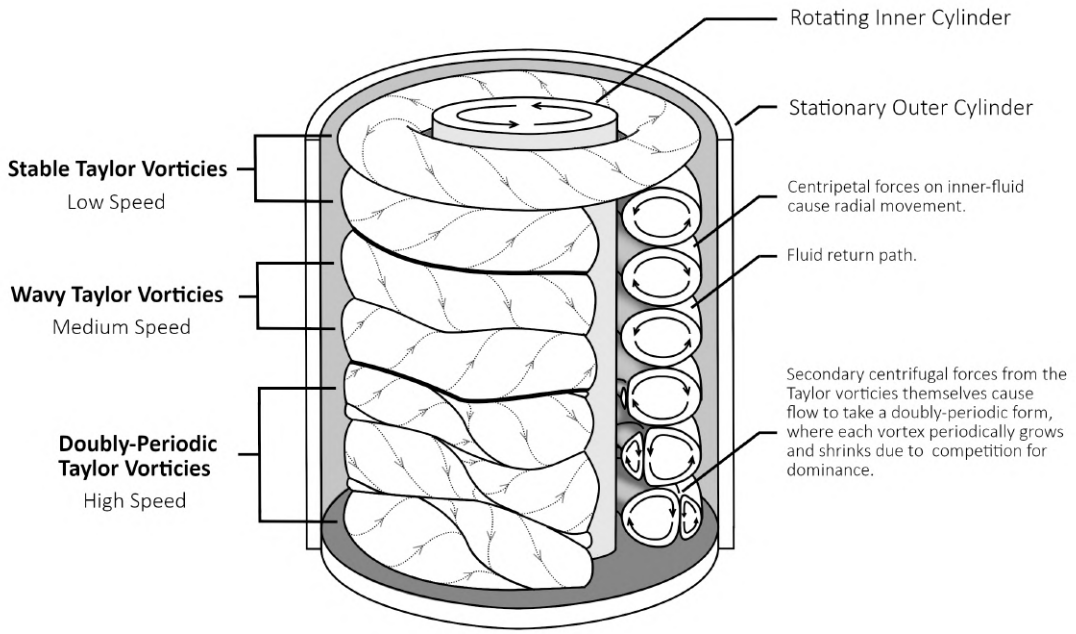

Figure 2.11: An illustration showing the development of Taylor-Couette centrifugal vorticies within the double cylinder experiment.

Gortler Instabilities

Gortler instabilities are a type of centrifugal instability that occurs within the vicinity of a boundary layer travelling over a curved surface. Under certain conditions, an instability manifests as pairs of counter-rotating vortices that are aligned in the stream-wise direction. This is a well-documented process experimentally. The source of this instability is the imbalance of the centrifugal force associated with travelling along a curved path, and also the radial pressure gradient. Görtler (1941) was the first to predict the existence of these instabilities. The Gortler number, is defined as

$$G_o = (U_\infty \theta/\nu)(\theta/R)^{1/2} \tag{2.2}$$

where U_∞ is the free-stream velocity, $\theta = (v\bar{x}/U_\infty)^{1/2}$ is momentum thickness which is related to the boundary layer thickness, ν is the kinematic viscosity, $\bar{x}$ is the distance from the leading edge and R is the radius of curvature of the wall. At low values of Gortler number, the centrifugal forces are small compared to the pressure forces. Beyond the critical Gortler number the centrifugal forces over-come the stabilising pressure gradient and the instability forms. Rayleigh (1880) showed that a sufficient condition for stability is an outward increase in circulation:

$$\delta(\Gamma^2)/\delta r < 0 \quad \text{anywhere in the flow} \tag{2.3}$$

where r is the radial position, Γ is the circulation defined as $\Gamma = rV$, and V is the tangential velocity. This criterion known as the Rayleigh circulation criterion is graphically illustrated in 4.1. It can be observed that in cases where the product of radius and velocity (circulation) are increasing with respect to radius, the flow is stable; and in cases where the product of radius and velocity are decreasing with respect to radius, the flow in unstable. With the presence of viscosity, the Rayleigh criterion is only a necessary condition for the instability. As the viscosity dampens the instability, there is a Reynolds number limit beneath which the instability does not form. Wheras the Rayleigh criterion only gives a necessary condition for the centrifugal instability, the G*ö*rtler number takes into account the viscosity to see if the instability will appear.

Bayly (1988) showed that this criterion holds for non-circular streamlines and Floryan (1986) proved its validity with boundary-layer velocity profiles. Moreover, they show that a non-monotonic velocity profile, such as a boundary layer flow through a curved channel always has the potential to manifest into an instability regardless of the concavity or convexity of the surface. This is illustrated in Figure 2.13. With

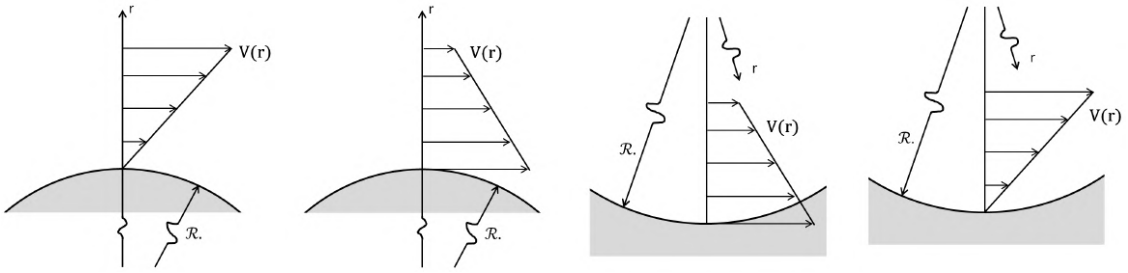

(a) Convex, stable **(b)** Convex, unstable **(c)** Concave, stable **(d)** Concave, unstable

Figure 2.12: A visual representation of the Rayleigh criterion showing under which conditions a centrifugal instability will manifest

respect to the Rayleigh criterion mentioned in Equation 2.3 and illustrated in Figure 4.1, Figure 2.13 shows that in any boundary layer flow through a curved pipe, the Rayleigh criterion is satisfied at either the top or bottom portion of the flow.

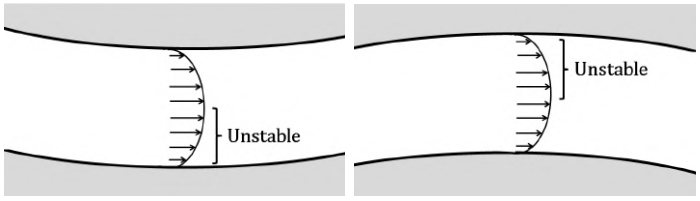

(a) Concave up **(b)** Concave down

Figure 2.13: A visual representation of the Rayleigh criterion showing under which conditions a centrifugal instability will manifest

Rogenski et al. (2016) conducted a study to determine the influence of stream-wise pressure gradient on the formation of this instability. The motivation for the study was to see if control of pressure gradient was a potential solution for inhibiting these instabilities. The numerical problem was formulated in a field equation in terms of the vorticity-velocity relationship (algorithm described in Malatesta et al. (2013)). They numerically tested three pressure gradient scenarios which were: favourable, neutral, and adverse. They found that the adverse pressure gradient slightly increased the growth rate of the vortices. Apart from that, changes of the pressure gradient had little effect on the vortices once they were established. They conclude that pressure-gradient tailoring isn't a feasible strategy to control this instability.

Es-Sahli et al. (2020) study the stability characteristics and flow structures asso-

ciated with curved free-shear flows such as the backwards-facing step. They use a numerical solution to a parabolised form of the Navier-Stokes equations. They study the form of instability in the cross-flow planes and find a mushroom-shaped cross section that evolves in the radial direction to the curve. Some geometries exhibited secondary instabilities in the form of secondary mushrooms in the perimeter of the primary instability. They found that very thin geometries with a spanwise distance of 0.3cm tended to suppress the formation of the instability and made mixing inefficient across the free shear layer. Mixing increased with spanwise separation. They also conducted a stability analysis to study the eigenmodes of these flows, from the symmetry of the resulting plot they determine that the instability is of varicose type, which is the same as the Kelvin-Helmholtz instability that dominates free-shear flows.

Dean Vorticies

If a fluid is moving along a curved pipe or channel it in most cases would have a fully developed boundary layer. The centrifugal force (U^2/R_C) (where U is the velocity and R_c the radius of curvature) induced from the bend will have a greater magnitude for the faster moving fluid close to the pipe axis than the fluid near the perimeter. This differential in centrifugal forces gives the fluid near the axis the compulsion to move towards the outer wall. The result is a pair of counter-rotating vortices known as Dean Vortices after Dean (1928). Rayleigh's circulation criterion is satisfied along the outer portion of the bend between the pipe axis and outer wall.

The Dean number is defined as

$$D_n = \frac{\sqrt{\frac{1}{2}(\text{inertial forces})(\text{centripital forces})}}{\text{viscous forces}} = \frac{\sqrt{\frac{1}{2}(\rho D_e^2 R_c \frac{v^2}{D_e})(\rho D_e^2 R_c \frac{v^2}{R_c})}}{\mu \frac{v}{D_e} D_e R_c} = R_e \sqrt{\frac{D_e}{2R_c}} \tag{2.4}$$

where ρ is density, μ is the dynamic viscosity, v is the axial velocity scale, D_e is the equivalent diameter, R_c is the radius of curvature, and Re is the Reynolds number.

Centrifugal Instabilities in Massively Separated Flows

A growing body of evidence suggests the existence of a global centrifugal instability in backward-facing step flows. Barkley et al. (2002) conducted a linear stability analysis of a backwards-facing step flow and found that the flow bifurcated from a nominally two-dimensional flow, to a three-dimensional structure at Re=748. The flow was found to comprise longitudinal vortices that were largely confined within

the recirculation zone and described as a 'flat roll' structure. They argued that the essential mechanism of this structure is centrifugal in nature. They argue that regions where the streamlines have a significant curvature, the centrifugal effects are strongest and force the fluid radially. Beaudoin et al. (2004) conducted an experimental study to find the three-dimensional stationary structure of a flow behind a backwards facing step ar $Re = 100$. Through ink dye visualizations and Particle Image Velocimetry they discover the presence of longitudinal vortices (Figure 2.14). They ascribed these vortices to being of a centrifugal origin due to the curvature of the flow as it passed over the step. Through a corresponding numerical simulation and plotting of Görtler number they showed that the region in the vicinity of the reattached flow, and outside of the recirculation bubble is centrifugally unstable.

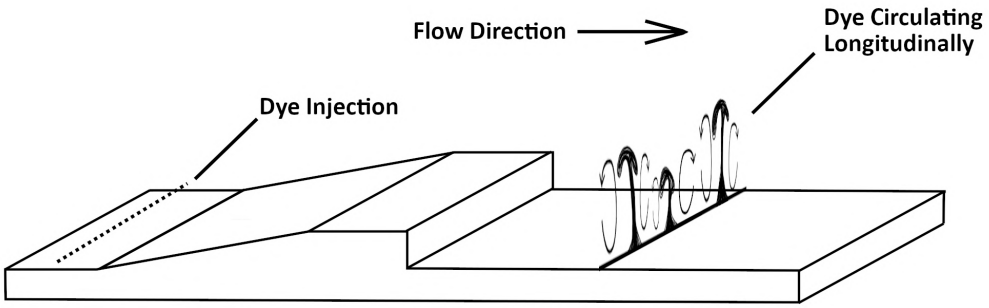

Figure 2.14: Illustrating the experiment by Beaudoin et al. (2004) showing the existence of longitudinal vortices of centrifugal origin using ink dye and PIV.

3

Research Outline

3.0.1 Summary of Literature Review

Heavy vehicles consume approximately 68% of all road vehicle fuel used, even though they account for a fraction of the commercial vehicle fleet. Moreover, fuel costs reportedly consume 33% of the total operating cost for the haulage business (Heyes 2013). These facts, coupled with increasingly stringent global regulations, continue to drive research into the improvement of heavy vehicle fuel economy. Though forebody and underbody drag reduction devices are commonly applied, it is a rare sight to find a device that acts on the base (rear) of the vehicle. In accordance with this goal, Choi et al. (2014) suggested two key areas that require development A) developing a deeper understanding of vortex activity that occurs in the base of a heavy vehicle, and B) the development of passive drag reduction devices that are based on unsteady principles that operate in the base of the heavy vehicle.

3.1 Scope

Through the literature review, justification has been provided for the following focusing of the scope:

- Heavy vehicles aerodynamics are focused on as heavy vehicles account for the second largest share of petroleum consumption despite their relatively small numbers around the world. Thereby a small improvement in a relatively small portion of the global traffic fleet could have a significant effect on overall transportation efficiencies.
- The base region of the truck has been identified as an area of interest. This is because there is a large drag reducing potential but there are few commercial devices that operate in this area.

- the tractor-trailer geometry is focused on as they are the the greatest in number and in terms of global heavy duty fuel consumption.
- The project will cover both fundamental and practical questions as there are gaps in both areas.

3.2 Research Gaps

From the literature review, a set of research gaps has been established and they are outlined below.

3.2.1 Fundamentals of massively separated flows

There is a lack of understanding regarding the unsteady flow features in the wake of heavy vehicles. Specifically the following gaps are identified:

- The source of the flapping behavior in massively separated flows remains unknown.
- It is understood that a causal sequence of instabilities is what leads to turbulence. Less clear is how consecutive instabilities interact with one another.

3.2.2 Development of a novel drag reduction device

The need practical and effective drag reduction devices is highlighted by the fact that there are few commercial devices that operate on this region. The wavy geometry has been shown to significantly reduce drag in fundamental studies. However, the device has not yet been evaluated in the context of a heavy vehicle.

- A device based on the principle of a wavy geometry has not yet been evaluated in the context of a heavy vehicle.

3.3 Aims

From the identified research gaps, the aims of the project are as follows:

- To develop fundamental understanding regarding the unsteady flow behind a heavy vehicle.
- To evaluate the applicability of a drag reduction device that uses a wavy

geometry as it's functional principle.

3.4 Objectives

1. To develop fundamental understanding of massively seperated flows.
   (a) To uncover the source of the flapping behaviour in massively seperated flows.
   (b) To understand the mechanism of operation behind the base cavity and the wavy geometry.
2. To develop and evaluate a novel drag reduction device based on a wavy profile.
   (a) To determine the drag reducing potential of a base drag reduction device based on the wavy principle.
   (b) To establish the influence of the device on the unsteady flow behind a tractor-trailer geometry.
   (c) To determine how geometrical parameters affect drag reduction performance.
   (d) To develop a fundamental mechanism linking base vortices and drag.

3.5 Methodology

To address the research objectives, two primary CFD studies are proposed. The first is a fundamental study on the backward-facing step geometry. The second is a study on a popular tractor-trailer geometry known as the Generic Conventional Model (GCM). The methodology is briefly described here but is described in more detail in the chapters pertaining to those studies.

3.5.1 3D Backward-facing step study

The backward-facing step is chosen to study fundamental aspects of massively separated flow. Despite the fact that a 3D square-backed geometry is more analogous to the flow in the wake of a heavy vehicle, the justification choosing the backwards-facing step for detailed study is because there are fundamental gaps in understanding of massively separated flows in general. Without the complication of a third dimen-

sion, the backwards facing step is already a non-trivial phenomena to investigate with effects such as non-linearity, turbulence and several instability modes. In response to this complexity, the simplest relevant geometry is chosen which is the Backwards-Facing Step. A high Reynolds number is chosen since this parallels the flow regime found during highway travel. In order to ensure the validity of the model, the simulation is set to replicate an experiment by Vogel and Eaton (1985) which has been used as a benchmark study by others (Shur et al., 2008).

3.5.2 Generic Conventional Model study

The purpose of this study is to test the performance of the proposed wavy device. The primary objective is to determine the change in drag reduction possible with the modification. A second objective is to understand how parameters affect its performance. This study will replicate wind-tunnel experiments from Storms et al. (2006) using the standardised tractor-trailer geometry known as the Generic Conventional Model (GCM). Using this set-up ensures the validity of the model. Furthermore, it gives an objective benchmark to compare the performance of the proposed device with other existing devices.

3.6 Resources

3.6.1 Supercomputer Facility

Computations are conducted on the latest-generation Cray XC40 petascale supercomputing system supported by the Pawsey Supercomputing Centre in Western Australia. The Magnus system comprises eight compute cabinets, each holding 48 blades, with four nodes per blade, with two compute processors per node. Each compute node hosts two 12-core, Intel Xeon E5-2690V3 “Haswell” processors running at 2.6 GHz, for a total of 35,712 cores, delivering in excess of 1 PetaFLOP of computing power.

Initially a 50,000 core-hour allocation was awarded under the ’directors share’ scheme to test the system and install all software. This initial allocation was granted on 6th February 2017. At a later date, January 10th 2018, an additional 150,000 core-hours was granted as part of a successful competitive merit allocation application.

4

Mathematical Models

All computations have been performed using the models described in this chapter using the Star CCM+ flow solver. The general equations that govern fluid behaviour is concisely written as the Navier-Stokes equation in the 3D Cartesian frame of reference. They are a set of Partial Differential Equations (PDEs) that describe the laws of conservation for:

- Conservation of Mass (Continuity Equation)
- Conservation of Momentum (Newtons 2nd Law)
- Conservation of Energy (1st Law of Thermodynamics)

4.1 Computational Fluid Dynamics Solver

4.1.1 Continuity Equation

The continuity equation describes the conservation of mass within a fluid. In Cartesian coordinates and in its differential form x_i this is expressed as:

$$\frac{\partial \rho}{\partial t} + \frac{\partial (\rho u_i)}{\partial x_i} = 0 \tag{4.1}$$

where ρ is density, t is time and u_i is the velocity vector. The above subscript i denotes tensor notation which implies summation for repeated indices in each dimension x, y and z. (McDonough, 2007)

4.1.2 Momentum Equation

The momentum equation describes the conservation of momentum, this encompass all forces that the fluid experiences. In Cartesian coordinates and in its differential

form this is written as:

$$\frac{\partial(\rho u_i)}{\partial t} + \frac{\partial(\rho u_i u_j)}{\partial x_j} = \rho f_i - \frac{\partial p}{\partial x_i} + \frac{\partial \tau_{ij}}{\partial x_j} \tag{4.2}$$

where f_i represents the body forces, p the pressure and τ_{ij} the viscous stress tensor, which is defined as:

$$\tau_{ij} = \mu \left[\left(\frac{\partial u_i}{\partial x_j} + \frac{\partial u_j}{\partial x_i} \right) - \frac{2}{3} \delta_{ij} \frac{\partial u_k}{\partial x_k} \right] \tag{4.3}$$

Where μ is the molecular viscosity and δ_{ij} is the Kronecker delta, which is defined as

$$\delta_{ij} = \begin{cases} 1 & \text{when i=j} \\ 0 & \text{otherwise} \end{cases} \tag{4.4}$$

(McDonough, 2007)

4.1.3 Energy Equation

The energy equation describes the principle that energy cannot be created or destroyed. In Cartesian coordinates and in its differential form this is written as:

$$\frac{\partial \rho E}{\partial t} + \frac{\partial}{\partial x_j}[u_i(\rho E + p)] - \frac{\partial}{\partial x_j}(u_i \tau_{ij} - q_j) = 0 \tag{4.5}$$

where E is the total energy of the fluid, defined as:

$$E = \rho \left[e + \frac{1}{2} u_i u_j \right] \tag{4.6}$$

and e is the specific internal energy with $u_i u_j$ representing the kinetic energy.

The heat flux vector, q_i, is calculated using Fourier's Law that states:

$$q_i = -k \frac{\partial T}{\partial x_i} \tag{4.7}$$

where k is the heat transfer coefficient and T temperature.

These three laws combine to form the Navier-Stokes equation of viscous flows:

$$\frac{\partial \mathbf{W}}{\partial t} + \frac{\partial(\mathbf{F}^i + \mathbf{F}^v)}{\partial x} + \frac{\partial(\mathbf{G}^i + \mathbf{G}^v)}{\partial y} + \frac{\partial(\mathbf{H}^i + \mathbf{H}^v)}{\partial z} = 0 \tag{4.8}$$

where $\mathbf{W}$ is a vector of conserved variables defined by:

$$\mathbf{W} = (\rho, \rho u, \rho v, \rho w, \rho E)^T \tag{4.9}$$

where ρ is desntiy, u, v, and w are three components of velocity, p is pressure and E is total energy. The superscripts i and v in Equation 4.8 denote the inviscid and viscid components of the flux vectors $\mathbf{F}$ (in the x-direction), $\mathbf{G}$ (in the y-direction) and $\mathbf{H}$ (in the z-direction). The inviscid flux vectors, $\mathbf{F}^i$, $\mathbf{G}^i$, and $\mathbf{H}^i$, are given by:

$$\begin{aligned}
\mathbf{F}^i &= \Big(\rho u, \rho u^2 + p, \rho uv, \rho uw, u(\rho E + p)\Big)^T \\
\mathbf{G}^i &= \Big(\rho v, \rho uv, \rho v^2 + p, \rho vw, v(\rho E + p)\Big)^T \\
\mathbf{H}^i &= \Big(\rho w, \rho uw, \rho vw, \rho w^2 + p, w(\rho E + p)\Big)^T
\end{aligned} \tag{4.10}$$

while the viscous flux vectors, $\mathbf{F}^v$, $\mathbf{G}^v$ and $\mathbf{H}^v$, contain terms for the heat flux and viscous forces exerted on the body and are represented as:

$$\begin{aligned}
\mathbf{F}^v &= \frac{1}{Re}\left(0, \tau_{xx}, \tau_{xy}, \tau_{xz}, u\tau_{xx} + v\tau_{xy} + w\tau_{xz} + q_x\right)^T \\
\mathbf{G}^v &= \frac{1}{Re}\left(0, \tau_{xy}, \tau_{yy}, \tau_{yz}, u\tau_{xy} + v\tau_{yy} + w\tau_{yz} + q_y\right)^T \\
\mathbf{H}^v &= \frac{1}{Re}\left(0, \tau_{xz}, \tau_{yz}, \tau_{zz}, u\tau_{xz} + v\tau_{yz} + w\tau_{zz} + q_y\right)^T
\end{aligned} \tag{4.11}$$

where the term τ_{ij} is the viscous stress tensor and q_i is the heat flux vector. (McDonough, 2007)

4.2 Navier-Stokes Equation

The Navier-Stokes (N-S) equations elegantly describe viscous flows. Due to the non-linear terms in the equation numerical methods are used to solve the equations. In the case of turbulent flows, there results in a vast range of motions at different temporal and spatial scales. This is due to several instability mechanisms which quickly bring the flow into a chaotic state under the right conditions. There exists a class of simulations called Direct-Numerical-Solutions (DNS) which solve the N-S equations directly. For turbulent flows the domain has to be discritised to the Kolomogrov microscales; that is the temporal and spacial scales at which viscosity dominates where turbulent kinetic energy is dissipated into heat. For this reason instances of DNS are limited to minute control volumes and are often only employed for fundamental studies on turbulence. For the majority of practical engineering studies we simply don't have the computing resources in order to directly solve the N-S equations.

In order to overcome the problem there is a class of methodologies that employ a turbulence model. The most famous of which are based on the Reynolds-Averaged Navier-Stokes (RANS) equations. In this approach the equations are modified so that the fluctuating component of velocity which is associated with turbulence is separated from the mean part. Through subsequent manipulation of the equations the result is an additional term in the momentum transport equation known as Reynold stresses, which must be modelled. In this form, the viscous stress tensor (Equation 4.11) is approximated by the later discussed Boussinesq hypothesis. (McDonough, 2007) The Star CCM+ solver uses finite volume discretisation. This is a method of transforming the partial differential equations into a system of algebraic equations through sub-dividing through space and time. The resulting linear equations are solved with an algebraic multigrid solver. (Siemens, 2021)

4.2.1 General Transport Equations

When constitutive relations are brought into the conservation equations, a closed set of equations is obtained. All conservation equations can be written in terms of a generic transport equation. When integrated over a control volume V and through the application of Gauss's divergence theorem, the following integral form of the transport equation is obtained:

$$\overbrace{\frac{d}{dt}\int_V \rho\phi dV}^{\text{Transient Term}} + \overbrace{\int_A \rho\mathbf{v}\phi \cdot d\mathbf{a}}^{\text{Convective Flux}} = \overbrace{\int_A \Gamma\nabla\phi d\mathbf{a}}^{\text{Diffusive Flux}} + \overbrace{\int_V S_\phi dV}^{\text{Source Term}} \tag{4.12}$$

where ϕ represents the transport of any scalar property, A is the surface area of the control volume and $d\mathbf{a}$ denotes the surface vector. By setting ϕ, for example, to equal 1, u, v, w, E, or H, Y_i and selecting appropriate values for the diffusion coefficient Γ, and source terms, special forms of the partial differential equations for mass, momentum and energy conversation are obtained (Mathieu and Scott, 2000).

The four terms in Equation 4.12 are:

- The transient term: the time rate change of a fluid property ϕ inside the control volume.
- The convective flux: the net rate of decrease of a fluid property ϕ across the control volume boundaries due to convection.
- The diffusive flux: the net rate of increase of a fluid property ϕ across the

control volume boundaries due to diffusion.

- The source term: the generation of fluid property ϕ inside the control volume.

(Siemens, 2021)

4.2.2 Convective flux

The discretised convective term at a face can be rearranged as:

$$(\phi\rho\mathbf{v}\cdot\mathbf{a})_f = (\dot{m}\phi)_f = \dot{m}_f\phi_f \tag{4.13}$$

where $\dot{m}_f$ is the mass flow rate at the face.

Equation 4.13 makes use of the fluid property values ϕ_f at the face. There are a number of schemes available to find this. In this work the Second-Order Upwind scheme is used for RANS simulations, and the Hybrid Second-Order Upwind/Bounded-Central scheme is used for DES simulations.

Second-Order Upwind Scheme

For RANS simulations the following work makes use of the second-order upwind (SOU) scheme. The convective flux is computed as:

$$(\dot{m}\phi)_f = \begin{cases} \dot{m}_f\phi_{f,0} & \text{for } \dot{m}_f \geq 0 \\ \dot{m}_f\phi_{f,1} & \text{for } \dot{m}_f \leq 0 \end{cases} \tag{4.14}$$

where the face values $\phi_{f,0}$ and $\phi_{f,1}$, are linearly interpolated from the cell center values on either side of the face:

$$\begin{aligned} \phi_{f,0} &= \phi_0 + \mathbf{s}_0 \cdot (\nabla\phi)_{r,0} \\ \phi_{f,1} &= \phi_1 + \mathbf{s}_1 \cdot (\nabla\phi)_{r,1} \end{aligned} \tag{4.15}$$

where:

$$\begin{aligned} \mathbf{s}_0 &= \mathbf{x}_f - \mathbf{x}_0 \\ \mathbf{s}_1 &= \mathbf{x}_f - \mathbf{x}_1 \end{aligned} \tag{4.16}$$

and $\mathbf{x}_0$ and $\mathbf{x}_1$ are the position vectors of centroids of each cell. Here the vector $\mathbf{s}_0$ and $\mathbf{s}_1$ represent the spatial vector from centroid of two adjacent cells to their shared face. Furthermore, the gradients $(\nabla\phi)_{r,0}$ and $(\nabla\phi)_{r,1}$ of cells 0 and 1 are calculated according to:

$$\phi_{f,0} = \phi_0 + \mathbf{s}_0 \cdot (\nabla\phi)_{r,0} \tag{4.17}$$

Hybrid Second-Order Upwind/Bounded-Central

For Detached Eddy Simulation the following hybrid second-order upwind/bounded central scheme is used for complex turbulent flows

$$(\dot{m}\phi)_f = \dot{m}\left(\sigma_{HU}\phi_{SOU} + (1-\sigma_{HU})\,\phi_{BCD}\right) \tag{4.18}$$

where at face f, the values of ϕ blended between ϕ_{SOU} (from the second-order upwind scheme) and ϕ_{BCD} (from the bounded central-differencing scheme). Therefore σ_{HU} is a blending factor proposed by Travin et al. (2002) which chooses the upwind scheme for RANS computations and central differencing for LES depending on the respective vorticity and strain rate tensors $\mathbf{W}$ and $\mathbf{S}$. (Siemens, 2021)

4.2.3 Diffusive Flux

The diffusive flux in Equation (in the general transport Equation 4.12) describes the energy passing through internal cell faces through a diffusive process is discretised as:

$$D_f = (\Gamma\nabla\phi \cdot \mathbf{a})_f) \tag{4.19}$$

where Γ is the face diffusivity, $\nabla\phi$ is the gradient of the fluid property ϕ, and $\mathbf{a}$ is the surface area vector.

As fluid properties are only known in the center of each cell (ϕ_0, ϕ_1), the following decomposition is used to achieve an accurate second-order approximation of fluid property ϕ at the face:

$$\nabla\phi_f = (\phi_0 - \phi_1)\,\boldsymbol{\alpha} + \overline{\nabla\phi} - (\overline{\nabla\phi} \cdot \mathbf{ds})\boldsymbol{\alpha} \tag{4.20}$$

where

$$\boldsymbol{\alpha} = \frac{\boldsymbol{a}}{\boldsymbol{a} \cdot \boldsymbol{ds}}$$
$$\boldsymbol{ds} = \boldsymbol{x}_1 - \boldsymbol{x}_0$$
$$\overline{\nabla\phi} = \frac{(\nabla\phi_0 + \nabla\phi_1)}{2}$$

where $\boldsymbol{a}$ is the surface area vector of the interior face where the diffusion flux is to be calculated. Using this decomposition the diffusion flux at a face can be written as:

$$D_f = \Gamma_f \nabla \phi_f \cdot \boldsymbol{a} \tag{4.21}$$

where Γ_f is a harmonic average of the cell values. In the special case of a boundary face then ϕ_f is used instead of ϕ_1 and $\boldsymbol{x}_f$ is used instead of $\boldsymbol{x}_1$. The second and third terms in Equation 4.20 represent the cross-diffusion contribution which is essential for maintaining accuracy on non-orthogonal meshes. (Siemens, 2021)

4.2.4 Transient Term

For transient simulations time is treated as an additional dimension. Similarly to spacial dimensions, time is discretised into time-steps. The solution of the governing equations is calculated at progressive time-levels and at each progressive step requires the solution from previous time-levels.

Implicit Time Integration

The Euler implicit scheme is used in all transient simulations within this work. This first-order temporal scheme approximates the transient term in the general transport equation (Equation 4.12) using the solution at the current time level, $n+1$, and the one from the previous time level, n:

$$\frac{d}{dt}(\rho\phi V)_0 = \frac{(\rho\phi V)_0{}^{n+1} - (\rho\phi V)_0{}^{n}}{\Delta t} \tag{4.22}$$

(Siemens, 2021)

4.3 Turbulence & Methods of Modelling

Turbulent flows are characterised by a range of motions within the fluid occurring simultaneously at a great range of length and time scales. Therefore turbulence exhibit structures which fluctuate rapidly. In laminar flow the fluid layers slide smoothly past one another and the inertia within high frequency and small scale instabilities in insufficient to overcome the damping effect of viscosity. With further speed the viscous effects can no longer inhibit the instabilities from growing and

transforming the flow into a chaotic regime. With this transition many properties of the flow itself change including an increase of mixing fraction, heat transfer rate, diffusion and spreading rate. Moreover boundary layers become thicker and have improved diffusion of kinetic energy therefore boundary layers are less susceptible to separation (McDonough, 2007).

The non-linear convective term in the momentum equation (Equation 4.2) is the source of the unstable behaviour in turbulent flows. Though seemingly chaotic, there is some order to turbulence. Due to some fundamental imbalances of force inherent to the flow, large scale, highly energetic disturbances may form that could span across the entire flow domain that occur at a relatively low frequency. The energy that goes to produce these large energetic vortices originates from the potential energy of the fluid pressure and also the kinetic energy of the flow. As a result the larger vortex structures tend to have a preferential direction and characteristics that are unique to the flow (Mathieu and Scott, 2000). A famous example is the Karman vortex street shedding behind a cylinder. The production of large-scale disturbances will in itself cause new, smaller-scale instabilities that often operate on the boundaries of the larger structure. Not unlike a fractal pattern this series of progressively smaller instabilities continues down to the smallest scale known as the Kolomogrov micro-scale where the viscous forces damp out the volition converting its energy into heat. This process is known as the energy cascade. From a broad energetic point of view, the energy that once resided within the pressure and kinetic energy of flow ends up as heat; with the chain of instabilities facilitating the transfer of energy. Another facet of this process is that as one travels down the length scales, the once structured eddies become increasingly uniformly random which draws parallels with the kinetic theory of gasses; this is described as isotropic turbulence (McDonough, 2007).

The Navier-Stokes equation is elegant in that it encompass the complex behaviour of viscous flows. At the present moment there is no general solution to the Navier Stokes equation. For this reason we rely on numerical methods to solve the equations. The equations can be solved directly in a technique known as Direct Numerical Simulation (DNS). The difficulty with this lies with the structure of turbulence spanning a vast number of time and length scales. For this reason a very fine grid is required to capture all of the individual interactions. Therefore DNS is limited to extremely low Reynolds number flows, or very small control volumes; both of which make it's use in engineering applications limited (Mathieu and Scott, 2000). Various adaptations to overcome this problem involve modeling turbulence to varying

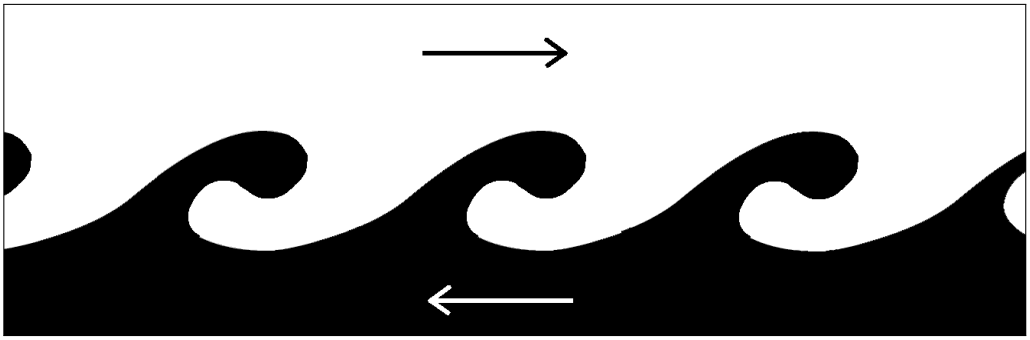

(a) Initial instability

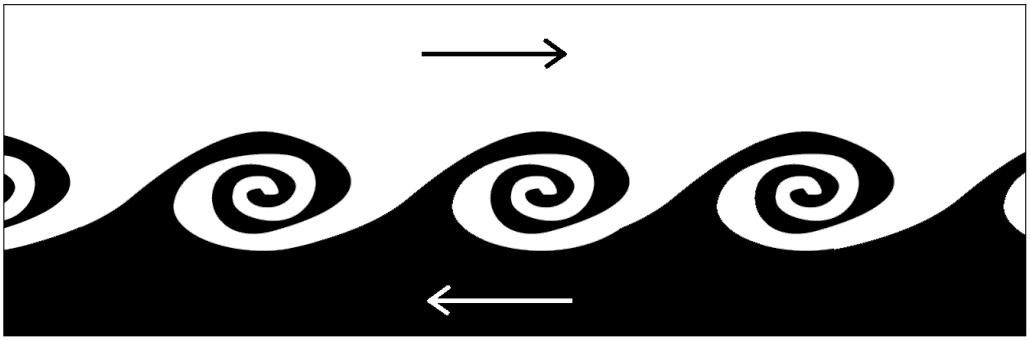

(b) Development of instability

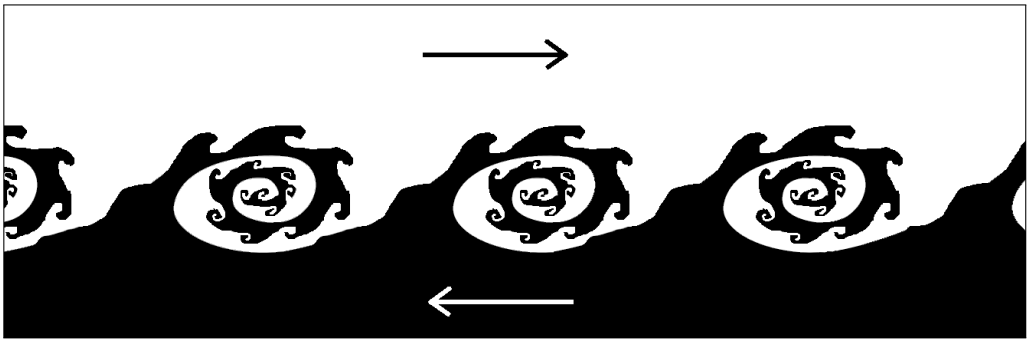

(c) Formation of secondary instabilities

Figure 4.1: A visual representation of the Rayleigh criterion showing under which conditions a centrifugal instability will manifest

degrees.

In the case of Large Eddy Simulation, the larger scale motions are resolved directly from the Navier-Stokes equations, whereas the smaller scale motions are modelled using a sub-grid scale (SGS) model. This technique exploits the isotropic properties of turbulence at small scales. This is achieved via low-pass filtering of the Navier-Stokes equations. As the length scale that needs to be modelled is determined by the statistical properties of turbulence which govern when they are isotropic, there is

a limit to the computational burden that can be freed through modelling (Mathieu and Scott, 2000). For this reason LES is still considered computationally expensive for high Reynolds number flows.

A method that relies on fully modelling turbulence is known as Reynolds-Averaged Navier-Stokes modelling. This method takes advantage of the Boussinesq Hypothesis (Boussinesq, 1877) which mandates that turbulence causes an apparent increase in the viscosity of the fluid due to the increased momentum transfer of momentum between particles facilitated by eddies; which is not unlike the root cause of viscosity which is momentum transfer between molecules moving with random motion. In this way, if the so-called eddy viscosity can be properly modelled, the macroscopic properties of the flow will remain true-to-nature. The downsides of eddy-viscosity based models relates to the assumptions of underlying the hypothesis, which fails for cases with high degrees of anisotropy, significant steam-line curvature, flow separation, recirculating flow or flows influenced by rotational effects (Mathieu and Scott, 2000).

Detached Eddy Simulation functions as a hybrid between the LES and RANS methodologies. In areas with sufficient tempo-spacial resolution it is able to resolve eddies in the same way as LES using a sub-grid scale model for isotropic turbulence. In other areas such as boundary layers in near-wall regions it uses RANS that has been shown to model the near-wall regions well (Siemens, 2021). Figure 4.2 illustrates the various degrees to which major models resolve versus model turbulence.

4.3.1 Reynolds Averaging

Turbulent flows are characterised by the random fluctuation of the pressure, temperature, velocity and density fields in space and time. The RANS method involves separating the random fluctuating component of the mentioned flow properties from their respective mean components.

$$\phi = \bar{\phi} + \phi' \tag{4.23}$$

The first and second terms on the right-hand side of Equation 4.23 represent the mean and fluctuating component of fluid property ϕ. To compute the mean value $\bar{\phi}$ there exist three methods:

- Time averaging
- Spatial averaging

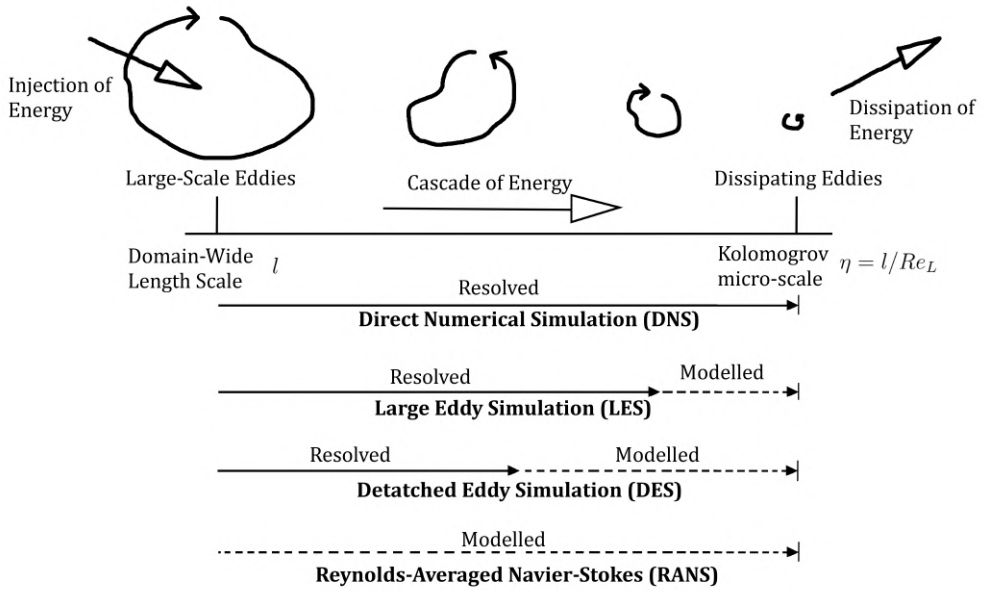

Figure 4.2: Illustrating the differences in resolved versus modelled turbulence between the major methods of CFD simulation

- Ensemble averaging

Time averaging

Time averaging is where the flow property is averaged over time such that

$$\bar{\phi} = \lim_{T\to\infty} f(x) \int_{i}^{i+T} u_i(t)dt \tag{4.24}$$

This sort of averaging is suitable for flows that do not vary with time on average. In practical terms $T \to \infty$ that the integration time is sufficiently larger than the period of the slowest assumed fluctuations. (McDonough, 2007)

Spatial averaging

In the case of spatial averaging, the fluid parameter ϕ is averaged over the spacial directions using a volume integral

$$\bar{\phi} = \lim_{V\to\infty} \frac{1}{V} \int\int\int_{V} \phi(x,t)dt \tag{4.25}$$

where V represents the volume of the domain. This technique is suited only to homogeneous turbulence who's properties remain constant with respect to direction. (McDonough, 2007)

Ensemble averaging

Ensemble averaging is similar to time-averaging but differs in that instead of dividing by time T, the mean of the flow parameter ϕ is obtained by taking a sum over all samples, N, and is defined by

$$\bar{\phi} = \lim_{N\to\infty} \frac{1}{N} \sum_{n=1}^{N} \phi(x,t) \tag{4.26}$$

This method is applicable to flows that decay in time. The ergodic hypothesis states that all three methods of averaging turbulent flows are equivalent for flows that satisfy the conditions of homogeneity and stationarity.

The decomposed velocity field (Equation 4.23) may be substituted into the Navier-Stokes equation. For the continuity and energy equations remain the same due to their linearity with respect to velocity. With regards to the momentum equation there is a slight complication in that the convective term is non-linear. Through some careful mathematical manipulation the Raynolds-Averaged Navier-Stokes equations are derived

$$\frac{\partial(\rho u_i)}{\partial t} + \frac{\partial(\rho u_i u_j)}{\partial x_i} = \rho f_i - \frac{\partial p}{\partial x_i} + \frac{\partial}{\partial x_j}(\tau_{ij} + \tau_{ij}^R) \tag{4.27}$$

where the over-bar has been negated for the purpose of clarity. A similar result is obtained for the energy equation (Equation 4.5). Through comparison with the standard momentum equation (Equation 4.2) it is evident that an additional stress tensor term τ_{ij}^R has appeared. It can be seen that this term is coupled with the viscous stress tensor τ_{ij}. In physical meaning, this represents the viscosity-emulating effect of turbulence and is known as the Reynolds Stress tensor τ_{ij}^R. Through this manipulation, and by considering the temporal-averaging step, it can be seen that with accurate knowledge of the Reynolds stress tensor, the resulting flow will be equivalent to the time-averaged results of a turbulent flow.

The advantage of this approach is that by virtue of the fact that the time-derivative of a time-averaged value is by definition equal to zero, the only time-based term in Equation 4.27 is eliminated

$$\frac{\partial(\rho u_i)}{\partial t} = 0 \tag{4.28}$$

this significantly reduces the computational burden of solving these equation by reducing the dimensionality of the problem.

The central challenge with the RANS approach is modelling the Reynolds stress term. There are a variety of approaches to this problem and the majority of well-known methods at based on the Boussinesq hypothesis. (McDonough, 2007)

4.3.2 Boussinesq Based Models

Turbulence has the effect of making the apparent viscosity of the fluid increase. This is similar in principle to the fundamental source of viscosity which is random motion of particles. In the case of turbulence the increase in momentum exchange achieves a similar effect. The Boussinesq approximation is expresses the Reynolds stresses as a product of the eddy viscosity (mu_t). The Boussinesq eddy viscosity hypothesis states that

$$-\rho\overline{u_i'u_j'} = \mu_t\left[\left(\frac{\partial u_i}{\partial x_j}+\frac{\partial u_j}{\partial x_i}\right)-\frac{2}{3}\delta_{ij}\frac{\partial u_k}{\partial x_k}\right]-\frac{2}{3}\rho\delta_{ij}k \tag{4.29}$$

where k represents the specific energy of the fluctuations and is given by

$$k \equiv \frac{u_i'u_i'}{2} \tag{4.30}$$

The central paradigm behind models based on the Boussinesq hypothesis is that the Reynolds stresses may be calculated as the product of the dynamic eddy-viscosity, μ_t, and the strain-rate tensor of the mean flow

$$-\rho\overline{u_i'u_j'} = 2u_t - \frac{2}{3}\delta_{ij}k \tag{4.31}$$

where

$$S_{ij} = \frac{1}{2}\left(\frac{\partial u_i}{\partial x_j}+\frac{\partial u_j}{\partial x_i}-\frac{2}{3}\delta_{ij}\frac{\partial u_k}{\partial x_k}\right) \tag{4.32}$$

In order to calculate the eddy viscosity μ_t, further modelling is required and there are a variety approaches.

- Algebraic/zero-equation models eg. mixing length model (Prandtl, 1925)
- One-equation models eg. Spalart-Allmaras (Spalart and Allmaras, 1992)
- Two-equation models eg. $k-\omega$ (Wilcox, 1988), $k-\epsilon$ (Jones and Launder, 1972)
- Multi-equation models

A different class of models solves equations for all components of the Reynolds stress tensor rather than just the eddy viscosity. These are called Reynolds Stress Models. (Mathieu and Scott, 2000)

4.3.3 Viscosity-Dependant Parameters

Non-dimensionalised wall distances for turbulent flow, $y*$, and non-turbulent flow, y+, are respectively defined as

$$y* \equiv \frac{y_n k^{1/2}}{v} \tag{4.33}$$

$$y^+ \equiv \frac{y_n u_\tau}{v} \tag{4.34}$$

where k is the kinetic energy of turbulence, y_n is the distance from the closest wall, $u_\tau \equiv \sqrt{\tau_w/\rho}$ is the frictional velocity and τ_w represents the dynamic wall shear stress. Turbulent Reynolds numbers for the $k-\epsilon$ model (denoted by R_t) and for the $k-\omega$ model (denoted by R_ω) are respectively

$$R_t \equiv \frac{k^2}{v\epsilon} \tag{4.35}$$

$$R_\omega \equiv \frac{k^2}{v\omega} \tag{4.36}$$

(Siemens, 2021)

4.3.4 One-Equation Models

A one equation model is formulated to improve the ability of algebraic models to factor the effects of convection and diffusion of turbulence. In order to achieve this, an additional transport equation is included, in most cases for the determination of the kinetic energy of turbulence, k. The general form of this equation is

$$\frac{\partial k}{\partial t} + u_j \frac{\partial k}{\partial x_j} = \tau ij \frac{\partial u_i}{\partial x_j} - \epsilon + \frac{\partial}{\partial x_j}\left[\frac{\mu}{\rho}\frac{\partial k}{\partial x_j} - \frac{1}{2}\overline{u_i' u_i' u_k'} - \frac{1}{\rho}\overline{p' u_j'}\right] \tag{4.37}$$

where τ_{ij} stands for the production of turbulence, the terms within the square brackets are respectively, molecular diffusion, turbulent flux of kinetic energy, and lastly the pressure diffusion. ϵ stands for the specific dissipation rate of k defined as

$$\epsilon = \frac{\mu}{\rho}\overline{\frac{\partial u_i'}{\partial x_k}}\overline{\frac{\partial u_i'}{\partial x_k}} \tag{4.38}$$

the eddy viscosity for one-equation models is

$$\mu_t = \rho C_\mu l_{mix}\sqrt{k} \tag{4.39}$$

where C_μ is a model-specific coefficient (Siemens, 2021).

In one equation models the historical information of turbulent kinetic energy is better modelled due to the extra differential equation. This makes it useful is some classes of non-equilibrium flows. The downside to one-equation models is that there is no mechanism for the computation of length scale l. For this reason one-equation models fall short when it comes to highly turbulent flows. Typically the models are tuned for specific flows thus decreasing its ability to predict unknown flows. One relatively modern use of the Spalart-Allmaras has been in Detatched Eddy Simulation (DES) computations (Spalart, 1997).

Spalart Allmaras Model

This turbulence model (Spalart and Allmaras, 1992) solves a transport equation directly for the eddy viscosity. The kinematic eddy viscosity, (v_t), in the Spalart-Allmaras model is calculated by

$$v_t = \tilde{v}.f_{vl} \tag{4.40}$$

where

$$f_{vl} = \frac{\chi^3}{\chi^3 + c_{v1}^3} \text{ and } \chi = \frac{\tilde{v}}{v} \tag{4.41}$$

here f is a function, c refers to a constant, v is the molecular viscosity and $\tilde{v}$ is the undamped eddy viscosity. The material derivative (time rate change of a particle moving with the flow) of v is governed by the following relation

$$\begin{aligned} \frac{D\tilde{v}}{Dt} &= c_{b1}(1 - f_{t2}\tilde{S}\tilde{v} + \frac{1}{\sigma}\left(\nabla \cdot ((v + \tilde{v})\nabla\tilde{v}) + c_{b2}(\nabla\tilde{v})^2\right) \\ &\quad - \left(c_{w1}f_w - \frac{c_{b1}}{\kappa^2}f_{t2}\right)\left(\frac{\tilde{v}}{d}\right)^2 + f_{t1}\Delta U^2 \end{aligned} \tag{4.42}$$

where the right-hand terms are (from left to right) the production term, the diffusion term and the near-wall term respectively. The last term models turbulent transition downstream of tripping. The subscripts b, w and t stand for basic, wall and trip respectively. σ signifies the turbulent Prandtl number and d is wall-distance.

The term in Equation 4.42 $\tilde{S}$ is defined by

$$\tilde{S} = S + \frac{\tilde{v}}{k^2 d^2} f_{v2}, \qquad f_{v2} = 1 - \frac{\chi}{1 + \chi f_{v1}} \tag{4.43}$$

The function f_w in Equation 4.42 is computed as

$$f_w = g\left(\frac{1 + c_{w3}^6}{g^6 + c_{w3}^6}\right)^{1/6} \qquad , \qquad g = r + c_{w2}\left(r^6 - r\right), \qquad r = \frac{\tilde{v}}{\tilde{S}k^2 d^2} \tag{4.44}$$

the function f_w approaches a constant value for large values of r. Values for r where this happens can be shortened to around a value of 10. The wall boundary condition is satisfied where $\tilde{v} = 0$.

The function f_t2 in Equation 4.42 is defined as

$$f_{t2} = c_{t3} \cdot e^{-c_{t4} \cdot \chi^2} \tag{4.45}$$

The function trip function f_t1 in Equation 4.42 is defined as

$$f_{t1} = c_{t1} g_t \cdot e^{-c_{t2} \frac{\omega_t^2}{\Delta U^2} (d^2 + g_t^2 d_t^2)} \tag{4.46}$$

where d_t is the distance from the location within the field to the trip point, ω_t is the wall vorticity at the trip, ΔU is the difference in velocity between the field point and trip location. $g_t = min(0.1, \Delta U \omega_t \Delta x)$ where Δx is the grid spacing along the wall at the trip point (Siemens, 2021).

4.3.5 Two-Equation Models

The most popular turbulence models are currently two-equation models. These models are 'complete' in the sense that they can be used to predict the properties of a flow without any prior knowledge of the turbulence structure or geometry. The common thread of these methods is the calculation of turbulent kinetic energy k and turbulence length scale l through two transport equations. The choice of the second variable is what differentiates methods and they include:

- ϵ - dissipation rate of turbulence
- ω - k-specific dissipation rate
- τ - turbulent time-scale

k-epsilon model

The $k - \epsilon$ model is one of the most widely used turbulence models. It is notable for its good convergence properties and stability and was developed by model Launder and Spalding (1983). In this approach the turbulent kinetic energy k, and the rate of dissipation of turbulence energy, ϵ. In this approach, ϵ is used to calculate the

turbulent scale using an additional transport equation. The eddy viscosity μ_T is derived from

$$\mu_T = C_\mu \rho \frac{k^2}{\epsilon} \tag{4.47}$$

where C_μ is a model coefficient.

The weakness of this model have been shown to be classes of flows with adverse pressure gradients, separated flow, swirl, buoyancy, and unsteady flows (Siemens, 2021).

k-omega model

Another class of two-equation turbulence models computes the specific rate of dissipation (of the turbulence kinetic energy k into internal thermal energy) ω, rather than just the rate of dissipation ϵ. This model was originally conceived by Kolomogrov himself, though later developed for use by Wilcox (1988). The eddy viscosity is obtained by

$$\mu_T = \rho \frac{k}{\omega} \tag{4.48}$$

The $k-\omega$ model has better performance than the $k-\omega$ in adverse gradient flows but besides that shares many of the same issues as the $k-\epsilon$ model. A hybrid between the two models known as the SST (Shear Stress Transport) model takes advantage of the robust and accurate formulation of the $k-\omega$ model in the near-wall regions, while maintaining the lack of sensitivity to the free-stream values that $k-\epsilon$ provides. The result is a turbulence model that can accurately handle separated flows. To achieve this, Menter (1994) transformed the $k-\epsilon$ model into the same format as the $k-\omega$ formulation. Through doing so a cross-diffusion parameter is introduced into the transport equation. The SST model then includes terms to account for the transport of the principal shear stress. Through doing so the performance in all adverse-pressure gradient flows was significantly improved. In both the RANS studies and the DES studies in this thesis, the $k-\omega$ SST model is used and described herein.

Turbulence transport equations used in the $k-\omega$ models are given by

$$\frac{\partial}{\partial t}(\rho k) + \frac{\partial}{\partial x_j}(\rho U_j k) = \frac{\partial}{\partial x_j}\left[\left(\mu + \frac{\mu_t}{\sigma_k}\right)\frac{\partial k}{\partial x_j}\right] + \rho(P - \beta^* \omega k) \tag{4.49}$$

$$\frac{\partial}{\partial t}(\rho \omega) + \frac{\partial}{\partial x_j}(\rho U_j \omega) = \frac{\partial}{\partial x_j}\left[\left(\mu + \frac{\mu_t}{\sigma_\omega}\right)\frac{\partial \omega}{\partial x_j}\right] + \rho\left(\frac{\alpha}{v_t}P - \frac{\beta}{\beta^* \omega^2}\right) + \rho S_l \tag{4.50}$$

In the transport equation for k and ω above, the production of turbulence, P, and the dissipation rate specific to k, P_ω is defined by

$$P_k = \tau ij^R \frac{\partial u_i}{\partial x_j}, \qquad P_\omega = \rho \frac{\alpha}{v_t} P_k \tag{4.51}$$

the SST model has been developed as a blend of the $k-\epsilon$ and $k-\omega$ models in order to take advantage of the independance of free-stream value of the $k-\epsilon$ model. This is achieved in practice by the blending of the model values for α, β, σ_k^{-1}, and σ_ω^{-1} from both models. This is achieved by the following equation

$$B \begin{pmatrix} a \\ b \end{pmatrix} \equiv F_1 a + (1 - F_1) b \tag{4.52}$$

The blending function is defined by

$$F_1 = tanh(arg_1^4) \tag{4.53}$$

where

$$arg_1 = min \left[max \left(\frac{k^{1/2}}{B^* \omega y}, \frac{500v}{y_n^2 \omega} \right) \ , \ \frac{2k\omega}{y_n^2 max(\nabla k \cdot \nabla \omega, 0)} \right] \tag{4.54}$$

In the SST model, a vorticity-dependent limiter is included on the shear stress (Siemens, 2021)

$$F_2 = tanh(arg_2^2), \quad arg_2 = max \left(\frac{2k^{1/2}}{\beta^* \omega y}, \frac{500v}{y^2 \omega} \right) \tag{4.55}$$

Wall Functions

The near-wall characteristics of flows have have a drastic effect on the overall flow, so special attention must be given to these regions. By virtue of the fact that the volume is discritised, in the near-wall regions it is not possible to fully resolve the turbulent flow structure within the boundary layer.

The inner region of the boundary layer can be categorised by their behaviour and are as follows:

- Viscous Sublayer
  The fluid layer in direct contact with the wall is dominated by viscosity due to

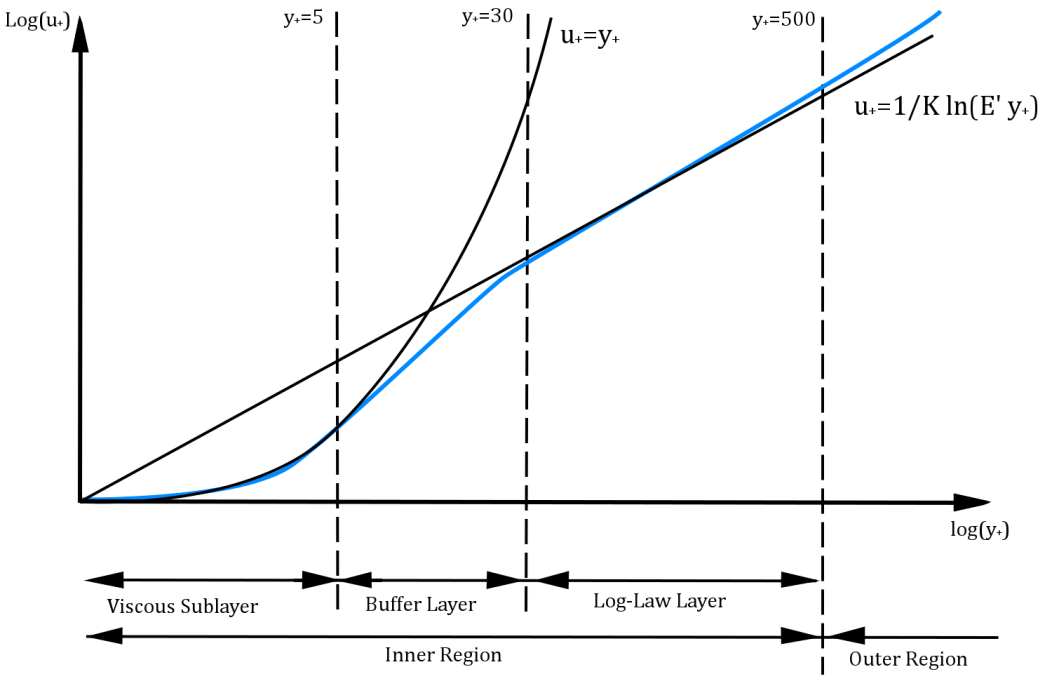

Figure 4.3: Illustrating the behaviour of the various near-wall regions

the low Reynolds number present. In this layer the non-dimensionalised flow speed u^+ is directly proportional to wall distance y^+

- Log-Law Layer
  The turbulent log-law layer is dominated by viscous and turbulent viscosity effects equally and is characterised by a logarithmic relationship between flow speed u^+ and y^+

- Buffer Layer
  This is the region that represents the transition from the viscous and log-law layers.

Traditionally there are two approaches to reconstruct the effects of the wall. The low $y+$ method resolves the viscous sublayer directly and needs minimal modelling to predict the flow at the wall-boundary. In this case the transport equations are solved directly to the wall cell where the wall shear stress is computed as a laminar flow (ie. proportional to velocity). In order to resolve the boundary layer down to the viscous sub-layer, a sufficiently fine mesh is required with a non-dimensionalised wall distance of $y^+ \approx 1$. Despite it's appeal for the fact the solution is direct, the downside is it is computationally expensive, particularly for high Reynolds numbers flows where the viscous sublayer is particularly thin.

The high y^+ method does not resolve the viscous layer at all, instead a model known as a wall-function is used to get the boundary equations for the continuum equations. The specific parameters are derived from turbulent boundary layer theory including, wall shear stress, turbulent production and turbulent dissipation. This approach mandates that the near-wall cells lie within the log-law layer of the boundary layer at y^+ >30. Due to the required cell count is significantly.

The challenge with either method is that the the y+ values need to be precisely controlled and also that simulations with intermediate resolutions are not possible. There exists a methodology known as the all y^+ that is able to blend between the two regimes (Siemens, 2021). The benefit is greater flexibility in meshing and furthermore this is the chosen treatment for all simulations in this thesis.

k-omega wall treatment

Within the $k-\omega$ model that is used in this work, a wall-treatment strategy must be used in order to determine:

- The reference velocity u^*
- The turbulent production G_k used in the wall-cell
- a special value of specific turbulent dissipation ω in the wall cell

For the all-y^+ formulation, the blending function g is defined in terms of the wall-distance Reynolds number (Siemens, 2021)

$$g = exp\left(-\frac{Re_y}{11}\right) \tag{4.56}$$

where $Re_y = \sqrt{k}y/\nu$ is the wall-distance-based Reynolds number, k is the turbulent kinetic energy production, y is wall distance and ν is the kinematic viscosity.

The reference velocity u^* is a parameter used within the calculations of turbulent production and dissipation and is defined as

$$u^* = \sqrt{g\nu u/y + (1-g)\beta^{1/2}k} \tag{4.57}$$

where u is the flow speed, and β is the closure coefficient described in Section 4.3.5

The wall-cell production is given by

$$G_k = g\mu_t S^2 + (1-g)\frac{1}{\mu}\left(\rho u^* \frac{u}{u^+}\right)^2 \frac{\partial u^+}{\partial y^+} \tag{4.58}$$

where g is defined in Equation 4.56, μ_t is the turbulent viscosity, S is the modulus of the mean strain rate $\boldsymbol{S}$, μ is the viscosity, ρ is density, u is flow speed, y^+ and u^+ are the non-dimensionalised wall-distance and flow speed, respectively defined as

$$y^+ = \frac{yu_t}{\nu} \tag{4.59}$$

$$u^+ = \frac{1}{\kappa} ln(y^+) + C^+ \tag{4.60}$$

where y is the distance to the wall, u_t is the friction velocity, κ is the Von Karman constant, and C^+ is a constant.

The wall-cell specific dissipation ω is given by

$$\omega = g\frac{6\nu}{\beta y^2} + (1-g)\frac{u^*}{\sqrt{\beta^* \kappa y}} \tag{4.61}$$

4.3.6 Large-Eddy Simulation (LES)

Large Eddy Simulation (LES) is a transient methodology in which the larger scales of turbulence are directly resolved, whereas the smallest-scale motions are modelled. The justification for this technique is by virtue of the fact that as only a small fraction of the turbulence is modelled, it is more true-to-nature. Furthermore, the hypothesised isotropic and universal properties of small-scale turbulence means that models are more based on theory rather than empirical results. Despite this strong justification, LES remains computationally expensive and therefore unfeasible for the majority of studies.

Contrasting with the RANS modelling approach, the LES approach uses a spatial filter rather than a time averaging process. In a similar vein to RANS, each solution variable ϕ is decomposed into a filtered value $\tilde{\phi}$ and a sub-grid value ϕ' such that the variable becomes

$$\phi = \tilde{\phi} + \phi' \tag{4.62}$$

where ϕ represents the velocity components, pressure, energy or species concentration (Mathieu and Scott, 2000).

The decomposed quantities are subsequently substituted into the Navier-Stokes equations which yields new equations for the filtered quantities. The mass and momentum equations can then be respectively written as

$$\frac{\partial \rho}{\partial t} + \nabla \cdot (\rho \tilde{\boldsymbol{v}}) = 0 \tag{4.63}$$

$$\frac{\partial}{\partial t}(\rho \tilde{\boldsymbol{v}}) + \nabla \cdot (\rho \tilde{\boldsymbol{v}} \times \tilde{\boldsymbol{v}}) = -\nabla \cdot \tilde{p}\boldsymbol{I} + \nabla \cdot (\boldsymbol{T} + \boldsymbol{T}_t) + \boldsymbol{f}_b \tag{4.64}$$

where ρ is density, $\tilde{\boldsymbol{v}}$ and $\tilde{p}$ are respectively the filtered velocity and pressure, $\boldsymbol{I}$ is the identity tensor, $\boldsymbol{T}$ is the stress tensor, $\boldsymbol{f}_b$ is the resultant of the body forces (gravity, centrifugal etc.)

The filtered equations can then rearranged into a form that is identical to the unsteady RANS equations. The difference being that the turbulent stress tensor $\boldsymbol{T}_t$ now represents the subgrid scale stresses. These stresses represent the interaction between the larger resolved eddies, and the smaller unresolved eddies and are modelled using the Boussinesq approximation

$$\boldsymbol{T}_t = 2\mu_t \boldsymbol{S} - \frac{2}{3}(\mu_t \nabla \cdot \tilde{\boldsymbol{v}} + \rho k)\boldsymbol{I} \tag{4.65}$$

where $\boldsymbol{S}$ is the mean strain rate tensor, $\tilde{\boldsymbol{v}}$ is the filtered velocity, ρ is the density, k is the sub-grid scale turbulent kinetic energy, and μ_t is the sub-grid scale turbulent viscosity which must be described by a sub-grid scale model that accounts for the effects of the small eddies on the over-all flow. The original and most basic sub-grid scale model is the Smargorinsky subgrid scale model which is based on a mixing-length hypothesis to model the turbulent viscosity μ_t as

$$\mu_t = \rho \Delta^2 S \tag{4.66}$$

where rho is the density, Δ is the length scale or grid filter width and S is the modulus of the mean strain rate. The length scale Δ is related to the cell volume V and wall distance d as

$$\Delta = \begin{cases} f_v C_s V^{1/3} & \text{if length scale limit is not applied} \\ f_v \ \min(\kappa d, C_s V^{1/3}) & \text{if length scale limit is applied} \end{cases} \tag{4.67}$$

where C_s is a model coefficient, κ is the von Karman constant, and f_v is the Van Driest damping function defined as

$$f_v = \begin{Bmatrix} 1 & \text{no damping} \\ 1 - exp\left(-\frac{y^+}{A}\right) & \text{standard} \\ \sqrt{1 - exp\left(-\frac{y^+}{A}\right)^3} & \text{modified} \end{Bmatrix} \tag{4.68}$$

where A is a model coefficient (Siemens, 2021).

Shehadi (2018) conducted a study of Large Eddy Simulation on a backwards-facing step geometry. They find that a symmetric three-layered wall-normal meshing strategy in conjunction with an SGS-free model is the best compromise between computational efficiency and accuracy. The accuracy of the results is most sensitive to spanwise grid resolution.

4.3.7 Detached-Eddy Simulation (DES)

Detached-Eddy Simulation is an unsteady modelling approach that combines aspects of Raynolds-Averaged Navier-Stokes (RANS) and the Large Eddy Simulation (LES) methods. In flows that are time-varying such as vortex shedding and massively seperated flows, a transient simulation often yields better results. In such cases the unsteady RANS approach often yields better results. However, good results are contingent on the property that the time-scales of turbulence are disparate from the mean-flow unsteadiness; which is often not the case. In the DES approach, turbulence models are used such that the boundary layers and irrotational flow regions are solved using a standard RANS closure model. However, in regions where the grid is fine enough, a basic LES sub-grid scale model is emulated in detached flow regions. By doing so, one benefits from an accurate and computationally efficient reproduction of the boundary layer characteristics using RANS, and also an accurate portrayal of the unsteady behaviour within separated regions through LES. The DES formulation is able to automatically blend between the two models depending on the optimality of the geometry (Mathieu and Scott, 2000). There are several variants to the DES model depending on what RANS model is employed and these include

- Spalart-Allmaras DES
- Elliptic Blending K-Epsilon DES
- SST K-Omega DES

and the following variants are also available

- Detached Eddy Simulation (DES)
- Delayed Detached Eddy Simulation (DDES)
- Improved Delayed Detached Eddy Simulation (IDDES)

The DDES model (Menter and Kuntz, 2004) is an improvement in that it is better able to distinguish between RANS and LES regions through the incorporation of a delay factor. The IDDES method is a further improvement in that it allows RANS in much thinner near-wall cell distances which was one of the shortcomings of DES. This is achieved through adding a dependence of length-scale on wall-distance. The downside of DES is that the results are very dependent on the grid so some special attention must be taken during this phase.

In this work, the SST K-Omega, IDDES formulation is used because of its state-of-the-art formulation.

DES Methodology

The respective momentum equations for the RANS averaged velocity $\bar{\boldsymbol{v}}$ and the LES filtered velocity $\tilde{\boldsymbol{v}}$ are defined as

$$\frac{\partial}{\partial t}(\rho\bar{\boldsymbol{v}}) + \nabla\cdot(\rho\bar{\boldsymbol{v}}\times\bar{\boldsymbol{v}}) = -\nabla\cdot\bar{p}\boldsymbol{I} + \nabla\cdot\left(\boldsymbol{T} + \boldsymbol{T}_t^{RANS}\right) + \boldsymbol{f}_b \tag{4.69}$$

$$\frac{\partial}{\partial t}(\rho\tilde{\boldsymbol{v}}) + \nabla\cdot(\rho\tilde{\boldsymbol{v}}\times\tilde{\boldsymbol{v}}) = -\nabla\cdot\bar{p}\boldsymbol{I} + \nabla\cdot\left(\boldsymbol{T} + \boldsymbol{T}_t^{RANS}\right) + \boldsymbol{f}_b \tag{4.70}$$

The Reynolds-stress tensor $\boldsymbol{T}_t^{RANS}$ is a function of time and length-scale

$$\boldsymbol{T}_t^{RANS} = f(\nabla\cdot\bar{\boldsymbol{v}}, k, \epsilon) \tag{4.71}$$

$$\boldsymbol{T}_t^{LES} = f(\nabla\cdot\tilde{\boldsymbol{v}}, \Delta) \tag{4.72}$$

in Equation 4.72, the filter width plays a crucial role that not only defines the subgrid-scale eddy viscosity, but also defines the transition region between LES and RANS.

The similarity between Equation 4.73 and Equation 4.70 suggests that a unified approach can be used to solve for a quantity $\hat{u}_i$, that is dependant on the local definition

$$\frac{\partial}{\partial t}(\rho\hat{\boldsymbol{v}}) + \nabla \cdot (\rho\hat{\boldsymbol{v}} \times \hat{\boldsymbol{v}}) = -\nabla \cdot \hat{p}\boldsymbol{I} + \nabla \cdot \left(\boldsymbol{T} + \boldsymbol{T}_t^{RANS}\right) + \boldsymbol{f}_b \tag{4.73}$$

where the modelled stress tensor $\boldsymbol{T}_t^{model}$ is defined as

$$\boldsymbol{T}_t^{model} = f_\Delta \left(\frac{\Delta}{l_k}\right) \boldsymbol{T}_t^{RANS} \tag{4.74}$$

where Δ is the local measure of the grid size, l_k is the turbulent length-scale, and f_Δ is a damping function that depends on the DES variant (DDES or IDDES) (Siemens, 2021).

IDDES Formulation

The SST K-Omega Detached Eddy model combines features of the SST K-Omega RANS model within boundary layers with the LES methodology in unsteady separated regions of flow. The DES formulation of the SST K-Omega model is obtained through the modification of the dissipation term in the transport equation for kinetic energy.

For the IDDES formulation of Shur et al. (2008), the specific dissipation rate ω in Equation 4.49 is replaced by $\tilde{\omega}$ defined as

$$\tilde{\omega} = \frac{\sqrt{k}}{l_{HYBRID}\beta^* f_{\beta^*}} \tag{4.75}$$

where β^* is a $k-\omega$ model coefficient and f_{β^*} is the free-shear modification factor.

and

$$l_{HYBRID} = \tilde{f}_d(1 + f_e)l_t + (1 - \tilde{f}_d)C_{DES}\Delta_{IDDES} \tag{4.76}$$

The length scale calculations are supplemented by two more functions to add Wall-Modeled LES (WMLES) capability, a blending function f_b, and the elevating function f_e

$$f_B = min\left[2exp\left(-9\alpha^2\right), 1\right] \tag{4.77}$$

$$\alpha = 0.25 - \frac{d}{\Delta} \tag{4.78}$$

$$f_e = max\left[\left(f_{e1} - 1\right), 0\right] \psi f_{e2} \tag{4.79}$$

$$f_{e1} = \begin{cases} 2exp(-11.09\alpha^2) & \text{for } \alpha \geq 0 \\ 2exp(-9\alpha^2) & \text{for } \alpha < 0 \end{cases} \tag{4.80}$$

$$f_{e2} = 1 - max(f_t, f_l) \tag{4.81}$$

$$f_t = tanh\left[\left(C_t^2 r_{dt}\right)^3\right] \tag{4.82}$$

$$f_l = tanh\left[\left(C_t^2 r_{dt}\right)^1 0\right] \tag{4.83}$$

$$r_{dt} = \frac{\nu_t}{\sqrt{\nabla \boldsymbol{v} : \nabla \boldsymbol{v}^T \kappa^2 d^2}} \tag{4.84}$$

$$r_{dl} = \frac{\nu}{\sqrt{\nabla \boldsymbol{v} : \nabla \boldsymbol{v}^T \kappa^2 d^2}} \tag{4.85}$$

where C_t and C_l are model coefficients, ν is the kinematic viscosity, $\nu_t = \mu_t/\rho$, where μ_t is the turbulent eddy viscosity, κ is the von Karman constant, d is the distance to the wall, and ψ is the low-Reynolds number correction function which is empirically based (Siemens, 2021).

5

3D Backwards-Facing Step Study

In the literature review is has been made clear that in order to develop new drag reduction devices for heavy vehicles, a better understanding of fundamental aspects of massively separated flows is first required. For those seeking this kind of understanding, the Backwards Facing Step is the geometry of choice since it is is the most simple geometry which shares the essential flow features of such flows. Thereby through the identification of gaps in understanding that concern this geometry, we can make steps towards further understanding massively separated flows in general.

There is an idea that turbulent massively separated flows comprise a number of coherent motions. At present, there is little is known about the existence of coherent motions within turbulent flow behind a backward-facing step. The primary objective in this study is to identify and explain coherent motions in turbulent flow behind a backward-facing step. To do this, we employ a selective-filter based decomposition method to a 2D bisecting plane section. The technique allows the visualisation and interpretation of behaviours that occur at specific frequencies. We also apply a variant of the Q-criterion technique to identify the rotational direction of vortices within the decomposed modes. We apply these techniques to numerically derived data from a high-fidelity 3D Improved Delayed Detached Eddy Simulation (IDDES) solution of high Reynolds number ($\mathrm{Re}_H = 28{,}000$) flow over a backward-facing step.

5.1 Computational Set Up & Validation

The solution domain was modelled from the experiments of Vogel and Eaton (1985) that features a step of height h=3.8 cm and an expansion ratio of 5. The width of the present domain differs in that it is 7.6 cm. This is mainly in regard to computational resources. The boundary conditions were as follows. The side-walls were symmetry planes, the bottom and top surfaces were wall boundaries, there was a

mass flow outlet downstream, and the inlet was upstream of the step. The inlet velocity profile was generated in a separate channel simulation to match the characteristics of the boundary layer in Table 5.1. Other inlet parameters (turbulence intensity and temperature) were also derived from this separate channel simulation. The positive x-axis, y-axis and z-axis correspond to the stream-wise, span-wise and vertical directions respectively. Figure 5.1 illustrates the geometric proportions of the domain along with boundary assignments.

The Spalart-Allmaras formulation of the Improved Delayed Detached Eddy (IDDES) turbulence model was applied (Shur et al., 2008). The finite-volume method is used to discretise the Navier-Stokes equation and the SIMPLE algorithm is used to couple the pressure and velocity equations. Air is the working fluid with a constant density of 1.184 kg/m^3 and dynamic viscosity of 1.855 Pa.s. An implicit unsteady solver was employed with a 2nd-order temporal discretisation scheme. The time step was 7.692 x 10^{-5} seconds with a total of 39001 steps that yields 3 seconds of simulation time; each time step featured seven inter-iterations. In order to ensure that the flow had sufficiently developed, data was analysed from one second of simulation time and onwards. A segregated flow solver was applied with a Hybrid-BCD convection scheme with an upwind blending factor of 0.15. The mesh is an unstructured trimmer configuration with a total of 10.44 x 10^6 cells. In order to achieve greatest accuracy, the number of cells chosen was based on the available computing power. A grid independence study is not appropriate for DES simulations because the PDE itself changes with grid size (Spalart, 2001). Regions of refinement focused on the step vicinity and also downstream to allow for the development of the boundary layer after reattachment. Cells within the refinement region featured a uniform target volume of 1 mm^3. Figure 5.2 shows the mesh structure taken at the planar bisection of the geometry.

The commercial CFD package Star-CCM+ was employed using a latest-generation Cray XC40 petascale supercomputing system supported by the Pawsey Supercomputing Centre. Magnus comprises eight compute cabinets, each holding 48 blades, with four nodes per blade, with two compute processors per node. Each compute node hosts two 12-core, Intel Xeon E5-2690V3 Haswell processors running at 2.6 GHz, for a total of 35,712 cores, delivering in excess of 1 PetaFLOP of computing power. The entire simulation was run with 144 processor cores requiring a total of 25,000 core-hours of processing time over a 24 hour period approximately. The resulting flow that is shown in Figure 5.3 was validated against experimental measurements by Vogel and Eaton (1985) and also the original IDDES results by Shur

Table 5.1: A summary of the inlet boundary layer conditions

Reference Conditions:	
U_{Ref}	11.3 m/s
Re_H	28,000
Inlet Boundary-Layer Parameters:	
Boundary-layer thickness δ_{99}	4.05 cm
Momentum thickness θ	0.468 cm
Momentum-thickness Reynolds number Re_θ	3370
Shape factor H	1.389
Skin friction (log-law fit) C_f	0.00312

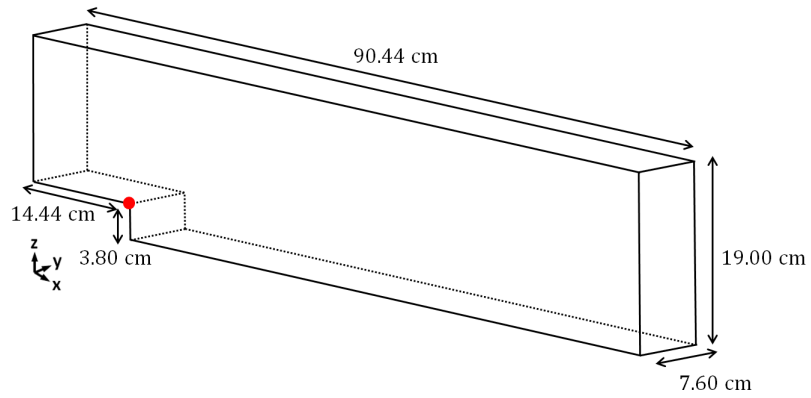

Figure 5.1: A schematic of the simulation domain. The origin is denoted with red axes.

et al. (2008). A comparison of the skin friction coefficient along the bottom surface shows good agreement with experimental results (Figure 5.4). From this, the time-averaged reattachment point was found to be x/h = 6.71.

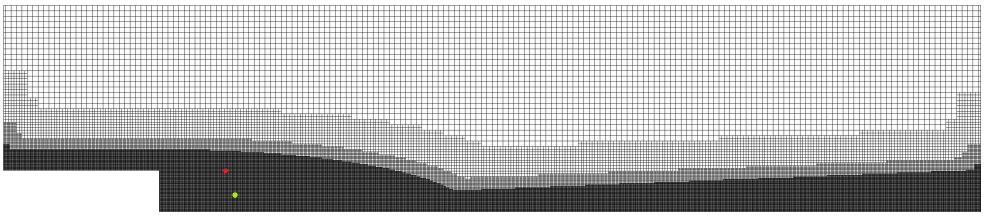

Figure 5.2: A planar bisection of the domain showing the extent of mesh refinement and also the frequency probe locations (*green* : shear layer probe x = 8.2 cm, y = -0.3 cm ; *red* : wake probe x = 9.5 cm, y = -2.3 cm)

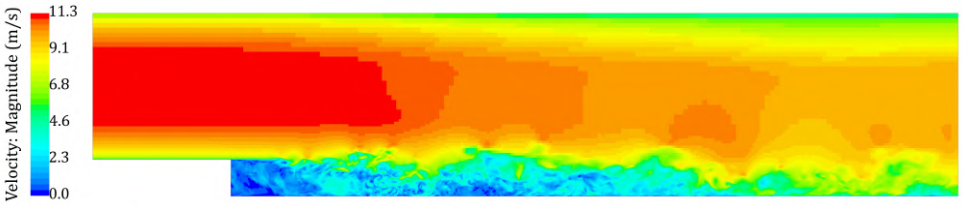

Figure 5.3: a velocity plot of the bisecting plane showing the incoming boundary layer velocity profile, and also the extent of turbulent flow beyond the step edge.

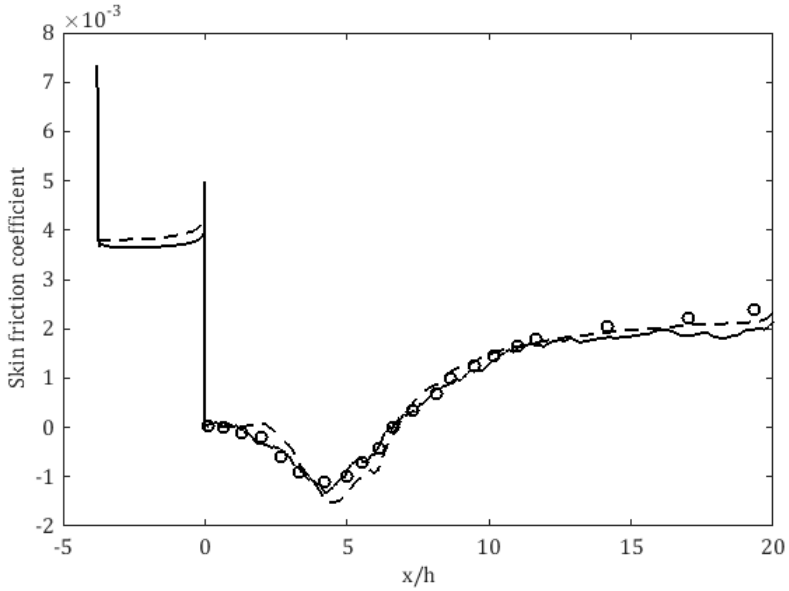

Figure 5.4: Comparison of skin-friction coefficient along the centerline at the bottom surface, compared with the experimental and simulated results:
——, present study; ∘ experiment by Vogel and Eaton (1985); - - -, simulation by Shur et al. (2008).

5.1.1 Development of inlet conditions

It it well known that the in this geometry, the inlet boundary layer can have an influence on the characteristics of the flow over the backward-facing step. Therefore to get results that are comparable with that of Vogel and Eaton (1985), the same inlet boundary layer conditions had to be created. The experimental boundary layer parameters are specified in Table 5.1. In order to reproduce these parameters, a separate channel simulation was used. The channel simulation has a cuboidal geometry that features where the top and side walls of the domain were defined as symmetry planes, whilst only the bottom wall was defined as a no-slip boundary. The inlet was specified with the target free-stream velocity of 11.3 m/s.

The dimensions of the channel are as follows. The width was set to be the same as the backward-facing step, 7.6 cm. A channel length of 5 m was deemed sufficient to develop a boundary layer of the adequate thickness. From Figure 5.5 it can be seen that the height of the channel is much higher than the boundary layer thickness. This was a matter of design. Previous attempts used the test-case height. In that case, it was found that the mean flow speed was highly coupled with the formation of the boundary layer. This was a problem because a certain free-stream velocity was targeted. It was found that as the boundary layer grew, the free-stream velocity increased. This is logical by considering the mass conservation through a flow-normal plane at any point in the channel. For this reason the channel height was maximized within reason to a value of H = 2 m. This reduced this effect to an acceptable level.

In the DES study of the backward-facing step, it was proposed that a spalart-allamaras variant was to be employed. For this reason, a spalart-allamaras RANS turbulence model was used. Figure 5.6 shows the development of the boundary-layer thickness δ. A quadratic form was fit to the relationship. The expression $\delta = -0.0011x^2 + 0.0192x$ was obtained for boundary-layer thickness against x-distance along the channel. This expression was solved for the distance x at which the correct boundary layer thickness of 4.05 cm had developed. The distance was found to be 2.455 meters. A plane section was created at this location in order to extract the characteristics of the boundary layer at this location. Figure 5.7 shows the position of the extracted plane. The extraction plane was the same size as the inlet in the backward-facing step set-up, which was 15.2 cm high and 7.6 cm wide. In addition to the velocity, the turbulent viscosity ratio, and temperature were extracted. These parameters are the inlet parameters for the backward-facing step. The original set up (Vogel and Eaton, 1985) described a boundary layer on

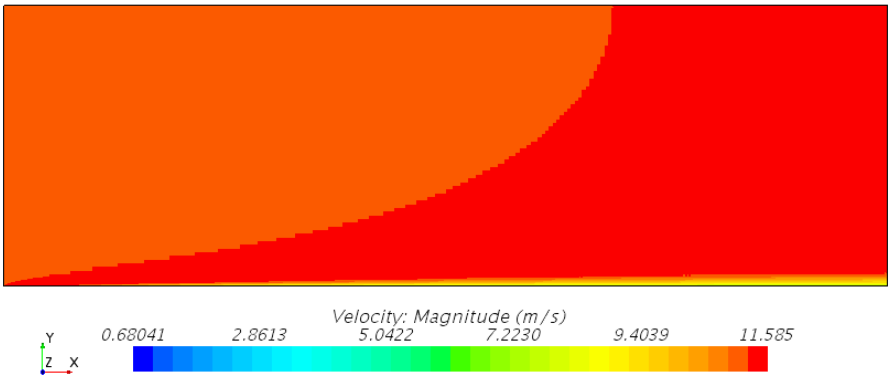

Figure 5.5: Showing the channel simulation used to develop the inlet boundary layer conditions.

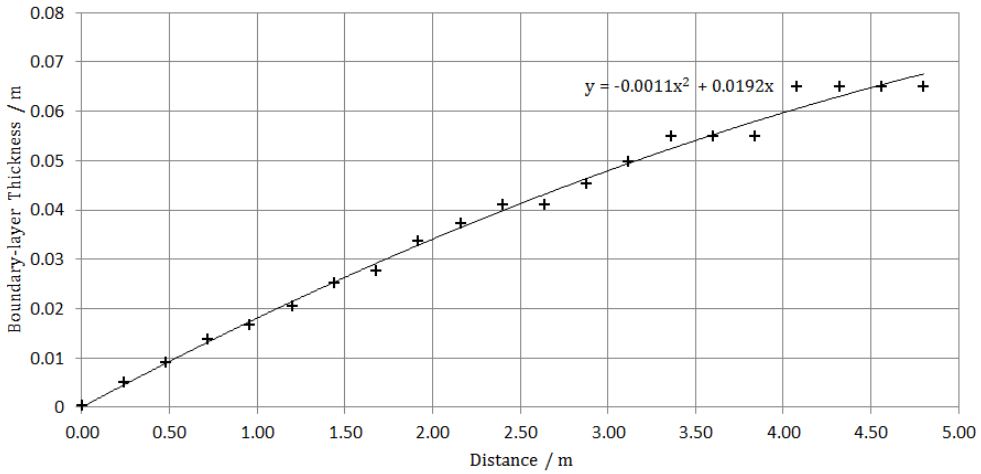

Figure 5.6: The boundary-layer thickness δ plotted against the distance x from the start of the channel

both top and bottom surfaces, in our channel simulation however there was only a boundary layer along the bottom surface. For this reason the properties on the extracted plane were mirrored about the minor center axis. This gave the effect of a boundary layer on both surfaces.

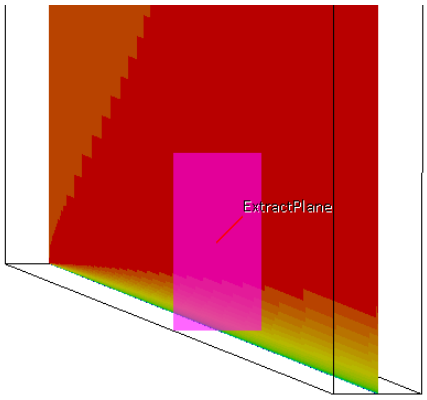

Figure 5.7: Showing the extraction plane at the appropriate location.

5.2 Analytic Techniques

5.2.1 Selective-Filter Based Decomposition

In this section, the filter based visualisation technique is presented. It serves to isolate and visualise the behaviour of specific frequency components of the flow. This method could be universally applied to both 2D and 3D data, aswell as experimental data such as PIV for example. First, the velocity and pressure time histories were extracted from the 2D bisecting plane of the domain. A subsequent interpolation yielded a set of evenly spaced points throughout the plane with 905 x 191 nodes in the x and z direction respectively. The time history of this plane is represented by parameter vector $\mathbf{S}$ which constitutes measurements of pressure, x velocity and z velocity taken at sample point i. The pertubation vector $\mathbf{S}'$ was obtained by subtracting the mean vector ($\mathbf{S}' = \mathbf{S} - \bar{\mathbf{S}}$). Finally, $\mathbf{S}'$ was passed through a sixth order elliptic band pass filter to yield the filtered vector

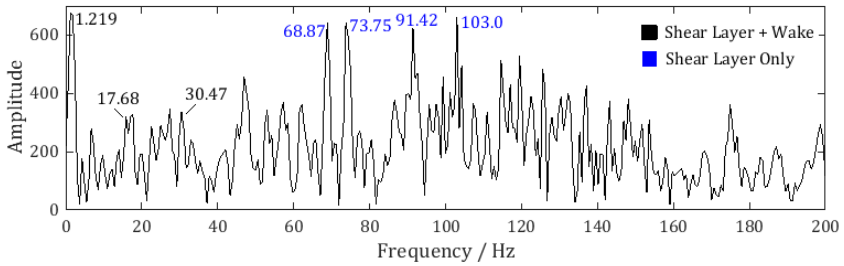

Figure 5.8: A Fourier transform taken at the shear layer probe. Colours indicate how measured frequencies coincided with other probe locations.

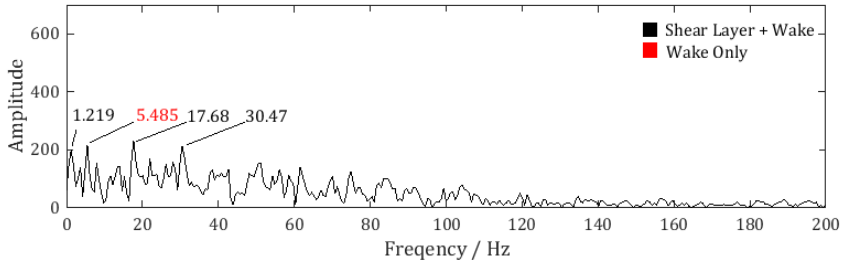

Figure 5.9: A Fourier transform taken at the wake bubble probe. Colours indicate how measured frequencies coincided with other probe locations.

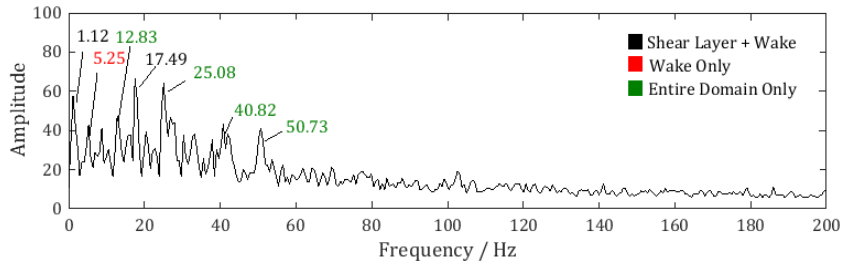

Figure 5.10: A Fourier transform taken as an average of each node location to represent the domain-wide spectral characteristics (905 x 191 nodes throughout the domain). Colours indicate how measured frequencies coincided with other probe locations.

5.2.2 Vortex Rotation

In order to identify vortex behaviour within the filtered results, an improvement to the the Q-criterion formulation (Dubief and Delcayre, 2000) was applied. The Q-Criterion is defined as

$$Q = \frac{1}{2}(|\boldsymbol{\Omega}|^2 - |\boldsymbol{S}|^2) \tag{5.1}$$

where $\boldsymbol{\Omega}$ is the vorticity tensor and $\boldsymbol{S}$ is the rate of strain tensor. A vortex is defined as regions where there is a high vorticity, but low rate of strain (ie. Q is larger than some threshold). This allows the differentiation of vorticity due to a vortex, as opposed to vorticity due to shear.

Table 5.2: A summary of identified frequencies of interest.

Frequency /Hz	Strouhal Number	Lower Cut-off /Hz	Upper Cut-off /Hz
1.219	0.004	-	3.07
5.485	0.018	4.266	7.31
12.83	0.043	11.66	14.58
17.68	0.059	16.64	21.33
26.82	0.090	26.24	29.74
30.47	0.102	29.26	32.30
40.82	0.137	39.65	41.40
50.73	0.171	47.23	53.07
68.87	0.232	67.04	71.92
73.75	0.248	71.92	76.19
91.42	0.307	88.99	94.47
103.0	0.346	101.8	103.60

We propose the following modification in order to gain insight into the rotational direction of the vortex. Due to the fact that this is a 2D problem, the vorticity vector becomes a scalar. Therefore by simply multiplying the Q-criterion by the sign of vorticity, the rotational information is stored

$$Q' = Q \cdot \overbrace{[Q > T]}^{\text{Threshold}} \cdot \overbrace{[2(\Omega > 0) - 1]}^{\text{Extract Vorticity Sign}} \tag{5.2}$$

where $>$ is the rational operator and T is the vortex strength threshold. Using a right-hand rule convention, a negative value implies a clockwise rotation and vice versa. The utility of this modification is shown by comparing two plots of the flow field around a Karman vortex street behind a cylinder. Figure 5.11 shows the standard Q-Criterion formulation (Eq. 5.1) applied to a Karman vortex street in the wake of a cylinder. Here the threshold T was set so vortices are revealed where Q>0. It identifies the location of the vortices but gives no indication with respect to their rotational direction. Contrasting with Figure 5.12 where the modified Q-Criterion has been applied (Eq. 5.2), the alternate rotational directions of each of the shed vortices is shown. A negative value corresponds with a clockwise rotation and vice-versa.

Before applying the Q-Criterion to this particular data-set, a spatial Gaussian filter

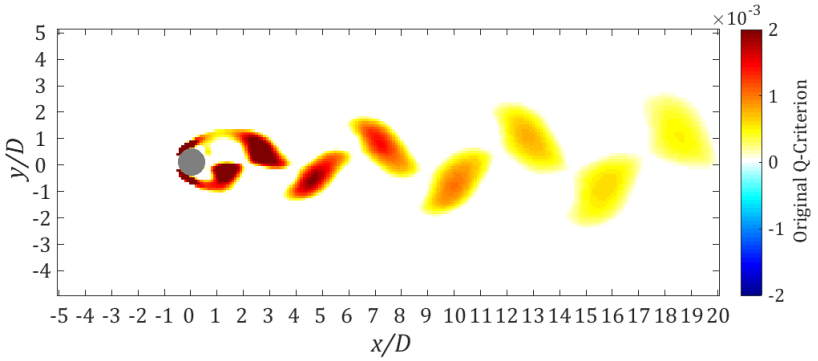

Figure 5.11: The existing Q-Criterion formulation (Dubief and Delcayre, 2000) applied on the Karman vortex street behind a cylinder.

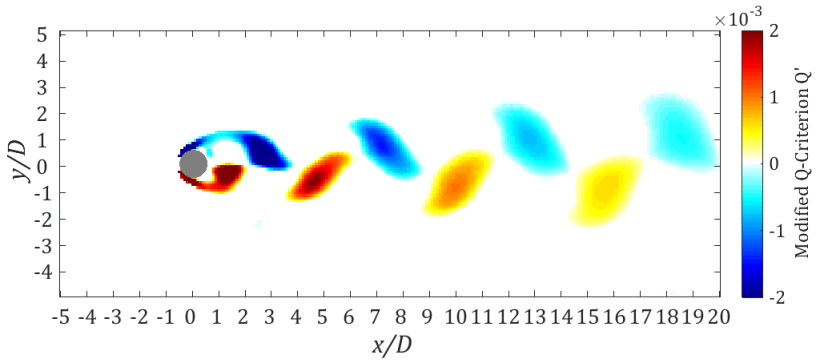

Figure 5.12: The modified Q-Criterion formulation, Q' , applied on the Karman vortex street behind a cylinder. Illustrating that rotational information is stored in the sign of the scalar. A positive value denotes an anti-clockwise rotation vice versa.

was applied with a filter width of 40 nodes and a standard deviation of $\sigma = 10$. It was found that this helped to distinguish the coherent structures over the noise. In the analysis, the vortex identification results were super-imposed onto the filtration results.

5.3 Results & Discussion

5.3.1 Large-scale centrifugal structures

Starting with the analysis of the St = 0.018 mode, large-scale pressure fluctuations are evident in the flow (Figure 5.13). Through observing the time series, they are

seen to propagate downstream at a speed of approximately 0.28 U_{ref}. Superimposed onto the large fluctuations, is a striation of pressure fluctuations that correspond to the step edge which extends downstream from the step. From the overlaid Q-criterion plot, it is clear that these pressure striations are associated with vortical structures. High-pressure and low-pressure regions correspond with the anticlockwise and clockwise rotation respectively. Figure 5.14 shows the same sequence of frames, but stream-wise velocity is plotted. At the bottom, there are consecutive regions of forwards and backwards motion; and at the top, the motions are inverted. By considering the direction of movement, these are identified as large-scale convective structures with alternating rotational directions (herein referred to as the global mode). This is substantiated by a line-integral convolution of the velocity field shown in Figure 5.15 that clearly shows they are convective structures. Comparing Figure 5.13 and Figure 5.14, it is observed that high-pressure regions and the low-pressure regions correspond with anti-clockwise and clockwise rotation respectively. By inspecting Figure 5.14, the vortices identified by the modified Q-Criterion method lie exactly at the interface between the forwards-moving and backwards-moving (red and blue) regions of the flow. By considering that a shear condition is present at this interface, these vortices are identified as Kelvin-Helmholtz vortices. The large-scale convective structures have been reported in several other studies including Dejoan and Leschziner (2004), Lee and Sung (2002), Neumann and Wengle (2004), Hasan (1992), Kostas et al. (2005). Hudy et al. (2007), for example describe wake-mode shedding in which large-scale structures are found to develop in place before accelerating downstream. They contrast this with shear mode shedding which is associated with the vortices that grow and develop in the shear layer. It is possible that these large-scale structures are associated with the wake-mode shedding and the vortices that correspond with the step edge correspond to the shear-mode shedding.

Here we consider that these convective structures (Figure 5.13, Figure 5.14 and Figure 5.15) are caused by centrifugal effects. As flow near the shear layer progresses past the step it experiences a strong curvature. Due to the change in angular momentum along the curve, the local fluid feels a centripetal force in the radial (upwards) direction. The result is a circulating flow where centripetal forces are responsible for the migration of fluid radially, and the pressure forces are responsible for its return. To explain the forwards-propagating pressure waves we derive inspiration from the well-known Taylor-Couette experiment (Coles, 1965). The experiment comprises two rotating cylinders that may either be co-rotated or counter-rotated. At the first critical Reynolds number, the centrifugal instability manifests as a vertical series

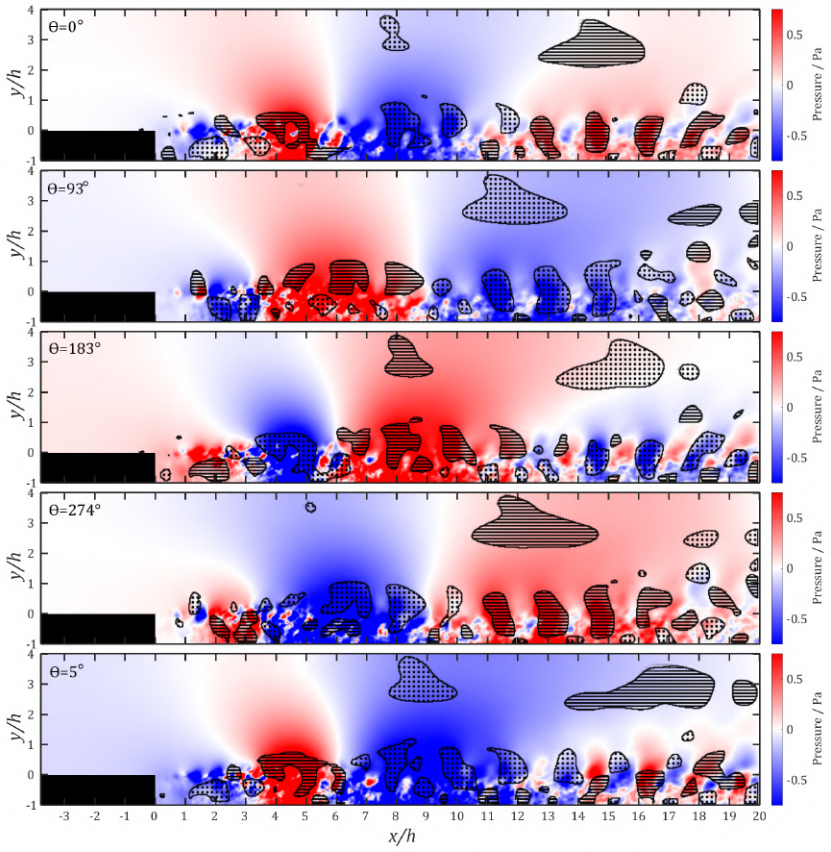

Figure 5.13: A time series of the St = 0.018 fluctuation showing the propagating pressure waves and also the pressure striations that correspond with the step height. Overlaid are the Q-Criterion results showing the detection of vortices (dotted – clockwise; striped – anticlockwise).

of stable streamwise vortex tubes. As speed is increased further, the tubes begin to show waviness due to the centrifugal effects from the newly arisen circular flow. With further acceleration, the convection patterns take on a cellular form known as doubly periodic Couette flow. The cells can be observed to propagate forwards at speeds slower than the flow speed. We propose that due to the high Reynolds number involved, a similar phenomenon arises. Therefore in Figure 5.16 we present our best estimate as to what these structures may look like in 3D. The concept was derived by associating the morphology of doubly periodic-Couette flow with our results (Figure 5.15). Furthermore, the known three-dimensionality of this flow supports the idea that these structures are not 2D.

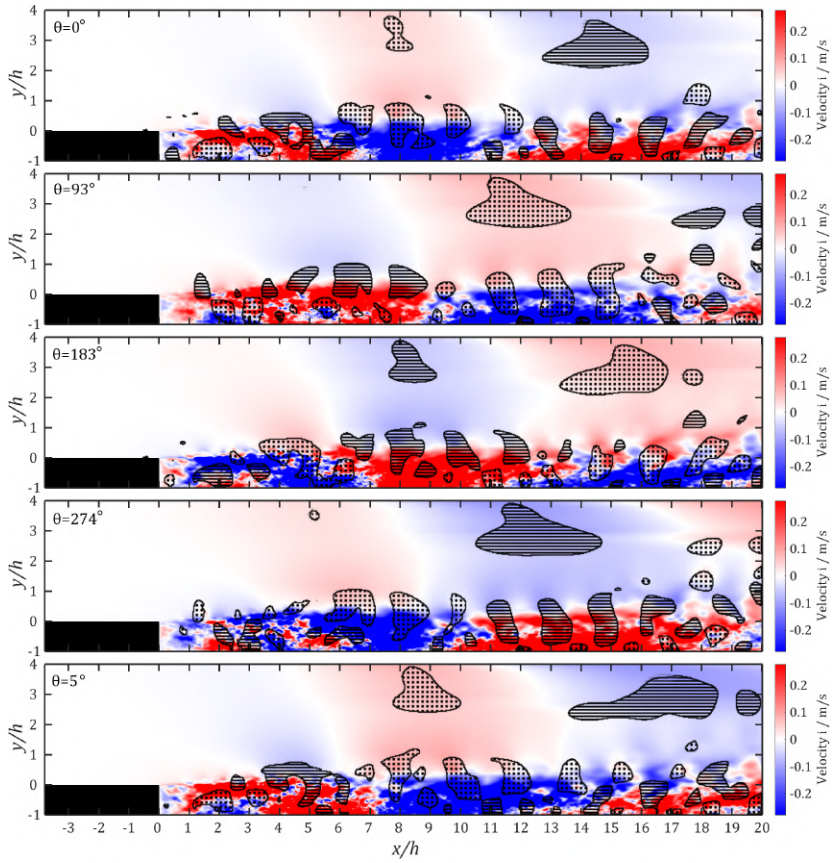

Figure 5.14: A time series of the St = 0.018 fluctuation showing the horizontal (x) velocity. Overlaid are the Q-Criterion results showing the detection of vortices (dotted – clockwise; striped – anticlockwise).

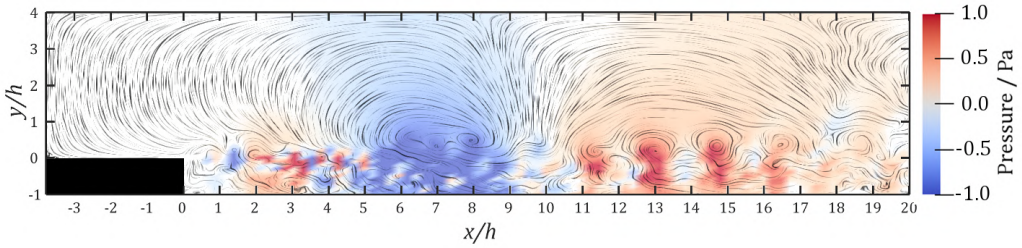

Figure 5.15: A line-integral convelution showing the large scale vortex structures believed to be of centrifugal origin.

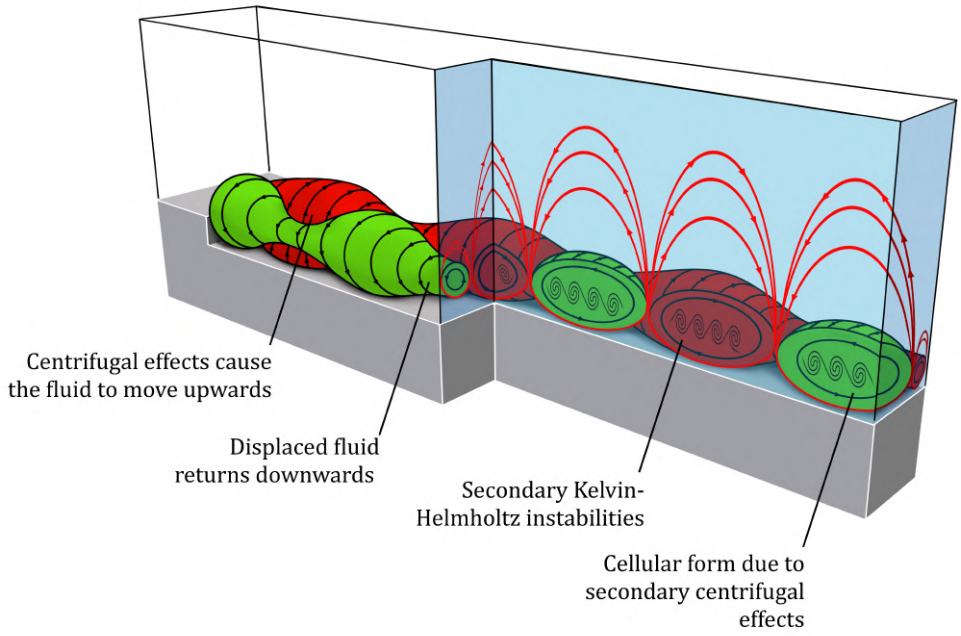

Figure 5.16: A schematic of what the global instabilities may look like in 3D.

Further evidence for the centrifugal hypothesis can be presented by testing the Rayleigh's criterion for this type of flow. Figure 5.17 shows that the velocity profile is clearly non-monotonic and is experiencing a curvature in mean flow. (Floryan, 1986) proved that this condition is susceptible to a centrifugal instability . This can be further illustrated by looking at the Deans number which represents the severity

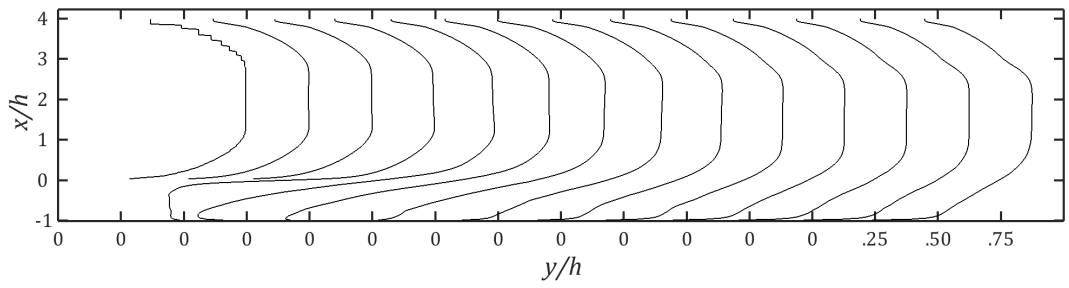

Figure 5.17: Velocity profile of the flow in the center showing a fully developed boundary layer with a non-monotonic velocity profile.

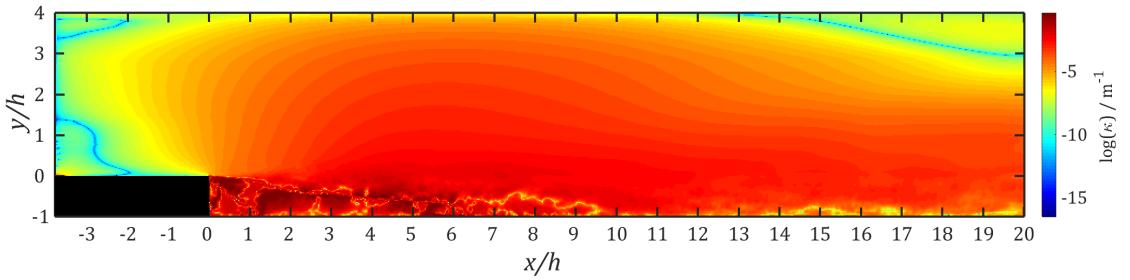

Figure 5.18: Radius of curvature κ of the time-averaged flow field showing the regions of high curvature beyond the step. Plotted as $\log(\kappa)$ for improved presentation.

of centrifugal forces. Therefore it is a suitable criterion to predict the conditions for centrifugal instabilities. In a fluid domain, the Deans number may be defined as

$$Dn = R_e \sqrt{\frac{D_e}{2R_c}} \tag{5.3}$$

Where R_e is the local Reynolds number, R_c is the local radius of curvature of the flow, and D_e is the Huebscher equivalent diameter defined as $D_e = 1.30(ab)^0.625/(a+b)^0.25$ where a and b are the width and height of the channel. The local radius of curvature can be computed from the work of Theisel (1995) using

$$\Re(V) = \frac{u \cdot det[V, V_x] + v \cdot det[V, V_y]}{\|V^3\|} \tag{5.4}$$

where $\Re(V)$ is the radius of curvature of the flow field and $V(x,y) = (u(x,y), v(x,y))^T$ is velocity vector field. The time-averaged flow field was used to compute the radius of curvature field shown in Figure 5.18.

The Reynolds number based on the step height is computed using

$$Re_H = \rho v H / \mu \tag{5.5}$$

where $\rho = 1.225 kg/m^3$ is density, v is local flow speed, $H = 3.8 \times 10^{-2} m$ is the step height and $\mu = 1.81 \times 10^{-5} Pa.s$ is the dynamic viscosity. The resulting plot is shown in 5.19.

By using both the curvature field (Figure 5.18) and the Reynolds number field (Figure 5.19), the Dean number field is computed using Equation 5.3. Figure 5.20

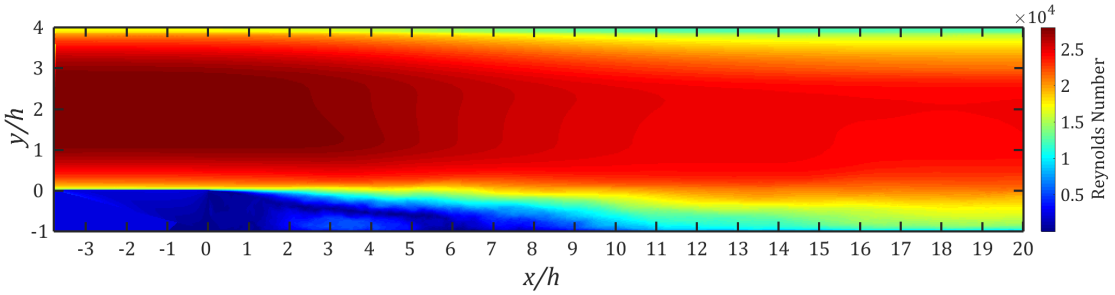

Figure 5.19: The local Reynolds number using the time-averaged flow field

shows that the Deans number is in excess of $D_n = 1500$ in the region beyond the step between $x/h \approx 3$ and $x/h \approx 15$. This indicates that the conditions for a centrifugal instability to manifest are present. This value of Dean number can be better understood through comparison with other studies that were carried out at a similar Dean number. Rütten et al. (2005) conducted a LES study on the low-frequency oscillation of Dean vortices at $D_n = 1400$ around a ninety-degree pipe bend. They find two dominant frequencies one at $St \approx 0.2 - 0.3$ which is prescribed to a shear layer instability, and also a lower frequency oscillation at $St \approx 0.01$. Both of these frequencies correspond with the global mode and the (later discussed) shear mode at $St = 0.018$ and $St = 0.232$ respectively. Interestingly. the authors of that study draw similar conclusions about the flow characteristics of the lower frequency mode. They also observe that the Dean vortices that form are oscillatory in nature in that they alternately dominate the flow and rotate in either the clockwise or anti-clockwise directions. The correspondence between our results reinforces the schema proposed in Section 5.3.1. There is likeness with other areas such as with a study by Bell et al. (2016) who study the dynamics of vorticies behind high speed trains using proper orthogonal decomposition. They find the streamline vortex that arises in the wake of the train has an oscilitary nature that alternate in dominance. Though not identified in that study, the cause of such a streamline vortex may be centrifugal in nature.

5.3.2 Kelvin-Helmholtz instabilities from the shear layer

Focusing attention on the higher frequency modes, the frequency of St = 0.232 is chosen for a start. From experimental observations, correspondence can be expected with span-wise vortical structures that originate from the shear layer. Driver et al.

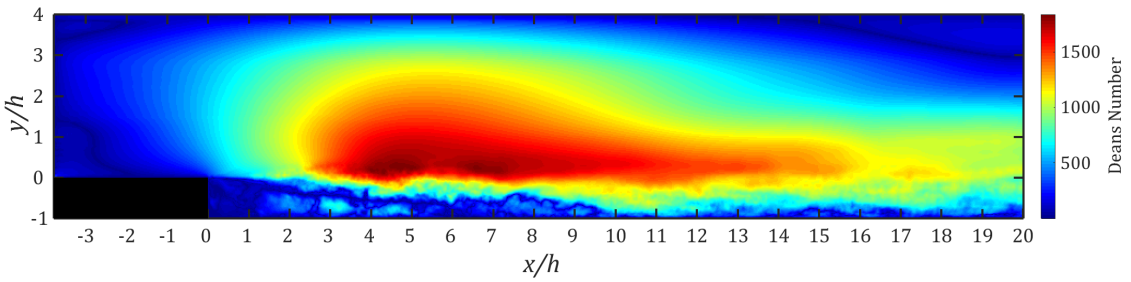

Figure 5.20: The Deans Number field showing areas with both high momentum and high curvature which are post prone to centrifugal instabilities

(1987) reported that the majority of energy was held within this mode. A primary correlation is that the frequency plot (Figure 5.8) shows that this is one of the most dominant modes within the shear layer. Figure 5.21 shows that pressure waves originate from a location approximately one step height distance from the step. This corresponds with the onset of instabilities visible through a volume rendering of the shear layer in Figure 5.22. The fluctuations can be seen to propagate downstream, grow in size and dissipate. This mechanism is often attributed to the Kelvin-Helmholtz instability (Hudy et al., 2007; Schram et al., 2004). So far the observations fit well with current understanding of the phenomena. However, the Kelvin-Helmholtz origin of the vortices normally carries connotations about unidirectional coherent structures. Schematic diagrams found in literature represent the shear layer this way, for example in Spazzini et al. (2001) and Driver et al. (1987). Our vortex identification plot on the other hand (Figure 5.21) shows that in this case, these shear layer-born vortices may rotate in either direction. The stream of vortices in Figure 5.21 B is more reminiscent of a Karman vortex street than the unidirectional stream of vortices that is normally observed. Moreover, by Figure 5.21 D the vortices have developed into a series of anticlockwise rotations. It is suspected that interaction between the shear-mode vortices and other instabilities, such as the previously discussed centrifugal instability, cause this behaviour at high Reynolds numbers.

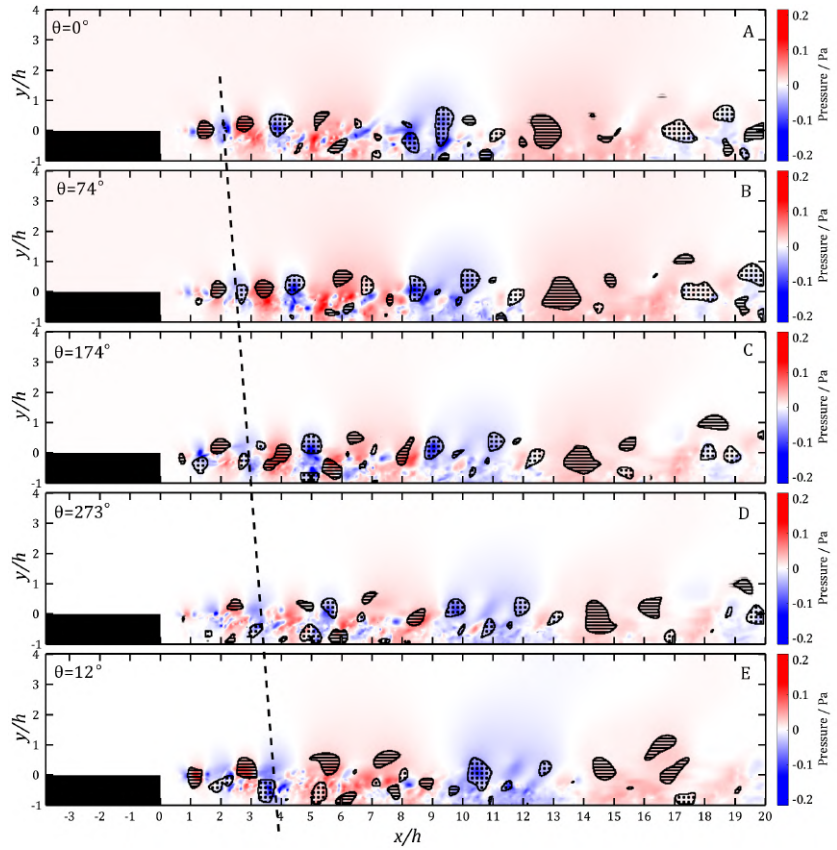

Figure 5.21: A time series of forward propagating pressure waves at St=0.232 (Dashed line showing the propagation of a single fluctuation with time; dotted – clockwise vortices, striped – anticlockwise vortices).

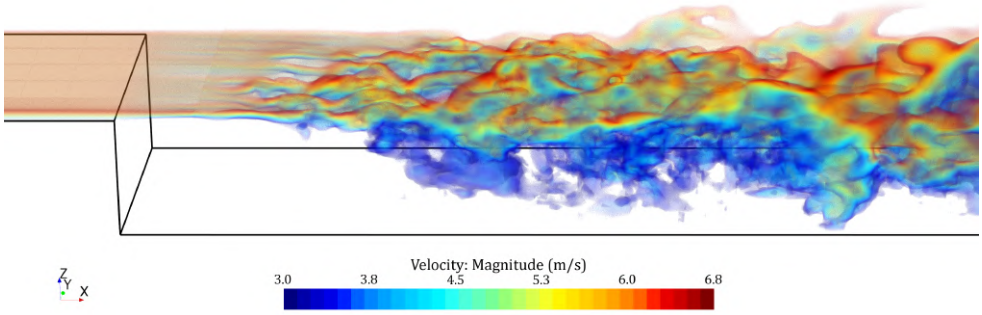

Figure 5.22: A volume rendering of the shear layer showing the onset of the shear layer instability and turbulence.

5.3.3 Behaviour of the entire range of frequencies

Now we inspect the entire range of frequencies to observe holistic trends. The first, most striking observation is that the plots from every frequency range look similar. They all to one degree or another contain both the large-scale global mode pressure waves, as well as the step-edge born structures. This indicates that the two forms identified are the most essential instabilities in this flow. Clearly the centrifugal instability manifests at several different frequencies. A potential explanation is that, by virtue of the boundary layer, there are a number of flow speeds present at the curvature. The result is a continuous range of underlying conditions that manifest as a set of distinct instabilities. The easiest frequencies to distinguish are the highest three frequencies (St = 0.248, St = 0.307, St = 0.346). The spectral analysis shows that these frequencies are only dominant in the shear layer and so these are likely to be a purely shear mode fluctuation. The fact that the pressure fluctuations in these plots seem to dissipate as they progress reinforces this idea. Another frequency that stands out is the previously discussed St = 0.018 mode. This is the only frequency where the vortices are orderly in their appearance and rotation. Moreover, this frequency was only prominantly found in the seperation region and not the shear layer. This indicates that it is a purely centrifugal mode. The striation of vorticies observed at this frequency may strictly be secondary instabilities.

5.3.4 General Observations

Now we inspect the entire range of frequencies to observe holistic trends. The first, most striking observation is that the plots from every frequency range look similar. They all to one degree or another contain both the large-scale global mode pressure waves, as well as the step-edge born structures. This indicates that the two forms identified are the most essential instabilities in this flow. The centrifugal instability manifests at several different frequencies. A potential explanation is that, by virtue of the boundary layer, there are a number of flow speeds present at the curvature. The result is a continuous range of underlying conditions that manifest as a set of distinct instabilities. The most orderly structures occur at the higher frequencies identified (St = 0.248, St = 0.307, St = 0.346). The spectral analysis shows that these frequencies are only dominant in the shear layer and so these are likely to be a purely shear mode fluctuation. Another frequency that stands out in its orderly form is the previously discussed St = 0.018 mode. This is the only frequency where

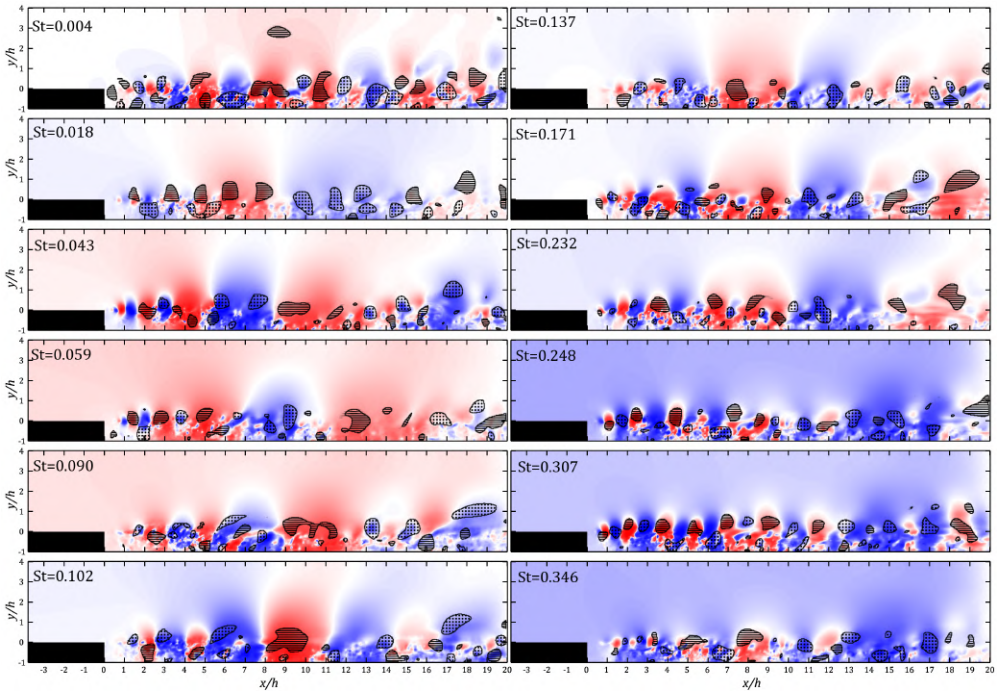

Figure 5.23: Instantaneous images from all twelve modes with their respective vortex identification results overlaid (dotted – clockwise vortices, striped – anticlockwise vortices).

the Kelvin-Helmholtz vortices are orderly in their appearance and rotation. It is possible that at the other frequencies there is an interplay between the shear-mode mechanism and the centrifugal mechanism that leads to their irregular structure. The energy cascade describes the conversion of energy from large-scale flow structures through a causal chain of instabilities down to the Kolmogorov microscale where energy is eventually dissipated by viscous effects. Regarding the secondary vortices identified within the global mode instability, it is possible that this mechanism facilitates the transfer of energy from the global mode towards turbulent dissipation. The identification of secondary instabilities in this work gives some insight into secondary processes which are not discernible through methods based on linear analysis.

5.4 Conclusions

In this chapter, a filter-based decomposition technique that is used to visualise coherent motions at frequencies of choice is presented. This is used in combination with a modification to the well-known Q-criterion vortex identification technique. The modification imprints the direction of rotation onto the result through a multi-

plication with the sign of local vorticity. Both techniques are applied simultaneously to study coherent structures within turbulent flow over a backwards facing step at Re = 28,000. The essential finding was the presence of large convective structures that move forward in time and alternate in polarity with a frequency of $St = 0.018$. Through a plot of Dean number we show that the conditions are ripe for a centrifugal instability and so identify these structures as a global Dean instability. Converse to the conventional Dean instability (a pair of stable counter-rotating vorticies), the vorticies here are seen to alternate in polarity. Taking inspiration from the Taylor-Couette experiments, it is hypothesised that the source of these structures are related to the doubly periodic Couette flow that arise from secondary centrifugal forces. Rütten et al. (2005) describe a similar phenomenon in flow around a pipe bend at similar Deans number. Kelvin-Helmholtz instabilities were also identified at higher frequencies ($St = 0.248$, $St = 0.307$, $St = 0.346$). It was found that the vorticies from the shear layer rotate in either direction and is hypothesised that the underlying shear condition of the flow may influence this behaviour. It is suggested that the structures found at higher frequencies correlate with shear-mode vortex shedding, and the lower frequency structures correspond with wake-mode shedding. Through an inspection of the remainder of frequency plots, it was found that all of the plots to one degree or another had both large-scale pressure fluctuations and also small fluctuations that originate from the step. This implies that the centrifugal instability and the shear mode instability are the two essential instabilities present in this flow.

There are several noteworthy limitations to the first part of study. The first important limitation is that due to the large amounts of data, a single plane was the most pragmatic choice for analysis. As a result, however, there was limited three-dimensional information. The second important limitation regards the computational constraints. The high temporal and special fidelity granted exceptional validation results, however for the same reasons only three seconds of simulated time could be obtained. An implication is that the flow may have still been transitionary. Moreover, centrifugal instabilities are known to exhibit path dependant behaviour. For example, in the Taylor-Couette flow, Coles (1965) showed that twenty-six distinct states were achievable at the same Reynolds numbers by changing the velocity path that the cylinders took to get to their final speeds. An implication of path-dependence for all studies of this kind is that the same boundary conditions may not necessarily result in exactly the same flows. Thereby the frequencies and structures identified are presented as a snap-shot into the underlying turbulent flow at

this moment. An informational flow chart is presented in Figure 5.24 to facilitate comprehension.

The chapter is summarised with the following key findings:

- Large-scale, coherent, convective structures were found and identified as Dean vortices.
- Secondary Kelvin-Helmholtz instabilities found within the convective structures. They are suspected to act as an energy transfer mechanism towards turbulent dissipation.
- Selective-filtering based flow decomposition, improved vortex identification, and Deans number techniques are presented.

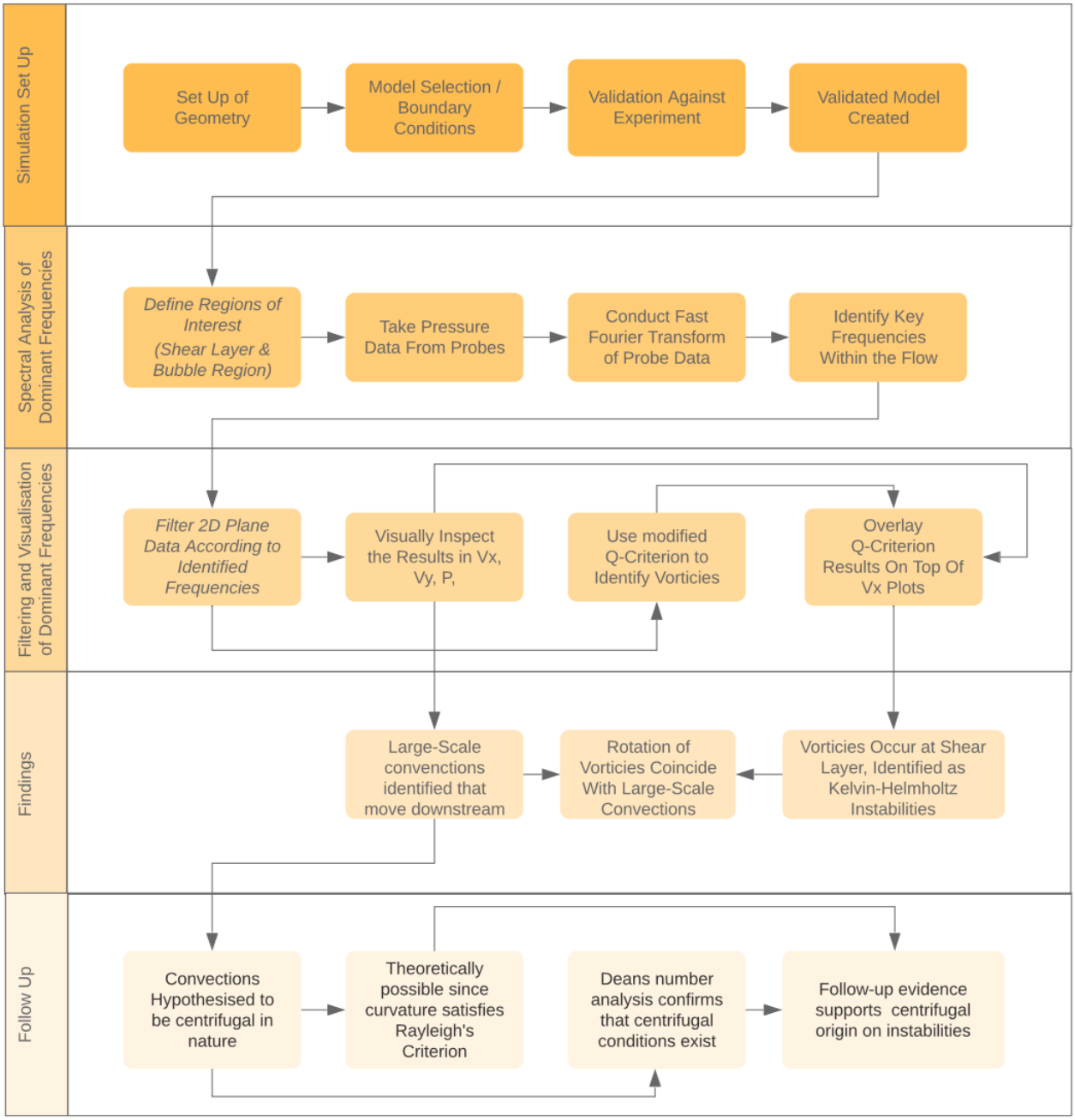

Figure 5.24: A summarising informational flow chart of this chapter to illustrate which results led to which findings.

6

Wavy Drag Reduction Device

This chapter entails the evaluation of the wavy drag reduction device on a tractor-trailer geometry.

6.1 Design of Wavy Device

The design of the base drag reduction device is intended to incorporate aspects of the Harbour Seal whisker while maintaining certain characteristics that are of practical and of research interest. The design has been created to satisfy the following criteria:

- Incorporate a wavy design.
- Practical for real-life application.
- Nominally two dimensional.
- Should not go beyond width and height confines of truck.

Given these set out objectives, the designs shown in in Figure 6.1 were developed. As can be seen it features an extension of the trailer walls from the base region into the wake of the truck. The trailing edge of the extrusion features a nominally 2D sinusoidal profile which takes inspiration from the semi-elipsoid studied by Tombazis and Bearman (1997) that was shown to have a drag reduction in the order of 10%. The designs feature sinusoidal profiles with varying wavelength k, from $k = 1$ to 4. The dimensions of the wavy extrusion were chosen with reference to the width W of the truck (2.59 m) such that the peak to peak amplitude was $W/4$ and the thickness of the extrusion was $W/100$. Figure 6.2 illustrates the geometric proportions of the device.

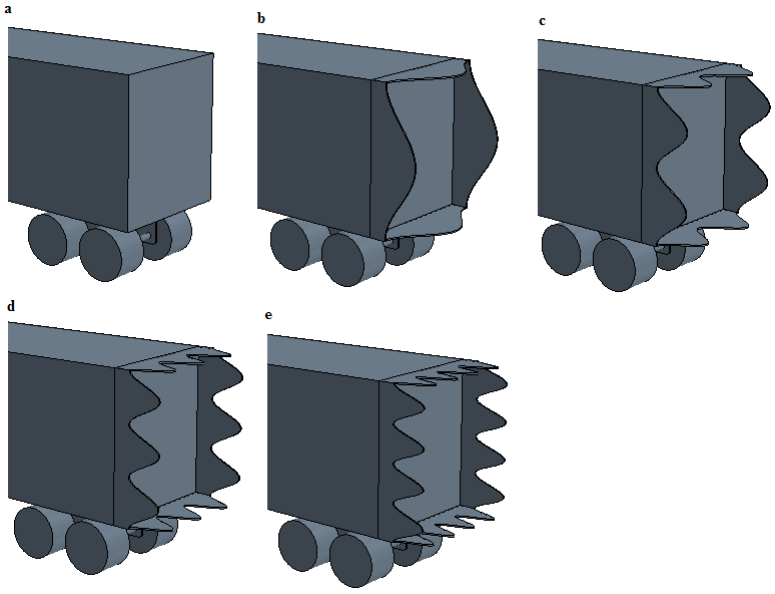

Figure 6.1: Showing the configurations of geometry tested in this study. (a - baseline; b to f - k=1 to k=4

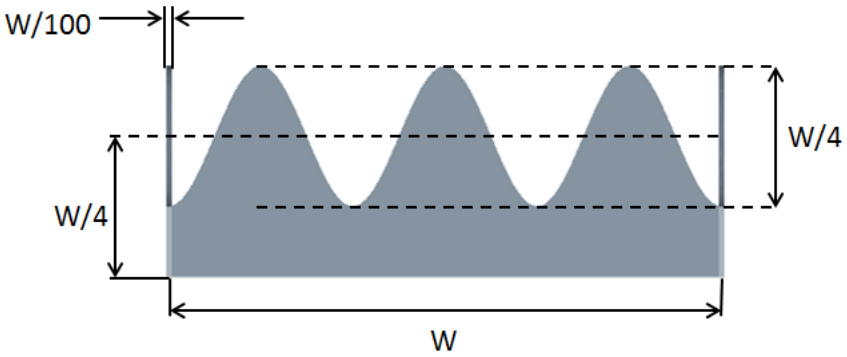

Figure 6.2: details of the geometry of the wavy drag reduction device.

6.2 Design of Study

Based on studies of comparable geometries such as Tombazis and Bearman (1997), it is hypothesised that the device will lower drag through a stabilisation of vortex shedding behaviour in the wake of the vehicle. The study in this section seeks to test this hypothesis. The first part of the study aims to obtain overall drag reduction performance data through RANS, which is widely regarded as a good model for benchmarking drag performance.

The second part of the study concerns understanding the function of the device from an unsteady perspective. This is achieved through a series of spectral analysis and qualitative analysis of vortex shedding behaviour.

6.2.1 Generic Conventional Model Geometry

As detailed in the literature review, the Generic Conventional Model (GCM) is a geometry that has been studied extensively by a U.S. Department of Energy research consortium Storms et al. (2006). The geometry was chosen for a number of reasons including:

- Availability of experimental data for validation.
- Wide array of tested devices on this geometry serves as a benchmark to compare inter-device performance.
- Geometrically simple, suitable for meshing with reasonable cell count.

Figure 6.3 shows the orthographic Generic Conventional Model geometry drawings as per Storms et al. (2004). The 3D model used in the study shown in Figure 6.4 was created from these drawings.

The model is based on the U.S. '18 wheeler' tractor-trailer configuration of heavy vehicles. It features an elongated locomotive with the engine at the front of the vehicle featuring aerodynamic styling in the form of a frontal bumper, side fairings, and a 'side extender' device that fills 60 % of the tractor-trailer gap. The side-extenders were recommended for use in studies due to the significant instabilities found in no-extender geometries that affect overall drag coefficient (Storms et al., 2006). The trailer features a slight radius of curvature on the leading edges on both sides, but besides that is devoid of any aerodynamic styling. The original geometry was created at a 1/8th scale. In the first part of the study the scaled geometry is used for reliable comparison with existing results; the second part of the study concerns the full-size geometry for real-world performance considerations. In the scaled geometry the supporting columns that are used to support the model in the wind tunnel are included for maximum geometrical likeness with wind tunnel data.

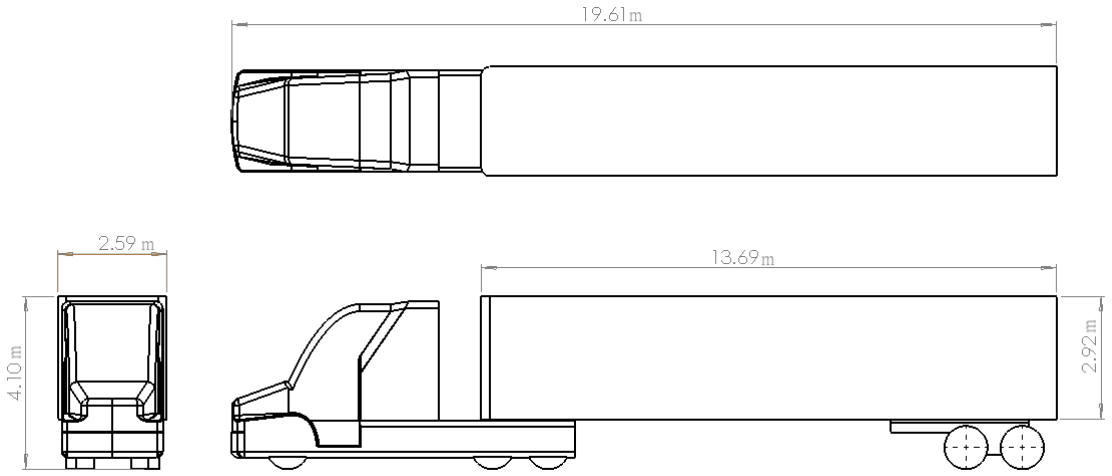

Figure 6.3: Showing the orthographic drawings of the Generic Conventional Model based on Storms et al. (2004).

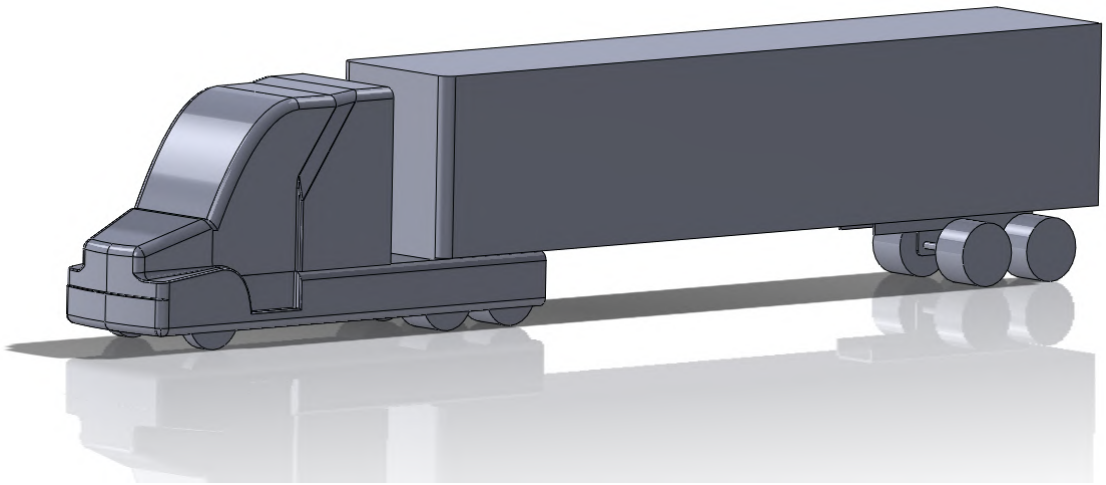

Figure 6.4: Showing the 3D model of the GCM created that was based on the drawings..

6.3 1/8th Scale-Model Simulations (RANS)

Steady state simulations of the GCM geometry are conducted in order to compare with existing studies of this geometry. Therefore the exact same test conditions are employed with experiments from Storms et al. (2006) and are outlined in the following section.

Simulation Domain

A 1/8th scale model of a tractor-trailer geometry known as the Generic Conventional Model (GCM) was used. The geometry was placed inside of a wind tunnel with a width, height and length of 2.13 m, 3.05 m and 4.57 m respectively. The origin of the domain was defined as the point on the road at the very front of the truck along the symmetrical centreline of the truck. The direction of the positive x, y and z axes corresponds to the down-stream, leftward and upward directions respectively. For Reynolds number calculations the trailer width of 32.3 cm is used as the characteristic length. The nominal flow speed was mach 0.15 which corresponds to a Reynolds number of 1.1 million; scaling to a life-sized truck this corresponds to a highway speed of 22.8 km/h.

Replicating the boundary layer characsteristics from the inlet is an important part of ensuring that the simulation matches against the experimental results. In the original experiment, the boundary layer thickness was measured to be 5.3 cm at a location of x= -13.33 cm. The distance to generate the required boundary layer thickness has been derived from the empirical relation from Schlichting et al. (1955)

$$\delta = 0.37x/Re_x^{0.8} \tag{6.1}$$

where δ is the boundary layer thickness and Re_x is the Reynolds number whose characteristic length is the distance from the start of the plate. From this relation the theoretical development of the boundary layer was obtained (Figure 6.5). By solving this relation for distance x, the upstream distance from the model that is required to generate a boundary layer of 5.3 cm was found to be 3.7525 m . Figure 6.6 shows the positioning of the geometry within the said domain.

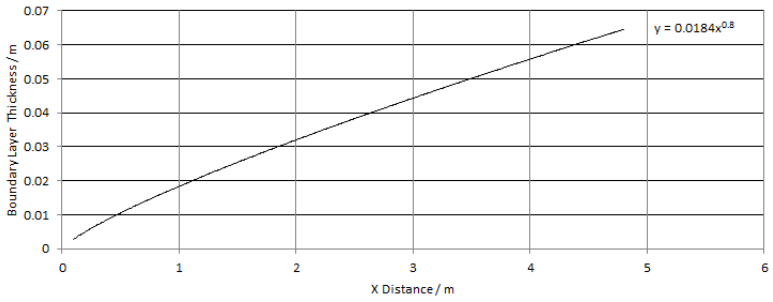

Figure 6.5: Model of the theoretical development of the boundary layer as a function of distance over a flat plate. This was used to calculate the distance between the inlet and test geometry required to generate a boundary layer of 5.3 cm.

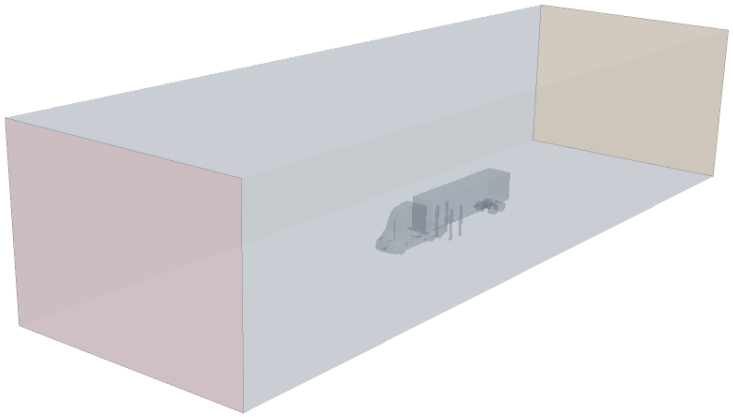

Figure 6.6: Illustrating the proportions of the entire domain and also the positioning of the geometry within.

6.3.1 Numerical Set Up

CFD Models

The following study employs the SST K-Omega turbulence model developed by Wilcox (2005), primarily for its improved performance within adverse pressure gradients. As such it is suitable to study the massively separated flow in the rear of the truck. Similar to the k-epsilon model, the k-omega turbulence model is a two-equation model that solves transport equations for the turbulent kinetic energy (k). It differs in that instead of solving for turbulent dissipation (ϵ), it solves instead for the specific dissipation (ω). The specific dissipation is defined as the turbulent dissipation per unit kinetic energy ($\omega \approx \varepsilon/k$) and can be considered to be analogous to a turbulent viscosity. One of the key advantages of the k-omega model is that it may be applied throughout the boundary layer, including the viscous-dominated regions near the wall. One disadvantage is the sensitivity of ω to conditions in the freestream. As such it is considered to be less stable than the k-epsilon model. The shear stress transport (SST) k-omega model devised by Menter (1992) seeks to merge the advantages of both the k-epsilon, and the k-omega model. It essentially introduces a blending function so that the model behaves like the k-omega model in the near wall areas and like the k-epsilon model far from the wall. The a complete outline of the model is provided in Chapter 4. In their study of turbulence models

in a backwards facing step geometry, Smirnov et al. (2018) shows that both RANS and IDDES are valid for the study of massively separated flows.

Meshing

The trimmer mesh was used that generates cuboidal mesh with a total of 2.92 x 10^6 elements. A default size of 10 cm was defined in the majority of the domain. A cuboidal volume of refinement was defined in the general vicinity of the vehicle. The volume of refinement extended behind the vehicle to appropriately capture the wake behaviour. Within the volume of refinement, cells were targeted to a size of 2 cm. Close to the vehicle surface, the target size was 1 cm, and the minimum possible size was 0.25 cm. Prism layers were defined in the vicinity of the surface with a total thickness of 6 cm and 13 layers with a stretching factor of 1.3. Figure 6.7 shows the volume of refinement, the structure of the mesh and the prism layers.

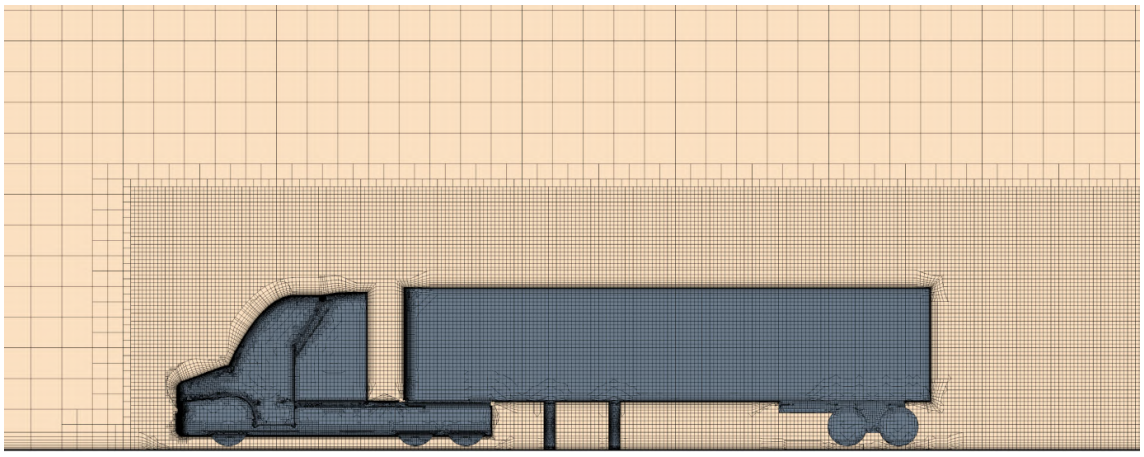

Figure 6.7: A plane section showing details of the mesh.

Physics

The simulation was using the SST K-Omega turbulence closure model which is recommended for massively separated flows. The working fluid was air with a density of 1.18415 kg/m^3 and a viscosity of 1.85508 x $10^{-}5$ Pa-s. A segregated solver was applied with a 2nd-order convection scheme. The remainder of the relevant computation parameters are shown in Table 6.1.

Table 6.1: Table of extended parameters used in the 1/8th scale SST (Menter) k-Omega simulations.

Property	Value	Property	Value
Curvature Correction Option	Off	Secondary Gradients	On
Realizability option	Durbin Limiter	Kappa	0.41
Compressibility Correction	True	BetaStar	0.09
Low Re Damping Modification	Flase	Sigma_k1	0.85
Convection	2nd-Order	Sigma_w1	0.5
Constitutive Option	Linear	Beta2	0.0828
Normal Stress Term	False	Sigma_k2	1.0
Tke Minimum	1E-10	Sigma_w2	0.856
Sdr Minimum	1E-10	a1	0.31

Validation

Validation of the model is based on two characteristics, the drag coefficient, and the pressure distribution along the surface. These are compared with experimental results from Storms et al. (2006). The drag coefficient was computed using

$$C_D = \frac{2L}{\rho A V^2} \tag{6.2}$$

where L is the characteristic length set to the width of the geometry of 32.38 cm; A is the frontal area of the vehicle computed as 0.166 m^2; ρ is the density of air as 1.18415 kg/m^3 and V is the inlet velocity.

The pressure distribution comparison is achieved through calculating the pressure coefficient at several points along the planar bisection of the truck. The pressure coefficient C_p is defined as:

$$C_p = \frac{p - p_\infty}{p_0 - p_\infty} \tag{6.3}$$

where p is the local pressure, p_∞ is the pressure in the freestream taken at a reference point in the wall of the test section, and p_0 is the stagnation pressure taken at a reference probe at the stagnation point at the bumper. According to the reference study, the reference free stream pressure probe was taken at the right wall at x = 145.8 cm, z = 84.2 cm. The stagnation probe was positioned above the origin at z = 10 cm. p_∞ and p_0 were measured to be -0.95 Pa and 131.0 Pa respectively.

From this a plot of C_p versus x distance along the centreline of the geometry on both top and bottom surfaces were obtained. 6.8 shows good correspondence between the experimental results published within Hyams et al. (2011) that reference an experiment conducted by Storms et al. (2006). Moreover, the computed drag coefficient of 0.436 is close to that measured by Storms et al. (2006) which was 0.427. This represents a 2.06% error in the computation of drag coefficient. The high degree of accuracy may be attributed to accurate replication of wind-tunnel conditions which include the incoming boundary layer and identical geometry that include supports used in the experiment. The chosen time-stop of one thousand iterations is supported by convergence analysis graph of drag coefficient versus the number of iterations. Figure 6.9 shows numerical convergence after approximately five hundred iterations.

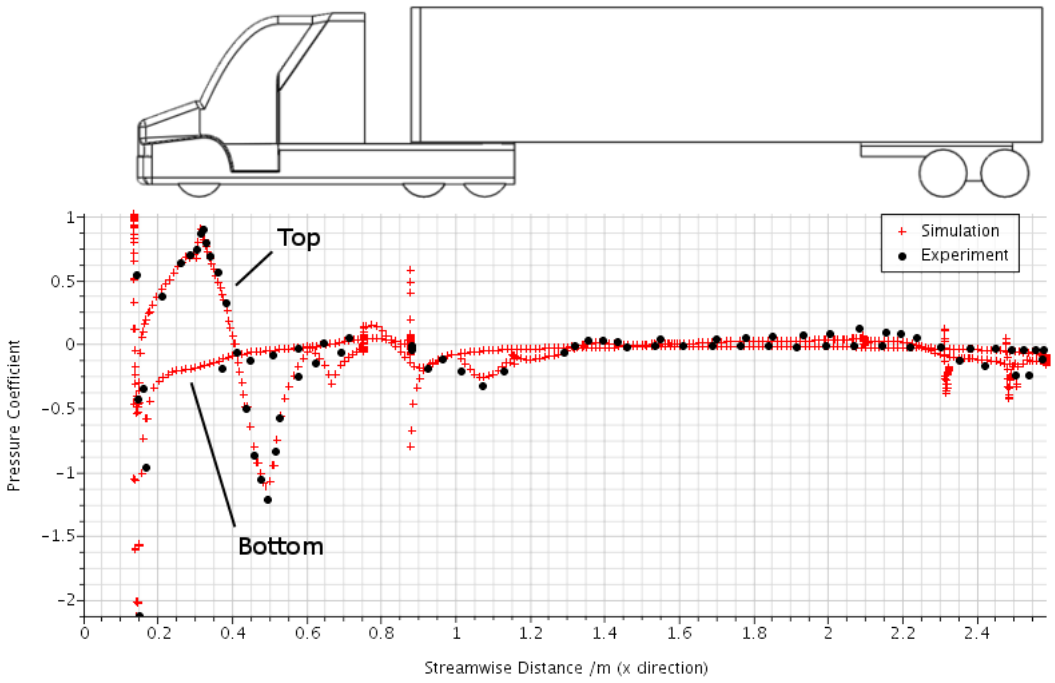

Figure 6.8: showing the close resemblance between simulated results and experimentally measured pressure coefficient readings from Storms et al. (2006).

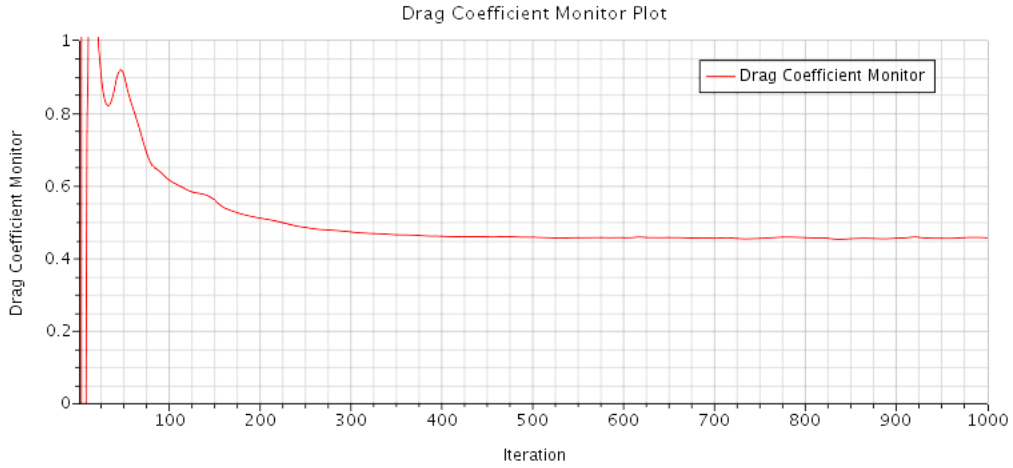

Figure 6.9: Drag coefficient vs. iteration, showing that the solution has converged after 1000 iterations.

6.3.2 Overall Drag Performance Results

Six simulations were run with the baseline, k=1, k=2, k=3, k=4, and k=5 geometries (Figure 6.1), the drag coefficient results are shown in Figure 6.10. They show that depending on the wave number, the device may increase or decrease the drag. The device with only one wavelength (k=1) shows a slight increase in drag, bringing the drag coefficient up to 0.460 from the baseline of 0.436. This represents a 5.5% increase in drag. The majority of the devices (k=2 to k=5) show a roughly similar drag reduction performance, with the best performer (k=2) showing a 22.93% drag reduction.

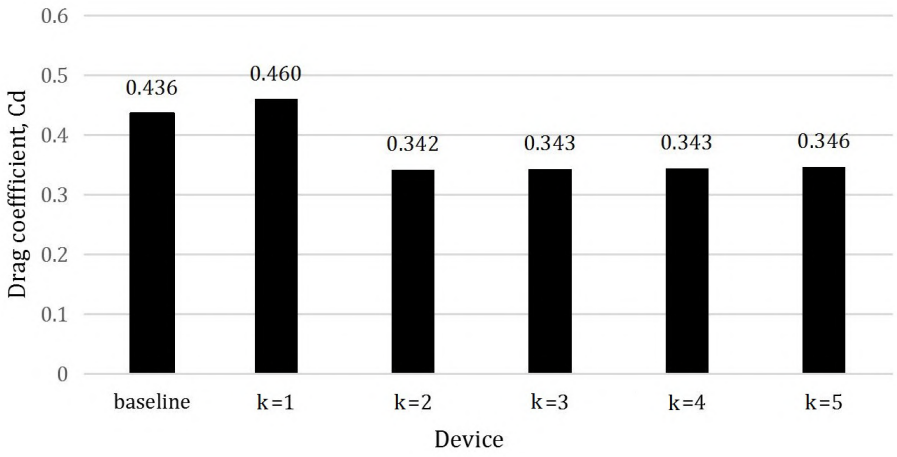

Figure 6.10: Comparison of drag coefficient Cd among tested devices.

These results were compared with experimentally derived results in the same conditions from Storms et al. (2006). Figure 6.10 shows the range of devices tested experimentally from Storms et al. (2006). Two results from this simulated study are included in this comparison, namely the baseline simulation, and the best performing wavy device (k=2). This comparison shows firstly that the drag coefficient generated from the simulation was accurate when compared with the reference study. Secondly, it shows that the performance of the wavy device was in-line with the best performing base drag reduction device, namely the boat tail with 20 degree flaps. What is notable about this device is that it is a nominally 2-D device rather than being 3D like the boat-tail. Given the similarities in performance with the boat-tail, applicators of the device may opt for this 2D design which would be structurally easier to apply.

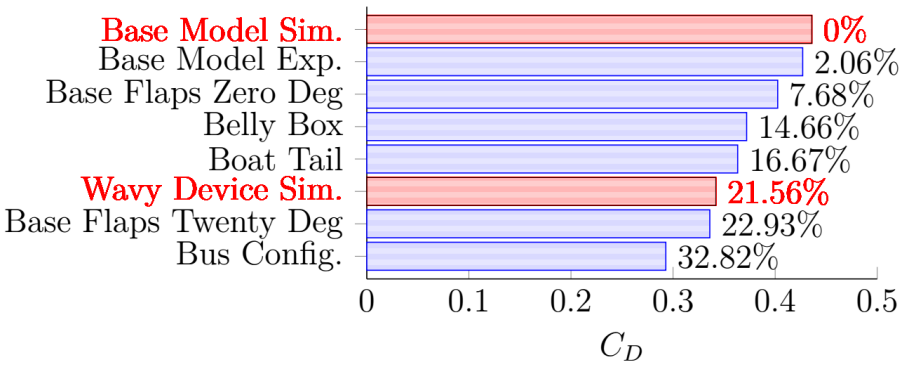

Figure 6.11: Comparison of best performing simulation results (red) with best performing experiments (blue) from Storms et al. (2006). Percentages based on simulated base model drag coefficient.

Analysis of Wake Length

From the literature one of the metrics that was frequently measured was wake length. A lower drag coefficient is often associated with a shorter wake length. In this case wake length was determined by obtaining a pressure iso-surface within a control volume in the wake of the vehicle. This is a suitable measurement as the wake is often defined as the low pressure region in the wake. Therefore areas where pressure is below zero can be defined as within the wake, and areas where pressure is above zero can be defined as outside of the wake. Therefore the wake region can

be defined as the boundary between these two zones where pressure equals zero. Figure 6.12 shows the processing steps to obtain the wake length. Figure 6.12 (a) shows the control volume in the base of the vehicle, and Figure 6.12 (b) shows the corresponding $p = 0$ iso surface. The surfaces are coloured using velocity.

(a) Resampled volume taken at the base of the truck.

(b) Pressure isosurface taken at p=0 used to define boundary of wake.

Figure 6.12: Illustrating the method of defining an isosurface in order to measure wake size.

Figure 6.13 shows the wake length in the baseline, k=1, k=2 and k=3 geometries. From a visual perspective there is no apparent pattern of wake length with increasing wave number k. This is confirmed by a plot of wave number versus wake length and drag coefficient (Figure 6.14) which shows no distinct correlation. However, visually there does appear to be a link with the velocity of the flow at the wake bubble surface, with drag coefficient. That is to say the geometries with high drag values appear to show higher velocity flow on the wake interface. In order to investigate further the red intensity channel, which denotes high flow velocity was extracted from the RGB image as shown in Figure 6.15. Following this a histogram analysis yielded the statistical distribution of red color throughout the image. Subsequently, the trends of median red intensity and drag coefficient were plotted together as shown in Figure 6.16. From this it is clear that in this case, rather than wake length, the drag coefficient is more closely correlated with the intensity of flow at the wake boundary. This hints at a cause of the drag reduction mechanism being linked with the interaction of fast moving fluid with the wake bubble. It is hypothesised that the best performing devices play a role in shielding the wake region from the high velocity flow within the shear layer. This would have the effect of reducing shear-based momentum transfer from the free-stream to the wake region, thereby increasing wake pressure and reducing pressure drag. This is a theme that will be

developed in the following sections.

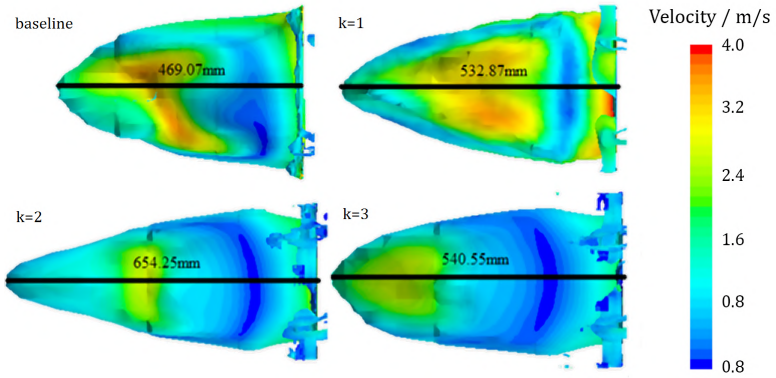

Figure 6.13: Comparison of wake lengths of four geometries

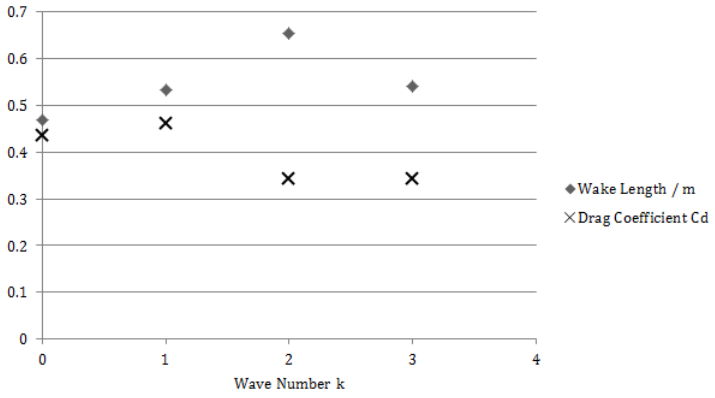

Figure 6.14: Contrasting wake length with drag coefficient at different wave numbers.

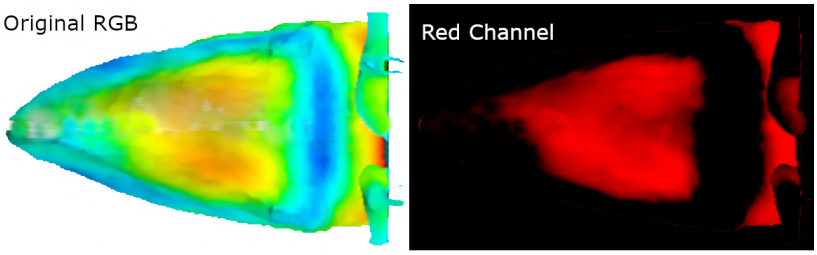

Figure 6.15: Showing extraction of the red color channel from the velocity plot of the wake.

Table 6.2: Color histogram analysis, showing statistical distribution of red intensity from wake analysis in Figure 6.13.

Geometry	Mean	Std. Dev.	Median
Baseline	0.468	0.323	0.498
k=1	0.578	0.332	0.659
k=2	0.454	0.369	0.435
k=3	0.412	0.336	0.392

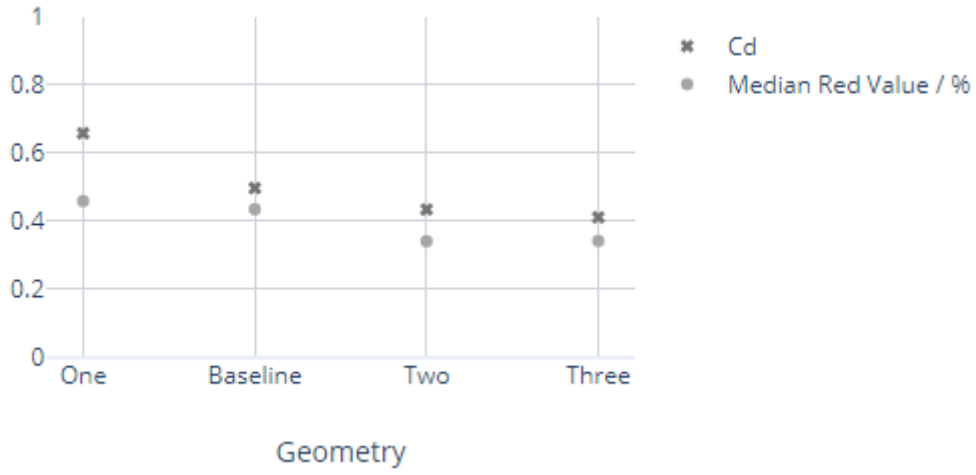

Figure 6.16: A plot comparing the drag coefficient trend with the trend in red intensity from the statistical histogram analysis. Showing that the drag coefficient is positively correlated with the intensity of high velocity flow in the wake interface.

6.3.3 Proposed Shear-Layer Drag Mechanism

Shear Force in a Viscous/Turbulent Regime

Following from previous reults that hint at a link between velocity in the shear layer and drag coefficient, a proposed mechanism between the two is outlined in this section. Following from this further results will investigate the proposed mechanism within this framework.

In a shearing flow, momentum (per unit volume = ρu) is transferred from a region with high velocity to that with low velocity. The resistive behavior of the fluid to such deformation is characterized by its viscosity. This is expressed in Newton's law of viscosity for laminar flows that relates shear stress with the rate of deformation

$$\tau = \nu\rho\frac{\partial u}{\partial y} \tag{6.4}$$

where τ is the shear stress, ν is the kinematic viscosity of the fluid, u is the velocity and y is the direction normal to velocity. From Equation 6.4 it is plain to see that the shear stress is directly proportional to the rate of change of momentum per unit volume; where the kinematic viscosity is the constant of proportionality.

In large shear stress environment such as this one, instabilities in the flow result in turbulence that quickly engulf the entire shear region. Turbulence enhances mixing and momentum transfer and in effect makes the fluid behave as if it were more viscous. In a turbulent flow the so-called apparent shear stress is expressed as

$$\tau = \rho(\nu + \nu_T)\frac{\partial u}{\partial y} \tag{6.5}$$

where ν is the kinematic viscosity and ν_T is called the eddy viscosity or momentum exchange coefficient. In most practical cases, $\nu_T >> \nu$ and Equation 6.5 becomes (Chanson, 2004a)

$$\tau = \nu_T\rho\frac{\partial u}{\partial y} \tag{6.6}$$

The Link Between Shear-Force and Pressure Drag

In a flow the stress is a field with both normal stress and shear stress components that varies according to position. In order to deduce x-force from the 3D stress tensor it must be integrated with respect to the area as follows

$$F_x = \int_A \sigma_{xx}dA + \int_A \tau_{yx}dA + \int_A \tau_{zx}dA \tag{6.7}$$

where σ_{xx} is the normal stress in the x direction, τ_{yx} and τ_{zx} are the shear stresses in the x-direction with respect to shearing in the y-direction and z-direction respectively. Considering an infinitesimal fluid parcel resting on the base of the vehicle, the presence of the solid boundary would prevent any shearing deformation of the fluid. By definition a shear stress cannot exist in this location. Therefore, moving from the wake region where shearing is possible, to the base where it is not, the components of shear stress with base-normal directions (τ_{yx} and τ_{zx}) are eventually

experienced as a normal stress acting on the base (σ_{xx}); in other words the shearing action on the wake results in a low pressure at the base. At the base surface Equation 6.8 then reduces to

$$F_x = \int_A \sigma_{xx} dA \tag{6.8}$$

This low pressure is balanced by an equal and opposite force that occurs at the base boundary through its structural members then onto the main body of the vehicle. This is the chain of events that results in the body of the vehicle experiencing a drag force. This mechanism is illustrated in Figure 6.17.

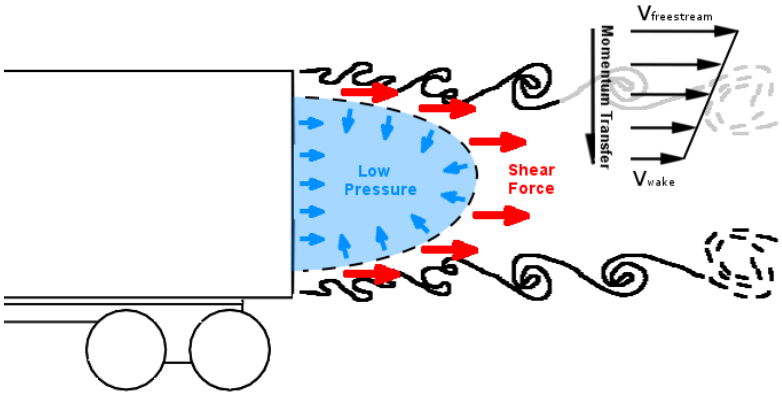

Figure 6.17: Showing the mechanism relating shear-layer instabilities with base pressure and drag.

Key Variables That Influence Drag Force

Following from this proposed mechanism and through inspection of Equation 6.6 the variables that would result in a decrease of base drag force are the corresponding decrease of:

- ν_T the eddy viscosity which is a function of the flow field rather than the fluid properties.
- $\frac{\partial u}{\partial y}$ the rate of change of velocity with respect to the directions perpendicular to the flow.

noting that the density ρ is assumed to remain constant.

6.3.4 Investigation of Momentum Transfer Across Shear Layer

Motivation

From mechanism outlined in Section 6.3.3, a higher shear stress in the shear layer would ultimately induce a higher drag force at the base of the vehicle. The shear force is fundamentally affected by mechanisms that increase the rate of momentum transfer which are: an increase in viscosity; or an increase in turbulent momentum exchange (turbulent viscosity). In order to verify this hypothesis this section aims to study the link between velocity rate at the shear layer and drag.

It was expected that the geometry with the greatest drag would show evidence of greater momentum exchange. Noting that the re-circulation region within the wake has a small or even negative component of streamwise velocity, greater overall momentum exchange means a higher velocity within the wake in the stream-wise direction. This is due to the direction of stream-wise momentum transfer being from the free-stream towards the wake center; momentum from the free-stream is carried into the wake. In addition to looking at the overall velocity change, the rate of velocity change will also be examined by looking at the gradient of the $\partial u/\partial y$ curve. The rate of momentum transfer is directly proportional to the gradient as outlined in Equation 6.6. This will yield information regarding the rate of momentum transfer at this local point. Using heat as an analogy, the velocity within the wake indicates how much energy has been transferred overall up to this point (ie. temperature), and the shearing rate tells us the local rate of energy transfer (ie. heat transfer coefficient). Overall momentum exchange and the local rate of momentum transfer $\partial u/\partial y$ are exclusive concepts. The former is measured by stream-wise velocity within the wake whereas the latter is measured by looking at the gradient of velocity. A higher rate of momentum transfer $\partial u/\partial y$ does not necessarily indicate greater overall energy transfer, only a higher rate of transfer at the measured location.

Set Up of Measurements

The shearing velocity rate refers to the change in stream-wise velocity with respect to the direction perpendicular to the shear-layer ie. $\partial u/\partial y$ and -$\partial u/\partial y$ at the top and bottom shear layers of the wake respectively, and $\partial u/\partial x$ and -$\partial u/\partial x$ on the left and right shear layers respectively. In this investigation the shear rate on the top of the wake at an arbitrary location downstream of the top trailing edge of the trailer was chosen to sample stream-wise velocity. This location on the symmetry plane was chosen in order to negate any effects due to asymmetry, and the top shear

layer was chosen as opposed to the bottom due to less interference from the ground and wheel geometry. A line probe that consisted of one hundred sample points was placed a distance of one trailer width downstream of the trailing edge. The position of the probe is shown in Figure 6.18. The domain of this line probe covered 20cm on either side of the shear layer and this was chosen on a visual basis to cover the region in which the shear layer was most pronounced. A line probe was taken at the conclusion of each of the five RANS simulation described in Section 6.3 with the wavy device of varying wave number.

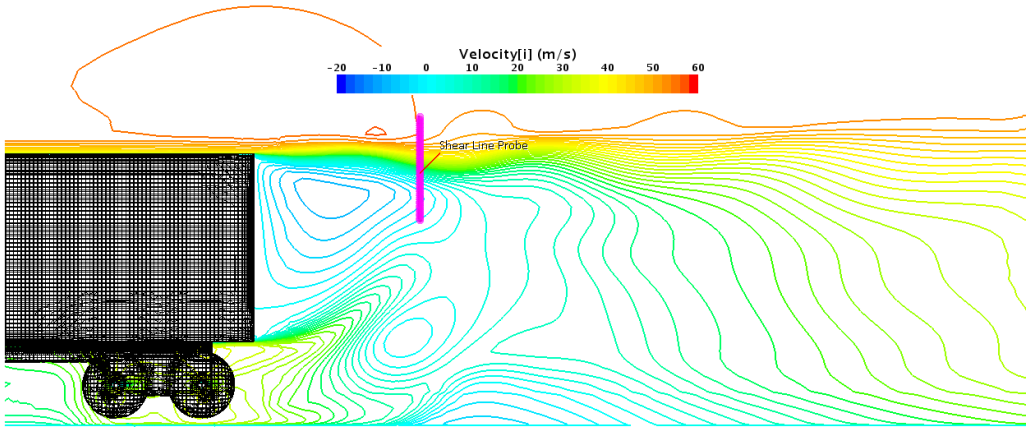

Figure 6.18: Showing the positioning of the vertical line probe

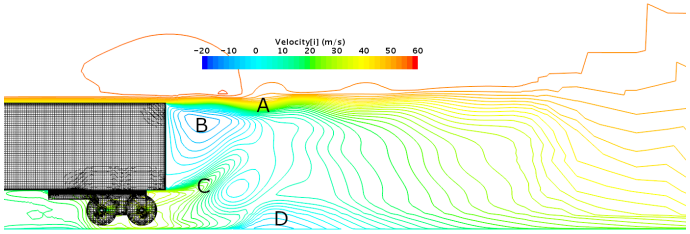

(a) No Device

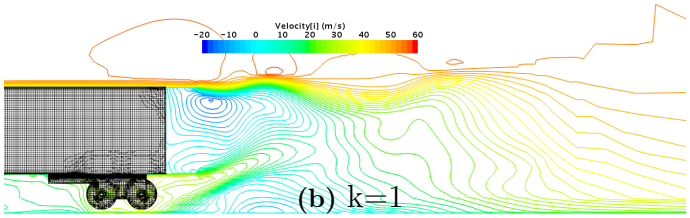

(b) k=1

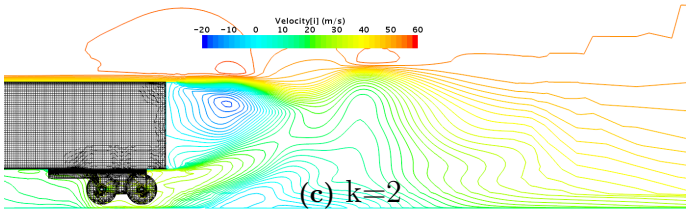

(c) k=2

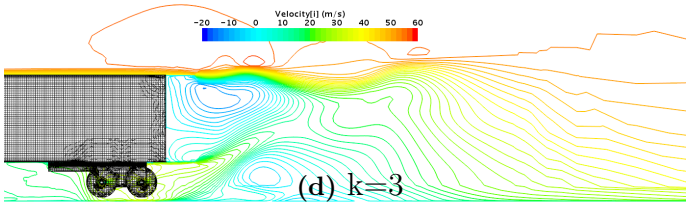

(d) k=3

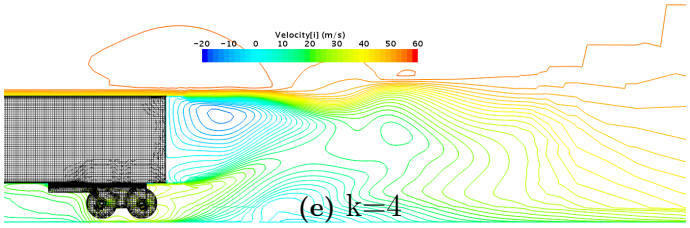

(e) k=4

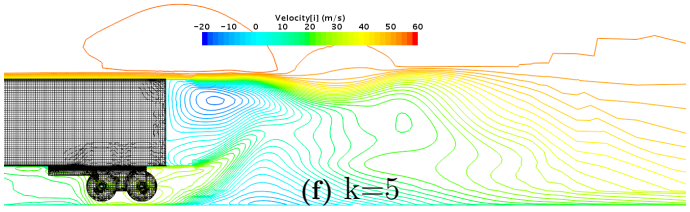

(f) k=5

Figure 6.19: Showing stream-wise velocity contours in the wake of the truck.

Results

Velocity plots were produced from the velocity vectors within the bisecting plane of the wake region. The plots for each geometry with wave-numbers corresponding to $k = 1$ to $k = 5$ are shown in Figure 6.19.

Prominent features of the base region flow flow are labeled in Figure 6.19 and are so identified as follows:

(A) ***Free shear layer***: The free shear layer appears at the boundary between the free-stream and the wake region. It is characterised by a high velocity component in the outer region and a low or negative velocity within the wake bubble. The shearing action of the flow is known to generate Kelvin-Helmholtz instabilities that degenerate into complete turbulence at real-world speeds. This is the primary region of interest in this section as it facilitates momentum transfer into the wake.

Effect of the wavy geometry: The geometry transposes the shear layer backwards by an amount that is equal to the length of the protrusion. Through inspection of Figure 6.19(a) and Figure 6.19(b), it can be seen that the boundary layer remains adhered to the extended surface on the top of the truck until it reaches the end of the geometry and the shear layer begins. Also noticeable is the greater diversity in velocity of the shear layer, the negative velocity of the wake bubble is more pronounced in Figure 6.19(b) than in Figure 6.19(a). This may be due to the transposition of the shear layer towards the center of the wake bubble where the reverse flow is strongest. This is evidence of the device shielding the wake region from the free stream allowing for a more uninterrupted reverse flow to occur. The effect of the shear layer will be further studied in the upcoming sections.

(B) ***Wake bubble***: The wake bubble is the region of low pressure in the wake of the vehicle. This low pressure is known to pull on the base face and is a major contributor to the overall drag of the vehicle. Similar to the previously discussed backwards-facing step, the wake bubble is known to oscillate at a low frequency and this is known as bubble-pumping. Following from the previous section the likely cause of this effect is centrifugal effects.

Effect of the wavy geometry: Comparing Figure 6.19(a) with Figures 6.19(b),(c),(d), and (e), the wake bubble with no geometry looks short and small, whereas with the device it appears longer. This result is consistent with the previous wake

bubble analysis and may be related to the observed shielding of the wake region from degradation from the free-stream flow. From Figure 6.19, there appears to be two regimes of wake shape. The first is a wake pattern consistent with highly concentric and orderly streamlines that center of the wake center, these seems to be consistent with the even wave-number geometries k=0, k=2, k=4. In the second regime the wake is highly skewed with streamlines stretching further out with the flow in various parts before coming back inwards towards the wake center. This pattern seems consistent with the odd geometries k=1, k=3, k=5. This effect will be further studied in the upcoming sections.

(C) ***Undercarriage flow***: This jet-like flow originates from the space between the axel housing. This feature may be specific to this Generic Conventional Model. A real truck would normally feature a more complicated geometry in this region that may include axles, support structure, hydraulic cables etc. which would contribute to flow instabilities and perhaps hinder the flow in this region.

Effect of the wavy geometry: Comparing Figure 6.19(a) with Figures 6.19(b),(c),(d), and (e), the undercarriage flow appears short lived in the no-device situation. The kinetic energy from the undercarriage flow is quickly dissipated into the wake and it can be reasonably deduced that this kinetic energy is lost to turbulence within the wake. In the with-device geometries the undercarriage flow protrudes along the majority of the wake bubble bottom almost to the back of the wake bubble. This indicates that the kinetic energy of the jet experiences less dissipation and therefore extends further backwards. Similarly to the shear layer, the wavy device prevents disturbance of the jet with the reverse flow regions.

(D) ***Secondary re-circulation region***: This secondary re-circulation region is caused by a low pressure region that occurs downstream of the trailer above the ground plane. This low pressure region is related to the main wake bubble in that the cause of the low pressure is also due to shielding from the main flow. This region appears separated from the main wake bubble because the kinetic energy that the undercarriage flow contributes briefly interrupts the re-circulating flow before the momentum contribution from this flow is dissipated and a reverse flow is reestablished.

Effect of the wavy geometry: The secondary re-circulation region of the no-device geometry Figure 6.19(a) is distinct from the remainder in that without

the device there appears to be two low pressure re-circulation regions. The additional re-circulation region appears to hover between the wake bubble and the primary re-circulation region that is in its usual position on the floor. The additional re-circulation region appears to be related to a bifurcation of the undercarriage jet. It is possible that this additional re-circulation region is a natural part of this flow that cannot appear under the conditions of a strong undercarriage jet.

The primary focus of this current investigation was the momentum transfer within the shear layer. Figure 6.20 shows the results from the line probe that was placed within the shear layer. Along the vertical axis is stream-wise velocity; along the horizontal axis is vertical distance from the ground starting from within the wake and ending above the shear layer in the free-stream. The line-probe covers a distance of 20 cm around the shear layer. The general velocity profile in this region has a distinct 'S' shape. The start of the curve is synonymous with the bottom of the line probe that is found within the wake bubble where fluid velocity is low or reversed. Moving from this point upwards (right along the horizontal axis) the curve dips further to its most negative velocity. This represents the movement from the center of the re-circulation region to the place of maximum negative velocity which is just before the shear layer. Moving further along from this point the velocity can be seen to rapidly increase. This is the start of the shear layer where the momentum transfer from the high velocity flow in the free-stream is evident. Further along and the region of proportional increase is reached. This inflection point represents the center of the shear-layer. From inspection it is seen that this is the point of maximum gradient. Furthermore the turbulent shear stress equation (Equation 6.6) implies that maximum shear stress occurs at this inflection point where $\partial^2 u/\partial y^2 = 0$. This maximum shear stress is accompanied by a steep rise in velocity. Beyond the inflection point velocity continues to rise but with a diminishing return since momentum transfer rate is proportional to the velocity differential. As velocity approaches the free-stream velocity, the velocity difference reduces and the rate of increase accordingly falls which leads to asymptotic behavior towards to top of the shear layer. The conclusion of the line probe is within the free-stream which represents the source of all x-momentum along this probe.

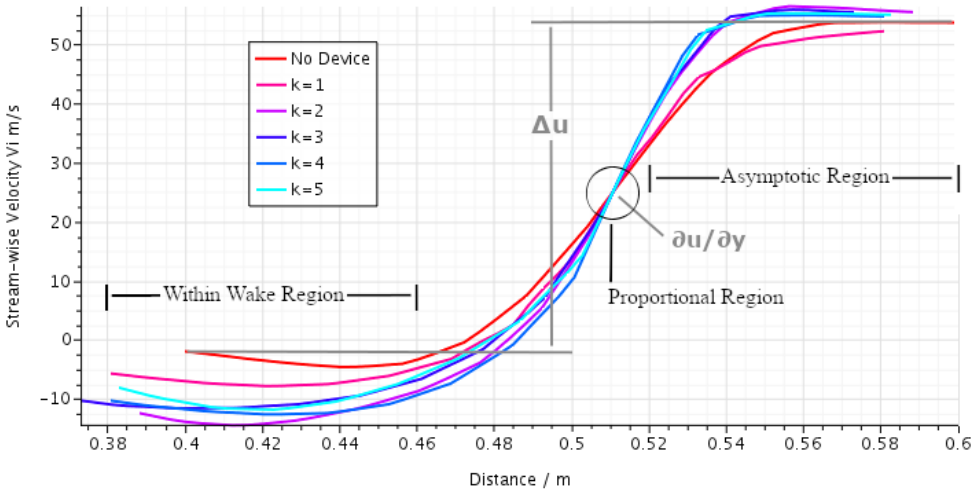

Figure 6.20: Comparison of stream-wise velocity within the shear layer comparing the no-device geometry with k=1 to k=5 geometries

Now that the general shape of the velocity distribution has been understood, the differences between each geometry will be examined with respect to the mentioned regions which are the: within-wake region; proportional region; and the asymptotic region.

1. *Within-wake region (0.38m<y ≤ 0.46m)*
   The most apparent difference between the no-device case and the with-device cases is that with no-device, the velocity at the bottom of the probe situated within the wake is almost zero. This contrasts with the with-device cases where there is a strong negative velocity. As discussed earlier this may be attributed to the shielding effect of the wavy geometry. Here it is shown that the device effectively hinders interaction of the shear layer with the recirculating flow of the wake region. Apart from the fact that the no-device case has a close-to-zero velocity at the start of the probe, there doesn't appear to be much correlation with wave number and velocity. The with-device geometries share the trait of a stronger negative velocity at the start of the probe, however moving from k=1 to k=5 the order from most negative velocity to least negative is: k=2, k=3, k=4, k=5, k=1. With exception of k=1 the trend seems to be that the lower the wavenumber k, the more negative the velocity at the start of the probe. This can be contrasted with the drag performance analysis in Figure 6.14 that shows k=2 is the most effective drag reduction and k=1 is distinct in that it has a worse drag performance than even the baseline no-device case. If

the shielding of the wake from the free-stream is related to performance, than it would appear that k=2 is the optimal geometry, and there are diminishing returns on increasing wave number from this point. However it should be noted that the difference in drag between k=2 and k=3 is marginal.

2. *Proportional Region ($y \approx 0.51m$)*
   The proportional region lies at the center of the shear layer where maximum stress and momentum exchange occurs. The gradients have been subsequently computed and the results from this analysis are shown in Table 6.3. From these results it can be seen that the du/dy gradient is least for the no-device geometry, second least is the k=1 geometry, and k=2 - k=5 geometries have a similarly steep gradient hovering around 1300 s^{-1}. The local rate of momentum exchange also follows this order based on the turbulent viscosity equation (Equation 6.6). This also roughly corresponds with the order of worst drag performance to best performance from Figure 6.14.

   This result is contrary to the hypothesis of this section that the performance of the device is linked with lowering the momentum exchange. If the hypothesis was correct one would expect the worst performing device to have the highest momentum exchange but this is not the case. This apparent contradiction may be resolved by considering that local rate of momentum exchange is not equivalent to overall momentum exchange into the wake. The overall momentum exchange into the wake is ultimately related to the degree that the inside-wake region has been influenced by the free-stream velocity. The free-stream velocity is the source of all stream-wise velocity into the wake. At one extremity, in the case of a complete and total momentum exchange into the wake, the velocity within the wake would be equal to the free-stream velocity. Therefore an effective measure of total momentum exchange into the wake is the difference between free-stream velocity, and the within-wake velocity Δu. Indeed when this is done the results roughly corresponds with theory, that is the best performing device has the highest velocity difference between the wake and free-stream Δu. The cause of the locally greater momentum exchange coefficient can be attributed to the higher Δu. Assuming a constant eddy viscosity ν and density ρ in the turbulent shear stress equation (Equation 6.6) a higher velocity differential directly leads to a higher shear stress. It can also be deduced that in order for the no-device geometry to have a greater overall Δu as is the case, an integration of the momentum exchange coefficient along the shear layer starting from the separation point to this probe location

Table 6.3: Results from shear layer investigation showing drag coefficient Cd, velocity change across shear layer Δu, and velocity gradient $\partial u/\partial y$. Normalised results are also shown with the ˜ notation.

Geometry	C_d	Δu	$\partial u/\partial y$ / s^{-1}	$\tilde{\Delta u}$	$\tilde{\partial u/\partial y}$
Baseline	0.436	55.6	866	0.601	0.819
k=1	0.460	57.8	1053	0.732	0.852
k=2	0.342	67.9	1344	0.934	1.000
k=3	0.343	65.9	1289	0.896	0.971
k=4	0.343	65.1	1440	1.000	0.959
k=5	0.346	63.2	1351	0.939	0.931

would yield an overall greater value than the with-device case. This points to the way that the device moves the separation edge further backwards thereby giving less integration length for momentum exchange to occur. The takeaway is that though the with-device case has a higher local momentum exchange coefficient due to the existence of a greater backwards flow, the no-device case has a longer shear layer length which gives more opportunity for greater momentum exchange. Moreover, it would appear as if the greater backwards flow strength of the with-device cases is directly related to there being less opportunity for momentum exchange in the up-stream parts of the shear layer due to the device. Then, the observed greater back-flow of the with-device cases is not the cause of the improvement, but is a symptom of reduced momentum exchange.

3. *Asymptotic Region (0.52m<$y \leq$ 0.60m)*
   In comparing the asymptotic regions, the k=1 geometry which has been identified as the worst-performing of all cases has yet to reach the free-stream velocity. This is evident by the positive gradient at the conclusion of the k=1 curve. This implies that the shear layer for this case is larger than the probe length. This is in comparison with the k=2:k=5 geometries where the shear layer is atleast atleast 2 cm shorter in width. Similarly to the development of a boundary layer, this thickness of the shear layer indicates a greater development of the shear layer at this point. Noting that the separation point of this geometry at the bisecting plane is identical to the other odd-number geometries (k=3, k=5) the expedited development of the shear layer cannot be attributed to the transposition of the separation point backwards. Therefore another mechanism would be responsible. Savory and Toy (1988) studied the

response of upstream turbulence to shear layer growth on surface-mounted hemispheres. They found that a higher the up-stream turbulence level corresponds to a more-quickly growing shear layer. From this the cause of the increased shear layer diffision may be related to the large singular protrusion that characterises the k=1 geometry. It is possible that this geometry allows for greater lateral flow from the corners of the base region which increases overall up-stream turbulence levels that ultimately results in a thicker shear layer.

Discussion of Momentum Transfer Across Shear Layer

Figure 6.21 shows the general trends of drag coefficient C_d, velocity difference across the shear layer Δu, and velocity gradient at the shear-layer inflection point $\partial u/\partial y$. The units of Δu and $\partial u/\partial y$ have been normalised through division with the maximum of the set such that the largest value will output unity and other values represent a percentile of this maximum. This is done for the purpose of simplified comparison in understanding the general trends.

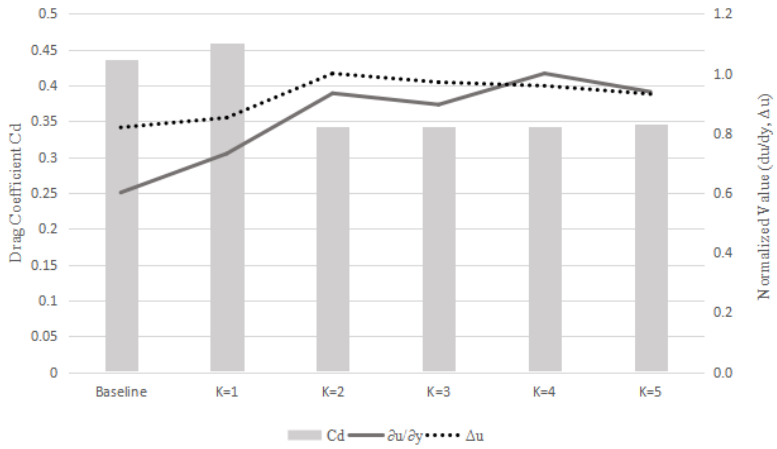

Figure 6.21: Comparison of the trends with changing geometry in variables Cd, Δu $\partial u/\partial y$

Starting with the extremities, the best performing geometry with the lowest drag coefficient, k=3, also corresponds with the highest velocity difference between the free-stream and the wake Δu. Likewise, the worst performing device corresponds with the second lowest velocity difference by a narrow margin. Recall that the root source of momentum within the wake is from the free-stream. These results appear to be congruent with the previously outlined hypothesis; momentum transfer

across the shear layer is a fundamental contributor to pressure drag in the wake, and better performing devices function by limiting momentum transfer. Further relation is shown in the results from k=2 to k=5 where there is a trend of slight decrease in Δu that corresponds with a slight increase in C_d. A step increase in Δu between geometries k=1 and k=2 also corresponds with step decrease in drag coefficient.

Mathematical Analysis of Shear Layer Body Forces

In the outset of this investigation of the shear layer, it was expected that the velocity gradient would decrease with the drag reduction. This was based on the theory outlined in Section 6.3.3 where it was shown that $\partial u/\partial y$ is directly related to shear stress. The idea was that a lower velocity gradient would yield a lower shear stress therefore decreasing base drag force. Since examining the data this seems not to be the case. The better performing devices were in-fact shown to correspond with a higher shear stress. Overall force on the other-hand is derived from a combination of shear and normal stresses. Normal force is caused by a momentum change in the control volume and is ultimately experienced by the surface of the control volume as a pressure. In order to further understand the unexpected behavior, a mathematical analysis of overall force has been conducted. Here only considering the forces on the x-y plane Equation 6.7 becomes

$$F_x = \int_A \sigma_{xx} dA + \int_A \tau_{yx} dA \tag{6.9}$$

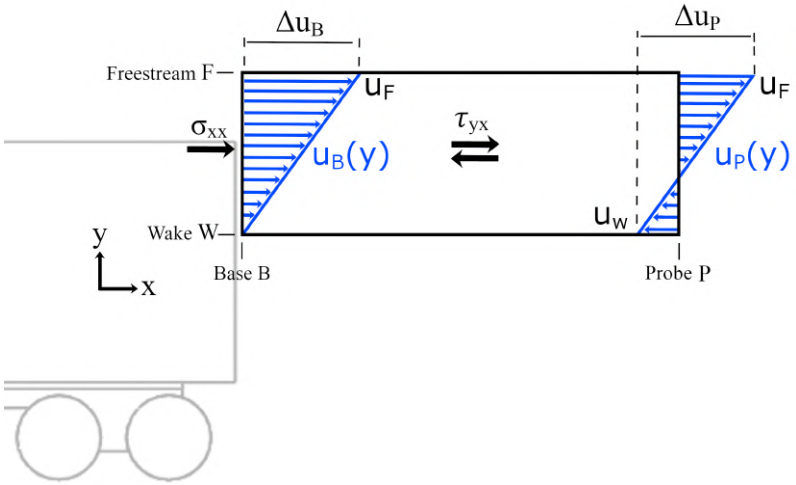

Figure 6.22: Control volume taken between base and shear layer probe, showing linearised velocity profile that is assumed.

Consider a control volume that encompass the region between the line probe and the base region as shown in Figure 6.22. The control volume lies on the x-y plane and is bounded by the freestream and the wake in the y-axis, and by the base and the probe locations in the x-axis. A linearised velocity profile is assumed at both the base and probe regions. The freestream velocity u_F is assumed constant and equal at both base and probe regions. The wake velocity is zero at the base given the no-slip condition, and the velocity at the probe position within the wake u_w is permitted to take a negative value given the re-circulation region that has been observed. This control volume may be analysed both in terms of shear stress and normal stress, in order to gain insight into their behavior and relative importance.

Shear Stress τ_{yx}

Consider the x-y shear stress component of drag force. By expanding the area integral, substituting the definition of shear stress $\tau = \nu_T \rho \frac{\partial u}{\partial y}$, and substituting assumed constants $\nu_T \rho = k$, Equation 6.7 becomes

$$F_{\tau_{yx}} = k \int_x \int_y u'(y)\, dy\, dx \tag{6.10}$$

bounds F and W can then be applied to the inner y integral. In the case of the line probe, these bounds represent an integration across the shear layer from the wake to the free-stream. From this the following is obtained

$$F_{\tau_{yx}} = k \int_x \int_{y=W}^{y=F} u'(y)\, dy\, dx \tag{6.11}$$

solving the definite y integral and substituting the integration bounds yields

$$F_{\tau_{yx}} = k \int_x \Big[u(y)\Big]_W^F dx \tag{6.12}$$

$$= k \int_x \Big[u_F - u_W\Big] dx \tag{6.13}$$

$$= k \int_x \Delta u\, dx \tag{6.14}$$

Now considering the x integral which represents an integration starting at the base $x = B$ and ending at the x-position of the line probe $x = P$, Equation 6.14 becomes

$$F_{\tau_{yx}} = k \int_B^P \Delta u(x)\, dx \tag{6.15}$$

$$\tag{6.16}$$

$\Delta u(x)$ represents how the difference in velocity $u_F - u_W$ varies with x position moving from the wake towards the probe location. Assuming $\Delta u(x)$ takes a straight line function of the form

$$y = \frac{y_2 - y_1}{x_2 - x_1}(x - x_1) + y_1 \tag{6.17}$$

$\Delta u(x)$ takes the form

$$\Delta u(x) = \frac{\Delta u_p - \Delta u_b}{p}(x) + \Delta u_b \tag{6.18}$$

Equation 6.16 subsequently becomes

$$F_{\tau_{yx}} = k \int \frac{\Delta u_p - \Delta u_b}{p}(x) + \Delta u_b\, dx \tag{6.19}$$

$$= k\Big[\frac{\Delta u_p - \Delta u_b}{2p}x^2 + \Delta u_b x\Big]_B^P dx \tag{6.20}$$

Substituting the integration bounds and simplifying this becomes

$$\boxed{F_{\tau_{yx}} = c_1\Big[\Delta u_P + \Delta u_B c_2\Big]} \tag{6.21}$$

where

$$c_1 = \frac{\nu_T \rho x_P}{2} \quad \text{and} \quad c_2 = \frac{2}{\nu_T \rho} + 1$$

From Equation 6.21 it is shown that the shear force linearly varies with the velocity difference at the wake Δu_p. An increase in velocity difference corresponds with an increase in shear force.

Normal Stress σ_{xx}

Through newtons law of momentum applied to the control volume in Figure 6.22

$$F_{\sigma_{xx}} = \sigma_{xx} A = \rho\Big(Q_P \bar{u_P} - Q_B \bar{u_B}\Big) \tag{6.22}$$

where A is cross-sectional area of the control surface, Q is flow-rate across said surface, and the mean velocities are given by

$$\bar{u_B} = \frac{u_F}{2} \qquad \text{and} \qquad \bar{u_P} = \frac{u_F + u_W}{2} \tag{6.23}$$

Considering that $Q = \bar{u}A$, Equation 6.22 becomes

$$F_{\sigma_{xx}} = \rho A\Big(\bar{u_P}^2 - \bar{u_B}^2\Big) \tag{6.24}$$

$$= \rho A\Big[\Big(\frac{u_F + u_W}{2}\Big)^2 - \Big(\frac{u_F}{2}\Big)^2\Big] \tag{6.25}$$

this simplifies to

$$\boxed{F_{\sigma_{xx}} = 4\rho A\Big(2u_F u_W + {u_W}^2\Big)} \tag{6.26}$$

From Equation 6.26 it is shown that normal force has a quadratic relationship with the wake velocity.

Modeling of Combined Effects

The respective contribution of each force to drag has been investigated herein. From the shear layer probe shown in Figure 6.20 it can be approximated that the free-stream velocity is approximately equal for all geometries. The greatest change between geometries is found in differences in wake velocity u_W. The best performing devices show a strong negative wake velocity that is related the the back-flow region within the wake. From this perspective, the sensitivity of the normal and shear force can be modeled against a changing u_W using the relations Equation 6.21 and Equation 6.26. Shown in Figure 6.23 is the shear and normal force acting on the control volume in units of N/m. This model uses the geometrical and flow parameters from the actual shear layer line probe, in addition to an assumed turbulent viscosity ratio of $\nu_T/\nu = 10{,}000$ which is representative of a highly turbulent flow.

This graph shows the linear behavior of shear force and the quadratic relationship of normal force against wake velocity u_W. Though shear force increases with an decreasing u_W, the effect is far outweighed by the positive contribution of the normal

force. At the approximate wake velocity of the best-performing device (u_W = -10) the shear force that contributes to drag is opposed by a normal force that has twice the magnitude. With a sufficient negative magnitude of u_W, the normal force cancels the shear force and further contributes to a reduction in drag through its pressure action on the base. By considering the control volume in Figure 6.22, it can be seen that based on this model, if u_W is zero, then the velocity profiles on the inlet and outlet are the same. Therefore there is no net momentum change across the control volume and the resultant normal force will equal zero. From this point, the wake velocity u_W can solely determine the net momentum change. If the wake velocity is negative there is a net negative momentum change which will create a force in the -x direction, and vice versa. Though the force contribution of shear force is relatively small, this does not negate the importance of reducing momentum transfer across the shear layer. Momentum transfer across the shear layer into the wake acts to minimise the helpful back-flow within the wake of the vehicle. Mechanisms for momentum transfer across the wake are not limited to shear driven momentum transfer. A convective transfer of momentum into the wake is also possible. Consider a fluid parcel traveling along the top of the trailer towards the base in the no-device case. Once that parcel crosses the trailing edge, it is immediately exposed to the negative pressure of the wake. This pressure would tilt the velocity vector of the said parcel downwards towards the wake. The full momentum of this parcel would act in direct opposition to the beneficial re-circulation of the wake. This effectively cancels out the recirculating flow. Through a protection of the wake region from exposure to the trailing edge flow, the device promotes a strong recirculating flow. This is justified by comparing wake velocities of various devices where the best performing devices have the highest magnitude of reverse flow velocity.

These concepts may shed light into the overall response of the drag to the various devices. Referring back to Figure 6.21, the step change in drag performance between the worst two performing devices (baseline and k=1), and the remaining geometries may be attributed to shielding and protection of the re-circulation region. This is supported by considering the two worst performing devices also had the least negative wake velocity. The preservation of this recirculating back-flow improves drag performance through normal force mechanism. Between the k=2 and k=5 geometries, there are only very slight changes in drag performance. The preservation of the backflow represents the most significant contribution to drag reduction, whereas the marginal change between geometries k=2 and k=5 may be related to variations

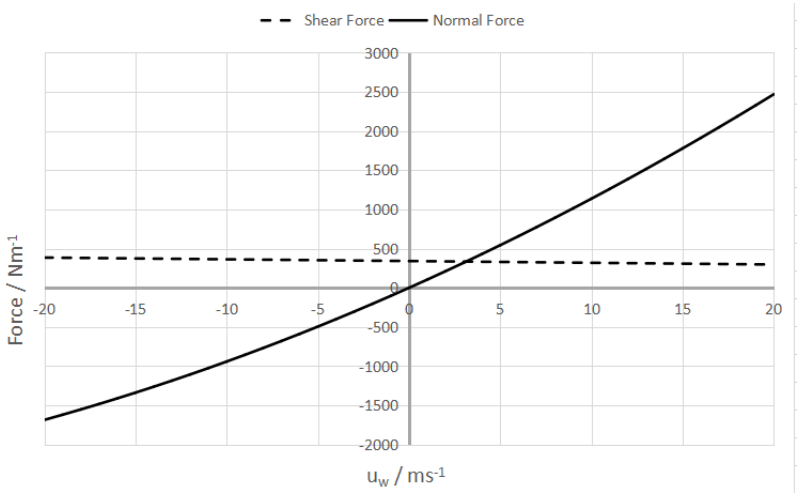

Figure 6.23: Theoretical relation wake velocity u_W and shear and normal forces upon the shear-layer control volume.

in shear based momentum transfer.

Summary of Investigation on Momentum Transfer Analysis Across Shear Layer

Based on an initial investigation of the wake region, a possible link between velocity gradient at the shear layer and the drag performance was uncovered. In order to investigate further, first a theoretical framework was developed that links shear forces and normal force with base drag. Based on this and under the assumption that shear force would be the prominent actor in the shear layer, it was predicted that better performing devices would reduce drag by minimizing the shear stress acting across the shear layer. To test this hypothesis, a line probe was positioned to capture the velocity profile within the shear layer and see how it responds to changes in geometry and drag. The results of this analysis were contrary to the outlined hypothesis of a reduction in shear force. It was actually found that shear stress increased with improving drag reduction which was somewhat inexplicable. The better performing devices were found to have a higher velocity difference Δu between the free-stream and the wake, which also explains why the shear stress is higher. Based on the theoretical framework the only remaining explanation was that the normal force must account for the decrease in drag and it's positive effect should be larger than the increase in drag caused by the increased shear stress. The framework was applied to a control volume defined to represent the shear layer. Simplifying assumptions were applied such as a liner velocity profile and a constant turbulent viscosity; in reality the velocity profile is non-linear and the turbulent viscosity is itself a function of the flow and coordinate position. The resulting

model was applied to the region between the probe and the base and it garnered some insights into the respective behavior of the shear force and the normal force. The shear force represents a drag caused by the shearing action of the shear layer; whereas the normal force is a result of the change of momentum of the air between the inlet and outlet of the control volume. The analysis theoretically showed that the shear force had a linear relationship with the wake velocity u_W and indeed the shear force increased with a decreasing u_W. However, the normal force and u_W was shown to obey a quadratic relation. It was shown that a strong reverse-flow region could act to reverse the direction of net-momentum change into the control volume and thereby contribute to a drag reduction. The beneficial effect of a strongly negative wake velocity far outweighed the increase in shear force caused by a greater Δu.

Though the simplifying assumptions of this model make it somewhat limiting to application, it does give some insights into the mechanisms at play. The revealed mechanisms correlate with the experimental results. Though the best performing devices had a higher Δu and therefore increased shear stress, they also had a strong recirculating flow within the wake who's effect has been found to decrease drag by a greater degree. Based on this it has been proposed that the devices shielding effect on the wake region promotes the stability and strength of the recirculating flow by preventing convective momentum transfer into the wake from the free-stream. Furthermore, the analysis has shown that reducing momentum transfer into the wake by any means should have a beneficial effect on drag. In studies such as Tombazis and Bearman (1997), the wavy shape was found to drastically alter the shear layer characteristics of the wake. Based on the outlined theory, a stabilisation of the shear layer could be a significant mechanism of drag reduction through its effect on overall momentum transfer into the wake. Due to fact that between the k=2 and k=5 geometries no significant changes in drag were observed in this study, it is possible that the steady state analysis presented in this section did not faithfully reproduce the stabilising mechanism of the device. Drag performance in this case may have been attributed to macro-aerodynamic effects such as the aforementioned reverse flow mechanism. Therefore the unsteady characteristics will be explicitly studied in an upcoming unsteady analysis of the shear layer.

6.4 Unsteady Analysis of Wavy Device

6.4.1 Introduction

According to Choi et al. (2008) there is a lack of understanding of the unsteady characteristics of devices that operate in the base region. Furthermore, the drag wavy reduction device has not been applied to a heavy vehicle to the best of the authors knowledge. Based on the work of Tombazis and Bearman (1997) it has been shown that such a device shows the potential to modify the unsteady characteristics of vortex shedding behind a truck, but whether this particular configuration of the wavy geometry would affect the unsteady characteristics behind a truck remained an open question. In this section the primary question concerns in which ways does the device affect the unsteady behavior in the wake of a truck. In Section 6.3, a possible mechanism for drag reduction was highlighted by looking at the wake characteristics behind the truck. Better performing geometries exhibited lower flow speeds at the wake-free-stream interface. The hypothesis is that the geometry modifies the wake in such a way where there is less interaction and momentum transfer between the free-stream and the wake. One of the objectives for this section is to study this aspect in more detail through spectral analysis and other means. Specifically, do better performing devices correspond with reduced unsteady activity in the wake flows?

As with most temporal phenomena, a Fourier transform remains the foremost valuable tool in making quantitative assessments regarding unsteady phenomena. A Fourier transform has been applied to pressure signals within the wake of the truck in order to carry out a spectral analysis. Since unsteady characteristics can vary with scale, the chosen scale of the vehicle was 1:1 for a better reflection of real-life characteristics. From Section 6.3 the drag reduction performance of the wavy device is known to vary with both flow-speed and wave number. With this in mind, a parametric study was conducted that looks at how geometrical wave-number and flow speed will affect drag reduction performance.

6.4.2 Simulation Set-Up

The three-dimensional turbulent flow of the incompressible flow was simulated using the Improved-Delayed Detached Eddy Simulation (IDDES) methodology that was outlined in Section 4.3.7. The geometry replicates exactly Section 6.3 and the experiments of Storms et al. (2006), except for the fact that all dimensions are scaled

back to 1:1 ratio such that they correspond with Figure 6.3. The width, height and length of the control volume were respectively 17.04 m, 24.4 m and 36.56 m. The mesh (Figure 6.25) features 5.36 million cells in a trimmer configuration that includes a prism layer with 13 layers and also a volume of refinement around the truck geometry that extends 10 m to the rear of the vehicle. Figure 6.25 shows the grid independence study upon which the mesh size was chosen, though it must be noted that strong convergence characteristics are not observed. This is expected as in DES, the Partial Differential Equation itself changes with grid spacing, as compared with RANS where the simulation converges towards the stable PDE solution (Spalart (2001)). A target size of 1.5 cm was used within the refinement region, and a target size of 15 cm outside of the refinement region. Since the grid-independence study is deemed unsuitable, the finest grid size possible with the given computational resources. This is justified since a progressivly finer grid is known to tend the exact solution of the Navier-Stokes equation.

The all y+ wall boundary treatment as described in Section 4.3.5 is applied to model the boundary layer. A constant density model is applied with air as the fluid with a density ρ of $1.18415 kg/m^3$ and a dynamic viscosity of $1.85508x10^{-5} Pa - s$. The Hybrid Gauss Least Squares gradient method is applied with the Venkatakrishnan limiter method. The SST (Menter) K-Omega turbulence model described in Section 4.3.5 is used for the RANS aspects of the DES model with a segregated flow option.

A first-order temporal discretisation scheme was used with a time step of $1 \times 10^{-3} s$.

Each simulation has 10,000 time steps with 5 inter-iterations, resulting in 10 seconds of simulated time. The residuals in Figure 6.26 show that the simulation had stabilised by 1 second of time. Twenty-four such simulations were conducted on this basis with a parametric study using six geometries (k=0, k=1, k=2, k=3, k=4, and k=5) at four speeds (v=6 m/s, 12 m/s 18 m/s, 24 m/s). The speeds were chosen to be within the range of a truck going down a highway (24 m/s = 86.4 kph). For the parametric study the time-averaged drag coefficient was determined using

$$\bar{C_d} = 2\bar{F}/\rho u^2 A \tag{6.27}$$

where $\bar{F}$ is the time-averaged force on the body, density ρ corresponds to 1.18415

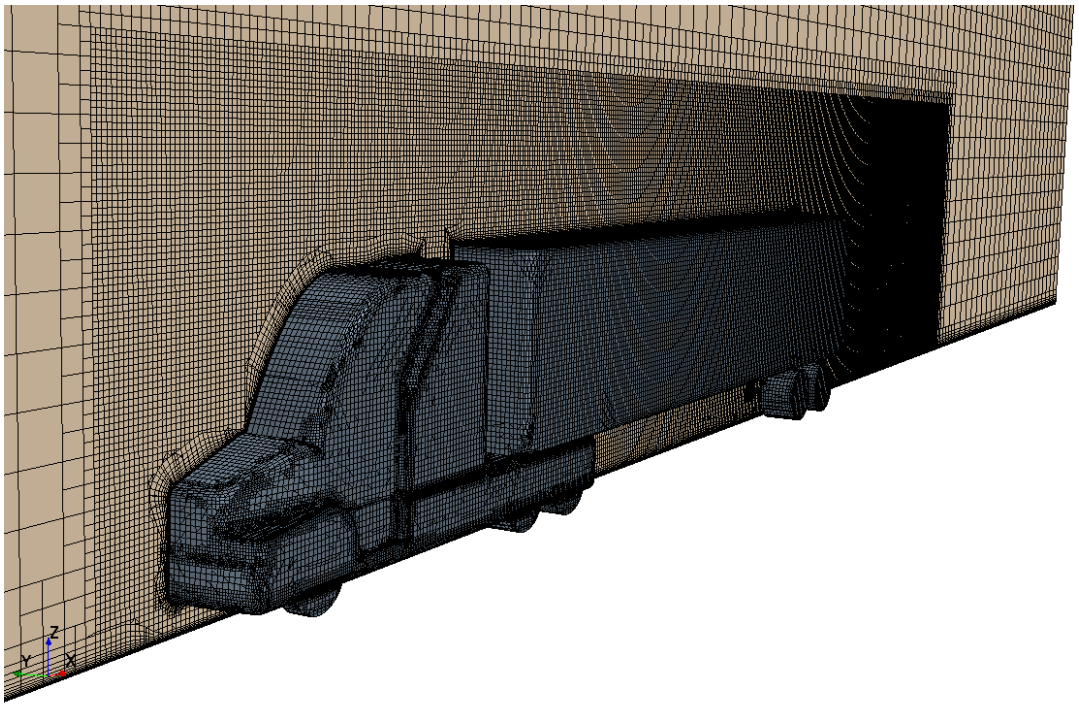

Figure 6.24: Showing mesh characteristics of IDDES model.

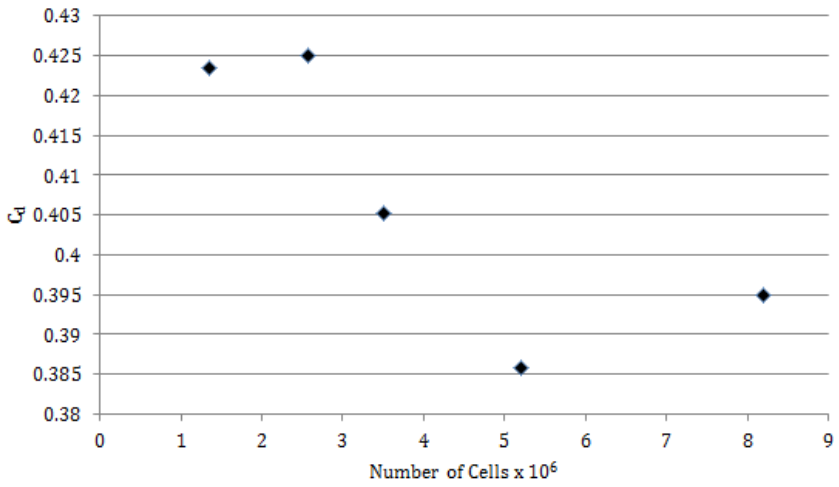

Figure 6.25: Grid independence analysis of mesh.

kg/m^3, reference area A which corresponds to the frontal area of the truck of 10.619 m^2 and the velocity u which corresponds to the inlet velocity.

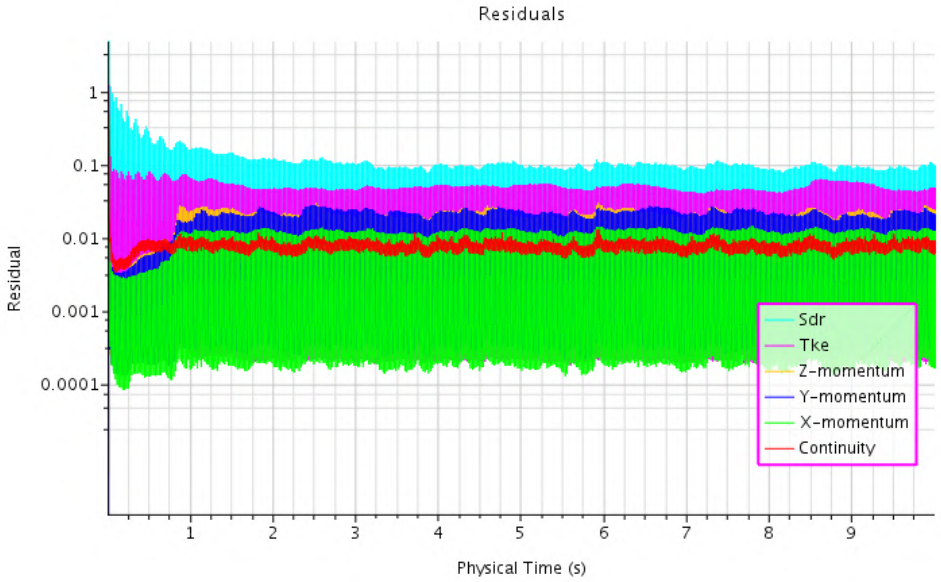

Figure 6.26: Residuals of baseline DES simulation.

6.4.3 Analysis of Parametric Study

The results of the parametric study are shown in Table 6.4. The no-device (baseline) readings were fairly consistent across the range of speeds within a 4.1% range. The drag coefficient measured in the simulations are not as accurate as the RANS study. The average drag coefficient of 0.395 represents a 7.5% difference from the experimentally measured value of 0.427; as compared with the difference of 2.06% in the RANS study. Moreover the performance of the device is worse, with the best drag reduction being 6.12% versus the 21.56% found in the RANS study. This could be due to a number of reasons including the change in scale of the model, from 1/8th scale to full-size, or due to deficiencies the DES model which may include insufficient spatio-temporal discretion or lack of fine tuning which is usual in DES. Without further investigation specific reasons cannot be concluded. Nevertheless, relative information may still yield useful insight and also information about unsteady characteristics which are not available from steady state analysis.

Following from this, Table 6.4 features a column which shows relative drag reduction performance, with reference to the baseline result. This information is graphed in Figure 6.27. The graph shows that performace of the device has a strong dependence of speed; certain geometries excel at certain speeds. This is visible by the trend of the best performing devices. At speeds of u = 6 m/s, 12 m/s and 18 m/s, the best performing devices are k=3, k=4, and k=5 respectively. This indicates that as speed increases, a higher wave-number device has the best performance. By looking at

Table 6.4: A summary of results from parametric study looking at the relationship between speed and geometry.

	6 m/s		12 m/s		18 m/s		24 m/s	
Geometry	C_d	$\Delta C_d/C_{d0}$	C_d	$\Delta C_d/C_{d0}$	C_d	$\Delta C_d/C_{d0}$	C_d	$\Delta C_d/C_{d0}$
Baseline	0.38588	0	0.40234	0	0.39618	0	0.39863	0
k=1	0.379959	-1.53448	0.392698	-2.39655	0.395907	-0.06897	0.409145	2.637931
k=2	0.37936	-1.68966	0.387426	-3.7069	0.385456	-2.7069	0.396431	-0.55172
k=3	0.368449	-4.51724	0.39249	-2.44828	0.379445	-4.22414	0.399111	0.12069
k=4	0.376765	-2.36207	0.382154	-5.01724	0.386002	-2.56897	0.392582	-1.51724
k=5	0.377697	-2.12069	0.388397	-3.46552	0.371931	-6.12069	0.400898	0.568966

individual geometries through the speed range, the majority of the geometries show a unimodal relationship with speed where there is a particular speed that it excels at, beyond-which or before-which the performance declines; with the exception of $k = 3$ which has a bimodal relationship. Though the majority of data points indicate some drag reduction, there is a trend that beyond the optimum speed, the device may even incur an increase in overall drag. For practical application to trucks, a device may be tailored to the cruising speed of the vehicle, for maximum performance.

There is a significant difference between the results shown in Figure 6.27 and the 1/8th scale RANS result. The RANS results show a roughly equal drag reduction with geometries with greater wavelength than k=1. The unsteady results on the other hand (Figure 6.27) show much more complex behavior. This alludes to the idea that unsteady phenomena play a significant role in the function of this device.

6.4.4 Unsteady Analysis of Shear Layer and Wake Region

In order to understand how the device affects unsteady characteristics of the truck, an unsteady analysis is performed in the following section. A single geometry was analysed on the basis of the best performing device from Section 6.3. Moreover, a speed of 24 m/s was chosen as it is in the order of highway speeds. Two pressure probes are positioned in the rear of the vehicle. One probe is positioned within the shear layer, and another in the wake region, at a distance of $w/2$ from the rear face. The positioning of the probes is shown in Figure 6.28. One analysis was performed on the baseline geometry and another identical analysis on the wavy device geometry to assess the differences.

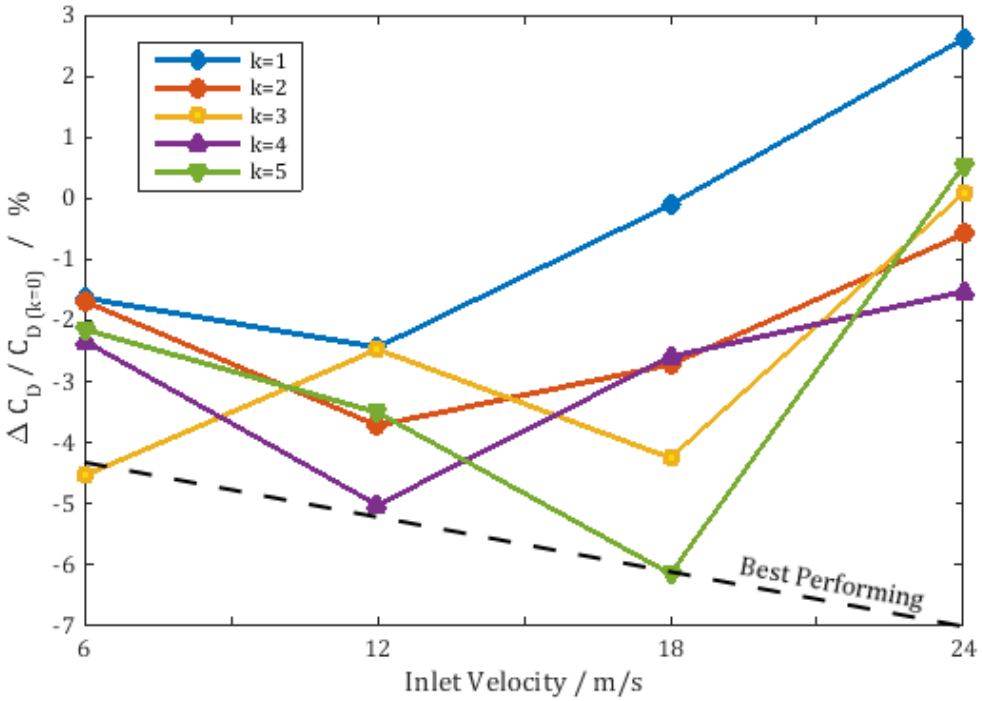

Figure 6.27: results of a parametric study to understand the relationship between drag reduction, Reynolds number, and geometric parameters.

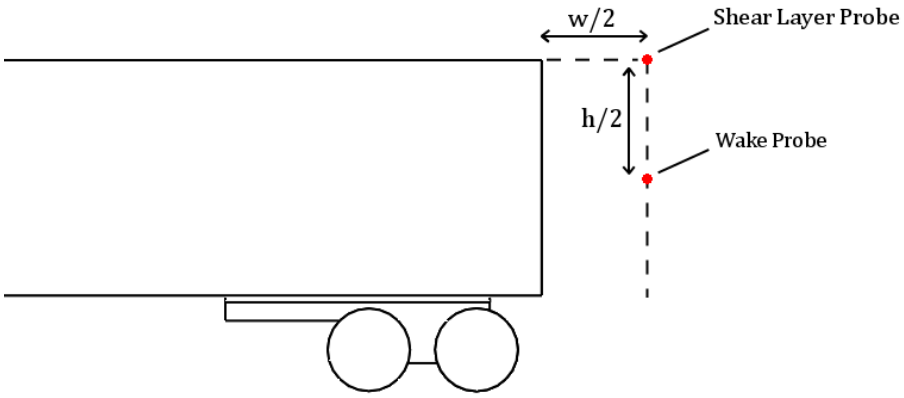

Figure 6.28: Showing probe locations for unsteady analysis

Figures 6.29 and 6.30 compare pressure signals with, and without the device; they show signals from the shear layer probe and wake region probe respectively. In order to quantify the disturbance levels, the Root-Mean-Squared (RMS) value is used and is given by the RMS equation in discrete form

$$x_{RMS} = \sqrt{\frac{1}{N_0}\sum_{k=1}^{N_0} x^2[k]} \tag{6.28}$$

where N_0 is the number of samples, k is the sample number, and x is the signal amplitude at position k.

The RMS and mean pressure results are tabulated in Table 6.5. From inspection of the results, Figure 6.29, and Figure 6.30, it is apparent that the device has a modulating effect on the signals in either location. In the shear layer the base pressure has been increased by 9.3%, and the RMS amplitude has been reduced by 14.2%. In the base region the base pressure has been increased by 12%, and the RMS amplitude reduced by -29.9 %. In both probe locations the unsteady activity has been reduced; within the shear layer, this is indicative of reduced amplitude of shear-layer-born vortices. This may be correlated to the finding in Section 6.3 where decreased velocities are found in the wake-freestream interface. The stabilising effect of the device on vorticies in the shear layer would reduce mixing of air in the free-stream and within the wake. The reduced momentum transfer between these regions would result in reduced shear force at the wake-freestream interface, which ultimately would have the effect of increasing base pressure thereby reducing drag. This correlates with the observance that the wake region enjoys a 12.0% increase in pressure with the inclusion of the device.

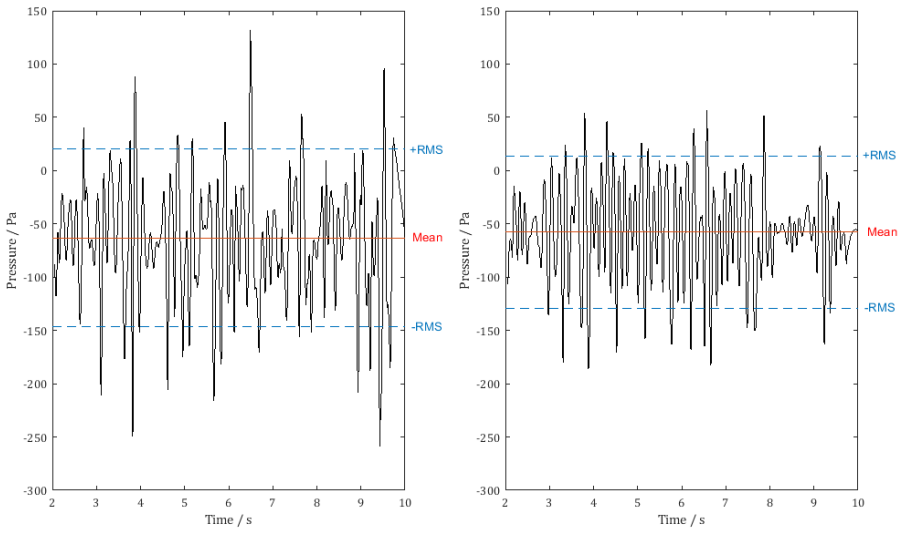

(a) without device **(b)** with device

Figure 6.29: Comparing pressure signals at the shear layer probe over a ten second sampling time of with and without device.

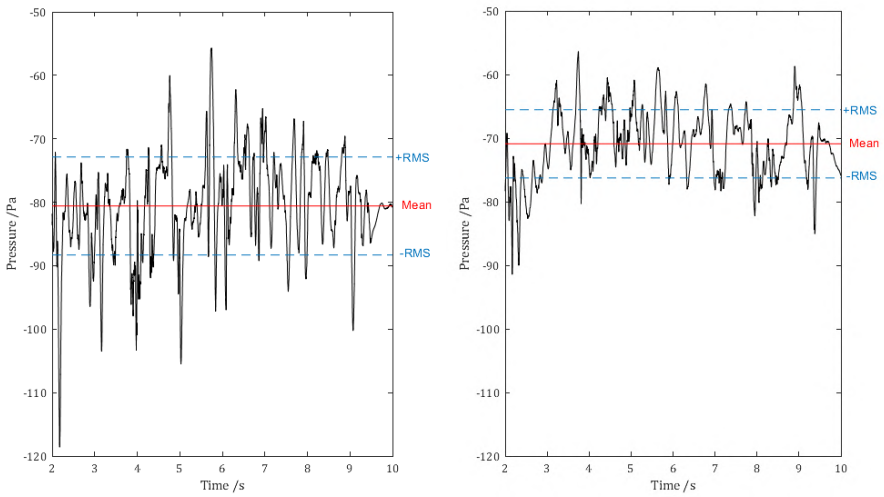

(a) without device **(b)** with device

Figure 6.30: Comparing pressure signals at the wake probe over a ten second sampling time of with and without device.

Table 6.5: A summary of results from analysis of time signals from pressure probes in wake region and shear layer.

	Shear Layer Probe		Wake Probe	
	Without Device	With Device	Without Device	With Device
$\bar{P}$ / Pa	-63.3	-57.4	-80.6	-70.9
$\Delta\ \bar{P}$ / Pa		+5.9 (+9.3 %)		+ 9.7 (+12.0 %)
P_{RMS} / Pa	83.4	71.5	7.7	5.4
$\Delta\ P_{RMS}$ / Pa		-11.9 (-14.2 %)		-2.3 (-29.9 %)

6.4.5 Spectral Analysis

In order to gain a deeper insight into how the device modifies the unsteady behaviour in the wake, a spectral analysis is performed on the signals from the shear-layer probe and wake-region probe. The Discrete Fourier Transform (DFT) is used to extract the frequency-domain information of the pressure signals so that the effect of the device on each frequency band can be understood. The Discrete Fourier Transform is given by

$$X_k = \sum_{n=0}^{N-1} x_n \cdot e^{-\frac{i2\pi}{N}kn} \tag{6.29}$$

for $0 \leq k \leq N-1$

where x_i are the values of a time-based signal. The output X_k is a complex number that encodes the amplitude and phase information of the Fourier decomposition of the signal.

The algorithm used to compute the DFT is known as a Fast Fourier Transform (FFT) of which the Cooley–Tukey algorithm (Cooley and Tukey, 1965) is used. In order to solve for the DFT coefficients, the algorithm takes a divide and conquer approach. A DFT of composite size $N = N_1 N_2$ is broken into many smaller DFTs of size N_1 and N_2. This has the effect of reducing computation time to $O(N\ log\ N)$

In most practical cases, the signal doesn't have an integer number of periods; that is, the start and end of the signal may have a non-zero value. In such cases the start and end of the signal are considered as discontinuities in the signal and therefore will introduce a large range of frequencies in the resulting spectral plot which may obscure any meaningful spectral information. The solution to this is to apply a windowing function onto the signal. In this case the Hanning window was used and is given by

$$w(n) = 0.5\left(1 - cos\left(2\pi\frac{n}{N}\right)\right) \tag{6.30}$$

for $0 \leq n \leq N$

where $w(n)$ are the window coefficients by which each signal point x_i is multiplied by. The result is a signal that starts and ends at zero, whilst maintaining the spectral information in the center of the signal.

The results of the spectral analysis on the shear-layer probe, and the wake-region probe are shown in Figure 6.31 and Figure 6.32 respectively.

The spectral plot in the shear layer (6.31) shows that the device has had the effect of broadly reducing spectral activity throughout the entire frequency range, with most reduction taking place in the lower frequency range ($0 \leq St \leq 0.8$). Also evident is a shifting of the major frequency peaks ($St = 0.77$, $St = 0.84$, $St = 0.94$) by a translation of $St \approx +0.138$ or an increase in frequency by 18.3%. Due to the fact that this probe in within the shear layer, it follows that highest amplitude spectral activity in this region is related to the Kelvin-Helmholtz vortex shedding. Thus it is shown that the device has increased shedding frequencies of this instability.

Moreover, through the inclusion of the device the amplitude of the most energetic frequency ($St = 0.77$) has increased from a value of 2.52×10^4 to a value of 2.80×10^4. This corresponds with an increase of 11.1%. In this way the device can be thought to take the kinetic energy involved in the shear layer instability, and package it more neatly into the main shedding frequency, and preventing the loss of energy into other competing frequency bands. In other words, the device has a stabilising effect on the vortex shedding behind the truck. In a related study on a study of a serrated trailing edge of an aerofoil by Thomareis and Papadakis (2017), they find that the serrations attenuates the energy of Kelvin-Helmholtz vortex shedding by decorrelating the span-wise coherence of the vortices. In this way vortices within each cell are free to develop and shed independently and this results in a weaker forcing of the separating shear layer. This way the natural frequency and the shedding frequency can remain independent and may explain why Figure 6.31 shows two main frequencies. Furthermore, Doddipatla et al. (2017) numerically and experimentally studied a bluff body with a wavy trailing face. They also find the suppression of the Kelvin-Helmholtz instability though attribute the effect to a redistribution of kinetic energy towards stream-wise vortices as the source of stabilisation.

Within the base region, the spectral plot shown in Figure 6.32 shows a significant reduction in spectral activity throughout the entire frequency range of $0 \leq St \leq 3$ by an average of 12.56%. It should be noted that amplitude of spectral activity in the wake region is an order of magnitude less than the activity in the shear layer. It is possible that most of the forcing dynamics originates from the shear layer, and is filtered until it reaches the wake region. This idea is consistent with the shape of the spectral plot which resembles exponential decay that is characteristic of the behaviour of a low-pass filter. This is also consistent with the property of turbulence whereby high frequency oscillations are quickly absorbed through viscosity and dissipated into heat, whereas lower speed, larger motions are able to propagate through the fluid. In the wake probes, there is little evidence that the frequency modes that correspond with the shear-layer vortex shedding existing in a pronounced way. The information pertaining to the relatively regular forcing frequency of the Kelvin-Helmholtz instability in the shear layer has been lost on the way to the wake. This type of behaviour is typical of non-linear systems such as the present fluid. Notwithstanding this observation, the shear-layer based energy reductions associated with the incorporation of the device are likely to be responsible for the reduction in spectral activity in the wake; this is supported from a logical basis as any unsteady activity in the wake would have derived from the energy in

the free-stream as the wake itself has no source of energy. This idea also explains the characteristic shape of each graph. Within the shear layer, there are some driving dynamics such as the Kelvin-Helmholtz instability which produce pronounced motions at certain frequencies. Contrasting with the wake probe where there is a broad range of frequencies that follow a shape typical of exponential decay. There are no distinct frequencies which indicate this region is wholly driven by activity from the free-stream.

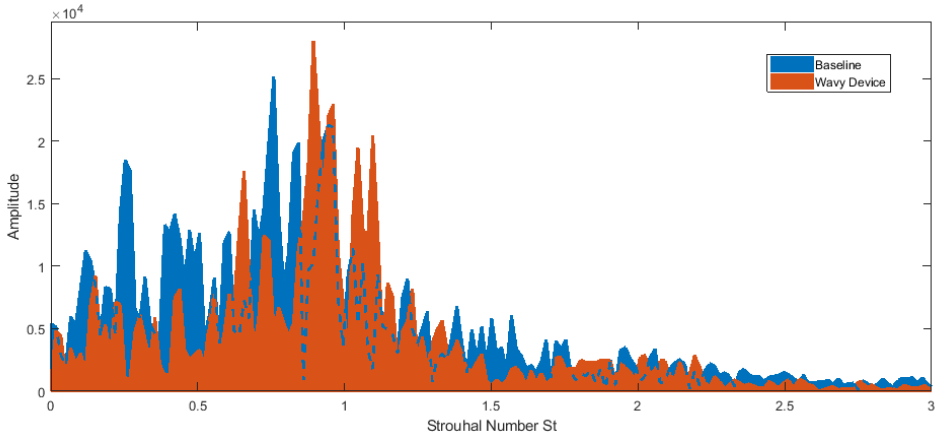

(a) Comparison of Fast Fourier Transform taken with pressure signal from shear layer probe, with and without device.

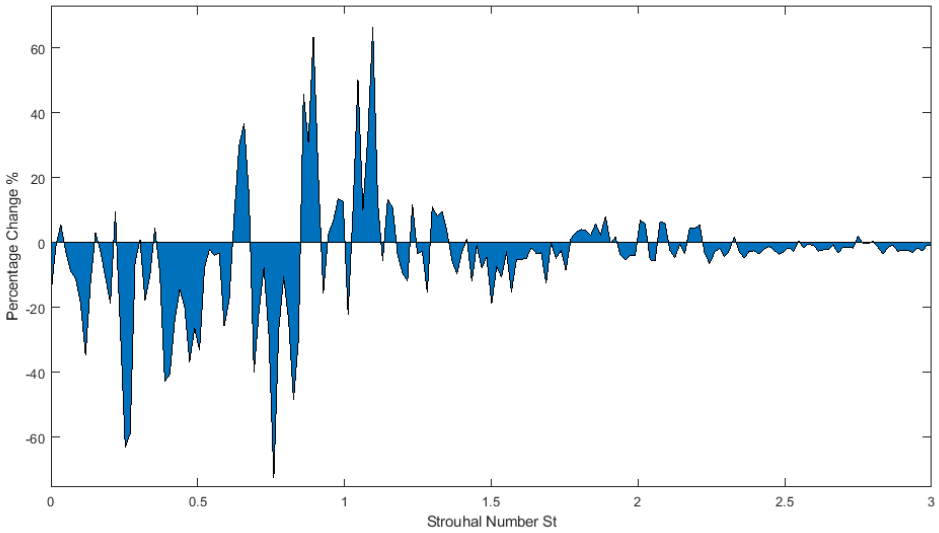

(b) Showing relative change of Fast Fourier Fourier transform values.

Figure 6.31: A comparison of spectral analysis of pressure data taken with a probe in the shear layer.

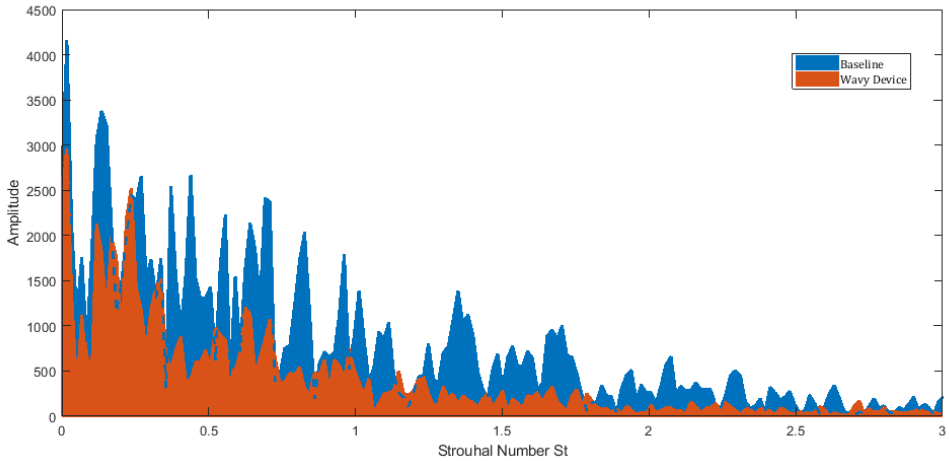

(a) Comparison of Fast Fourier Transform taken with pressure signal from wake region probe, with and without device.

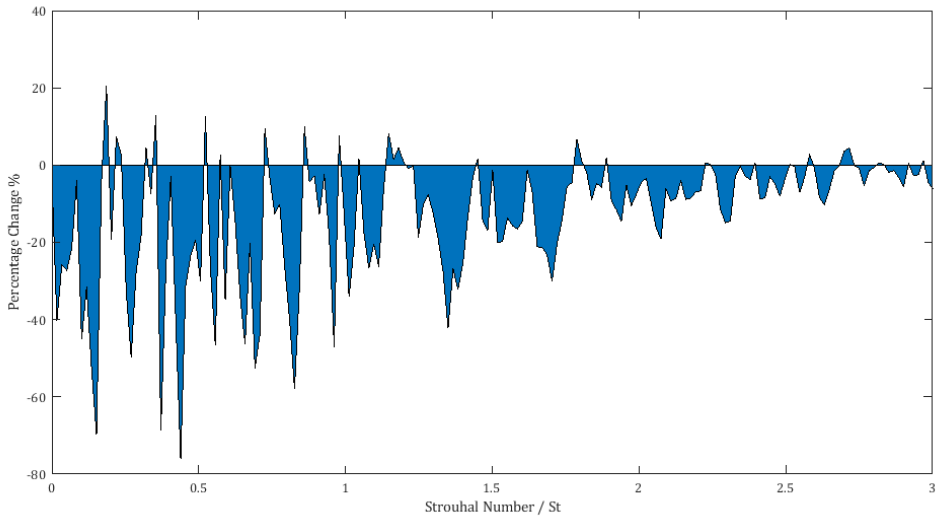

(b) Showing relative change of Fast Fourier Fourier transform values.

Figure 6.32: A comparison of spectral analysis of pressure data taken with a probe in the wake region layer.

6.4.6 Qualitative Analysis of Vortex Shedding

Vortex shedding behaviour is visualised in this section using Q-Criterion isosurfaces. A volume of interest is defined in the wake of the truck within which the vortex shedding behaviour is visualised. The Q-Criterion threshold of $50s^2$ is used in the plots. Isosurfaces are coloured by velocity which also helps to understand the relative position of shed vortices, those with higher velocity being closer to the free-stream and those with lower velocities being within the wake.

Figure 6.33, Figure 6.34, and Figure 6.35 show a time sequence of vortex visualisations with isotropic views, side views, and top views respectively. Each figure contrasts the without-device, and with-device cases. From these plots what is immediately visible are the expected Kelvin-Helmholtz vortex shedding that occurs within the shear layer as a series of vortex tubes that originate at the trailing edge of the truck and propagate downstream. As the vortex tubes propogate the ends of the tubes which become exposed to the slower moving wake region lag further and further behind the vortex body. The vortices that originate as parallel to the trailing edge of the truck develop as they travel to resemble hairpin vortices. The structure of vorticies that shed from the truck are consistent with literature.

The qualitative difference in vortex properties between the baseline and with-device cases is difficult to observe due to chaotic behaviour. In order to systematically analyse the changes in vortex behaviour, image processing of the vortex shedding sequence was conducted. The image processing methodology carried out essentially overlays all images in the sequence into a single image. The overlaying method employs the median intensity of the sequence. This technique produces a black color in areas where the vorticies are present for more than 50% of the sequence, and white in areas where vortices are not present for more than 50% of the sequence. Thereby producing a solid boundary the signifies the motion of the vortices. The image processing steps are illustrated in more detail in Figure 6.36. This method was employed for the image sequences with orthographic views, namely the side-view and top-view. It should be noted that the vortex shedding was produced within a cuboidal control volume; the

Figure 6.37 shows the results of this analysis. From the side-view (Figure 6.37 (a)) it is clear that the device has the effect of modulating the diffusion of the vorticies into the free-stream. Without the inclusion of the device, the mean-intensity line diverges more quickly towards the free-stream. The greatest difference in height is at a distance of approximately 2.5 m from the trailing edge of the truck. At this distance the difference in y coordinate between the two median intensity lines is approximately 0.4 m. It may be argued that the effect is due to the translation of the separation point by a distance of the length of the device. However, with the inclusion of the device, distance that it takes for the lines to reach a height of $/approx$ 1 m above the top surface is 2 m greater. As the mean length of the device is only 0.65 m, there is clearly a change in the vortex behaviour. This evidence is coherent with the presumed mechanism of action of the device of lowering momentum transfer through the shear layer presented in the previous section (Section 6.4). A lower

momentum transfer between adjacent regions in synonymous with a lower rate of diffusion. As vortices are also subject to diffusive forces, the stabilising effect on the shear layer that the device causes the vortices that shed to take a more streamlined path.

In the top-view shown in Figure 6.35 the difference is less pronounced and is only visible further down the wake. This may be a facet of the processing techniques rather than being an actual phenomena. From the side-view sequence shown in Figure 6.34 it can be seen that the earliest vortices to manifest originate from the rear wheel area. In the top-view shown in Figure 6.35, there is little distinction between the vortices produced in the wheel area and those produced in the wake. From an image processing point of view, the vortices produced in the wheel area cause the bulge in median intensity lines that is visible before the wake region. This bulge is likely to be masking the vortex activity taking place in the region of interest just downstream of base.

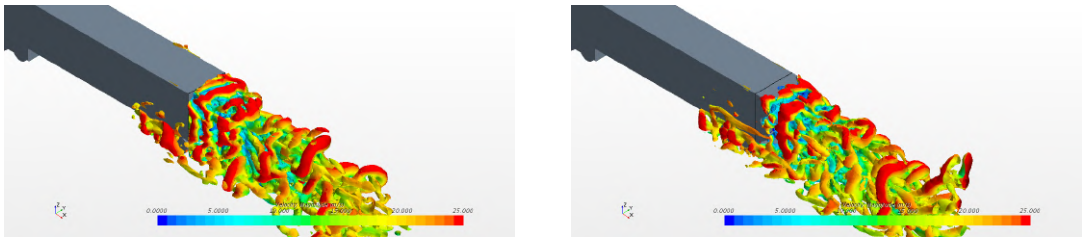

(a) t=0 s, no device

(b) t=0 s, with device

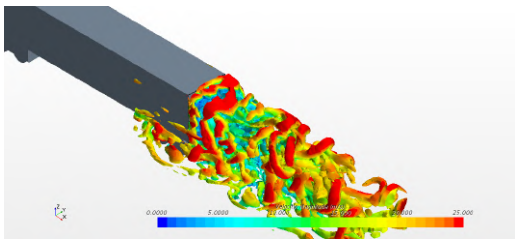

(c) t=2 s, no device

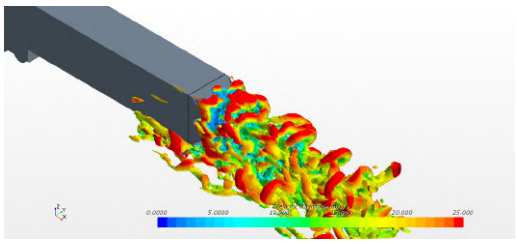

(d) t=2 s, with device

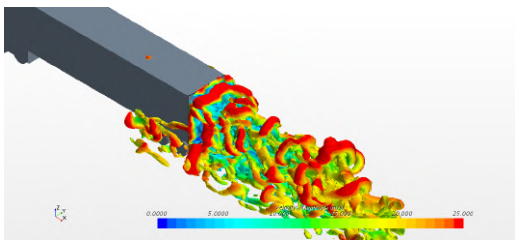

(e) t=4 s, no device

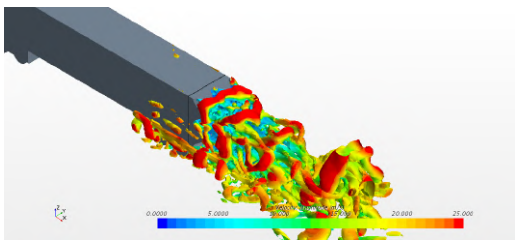

(f) t=4 s, with device

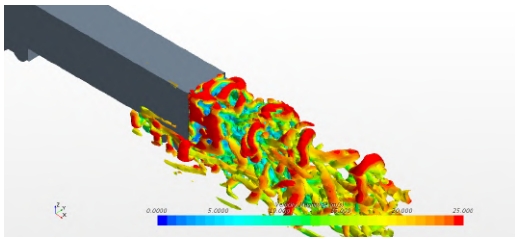

(g) t=6 s, no device

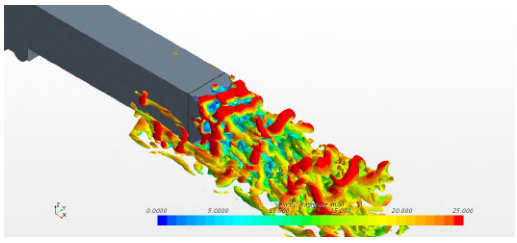

(h) t=6 s, with device

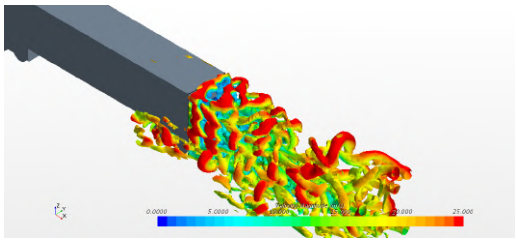

(i) t=8 s, no device

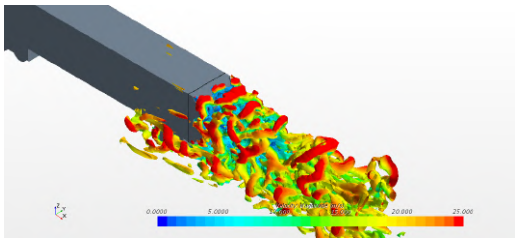

(j) t=8 s, with device

Figure 6.33: Image sequence comparing vortex shedding behaviour, isometric view.

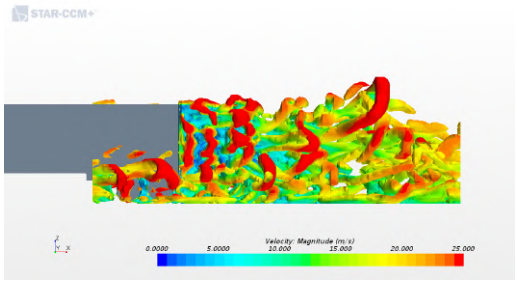

(a) t=0 s, no device

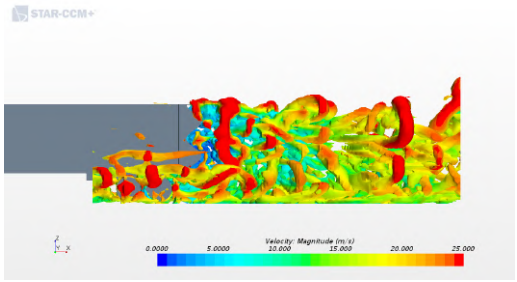

(b) t=0 s, with device

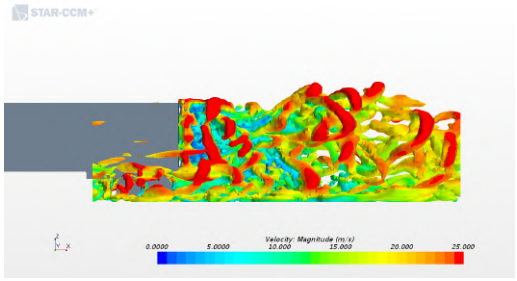

(c) t=2 s, no device

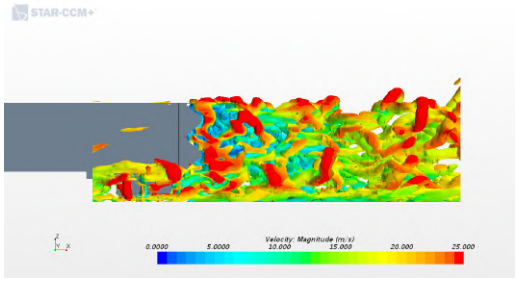

(d) t=2 s, with device

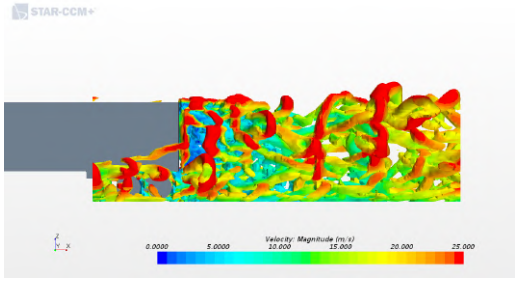

(e) t=4 s, no device

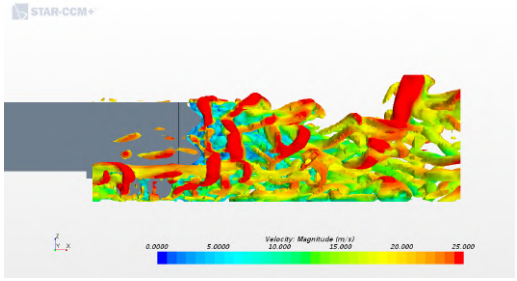

(f) t=4 s, with device

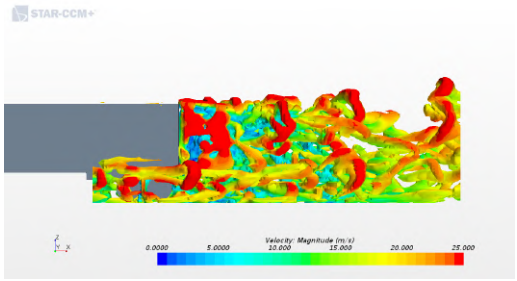

(g) t=6 s, no device

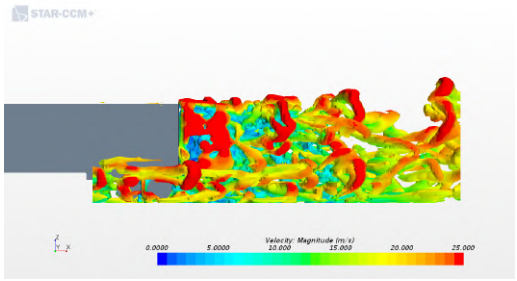

(h) t=6 s, with device

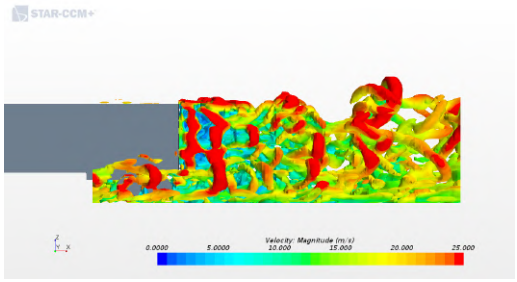

(i) t=8 s, no device

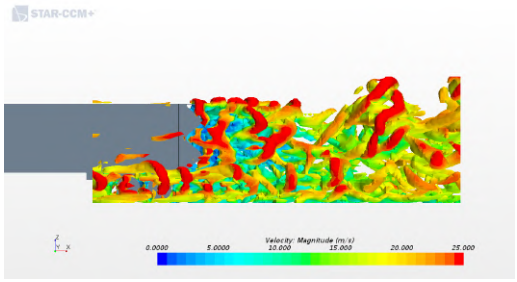

(j) t=8 s, with device

Figure 6.34: Image sequence comparing vortex shedding behaviour, side view

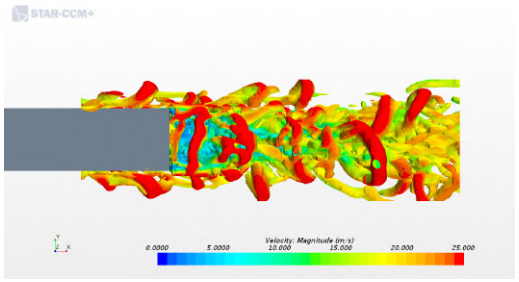

(a) t=0 s, no device

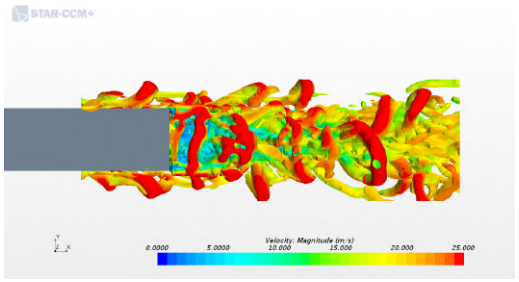

(b) t=0 s, with device

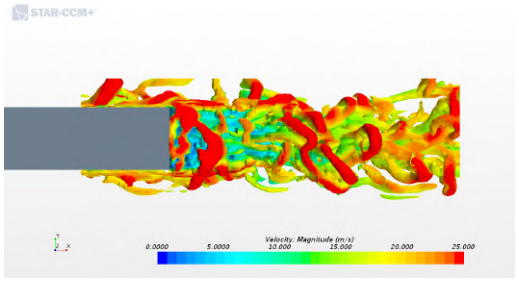

(c) t=2 s, no device

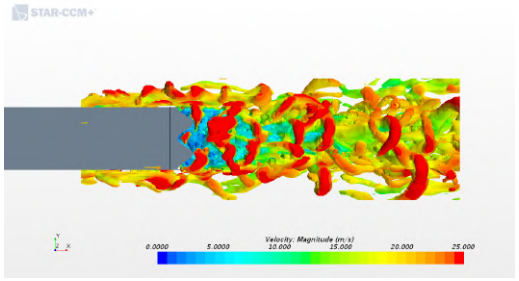

(d) t=2 s, with device

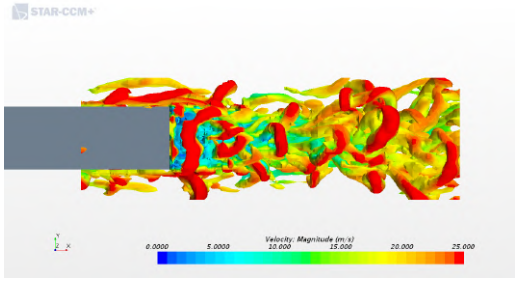

(e) t=4 s, no device

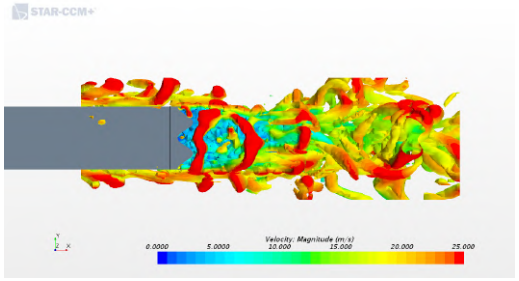

(f) t=4 s, with device

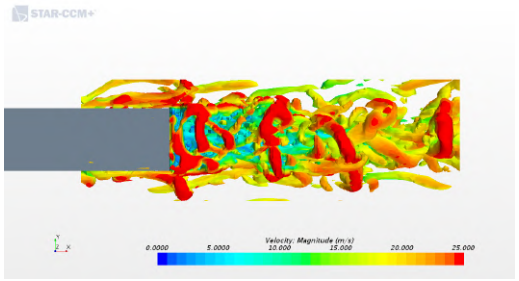

(g) t=6 s, no device

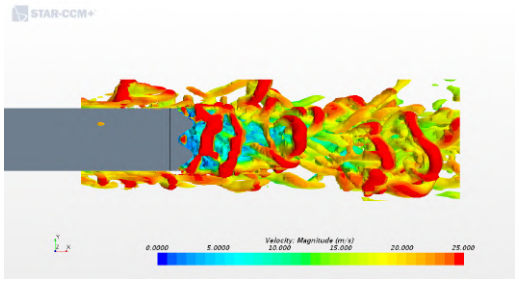

(h) t=6 s, with device

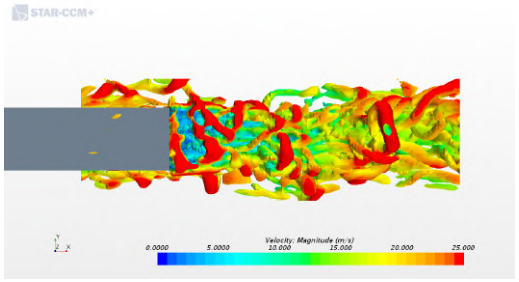

(i) t=8 s, no device

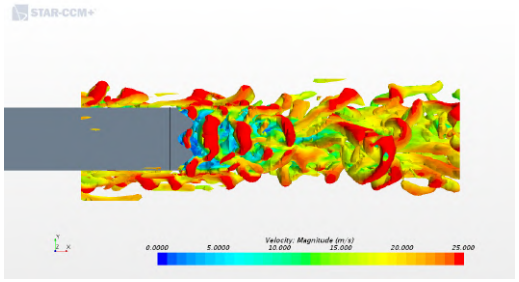

(j) t=8 s, with device

Figure 6.35: Image sequence comparing vortex shedding behaviour, top view

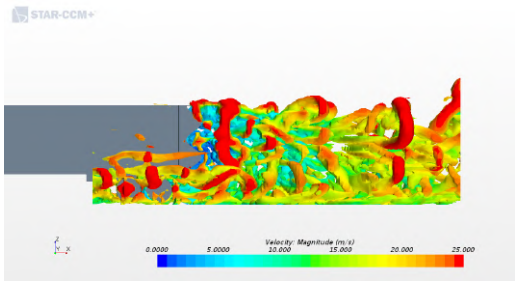

(a) Original Image

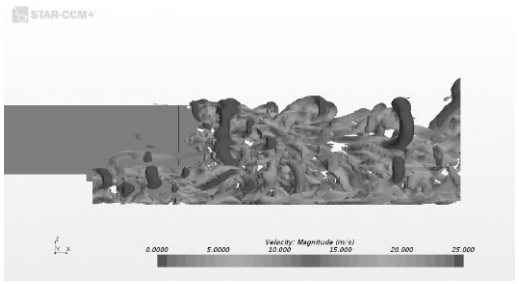

(b) Grey-Scale

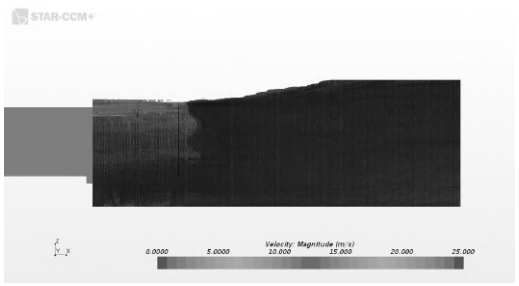

(c) Median Intensity of Sequence

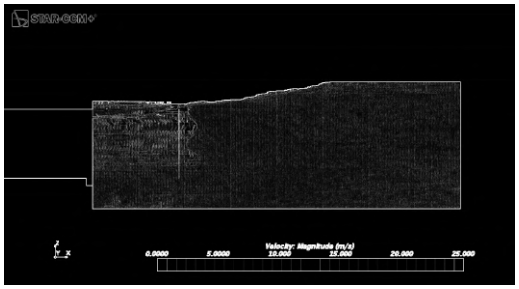

(d) Line Detection

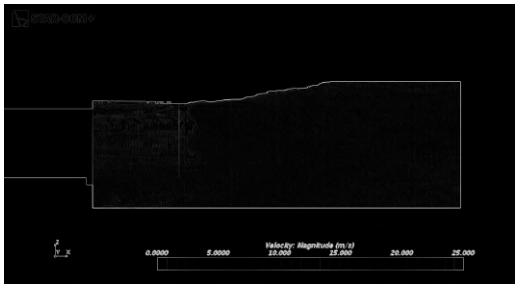

(e) Increase Contrast

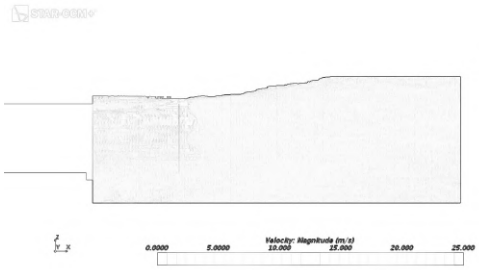

(f) Invert Colour

Figure 6.36: Image processing steps for qualitative comparison of Q-Criterion vortex iso-surface sequence.

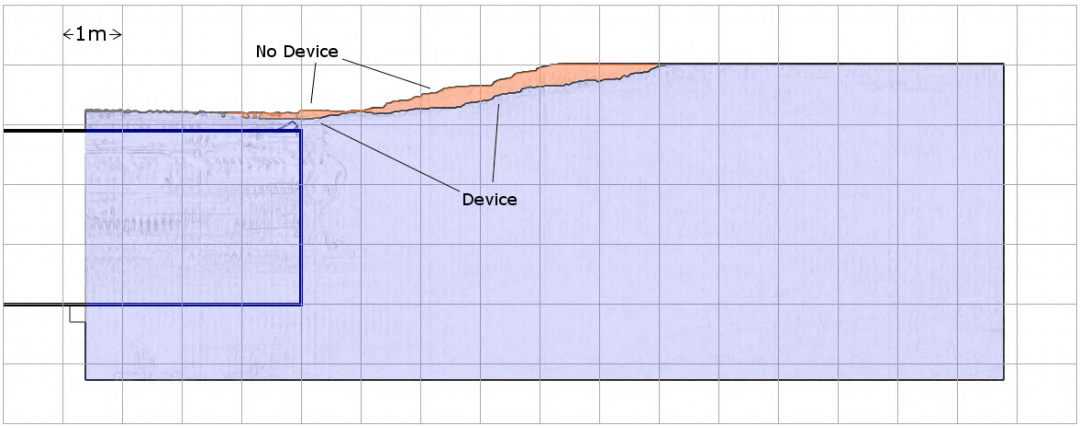

(a) Side View

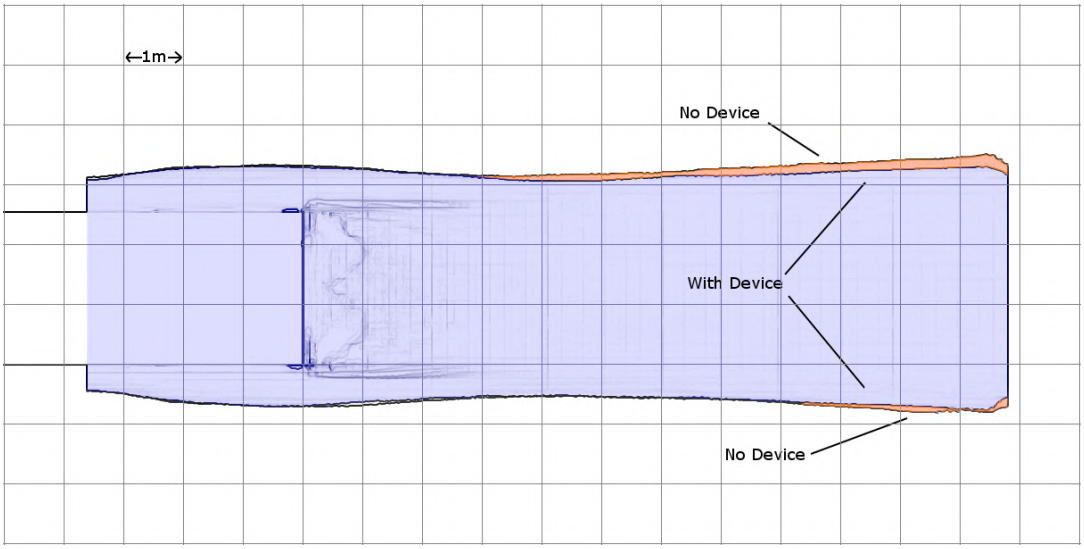

(b) Top View

Figure 6.37: Comparing the median distribution of vortices in the wake of the truck through image sequences between t=0 s and t=10 s

6.5 Summary

In this section a drag reduction device for the base region of heavy vehicles was introduced. The design is based on the shape of a harbour seal vibrissa which has been shown in previous studies to induce a drag reduction, such as in the work of Tombazis and Bearman (1997). In this section the function of the device was evaluated using two methodologies, namely a steady state approach using RANS, and an unsteady approach using IDDES.

With the steady state approach a $1/8^{th}$ scale model of the Generic Conventional Model was applied. The geometry was made to match the experiments from Storms et al. (2006) so that the model could be well-validated against experimental data. From this a well-validated model was created so that drag reduction performance metrics could be found. Validation of the model was performed using both surface-pressure coefficient values as using the drag coefficient. The pressure coefficient were taken along the bisecting plane at the surface of the geometry; these results match very well with experimentally derived pressure coefficient readings. Additionally, the computed drag coefficient was approximately 2% of the experimentally derived value. This high level of validation gives confidence in the performance of the model. On the basis of this model, the best performing device had a wave number of k=2 which delivered a 21.56 % drag reduction. When compared with other devices such as a belly box of a base cavity, this is considered a good performance. The performance of the device was comparable with the best performing device from the study by Storms et al. (2006) which was flaps at the base angled inward by 20 degrees.

The IDDES simulation focused on the unsteady mechanism of action of the device. The results show that performace of the device has a strong dependence on speed; certain geometries excel at certain speeds, As speed increases, a higher wave-number device has the best performance. By looking at individual geometries through the speed range, the majority of the geometries show a unimodal relationship with speed where there is a particular speed that it excels at, beyond-which or before-which the performance declines. Though the majority of data points indicate some drag reduction, there is a trend that beyond the optimum speed, the device may even incur an increase in overall drag. For practical application to trucks, a device may be tailored to the cruising speed of the vehicle, for maximum performance. To understand unsteady characteristics, a probe was positioned in the shear layer behind the vehicle, and another in the wake region of the vehicle. From analysis of

the time-series of the pressure signal, as well as spectral analysis of these signals, it is apparent that this device had a modulating effect on unsteady activity. Within the shear layer it had reduced the amplitude of the majority of frequencies except for the most dominant frequencies which are presumed to be associated with the Kelvin-Helholtz instability. For these instabilities, the device has slightly increased the shedding frequency and also slightly increased the energy contained within the vortices as visible through the increase in peak amplitude. In other-words it has had an effect of stabilising the shear layer, and consolidating the energy into one stable shedding mode.

Preliminary evidence showed a potential link between shear flow in the wake interface and drag. From this a theoretical outline was created linking shear stress with base drag force. Based on this theory it was hypothesised that better performing devices work by reducing shear stress across the shear layer. This prompted a detailed study into the shear layer behavior of different geometries. The findings were contrary to the outlined hypothesis, finding that shear stress actually increased with better performing devices. This led to a more detailed look at the theory through application of a simplified force analysis taken at the shear layer. The conditions found in the simulation were applied to this simplified model. Shear force was found to have an inverse-linear relationship with re-ciculation velocity, whereas pressure drag force was found to have a positive quadratic relationship. This highlighted that the main mechanism of drag reduction is through the pressure drag mechanism and that maintaining and supporting the reverse-flow of the wake is a powerful mechanism of drag reduction.

The fundamental cause of drag derived from the base region is a low-pressure volume of air in this area known as a wake. The low pressure has two sources, shear force from the surrounding fluid, and normal force from entrained air. From an unsteady perspective, the energy flux that supports this shear force derives from a transfer of momentum from the high velocity fluid in the free-stream towards the wake region. The Kelvin-Holmholtz instabilities in the wake serve to facilitate this transfer of momentum as the rotational vortices that shed from the rear of the vehicle incorporate vertical components of motion. The mechanism for drag reduction of the device then follows the reversal of this mechanism. Through the stabilisation of the shear layer, the momentum transfer into the wake is reduced. This reduces the energy available for shearing action of the wake thereby increasing the pressure at the base. This ultimately reduces the suction force at the rear of the vehicle which reduces drag. Evidence presented in this section supports

this hypothesis on several fronts. Evidence for a stabilised shear layer includes the spectral plot and RMS analysis of the shear layer probe signal showing reduced activity; evidence for reduced momentum transfer includes the image processing of Q-Critereon plots showing less vortex diffusion with the incorporation of the device; evidence for reduced shear force at the wake boundary includes the visualization of the wake-freestream interface showing reduced flow-speeds at the interface for the most effective devices; and finally evidence for an increased base pressure is demonstrated with pressure distribution plots at the rear face, and also pressure probe signals which both show an appreciable increase in base pressure.

From a practical standpoint, the flat, two-dimensional shape of each flap on the device makes it easier to design mechanisms that can comply with the door. Moreover, the performance is comparable to the boat tail which is currently the most popular device to be implemented in practice. On this basis the device has proven effective and practical. The unsteady parametric study has shown that the performance of each geometrical configuration (wave number k) is sensitive to speed. In general, the response of the performance of each device was uni-modal with relation to speed. That is to say certain geometries excel as certain speeds. If speed is not in the optimal range the device may actually increase drag rather than reduce it. In this way, the device should be tailored to the cruising speed of the vehicle. These results indicate that a wave-number of $k = 6$ may be ideal for a highway speed of approximately 24 m/s, however this is based on extrapolation of the data set, therefore more research is required.

7

Conclusions

As Heavy vehicles account for the second largest share of petroleum consumption despite their small proportion of road traffic, heavy vehicles have been the focus of this work. A small improvement in the global traffic fleet could have a significant effect on overall transportation efficiency. Despite large potential fuel savings, few practical drag reduction devices operate in the base of the vehicle. For this reason this area has been chosen as the region of interest. The tractor-trailer geometry is focused on as they are the the greatest in number and in terms of global heavy duty fuel consumption. In accordance with this goal, Choi et al. (2014) suggested two key areas that require development A) developing a deeper understanding of vortex activity that occurs in the base of a heavy vehicle, and B) the development of passive drag reduction devices that are based on unsteady principles that operate in the base of the heavy vehicle. Through a greater literature review the research outline has been refined to two primary objectives: to develop fundamental understanding of massively separated flows; and to develop and evaluate a novel drag reduction device based on a wavy profile. Based on these two objectives, the major structure of the work has been divided accordingly into a fundamental study of a backwards facing step, and a study of relevant truck geometries.

7.1 Review Of Objectives

Here the work is reflected on with respect to the objectives defined at the outset of the work.

Objective 1 (a) To uncover the source of the flapping behavior in massively separated flows.

From the literature review it was apparent that studying fundamental aspects of massively separated flows could lead to greater understanding of the unsteady behavior in the wake of a vehicle. The backwards-facing step was chosen as the simplest geometry that exhibited characteristics of massively separated flows. From an unsteady perspective, there were known to be two major phenomena that defined this flow. One which was well understood was the shear layer instability that manifested as a Kelvin-Helmholtz instability originating from the step and moving down-stream. The origin of another phenomena with a lower frequency than the shear layer instability was not so clear. Through a correlation of the frequency of this phenomena with the observed movement of the shear layer and reattachment points, this phenomena came to be known as flapping. This was a research problem that persisted through the decades. There had been various mechanisms proposed about its origin but none had been conclusively proven. Thus the primary goal of Chapter 5 was to uncover the mechanism of this flapping behavior. The physical setup of the simulation was set up to be exactly as Vogel and Eaton (1985) so that validation of the model could be proven. The model had an extremely high temporal and spacial resolution to best capture turbulent details; as such the model had to be solved in a super-computing facility. The idea behind the study was to first identify the frequencies at which each phenomena occurred, and then try to visualise them with a filter-based decomposition technique.

Based on the literature review only two dominant frequencies were expected. However, after conducting the spectral analysis at probe locations in the shear layer and in the wake region, a great multitude of dominant frequencies were identified. Though this complicated the matter it was decided to press on with the original methodology. The fields that were examined and decomposed are the horizontal and vertical components of velocity, and also pressure. Furthermore, a Q-Criterion vortex identification procedure was applied onto the velocity fields to identify vorticies. When the initial data came in it was difficult to interpret. The results did not look like the diagrams from the literature review. The only identifiable feature was perhaps the Kelvin-Helmholtz instability that manifested as a series of pressure fluctuations and vorticies that lined up with the step edge. Besides this there was a strange larger-scale phenomena that could not be explained. The hall-mark of this phenomena is larger-scale and lower frequency oscillations of the pressure and velocity fields. Contrary to initial expectations, all of the different frequencies seemed to exhibit a combination of both phenomena rather than each phenomena being isolated to specific frequency bands. The second phenomena was initially troublesome

to explain. After manipulating the data visualization by overlaying the Q-Criterion plots on top of the velocity and pressure oscillations, it became evident that the rotation of the shear-layer instabilities was related to the large-scale osculations. After applying a line-integral convolution to the images it became clear that these large-scale oscilations were in fact large convective structures of alternating polarity. Within the large convections were the shear-layer based instabilities and their direction of rotation depended on the polarity of the larger surrounding rotating structure. It is worth noting that these results are based on filtered data, by nature only the oscillating component of the flow remains. An apparent reversal in the rotation of the shear-layer instability may simply imply a reduction of rotation rate when considering the overall underlying shear conditions which would favor clock-wise rotations. Now that structures had been identified the next part was identifying the source of these structures. Through combing the literature there had been increasing evidence of a global centrifugal instability. These include from Barkley et al. (2002) who identified a global centrifugal instability through a numerical study and Beaudoin et al. (2004) who observed longitudinal vorticies of suspected centrifugal origin. To establish whether the conditions for centrifugal instabilities were present a spacial analysis of Dean number was conducted and its value of >1400 confirmed a sufficient ratio of destabilising centrifugal forces vs pressure forces. In this case the centripetal acceleration originates from the curved streamlines passing over the step. Recall the famous couette experiment with concentric rotating cylinders. At low rotation rates of the inner cylinder stable vortex tubes form aligned tangentially. This is caused by the tangential momentum of the inner fluid pushing outward, and the return flow caused by the resulting pressure. Upon greater rotation rates these tubes destabilise due to the centripetal acceleration of newly formed vortex tubes. After this the flow takes a cellular form. This was the primary inspiration for explaining the morphology of the large-scale convective structures. Due to the flows high velocity and deeply turbulent nature, one would expect higher-order instabilities such as the cellular couette flow to occur. The shear layer instabilities then seem to be a secondary instability from the shear conditions that the large instabilities create, which facilitates the transfer of energy down the energy cascade. In hindsight the findings of this study correlate with the idea in literature that there are two essential mechanisms at play. This study adds that at highly turbulent conditions, the two mechanisms may be coupled and occur at the same frequencies rather than occurring distinctly. Finally, evidence has been presented that the source of the second essential instability (flapping) is centrifugal in origin and takes the form similar to the cellular Taylor-Couette flow.

Objective 1 (b) To understand the mechanism of operation behind the base cavity and the wavy geometry.

Based on analysis of the effect of the wavy device on the wake behind the vehicle in Section 6.3.2, there was some preliminary evidence for a link between shear flow in the wake interface and drag. This was based on the fact that worse performing devices seemed to have higher flow velocities at the wake boundary. From this, a theoretical outline was developed linking shear stress with base drag force. Based on this theory it was hypothesised that better performing devices work by reducing shear stress across the shear layer. This prompted a detailed study into the shear layer behavior of different geometries. A line probe was positioned to allow measurement of the velocity gradient and also the absolute velocity change across the shear layer. The findings were contrary to the outlined hypothesis, finding that velocity gradient and therefore shear stress actually increased with better performing devices.

This prompted a re-visit of the theory. Upon examining the equations the only remaining mechanism of the reduced drag despite the increased shear stress is through the normal body force acting on the control volume. To investigate whether a reduction in body force was possible the theoretical equations were expanded upon to be applied to a control volume in the shear region between the base of the vehicle and the line probe. Simplifying assumptions include a linear velocity profile, a constant free-stream velocity in both base and line-probe locations, and also zero velocity at the base. Flow analysis of the simulations show a correlation with reverse flow in the wake with drag performance. Geometries that promoted reverse-flow in the wake seem to exhibit lower overall drag. The results of the simulation were applied to the simplified mathematical model, and then the magnitude of shear and normal body forces were plotted against wake velocity. The results show that shear force was found to have an inverse-linear relationship with re-ciculation velocity, whereas pressure drag force was found to have a positive quadratic relationship. This highlighted that the main mechanism of drag reduction is through the pressure drag mechanism and that maintaining and supporting the reverse-flow of the wake is a powerful mechanism of drag reduction. This is because a strong reverse flow can reverse the direction of net-momentum change into the control volume thereby contributing a body force in the opposite direction of the flow. This is not to say that shear-based momentum transfer is inconsequential to overall performance of the device. Any type of momentum transfer into the wake whether from entrainment,

instabilities, or shearing action would act in opposition to the beneficial reverse flow. As such stabilisation of the shear layer is still a theoretically valid avenue of drag reduction. Though its mechanism of action is not from a direct decrease of shear force, but rather to promote a stable recirculating flow.

Objective 2 (a) To determine the drag reducing potential of a base drag reduction device based on the wavy principle.

Section 6.3 concerned creating a viable geometry based on a wavy trailing edge, and determining the gross drag reduction potential such a device. The design of the device was based on the shape of a harbour seal vibrassae which has been shown in previous studies to induce a drag reduction, such as in the work of Tombazis and Bearman (1997). The design of the device features a protrusion that extends the perimeter of the base downstream by a distance of 1/4 trailer widths. The protrusion features a sinusoidal trailing edge with various number of wavelengths k, from k=1 to k=5. A steady state approach using the IDDES methodology was chosen due to the focus on overall drag reduction performance. Moreover, a scale model of $1/8^{th}$ scale was chosen in a simulation domain that exactly replicated a study by Storms et al. (2006). The validation results were excellent with a 2.06% error in computation of drag coefficient, and with a well-matched pressure coefficient comparison. The high validational performance gives confidence in the overall results. On the basis of this model several geometries were evaluated. The best performing device had a wave number of k=2 which delivered a 21.56 % drag reduction. When compared with other devices such as a belly box of a base cavity, this is considered a good performance. The performance of the device was comparable with the best performing device from the study by Storms et al. (2006) which was flaps at the base angled inward by 20 degrees with a drag reduction performance of 22.93 %.

From a practical standpoint, the flat, two-dimensional shape of each flap on the device makes it easier to design mechanisms that can comply with the door. Moreover, the performance is comparable to the boat tail which is currently the most popular device to be implemented in practice. On this basis the device has proven effective and practical. The unsteady parametric study has shown that the performance of each geometrical configuration (wave number k) is sensitive to speed. In general, the response of the performance of each device was uni-modal with relation to speed. That is to say certain geometries excel as certain speeds. If speed is not in the optimal range the device may actually increase drag rather than reduce it. In this way, the device should be tailored to the cruising speed of the vehicle. These

results indicate that a wave-number of $k = 6$ may be ideal for a highway speed of approximately 24 m/s, however this is based on extrapolation of the data set, therefore more research is required.

Objective 2 (b) To establish the influence of the device on the unsteady flow behind a tractor-trailer geometry.

Section 6.4.4 focused on the unsteady mechanism of action of the device. For this an unsteady solution of high spacial and temporal resolution was solved that employed the IDDES solution form. The simulation was run for 10 simulated seconds. To understand unsteady characteristics, a probe was positioned in the shear layer behind the vehicle, and another in the wake region of the vehicle. From analysis of the time-series of the pressure signal, as well as spectral analysis of these signals, it is apparent that this device had a modulating effect on unsteady activity. Within the shear layer it had reduced the amplitude of the majority of frequencies except for the most dominant frequencies which are presumed to be associated with the Kelvin-Helholtz instability. For these instabilities, the device has slightly increased the shedding frequency and also slightly increased the energy contained within the vortices as visible through the increase in peak amplitude. In other-words it has had an effect of stabilising the shear layer, and consolidating the energy into one stable shedding mode. The increase in amplitude of this particular mode may be related to the increase in re-circulation velocity and hence a stronger over-all shear condition. An analysis of vortex shedding behavior in the wake showed that the device also had the effect of reducing the diffusion of vorticies in the wake.

Objective 2 (c) To determine how geometrical parameters affect drag reduction performance.

A parametric study in Section 6.4.3 was conducted that that examines the performance of the different devices across different speed ranges. One baseline case and five geometries from k=1 to k=5, were examined at four speeds (6, 12, 18 and 24 m/s) totaling 24 simulations. The performance of each device was compared with the baseline case at each speed to give overall drag reduction percentage for each geometry. The results show that the drag performance of the device has a strong dependence on speed; certain geometries excel at certain speeds, As speed increases, a higher wave-number device has the best performance. By looking at individual geometries through the speed range, the majority of the geometries show a uni-modal relationship with speed where there is a particular speed that it excels at, beyond-which or before-which the performance declines. Though the majority of

data points indicate some drag reduction, there is a trend that beyond the optimum speed, the device may even incur an increase in overall drag. For practical application to trucks, a device may be tailored to the cruising speed of the vehicle, for maximum performance.

Objective 2 (d) To develop a fundamental mechanism linking base vortices and drag.

Leading from the theory developed in Section 6.3.3 that show the relationship between momentum transfer and drag, the unsteady analysis in Section 6.4 expanded the ideas into an unsteady perspective. The fundamental cause of drag derived from the base region is a low-pressure volume of air in this area known as a wake. The low pressure has two sources, shear force from the surrounding fluid, and normal force from entrained air. Based on the findings from this theoretical investigation, it was found that any source of momentum transfer into the wake could antagonise the beneficial reverse flow that had a significant effect on the drag reducing performance of the device. From an unsteady perspective, the Kelvin-Holmholtz instabilities in the wake serve to facilitate the transfer of momentum from the freestream into the wake as the rotational vortices that shed from the rear of the vehicle incorporate vertical components of motion. The mechanism for drag reduction of the device then follows the reversal of this mechanism. Through the stabilisation of the shear layer, the momentum transfer into the wake is reduced. Thereby the beneficial recirculating flow is supported rather than hindered. This ultimately reduces the suction force at the rear of the vehicle which reduces drag. Evidence presented in this section supports this hypothesis on several fronts. Evidence for a stabilised shear layer includes the spectral plot and RMS analysis of the shear layer probe signal showing reduced activity; evidence for reduced momentum transfer includes the image processing of Q-Critereon plots showing less vortex diffusion with the incorporation of the device; evidence for reduced shear force at the wake boundary includes the visualization of the wake-freestream interface showing reduced flow-speeds at the interface for the most effective devices; and finally evidence for an increased base pressure is demonstrated with pressure distribution plots at the rear face, and also pressure probe signals which both show an appreciable increase in base pressure.

7.2 Novelty and Contributions

Theoretical Contributions

Theoretical contributions of this work cover both fundamental aspects of massively separated flows in general, and also insights into how base-region drag reduction devices function. With respect to massively separated flows in general, the most important contribution of this work has been the identification of identification of large-scale convective structures in the wake of centrifugal origin. Most studies that have identified centrifugal structures have been at low Reynolds number, and studies that had been at high Reynolds number have been based on numerical stability analysis such as Barkley et al. (2002). To the authors knowledge this is first direct evidence of centrifugal instabilities that occur within high-Reynolds number turbulent flows. Another related contribution of the work is in understanding the structure of turbulence. Cantwell (1981) theorised that amongst an apparently chaotic behavior, turbulence is mainly comprised of a superposition of simpler organised eddys. This work has shown this in a direct way. Through a filter-based decomposition the morphology and behavior of each motion has been visualised and analysed. What was found was a combination of both the centrifugal and Kelvin-Helmholtz instability occurring synchronously at a multitude of frequencies simultaneously. Based on the fact that the Kelvin-Helmholtz instability was embedded into the larger-scale centrifugal structures, it is believed that the Kelvin-Helmholtz instability supports the transfer of centrifugal energy through the energy cascade.

With regard to heavy vehicle aerodynamics, the most important contribution of this work is a theoretical understanding about the mechanistic link between shear, vortices, base pressure and drag. Previous to this most evidence linking these phenomena remained superficial. In such studies devices that were found to reduce drag were also found to reduce wake length or to stabilise the shear layer. Despite this no direct causality between the phenomena had been examined. In this work a mechanistic outline had been composed whose results seemed to agree and explain certain experimentally derived findings. Contrary to initial expectations, better performing devices actually had higher shear conditions in the wake. Through the theoretical framework it was found that recirculating flow provided a higher impact drag reduction that reducing shear conditions in the wake. This is through the recirculating flows impact on the body foces at the base. The higher shear conditions in the wake also explained the consolidation of energy of the wavy device into specific frequency bands. Besides this, a new bio-inspired device has been devised and tested that

shows promising drag reducing potential.

Methodological Novelties

Besides theoretical contributions, this work has also developed some new methodologies that future researchers may employ in their own work. The filter-based decomposition method developed in this work has allowed the visualization of the constituent motions of turbulence. It is suitable for application in both experimental and theoretical applications and has been the primary tool for studying the turbulent structures discovered in this work. Another methodological contribution of this work is the modification of the Q-Criterion equation by multiplication of the sign of vorticity. This allows for the polarity of the identified vortex to also be visualized. As well as showing the presence of vorticies its rotation direction is determined by the sign of the identified vortex. Furthermore, this novelty has been applied successfully in this work and actually made an important contribution in identifying the link between the Kelvin-Helmholtz vorticies and the larger vorticies which are now known to be of centrifugal origin. The final methodological contribution of this work is the method of visualizing the localised Dean number. Previously Dean number is computed based on generalised statistics, in this work a method for computing localised Dean number has been found by incorporating the local radius of curvature. This allows the researcher to examine how conditions relevant to centrifugal instabilities may vary with position in the flow.

7.3 Future Work

PIV Study of Development of Centrifugal Instabilities

This research has uncovered the existence of a centrifugal instability as a constituent fundamental mechanism within turbulent massively-separated flow. Due to computational limitations only one Reynolds number was investigated at a relatively short time-span of ten seconds. Furthermore the Reynolds number of 28,000 that was chosen to replicate experiments from Vogel and Eaton (1985) is well into the highly turbulent regime. For these reasons there is limited understanding of the development of the centrifugal instability. The next logical step is to conduct a physical experiment of the same nature. The decomposition technique developed into this work is perfectly suited for application to Particle Image Velocimetry results that yield a time-developing flow-field. The primary benefit is to verify the results in a physical setting. With a physical experiment there is access to the entire range of flow speeds without limitations. This would allow the careful study of the centrifu-

gal instability throughout its forms and development. It is hypothesized that the instability will take a similar form to the centrifugal instability of the Taylor-Gortler experiment with similar bi-furications at different Reynolds numbers. The complication of this flow is that the shear-born Kelvin-Helmholtz instability is ubiquitous at all but very low Reynolds numbers potentially making it harder to spot the centrifugal instability. In the physical experiment one would include probes at both the shear-layer and also within the wake region or possibly even up-stream of the step. As seen in this computational study the centrifugal instability is known to be a global-mode instability so its effects will be felt up-stream of the step; whereas the Kelvin-Helmholtz instability a local convective instability that can only be detected down-stream of the step. A spectral analyses of the two probes may distinguish the centrifugal instability from the Kelvin-Helmholtz instability, allowing their respective developments and interactions to be individually studied. Furthermore, using Deans number a prediction could be made for the Reynolds number at which centrifugal instabilities would start to manifest.

Deeper Investigation into Drag Mechanism

The work studying the fundamental mechanism of drag on the vehicle represents and important step in bringing to light the inter-relations between phenomena that had been observed to be related to drag but whose had not been properly understood. These are phenomena such as the wake bubble size, momentum transfer, vortex shedding, pressure at base and the drag force. The work in this thesis represents a start to building a thorough understanding of the fundamental mechanism of drag creation in massively separated flow behind a bluff body. A deeper study is suggested that traces each of the parameters at different Reynolds numbers and finds their inter-relations. This study would answer questions such as to what degree does vortex shedding affect momentum transfer into the wake? Is momentum transfer related to the size of the wake bubble? Based on the work in this thesis it is understood that maintaining the reverse-flow within the wake is a key to drag reduction through reduction of normal-force based drag. With a deeper understanding into the fundamental mechanism and inter-relations, a framework for understanding which parameters should be optimized for and which are less relevant could be developed. This framework would subsequently be used to advise the development of new devices and may also be used to explain the performance of existing devices and highlight areas for improvement.

Design and Testing of Practical Device

The novel drag reduction device that has been studied has shown promise in drag

reduction performance while having a nominally 2D profile that in theory would be more practical. The next step is to conduct a detailed practical design that includes a folding mechanism for use with truck doors. The design is then to be manufactured and tested on a truck. Tests could include wind-tunnel testing as well as on-road testing for fuel consumption studies. One area of interest is the performance of the device at various Reynolds numbers. Furthermore the device could be optimized for highway velocity based on wave number or other geometrical modifications. The affect of wind hasn't been looked at in this study, the geometry should be studied at various yaw angles to understand the performance at different wind conditions. The unsteady analysis of the wake vorticies show that the device significantly reduces the perturbation amplitudes of the vortex shedding behavior. This would presumably translate into a reduction in noise which may be of interest to truck manufacturers or governments.

List of References

Ahmed, S. R., Ramm, G., and Faltin, G. Some salient features of the time-averaged ground vehicle wake. *SAE Transactions*, pages 473–503, 1984.

Allan, J. Aerodynamic drag and pressure measurements on a simplified tractor-trailer model. *Journal of Wind Engineering and Industrial Aerodynamics*, 9(1-2): 125–136, 1981.

Andereck, C. D., Liu, S., and Swinney, H. L. Flow regimes in a circular couette system with independently rotating cylinders. *Journal of fluid mechanics*, 164: 155–183, 1986.

Anderson, E. and Szewczyk, A. Effects of a splitter plate on the near wake of a circular cylinder in 2 and 3-dimensional flow configurations. *Experiments in Fluids*, 23(2):161–174, 1997.

Armaly, B. F., Durst, F., Pereira, J. C. F., and Schönung, B. Experimental and theoretical investigation of backward-facing step flow. *Journal of Fluid Mechanics*, 127:473–496, 1983.

Balkanyi, S. R., Bernal, L. P., and Khalighi, B. Analysis of the near wake of bluff bodies in ground proximity. In *Fluids Engineering*. ASME, 2002.

Bandyopadhyay, P. R. Instabilities and large structures in reattaching boundary layers. *AIAA Journal*, 29(7):1149–1155, jul 1991.

Barkley, D., Gomes, M. G. M., and Henderson, R. D. Three-dimensional instability in flow over a backward-facing step. *Journal of Fluid Mechanics*, 473, Dec 2002.

Bayly, B. Three-dimensional centrifugal-type instabilities in inviscid two-dimensional flows. *The Physics of fluids*, 31(1):56–64, 1988.

Bearman, P. W. and OWen, J. C. Reduction of bluff-body drag and suppression of vortex shedding by the introduction of wavy separation lines. *Journal of Fluids and Structures*, 12(1):123–130, 1998.

Bearman, P. W. and Tombazis, N. The effects of three-dimensional imposed disturbances on bluff body near wake flows. *Journal of Wind Engineering and Industrial Aerodynamics*, 49(1-3):339–349, 1993.

Bearman, P. Investigation of the flow behind a two-dimensional model with a blunt trailing edge and fitted with splitter plates. *Journal of fluid mechanics*, 21(2): 241–255, 1965.

Beaudoin, J.-F., Cadot, O., Aider, J.-L., and Wesfreid, J. E. Three-dimensional stationary flow over a backward-facing step. *European Journal of Mechanics - B/Fluids*, 23(1):147–155, jan 2004.

Bell, J., Burton, D., Thompson, M., Herbst, A., and Sheridan, J. Dynamics of trailing vortices in the wake of a generic high-speed train. *Journal of Fluids and Structures*, 65:238 – 256, 2016.

Bippes, H. and Görtler, H. Dreidimensionale störungen in der grenzschicht an einer konkaven wandthree-dimensional disturbances in the boundary layer along a concave wall. *Acta Mechanica*, 14(4):251–267, 1972.

Birkhoff, G. Helmholtz and taylor instability. In *Proc. Symp. Appl. Math*, volume 13, pages 55–76, 1962.

Boussinesq, J. *Essai sur la théorie des eaux courantes*. Imprimerie Nationale, 1877.

Brackston, R., De La Cruz, J. G., Wynn, A., Rigas, G., and Morrison, J. Stochastic modelling and feedback control of bistability in a turbulent bluff body wake. *Journal of Fluid Mechanics*, 802:726–749, 2016.

Bradley, R. Technology roadmap for the 21st century truck program. Technical Report Tech. Rep. 21CT-001, US Dep. Energy, Washington D.C., U.S.A., 2010.

Bruneau, C.-H., Creusé, E., Depeyras, D., Gilliéron, P., and Mortazavi, I. Coupling active and passive techniques to control the flow past the square back ahmed body. *Computers & Fluids*, 39(10):1875–1892, 2010.

Buil, R. M. and Herrer, L. C. Aerodynamic analysis of a vehicle tanker. *Journal of Fluids Engineering*, 131(4):041204, 2009.

Bushnell, D. M. and Moore, K. Drag reduction in nature. *Annual Review of Fluid Mechanics*, 23(1):65–79, 1991.

Cadot, O., Evrard, A., and Pastur, L. Imperfect supercritical bifurcation in a three-dimensional turbulent wake. *Physical Review E*, 91(6):063005, 2015.

Cai, J., Chng, T. L., and Tsai, H. M. On vortical flows shedding from a bluff body with a wavy trailing edge. *Physics of Fluids*, 20(6):064102, 2008.

Cantwell, B. J. Organized motion in turbulent flow. *Annual review of fluid mechanics*, 13(1):457–515, 1981.

Cao, Y., Li, Z., Ji, W., and Ma, M. Characteristics analysis of near-field and far-field aerodynamic noise around high-speed railway bridge. *Environmental Science and Pollution Research*, pages 1–17, 2021.

Castelain, T., Michard, M., Szmigiel, M., Chacaton, D., and Juvé, D. Identification

of flow classes in the wake of a simplified truck model depending on the underbody velocity. *Journal of Wind Engineering and Industrial Aerodynamics*, 175:352–363, 2018.

Castellucci, P. J. and Salari, K. Computational simulation of tractor-trailer gap flow with drag-reducing aerodynamic devices. Technical report, SAE Technical Paper, 2005.

Chandrasekhar, S. The hydrodynamic stability of viscid flow between coaxial cylinders. *Proceedings of the National Academy of Sciences*, 46(1):141–143, 1960.

Chandrasekhar, S. *Hydrodynamic and hydromagnetic stability*. Courier Corporation, 2013.

Chanson, H. 3 - introduction to mixing and dispersion in natural waterways. In Chanson, H., editor, *Environmental Hydraulics of Open Channel Flows*, pages 37 – 48. Butterworth-Heinemann, Oxford, 2004a.

Chanson, H. *Environmental hydraulics for open channel flows*. Elsevier, 2004b.

Choi, H., Jeon, W.-P., and Kim, J. Control of flow over a bluff body. *Annual Review of Fluid Mechanics*, 40(1):113–139, jan 2008.

Choi, H., Lee, J., and Park, H. Aerodynamics of heavy vehicles. *Annual Review of Fluid Mechanics*, 46:441–468, 2014.

Choi, J., Jeon, W.-P., and Choi, H. Mechanism of drag reduction by dimples on a sphere. *Physics of Fluids*, 18(4):041702, 2006.

Chrust, M., Goujon-Durand, S., and Wesfreid, J. Loss of a fixed plane of symmetry in the wake of a sphere. *Journal of Fluids and Structures*, 41:51–56, 2013.

Coles, D. Transition in circular couette flow. *Journal of Fluid Mechanics*, 21(03): 385, mar 1965.

Cooley, J. W. and Tukey, J. W. An algorithm for the machine calculation of complex fourier series. *Mathematics of Computation*, 19(90):297–301, 1965.

Cooper, K. R. Truck aerodynamics reborn-lessons from the past. Technical report, SAE Technical Paper, 2003.

Cooper, K. R. and Leuschen, J. Model and full-scale wind tunnel tests of second-generation aerodynamic fuel saving devices for tractor-trailers. In *SAE Technical Paper*. SAE International, 11 2005.

Cotrell, D. L. and Pearlstein, A. J. The connection between centrifugal instability and tollmien–schlichting-like instability for spiral poiseuille flow. *Journal of Fluid Mechanics*, 509:331–351, 2004.

Couette, M. *Etudes sur le frottement des liquides*. PhD thesis, 1890.

Croll, R. H., Gutierrez, W. T., Hassan, B., Suazo, J. E., and Riggins, A. J. Experimental investigation of the ground transportation systems (gts) project for

heavy vehicle drag reduction. Technical report, Sandia National Lab.(SNL-NM), Albuquerque, NM (United States), 1995.

D'Adamo, J., Godoy-Diana, R., and Wesfreid, J. E. Centrifugal instability of stokes layers in crossflow: the case of a forced cylinder wake. *Proc. R. Soc. A*, 471(2178): 20150011, 2015.

Dean, W. R. Fluid motion in a curved channel. *Proc. R. Soc. Lond. A*, 121(787): 402–420, 1928.

Dejoan, A. and Leschziner, M. Large eddy simulation of periodically perturbed separated flow over a backward-facing step. *International Journal of Heat and Fluid Flow*, 25(4):581–592, aug 2004.

Diczfalusy, B., Taylor, P., Cazzola, P., Cuenot, F., Chiavari, J., Elzinga, D., Fulton, L., Gibson, B., Kerr, T., Lee, S., Remme, U., Tam, C., Taylor, M., Tepes, P., and Trudeau, N. Energy technology perspectives. Technical report, The International Energy Agency, Paris, France, 2010.

Doddipatla, L. S., Hangan, H., Durgesh, V., and Naughton, J. Wake dynamics resulting from trailing-edge spanwise sinusoidal perturbation. *AIAA Journal*, 55 (6):1833–1851, 2017.

Drazin, P. Kelvin–helmholtz instability of finite amplitude. *Journal of Fluid Mechanics*, 42(2):321–335, 1970.

Drazin, P. G. and Reid, W. H. *Hydrodynamic stability*. Cambridge university press, 2004.

Driver, D. M., Seegmiller, H. L., and Marvin, J. G. Time-dependent behavior of a reattaching shear layer. *AIAA Journal*, 25(7):914–919, jul 1987.

Dubief, Y. and Delcayre, F. On coherent-vortex identification in turbulence. *Journal of Turbulence*, 1:N11, 2000.

Duell, E. G. and George, A. R. Experimental study of a ground vehicle body unsteady near wake. In *SAE Technical Paper*. SAE International, 03 1999.

Eaton, J. K. and Johnston, J. P. *Low Frequency Unsteadyness of a Reattaching Turbulent Shear Layer*, pages 162–170. Springer Berlin Heidelberg, Berlin, Heidelberg, 1982.

Englar, R. J. Advanced aerodynamic devices to improve the performance, economics, handling and safety of heavy vehicles. Technical report, SAE Technical Paper, 2001.

Es-Sahli, O., Sescu, A., and Afsar, M. *Nonlinear centrifugal instabilities in curved free shear layers*. 2020.

Evrard, A., Cadot, O., Herbert, V., Ricot, D., Vigneron, R., and Délery, J. Fluid force and symmetry breaking modes of a 3d bluff body with a base cavity. *Journal*

of Fluids and Structures, 61(Supplement C):99 – 114, 2016a.

Evrard, A., Cadot, O., Herbert, V., Ricot, D., Vigneron, R., and Délery, J. Fluid force and symmetry breaking modes of a 3d bluff body with a base cavity. *Journal of Fluids and Structures*, 61:99–114, 2016b.

Evstafyeva, O., Morgans, A., and Dalla Longa, L. Simulation and feedback control of the ahmed body flow exhibiting symmetry breaking behaviour. *Journal of Fluid Mechanics*, 817, 2017.

Fabre, D., Auguste, F., and Magnaudet, J. Bifurcations and symmetry breaking in the wake of axisymmetric bodies. *Physics of Fluids*, 20(5):051702, may 2008.

Faranda, D., Sato, Y., Saint-Michel, B., Wiertel, C., Padilla, V., Dubrulle, B., and Daviaud, F. Stochastic chaos in a turbulent swirling flow. *Physical review letters*, 119(1):014502, 2017.

Fish, F. E., Howle, L. E., and Murray, M. M. Hydrodynamic flow control in marine mammals. *Integrative and Comparative Biology*, 48(6):788–800, 2008.

Floryan, J. M. and Saric, W. S. Stability of gortler vortices in boundary layers. *AIAA journal*, 20(3):316–324, 1982.

Floryan, J. Görtler instability of boundary layers over concave and convex walls. *The Physics of fluids*, 29(8):2380–2387, 1986.

Friedrich, R. and Arnal, M. Analysing turbulent backward-facing step flow with the lowpass-filtered navier-stokes equations. *Journal of Wind Engineering and Industrial Aerodynamics*, 35:101–128, jan 1990.

Fureby, C. Large eddy simulation of rearward-facing step flow. *AIAA Journal*, 37 (11):1401–1410, nov 1999.

Furuichi, N. and Kumada, M. An experimental study of a spanwise structure around a reattachment region of a two-dimensional backward-facing step. *Experiments in Fluids*, 32(2):179–187, Feb 2002.

Garry, K. P. Some effects of ground clearance and ground plane boundary layer thickness on the mean base pressure of a bluff vehicle type body. *Journal of wind engineering and industrial aerodynamics*, 62(1):1–10, 1996.

Gaster, M. A theoretical model of a wave packet in the boundary layer on a flat plate. *Proceedings of the Royal Society A: Mathematical, Physical and Engineering Sciences*, 347(1649):271–289, dec 1975.

Gentile, V., Schrijer, F., Van Oudheusden, B., and Scarano, F. Low-frequency behavior of the turbulent axisymmetric near-wake. *Physics of Fluids*, 28(6):065102, 2016.

Gilliéron, P. and Kourta, A. Aerodynamic drag reduction by vertical splitter plates. *Experiments in fluids*, 48(1):1–16, 2010.

Grandemange, M., Gohlke, M., Parezanović, V., and Cadot, O. On experimental sensitivity analysis of the turbulent wake from an axisymmetric blunt trailing edge. *Physics of fluids*, 24(3):035106, 2012a.

Grandemange, M., Gohlke, M., and Cadot, O. Bi-stability in the turbulent wake past parallelepiped bodies with various aspect ratios and wall effects. *Physics of Fluids*, 25(9):095103, 2013a.

Grandemange, M., Gohlke, M., and Cadot, O. Statistical axisymmetry of the turbulent sphere wake. *Experiments in fluids*, 55(11):1–11, 2014.

Grandemange, M., Cadot, O., and Gohlke, M. Reflectional symmetry breaking of the separated flow over three-dimensional bluff bodies. *Physical review E*, 86(3): 035302, 2012b.

Grandemange, M., Gohlke, M., and Cadot, O. Turbulent wake past a three-dimensional blunt body. part 1. global modes and bi-stability. *Journal of Fluid Mechanics*, 722:51–84, 2013b.

Grandemange, M., Cadot, O., Courbois, A., Herbert, V., Ricot, D., Ruiz, T., and Vigneron, R. A study of wake effects on the drag of ahmed s squareback model at the industrial scale. *Journal of Wind Engineering and Industrial Aerodynamics*, 145:282–291, 2015.

Görtler, H. Instabilität laminarer grenzschichten an konkaven wänden gegenüber gewissen dreidimensionalen störungen. *ZAMM - Journal of Applied Mathematics and Mechanics / Zeitschrift für Angewandte Mathematik und Mechanik*, 21(4): 250–252, 1941.

Gunes, D. On the similarity of wind tunnel experiments and numerical simulation of heavy-duty trailer flow. *Progress in Computational Fluid Dynamics, an International Journal*, 10(3):168–176, 2010.

Gutierrez, W. T., Hassan, B., Croll, R. H., and Rutledge, W. H. Aerodynamics overview of the ground transportation systems (gts) project for heavy vehicle drag reduction. Technical report, Sandia National Lab.(SNL-NM), Albuquerque, NM (United States), 1995.

Haff, J. *A comparative study of engineering tools in heavy vehicle aerodynamics*. PhD thesis, 2015.

Hall, P. and Seddougui, S. On the onset of three-dimensionality and time-dependence in görtler vortices. *Journal of Fluid Mechanics*, 204:405–420, 1989.

Haller, G. An objective definition of a vortex. *Journal Of Fluid Mechanics*, 525: 1–26, Feb 2005.

Hammache, M. and Browand, F. On the aerodynamics of tractor-trailers. In *The Aerodynamics of Heavy Vehicles: Trucks, Buses, and Trains*, pages 185–205.

Springer, 2004.

Hanke, W., Witte, M., Miersch, L., Brede, M., Oeffner, J., Michael, M., Hanke, F., Leder, A., and Dehnhardt, G. Harbor seal vibrissa morphology suppresses vortex-induced vibrations. *Journal of Experimental Biology*, 213(15):2665–2672, 2010.

Hasan, M. A. Z. The flow over a backward-facing step under controlled perturbation: laminar separation. *Journal of Fluid Mechanics*, 238(-1):73, may 1992.

Hoerner, S. Fluid-dynamic drag: practical information on aerodynamic drag and hydrodynamic resistance.(pubished by the author). *New York*, 1965.

Howell, J., Sheppard, A., and Blakemore, A. Aerodynamic drag reduction for a simple bluff body using base bleed. Technical report, SAE Technical Paper, 2003.

Hudy, L. M., Naguib, A., and Humphreys, W. M. Stochastic estimation of a separated-flow field using wall-pressure-array measurements. *Physics of Fluids*, 19(2):024103, feb 2007.

Huerre, P. and Monkewitz, P. A. Local and global instabilities in spatially developing flows. *Annual Review of Fluid Mechanics*, 22(1):473–537, jan 1990.

Hyams, D. G., Sreenivas, K., Pankajakshan, R., Nichols, D. S., Briley, W. R., and Whitfield, D. L. Computational simulation of model and full scale class 8 trucks with drag reduction devices. *Computers and Fluids*, 41(1):27–40, 2011.

Islam, A., Gaylard, A., and Thornber, B. A detailed statistical study of unsteady wake dynamics from automotive bluff bodies. *Journal of Wind Engineering and Industrial Aerodynamics*, 171:161–177, 2017.

Johari, H., Henoch, C. W., Custodio, D., and Levshin, A. Effects of leading-edge protuberances on airfoil performance. *AIAA journal*, 45(11):2634–2642, 2007.

Jones, W. and Launder, B. E. The prediction of laminarization with a two-equation model of turbulence. *International journal of heat and mass transfer*, 15(2):301–314, 1972.

Kaiktsis, L., Karniadakis, G. E., and Orszag, S. A. Unsteadiness and convective instabilities in two-dimensional flow over a backward-facing step. *Journal of Fluid Mechanics*, 321(-1):157, aug 1996.

Kaltenbach, H.-J. and Janke, G. Direct numerical simulation of flow separation behind a swept, rearward-facing step at re h= 3000. *Physics of Fluids*, 12(9): 2320–2337, 2000.

Khalighi, B., Zhang, S., Koromilas, C., Balkanyi, S. R., Bernal, L. P., Iaccarino, G., and Moin, P. Experimental and computational study of unsteady wake flow behind a bluff body with a drag reduction device. In *SAE Technical Paper*. SAE International, 03 2001.

Khalighi, B., Chen, K.-H., and Iaccarino, G. Unsteady aerodynamic flow investigation around a simplified square-back road vehicle with drag reduction devices. *Journal of fluids engineering*, 134(6), 2012.

Kim, J. J., Lee, E. J., and Lee, S. J. Wind tunnel tests on drag reduction of heavy vehicles using sinusoidal boat tails. *Journal of Mechanical Science and Technology*, 34(1):201–208, 2020.

Kim, W. and Choi, H. Effect of the spanwise computational domain size on the flow over a two-dimensional bluff body with spanwise periodic perturbations at low reynolds number. *Computers and Fluids*, 183:102 – 106, 2019.

Kostas, J., Soria, J., and Chong, M. S. A comparison between snapshot pod analysis of piv velocity and vorticity data. *Experiments in Fluids*, 38(2):146–160, Feb 2005.

Kowata, S., Ha, J., Yoshioka, S., Kato, T., and Kohama, Y. Drag force reduction of a bluff-body with an underbody slant and rear flaps. *SAE International Journal of Commercial Vehicles*, 1(1):230–236, 2009.

Krajnovic, S. and Davidson, L. Numerical study of the flow around a bus-shaped body. *J. Fluids Eng.*, 125(3):500–509, 2003.

Krajnović, S. and Davidson, L. Influence of floor motions in wind tunnels on the aerodynamics of road vehicles. *Journal of wind engineering and industrial aerodynamics*, 93(9):677–696, 2005.

Kruiswyk, R. and Dutton, J. Effects of a base cavity on subsonic near-wake flow. *AIAA journal*, 28(11):1885–1895, 1990.

Launder, B. E. and Spalding, D. B. The numerical computation of turbulent flows. In *Numerical Prediction of Flow, Heat Transfer, Turbulence and Combustion*, pages 96–116. Elsevier, 1983.

Le, H., Moin, P., and Kim, J. Direct numerical simulation of turbulent flow over a backward-facing step. *Journal of Fluid Mechanics*, 330:349–374, Jan 1997.

Lee, I. and Sung, H. J. Multiple-arrayed pressure measurement for investigation of the unsteady flow structure of a reattaching shear layer. *Journal of Fluid Mechanics*, 463, Jul 2002.

Lee, T. and Mateescu, D. Experimental and numerical investigation of 2-d backward-facing step flow. *Journal of Fluids and Structures*, 12(6):703–716, 1998.

Li, R., Barros, D., Borée, J., Cadot, O., Noack, B. R., and Cordier, L. Feedback control of bimodal wake dynamics. *Experiments in Fluids*, 57(10):1–6, 2016.

Lim, H.-C. and Lee, S.-J. Flow control of circular cylinders with longitudinal grooved surfaces. *AIAA journal*, 40(10):2027–2036, 2002.

Lin, C. C. Hydrodynamic stability. *Cambridge, UP*, 1955.

Littlewood, R. and Passmore, M. The optimization of roof trailing edge geometry

of a simple square-back. Technical report, SAE Technical Paper, 2010.

Littlewood, R. and Passmore, M. A. Aerodynamic drag reduction of a simplified squareback vehicle using steady blowing. *Experiments in fluids*, 53(2):519–529, 2012.

Malatesta, V., Souza, L. F. d., and Liu, J. T. Influence of görtler vortices spanwise wavelength on heat transfer rates. *Computational Thermal Sciences: An International Journal*, 5(5), 2013.

Malviya, V., Mishra, R., and Fieldhouse, J. Cfd investigation of a novel fuel-saving device for articulated tractor-trailer combinations. *Engineering Applications of Computational Fluid Mechanics*, 3(4):587–607, 2009a.

Malviya, V., Mishra, R., and Fieldhouse, J. D. Cfd investigation of a novel fuel-saving device for articulated tractor-trailer combinations. *Engineering Applications of Computational Fluid Mechanics*, 3(4):587–607, December 2009b.

Mariotti, A. and Buresti, G. Experimental investigation on the influence of boundary layer thickness on the base pressure and near-wake flow features of an axisymmetric blunt-based body. *Experiments in fluids*, 54(11):1–16, 2013.

Martín-Alcántara, A., Sanmiguel-Rojas, E., Gutiérrez-Montes, C., and Martínez-Bazán, C. Drag reduction induced by the addition of a multi-cavity at the base of a bluff body. *Journal of Fluids and Structures*, 48(Supplement C):347 – 361, 2014.

Mathieu, J. and Scott, J. *An introduction to turbulent flow*. Cambridge University Press, 2000.

Matsuoka, C. Kelvin-Helmholtz Instability and Roll-up. *Scholarpedia*, 9(3):11821, 2014. revision #182229.

McArthur, D., Burton, D., Thompson, M., and Sheridan, J. On the near wake of a simplified heavy vehicle. *Journal of Fluids and Structures*, 66:293–314, 2016.

McArthur, D., Burton, D., Crouch, T., Thompson, M., and Sheridan, J. Wake flows of highly detailed heavy vehicles. *International Journal of Automotive Technology*, 22(5):1227–1243, 2021.

McCallen, R., Couch, R., Hsu, J., Browand, F., Hammache, M., Leonard, A., Brady, M., Salari, K., Rutledge, W., Ross, J., Storms, B., Heineck, J., Driver, D., Bell, J., and Zilliac, G. Progress in reducing aerodynamic drag for higher efficiency of heavy duty trucks (class 7-8). In *SAE Technical Paper Series*. SAE International, apr 1999.

McCallen, R. C., Salari, K., Ortega, J. M., DeChant, L. J., Hassan, B., Roy, C. J., Pointer, W. D., Browand, F., Hammache, M., Hsu, T., et al. Doe's effort to reduce truck aerodynamic drag-joint experiments and computations lead to smart design.

AIAA paper, 2249:2004, 2004.

McDonough, J. M. Introductory lectures on turbulence: physics, mathematics and modeling. 2007.

Menter, F. R. Eddy viscosity transport equations and their relation to the k-epsilon model. *NASA STI/Recon Technical Report N*, 95, November 1994.

Menter, F. and Kuntz, M. Adaptation of eddy-viscosity turbulence models to unsteady separated flow behind vehicles. In *The aerodynamics of heavy vehicles: trucks, buses, and trains*, pages 339–352. Springer, 2004.

Molezzi, M. J. and Dutton, J. C. Study of subsonic base cavity flowfield structure using particle image velocimetry. *AIAA journal*, 33(2):201–209, 1995.

Morkovin, M. V. Nasa technical report: Recent insights into instability and transition to turbulence in open-flow systems. Technical Report 19880020695, NASA Langley Research Center, Hampton, VA, United States, August 1988.

Muirhead, V. U. and Saltzman, E. J. Reduction of aerodynamic drag and fuel consumption for tractor-trailer vehicles. *Journal of Energy*, 3(5):279–284, 1979.

Na, G., Park, G., Turri, V., Johansson, K. H., Shim, H., and Eun, Y. Disturbance observer approach for fuel-efficient heavy-duty vehicle platooning. *Vehicle System Dynamics*, 58(5):748–767, 2020.

Nash, J. F., Quincey, V., and Callinan, J. *Experiments on two-dimensional base flow at subsonic and transonic speeds*. HM Stationery Office, 1963.

Neto, A. S., Grand, D., Métais, O., and Lesieur, M. A numerical investigation of the coherent vortices in turbulence behind a backward-facing step. *Journal of Fluid Mechanics*, 256(-1):1, nov 1993.

Neumann, J. and Wengle, H. Coherent structures in controlled separated flow over sharp-edged and rounded steps. *Journal of Turbulence*, 5:N22, 2004.

Newton, I. Philosophiæ naturalis principia mathematica (mathematical principles of natural philosophy). *London (1687)*, 3, 1687.

Ong, R. S. B. and Roderick, N. On the kelvin-helmholtz instability of the earth's magnetopause. *Planetary and Space Science*, 20(1):1–10, 1972.

Ormonde, P. C., Cavalieri, A. V., da Silva, R. G., and Avelar, A. C. Passive control of coherent structures in a modified backwards-facing step flow. *Experiments in Fluids*, 59(5):88, 2018.

Ortega, J., Salari, K., Brown, A., and Schoon, R. Aerodynamic drag reduction of class 8 heavy vehicles: a full-scale wind tunnel study. Technical Report Tech. Rep. LLNL-TR-628153, Lawrence Livermore National Laboratory, Illinois, U.S.A., 2013.

Ortega, J. and Salari, K. Experimental investigation of the aerodynamic benefits of

truck platooning: Two-and four-vehicle platoons. Technical report, SAE Technical Paper, 2021.

Ortega, J. M., Dunn, T., McCallen, R., and Salari, K. Computational simulation of a heavy vehicle trailer wake. In *The Aerodynamics of Heavy Vehicles: Trucks, Buses, and Trains*, pages 219–233. Springer, 2004.

Park, H., Lee, D., Jeon, W.-P., Hahn, S., Kim, J., Kim, J., Choi, J., and Choi, H. Drag reduction in flow over a two-dimensional bluff body with a blunt trailing edge using a new passive device. *Journal of Fluid Mechanics*, 563:389–414, 2006.

Parkin, D., Sheridan, J., and Thompson, M. Numerical analysis of periodic open-loop flow control on bluff bodies in ground proximity. *Journal of Wind Engineering and Industrial Aerodynamics*, 145:339–350, 2015.

Parkin, D. J., Thompson, M. C., and Sheridan, J. Numerical analysis of bluff body wakes under periodic open-loop control. *Journal of fluid mechanics*, 739:94–123, 2014.

Pastoor, M., Henning, L., Noack, B. R., King, R., and Tadmor, G. Feedback shear layer control for bluff body drag reduction. *Journal of fluid mechanics*, 608:161–196, 2008.

Perry, A. and Passmore, M. The impact of underbody roughness on rear wake structure of a squareback vehicle. 2013.

Perry, A.-K., Almond, M., Passmore, M., and Littlewood, R. The study of a bi-stable wake region of a generic squareback vehicle using tomographic piv. *SAE International Journal of Passenger Cars-Mechanical Systems*, 9(2016-01-1610): 743–753, 2016.

Peterson, R. L. Drag reduction obtained by the addition of a boattail to a box shaped vehicle. *NASA Contractor Report*, 163113, 1981.

Phersson, L. R., Sheridan, J., Thompson, M. C., and Burton, D. M. Effect of sinusoidal forcing on bluff-body drag. In *International Conference in Numerical and Experimental Aerodynamics of Road Vehicles and Trains 2014*, 2014.

Pointer, D., Sofu, T., Chang, J., and Weber, D. Applicability of commercial cfd tools for assessment of heavy vehicle aerodynamic characteristics. *The Aerodynamics of Heavy Vehicles II: Trucks, Buses, and Trains*, pages 349–361, 2009.

Prandtl, L. Bericht uber untersuchungen zur ausgebildeten turbulenz. *Zs. angew. Math. Mech.*, 5:136–139, 1925.

Rao, A. N., Minelli, G., Zhang, J., Basara, B., and Krajnović, S. Investigation of the near-wake flow topology of a simplified heavy vehicle using pans simulations. *Journal of Wind Engineering and Industrial Aerodynamics*, 183:243–272, 2018.

Rao, A. N., Zhang, J., Minelli, G., Basara, B., and Krajnović, S. An les investigation

of the near-wake flow topology of a simplified heavy vehicle. *Flow, Turbulence and Combustion*, 102(2):389–415, 2019.

Rayleigh, L. On the stability or instability of certain fluid motions. *Scientific papers*, 3:594–596, 1880.

Richtmyer, R. D. Taylor instability in shock acceleration of compressible fluids. *Communications on pure and applied mathematics*, 13(2):297–319, 1960.

Rigas, G., Morgans, A. S., Brackston, R., and Morrison, J. F. Diffusive dynamics and stochastic models of turbulent axisymmetric wakes. *Journal of Fluid Mechanics*, 778, 2015.

Rodriguez, O. Base drag reduction by control of the three-dimensional unsteady vortical structures. *Experiments in Fluids*, 11(4):218–226, 1991.

Rogenski, J., de Souza, L., and Floryan, J. Influence of pressure gradients on the evolution of the görtler instability. *AIAA Journal*, pages 2916–2921, 2016.

Roshko, A. On the wake and drag of bluff bodies. *Journal of the aeronautical sciences*, 22(2):124–132, 1955.

Rott, N. Diffraction of a weak shock with vortex generation. *Journal of Fluid Mechanics*, 1(1):111–128, 1956.

Rouméas, M., Gilliéron, P., and Kourta, A. Analysis and control of the near-wake flow over a square-back geometry. *Computers and Fluids*, 38(1):60–70, 2009.

Rütten, F., Schröder, W., and Meinke, M. Large-eddy simulation of low frequency oscillations of the dean vortices in turbulent pipe bend flows. *Physics of Fluids*, 17(3):035107, 2005.

Savory, E. and Toy, N. The separated shear layers associated with hemispherical bodies in turbulent boundary layers. In *Advances in Wind Engineering*, pages 291–300. Elsevier, 1988.

Scarano, F. and Riethmuller, M. Temporal analysis of coherent structures in a turbulent bfs flow with piv. In *10th international symposium on applications of laser techniques to fluid mechanics. Lisbon, Portugal*, 2000.

Schäfer, F., m. Breuer, and f. Durst. The dynamics of the transitional flow over a backward-facing step. *Journal of fluid mechanics*, 623:85, Mar 2009.

Schlichting, H., Gersten, K., Krause, E., and Oertel, H. *Boundary-layer theory*, volume 7. Springer, 1955.

Schmidt, H.-J., Woszidlo, R., Nayeri, C., and Paschereit, C. The effect of flow control on the wake dynamics of a rectangular bluff body in ground proximity. *Experiments in Fluids*, 59(6):1–16, 2018.

Schram, C., Rambaud, P., and Riethmuller, M. L. Wavelet based eddy structure eduction from a backward facing step flow investigated using particle image ve-

locimetry. *Experiments in Fluids*, 36(2):233–245, feb 2004.

Sharpe, B. and Muncrief, R. Literature review: Real-world fuel consumption of heavy-duty vehicles in the united states, china, and the european union. Technical report, The International Council on Clean Transportation, Berlin, Germany, Feburary 2015.

Shehadi, E. Large eddy simulation of turbulent flow over a backward-facing step, 2018.

Shih, W., Wang, C., Coles, D., and Roshko, A. Experiments on flow past rough circular cylinders at large reynolds numbers. *Journal of Wind Engineering and Industrial Aerodynamics*, 49(1-3):351–368, 1993.

Shur, M. L., Spalart, P. R., Strelets, M. K., and Travin, A. K. A hybrid RANS-LES approach with delayed-DES and wall-modelled LES capabilities. *International Journal of Heat and Fluid Flow*, 29(6):1638–1649, dec 2008.

Siemens, S. D. I. S. Description of turbulence p. 45. 2021.

Smirnov, E., Smirnovsky, A., Schur, N., Zaitsev, D., and Smirnov, P. Comparison of rans and iddes solutions for turbulent flow and heat transfer past a backward-facing step. *Heat and Mass Transfer*, 54(8):2231–2241, 2018.

Sohn, S.-I. Singularity formation and nonlinear evolution of a viscous vortex sheet model. *Physics of Fluids*, 25(1):014106, 2013.

Spalart, P. R. Comments on the feasibility of les for wings, and on a hybrid rans/les approach. In *Proceedings of first AFOSR international conference on DNS/LES*. Greyden Press, 1997.

Spalart, P. Young-person's guide to detached-eddy simulation grids. *Seattle, Washington, NASA/CR-2001-211032*, 2001.

Spalart, P. and Allmaras, S. A one-equation turbulence model for aerodynamic flows. In *30th aerospace sciences meeting and exhibit*, page 439, 1992.

Spazzini, P. G., Iuso, G., Onorato, M., Zurlo, N., and Di Cicca, G. M. Unsteady behavior of back-facing step flow. *Experiments in Fluids*, 30(5):551–561, May 2001.

Steers, L. L. and Saltzman, E. J. Reduced truck fuel consumption through aerodynamic design. *Journal of Energy*, 1(5):312–318, 1977.

Stokes, G. G. *On the Steady Motion of Incompressible Fluids*, volume 1 of *Cambridge Library Collection - Mathematics*, page 1–16. Cambridge University Press, 2009.

Storms, B. L., Satran, D. R., Heineck, J. T., and Walker, S. A study of reynolds number effects and drag-reduction concepts on a generic tractor-trailer. *AIAA paper*, 2251:2004, 2004.

Storms, B. L., Satran, D. R., Heineck, J. T., and Walker, S. M. A summary of the

experimental results for a generic tractor-trailer in the ames research center 7-by 10-foot and 12-foot wind tunnels. 2006.

Swinney, H. L. and Gollub, J. P. Hydrodynamic instabilities and the transition to turbulence. *Hydrodynamic instabilities and the transition to turbulence*, 1981.

Taylor, G. Stability of a viscous liquid contained between two rotating cylinders phil. trans. r. soc. lond. a january. 1923.

Teter, J., Cazzola, P., and Gul, T. The future of trucks - implications for energy and the environment. Technical report, The International Energy Agency, Paris, France, 2015.

Theisel, H. *Vector Field Curvature and Applications*. PhD thesis, Rostock University, 11 1995.

Thomareis, N. and Papadakis, G. Effect of trailing edge shape on the separated flow characteristics around an airfoil at low reynolds number: A numerical study. *Physics of Fluids*, 29(1):014101, 2017.

Tombazis, N. and Bearman, P. A study of three-dimensional aspects of vortex shedding from a bluff body with a mild geometric disturbance. *Journal of Fluid Mechanics*, 330:85–112, 1997.

Travin, A., Shur, M., Strelets, M., and Spalart, P. R. Physical and numerical upgrades in the detached-eddy simulation of complex turbulent flows. In Friedrich, R. and Rodi, W., editors, *Advances in LES of Complex Flows*, pages 239–254, Dordrecht, 2002. Springer Netherlands.

Troutt, T. R., Scheelke, B., and Norman, T. R. Organized structures in a reattaching separated flow field. *Journal of Fluid Mechanics*, 143(-1):413, jun 1984.

Tsubokura, M., Nakashima, T., Kitayama, M., Ikawa, Y., Doh, D. H., and Kobayashi, T. Large eddy simulation on the unsteady aerodynamic response of a road vehicle in transient crosswinds. *International Journal of Heat and Fluid Flow*, 31(6):1075–1086, 2010.

Unaune, S. V., Sovani, S. D., and Kim, S. E. Aerodynamics of a generic ground transportation system: Detached eddy simulation. *SAE transactions*, pages 596–611, 2005.

Van Raemdonck, G. and Van Tooren, M. Time averaged phenomenological investigation of a wake behind a bluff body.

Varon, E., Eulalie, Y., Edwige, S., Gilotte, P., and Aider, J.-L. Chaotic dynamics of large-scale structures in a turbulent wake. *Physical Review Fluids*, 2(3):034604, 2017.

Vietri, M., Ferrara, A., and Miniati, F. The survival of interstellar clouds against kelvin-helmholtz instabilities. *The Astrophysical Journal*, 483(1):262, 1997.

Viswanath, P. Flow management techniques for base and afterbody drag reduction. *Progress in Aerospace Sciences*, 32(2):79 – 129, 1996.

Vogel, J. C. and Eaton, J. K. Combined heat transfer and fluid dynamic measurements downstream of a backward-facing step. *Journal of Heat Transfer*, 107(4): 922, 1985.

Volpe, R., Devinant, P., and Kourta, A. Unsteady experimental characterization of the natural wake of a squareback ahmed model. In *Fluids Engineering Division Summer Meeting*, volume 46230, page V01CT17A007. American Society of Mechanical Engineers, 2014.

Volpe, R., Devinant, P., and Kourta, A. Experimental characterization of the unsteady natural wake of the full-scale square back ahmed body: flow bi-stability and spectral analysis. *Experiments in Fluids*, 56(5):1–22, 2015.

Wang, Y., Sicot, C., Borée, J., and Grandemange, M. Experimental study of wheel-vehicle aerodynamic interactions. *Journal of Wind Engineering and Industrial Aerodynamics*, 198:104062, 2020.

Weinman, K., Wilhelmi, H., Bell, J., Heine, D., and Wagner, C. An assessment of the aerodynamic characterization of a compact car driving behind a heavy vehicle using computational fluid dynamics. In *22nd STAB/DGLR Symposium on New Results in Numerical and Experimental Fluid Mechanics XIII-Jahresbericht 2020*, pages 124–125. Springer Nature, 2020.

Weiss, J., Mohammed-Taifour, A., and Schwaab, Q. Unsteady behavior of a pressure-induced turbulent separation bubble. *AIAA Journal*, 53(9):2634–2645, sep 2015.

Wilcox, D. C. Reassessment of the scale-determining equation for advanced turbulence models. *AIAA journal*, 26(11):1299–1310, 1988.

Wilkins, S. J., Hosseinali, M., and Hall, J. W. Investigation of unsteady pressure fluctuations in flow over backward-facing step. *AIAA Journal*, 57(6):2447–2456, 2019.

Wood, R. M. A discussion of a heavy truck advanced aerodynamic trailer system. In *Int. Symp. Heavy Veh. Weights Dimens., 9th, University Park, PA*, 2006.

Xie, W., Xi, G., and Zhong, M. Effect of the vortical structure on heat transfer in the transitional flow over a backward-facing step. *International Journal of Refrigeration*, 74:465 – 474, 2017.

Yu, X., Jia, Q., Rashidi, M. M., and Yang, Z. Comprehensive investigating on the aerodynamic influences of the wheel contact patch. *Journal of Applied and Computational Mechanics*, 6(4):934–955, 2020.

Zdravkovich, M. Review and classification of various aerodynamic and hydrody-

namic means for suppressing vortex shedding. *Journal of Wind Engineering and Industrial Aerodynamics*, 7(2):145–189, 1981.

Zhang, H., Xin, D., and Ou, J. Wake control using spanwise-varying vortex generators on bridge decks: AÂ computational study. *Journal of Wind Engineering and Industrial Aerodynamics*, 184:185 – 197, 2019.

Zhang, J., Zhang, M., Li, Y., Huang, X., and Zheng, Z. Aerodynamics of high-sided vehicles on truss girder considering sheltering effect by wind tunnel tests. *Baltic Journal of Road & Bridge Engineering (RTU Publishing House)*, 15(2), 2020.

Zhao, P., Ge, Z., Zhu, J., Liu, J., and Ye, M. Quasi-direct numerical simulation of forced convection over a backward-facing step: Effect of prandtl number. *Nuclear Engineering and Design*, 335:374 – 388, 2018.

A

Appendix 1

A.1 Star CCM+ Java Macro to conduct parametric study of backward facing step with waviness

```
1  // STAR-CCM+ macro: RunBFSParaStudy.java
2  // Written by STAR-CCM+ 11.06.011
3  package macro; //WAS JUST 'macro'
4
5  import java.io.File;
6  import java.io.FileNotFoundException;
7  import java.io.FileOutputStream;
8  import java.io.FilenameFilter;
9  import java.io.PrintWriter;
10 import java.util.*;
11
12 import java.util.logging.Level;
13 import java.util.logging.Logger;
14 import star.common.*;
15 import star.cadmodeler.*;
16 import star.base.neo.*;
17 import star.vis.*;
18 import star.base.report.*;
19 import star.flow.*;
20 import star.meshing.*;
21
22 public class RunBFSParaStudy extends StarMacro {
23
24     double[] velocities = new double[]{ 2.06,4.12,6.18,8.25,10.31 };
25     String[] partnames = new String[]{"1W","2W","3W","4W","5W"};
26
27   public void execute() {
28         try {
29             execute0();
30         } catch (FileNotFoundException ex) {
31             Logger.getLogger(RunBFSParaStudy.class.getName()).log(Level.SEVERE, null, ex);
32         }
33   }
34
35   private void execute0() throws FileNotFoundException {
36
37     Simulation simulation_0 =
38       getActiveSimulation();
39
40         Region region_0 =
41       simulation_0.getRegionManager().getRegion("Region");
42
43     for(int i=0;i<5;i++){
44
45         // CHANGE PART AND GENERATE MESH
46         System.out.println("i = "+i);
```

```
47
48
49      SolidModelPart solidModelPart_0 =
50        ((SolidModelPart) simulation_0.get(SimulationPartManager.class).getPart(partnames[i]));
51
52      region_0.getPartGroup().setObjects(solidModelPart_0);
53
54      MeshPipelineController meshPipelineController_0 =
55        simulation_0.get(MeshPipelineController.class);
56
57      meshPipelineController_0.clearGeneratedMeshes();
58
59      meshPipelineController_0.generateVolumeMesh();
60
61      // CYCLE THROUGH VELOCITIES AND GENERATE REPORTS
62      for(int j=0;j<5;j++){
63          System.out.println("j = "+j);
64
65           Boundary boundary_1 =
66        region_0.getBoundaryManager().getBoundary("BFS.Inlet");
67
68      VelocityMagnitudeProfile velocityMagnitudeProfile_0 =
69        boundary_1.getValues().get(VelocityMagnitudeProfile.class);
70
71      velocityMagnitudeProfile_0.getMethod(ConstantScalarProfileMethod.class).getQuantity().setValue(velocities[j]);
72
73      PhysicsContinuum physicsContinuum_0 =
74        ((PhysicsContinuum) simulation_0.getContinuumManager().getContinuum("Physics 1"));
75
76      VelocityProfile velocityProfile_0 =
77        physicsContinuum_0.getInitialConditions().get(VelocityProfile.class);
78
79      velocityProfile_0.getMethod(ConstantVectorProfileMethod.class).getQuantity().setComponents(velocities[j], 0.0, 0
80
81      Solution solution_0 =
82        simulation_0.getSolution();
83
84      solution_0.clearSolution(Solution.Clear.History, Solution.Clear.Fields);
85
86      simulation_0.getSimulationIterator().run();
87
88      ForceReport forceReport_0 =
89        ((ForceReport) simulation_0.getReportManager().getReport("Force 1"));
90
91      forceReport_0.printReport();
92
93      AreaAverageReport areaAverageReport_0 =
94        ((AreaAverageReport) simulation_0.getReportManager().getReport("Surface Average 1"));
95
96      areaAverageReport_0.printReport();
97
98      String writeString = "\n" + forceReport_0.getValue().toString() + " , "  + Double.toString(areaAverageReport_0.ge
99      String savestr = System.getProperty("user.dir") + File.separator + "saveoutput.txt";
100 File f = new File(savestr);
101
102 PrintWriter out = null;
103 if ( f.exists() && !f.isDirectory() ) {
104     out = new PrintWriter(new FileOutputStream(new File(savestr), true));
105 }
106 else {
107     out = new PrintWriter(savestr);
108 }
109 out.append(writeString);
110 out.close();
111     }
112
113     }
114
115   }
116 }
```

B

Appendix 2

B.1 Complete set of results from Backwards-Facing Step Study

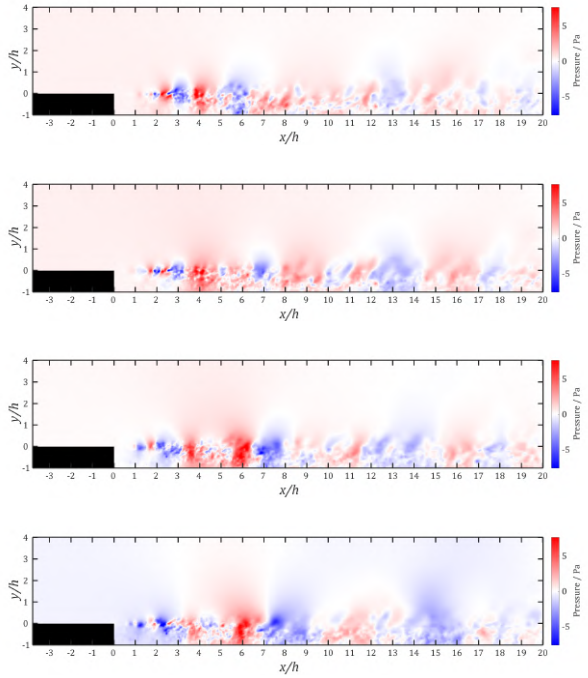

Figure B.1: Showing the pressure field of the planar bisection at a filter frequency of 1.219 Hz

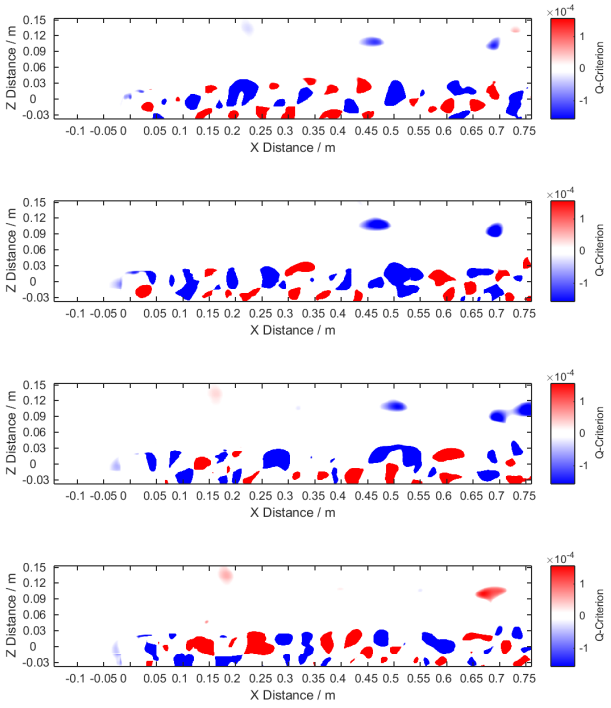

Figure B.2: Showing the rotation of vortices within the of the planar bisection at a filter frequency of 1.219 Hz

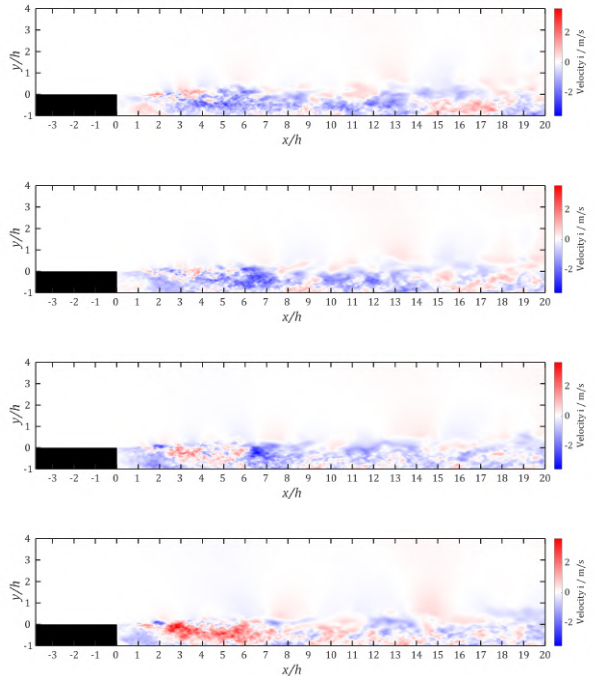

Figure B.3: Showing the vertical velocity field of the planar bisection at a filter frequency of 1.219 Hz

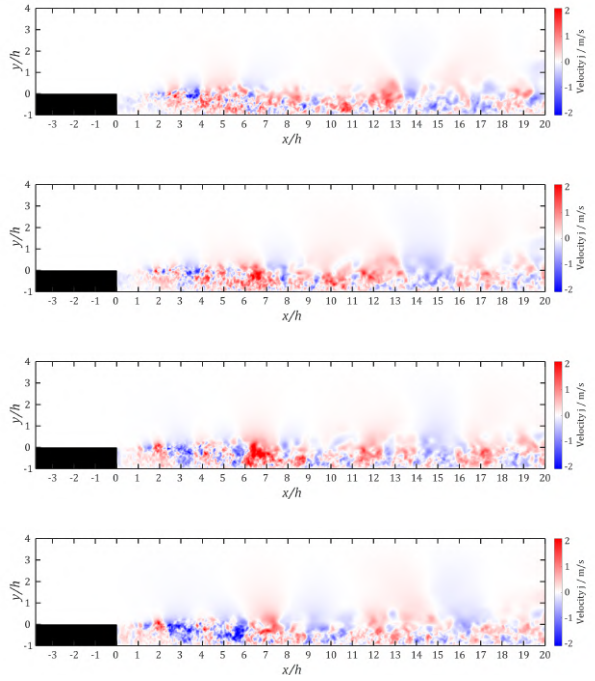

Figure B.4: Showing the horizontal velocity field of the planar bisection at a filter frequency of 1.219 Hz

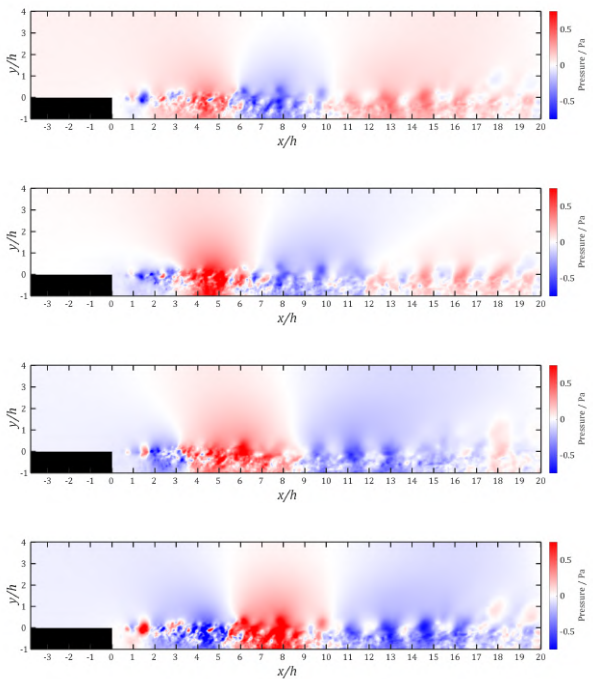

Figure B.5: Showing the pressure field of the planar bisection at a filter frequency of 5.485 Hz

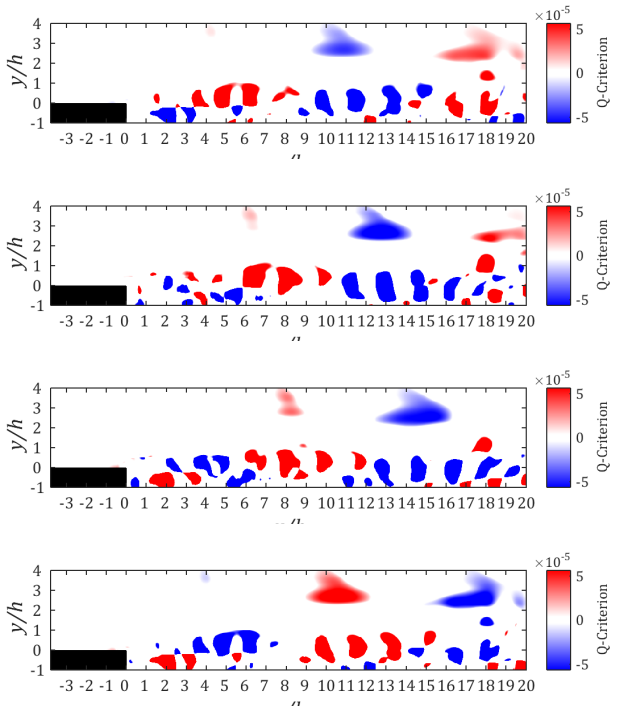

Figure B.6: Showing the rotation of vortices within the of the planar bisection at a filter frequency of 5.485 Hz

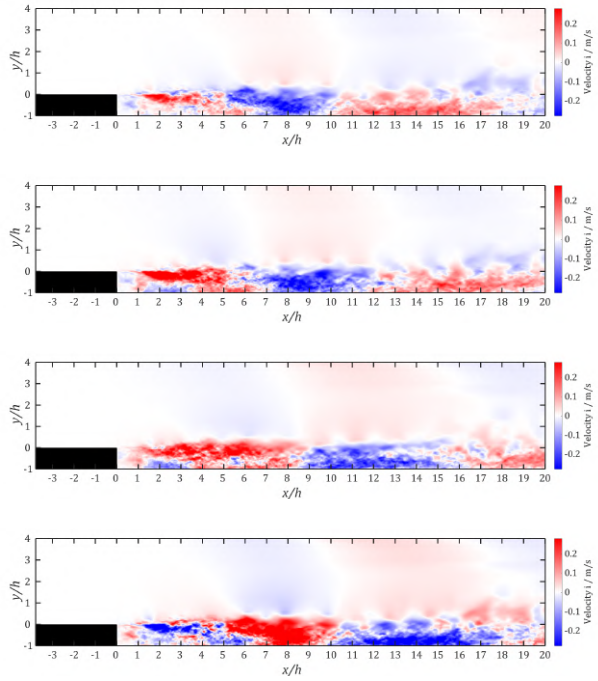

Figure B.7: Showing the vertical velocity field of the planar bisection at a filter frequency of 5.485 Hz

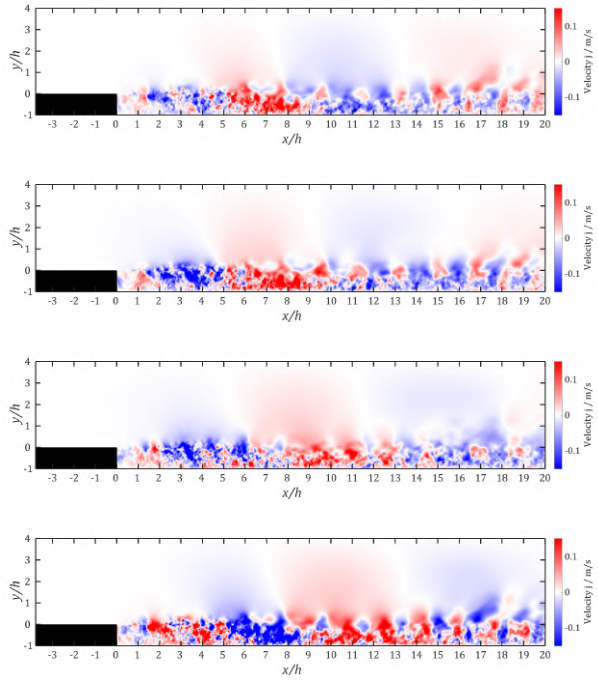

Figure B.8: Showing the horizontal velocity field of the planar bisection at a filter frequency of 5.485 Hz

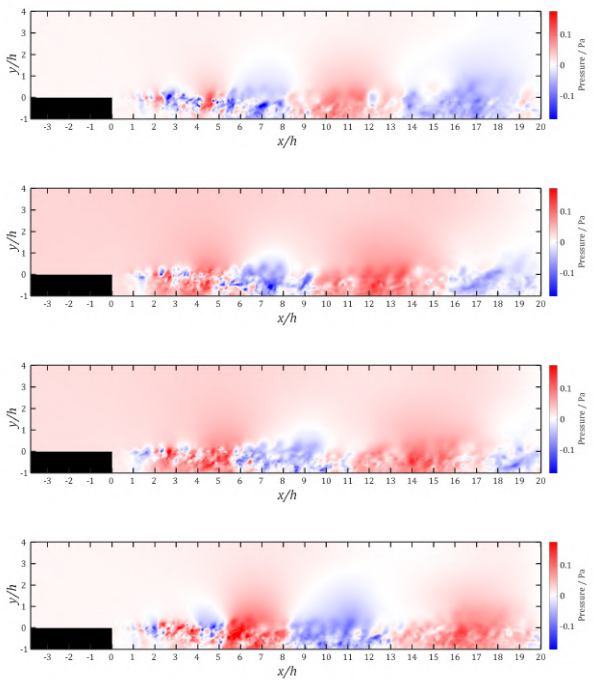

Figure B.9: Showing the pressure field of the planar bisection at a filter frequency of 12.83 Hz

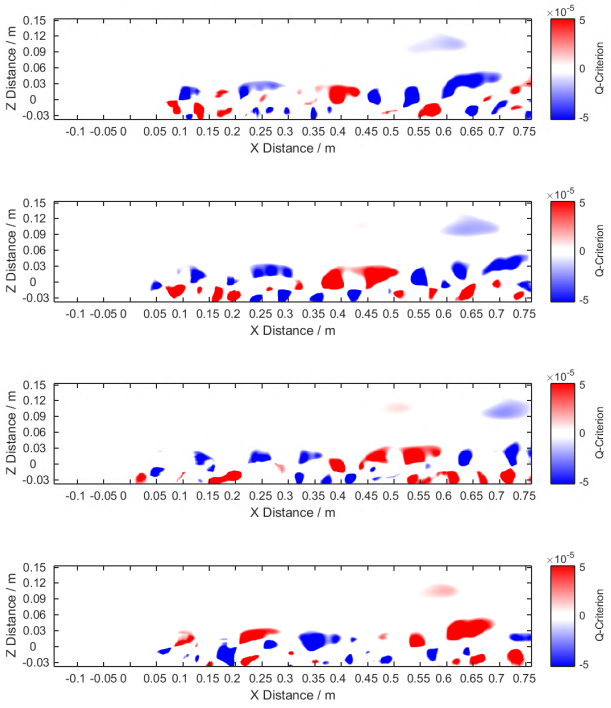

Figure B.10: Showing the rotation of vortices within the of the planar bisection at a filter frequency of 12.83 Hz

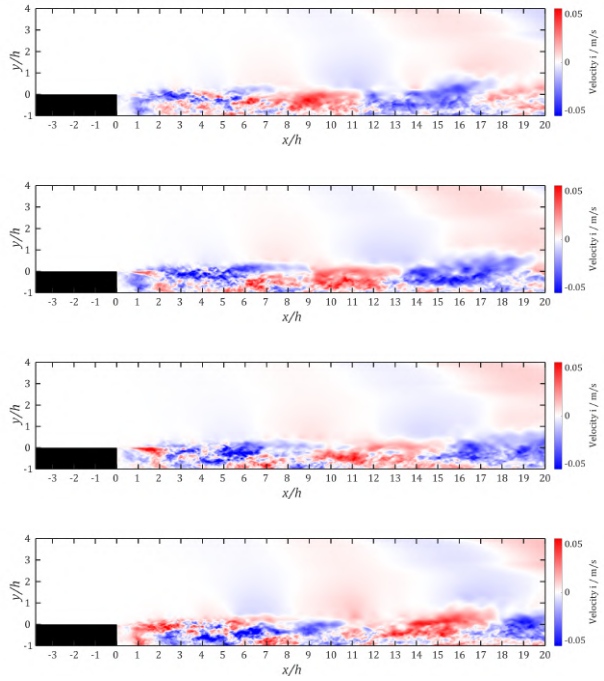

Figure B.11: Showing the vertical velocity field of the planar bisection at a filter frequency of 12.83 Hz

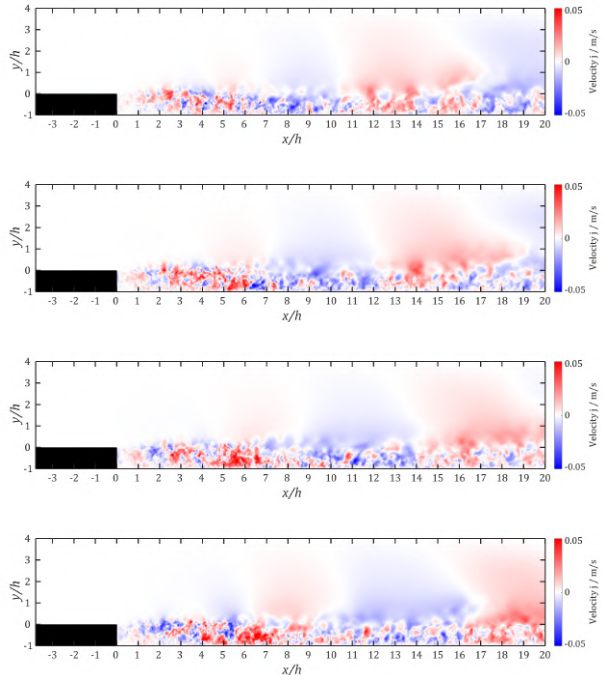

Figure B.12: Showing the horizontal velocity field of the planar bisection at a filter frequency of 12.83 Hz

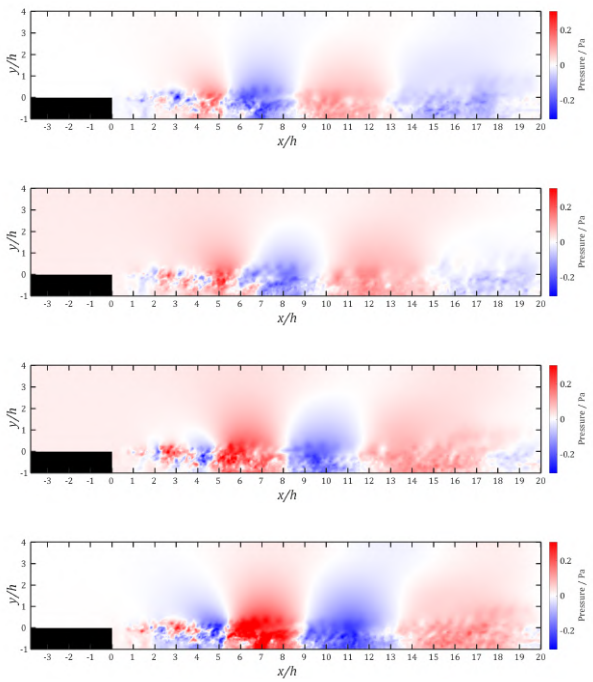

Figure B.13: Showing the pressure field of the planar bisection at a filter frequency of 17.68 Hz

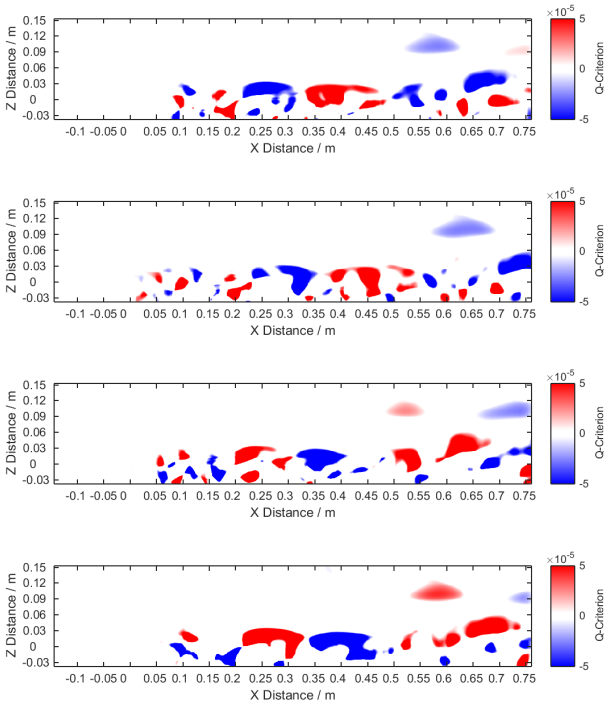

Figure B.14: Showing the rotation of vortices within the of the planar bisection at a filter frequency of 17.68 Hz

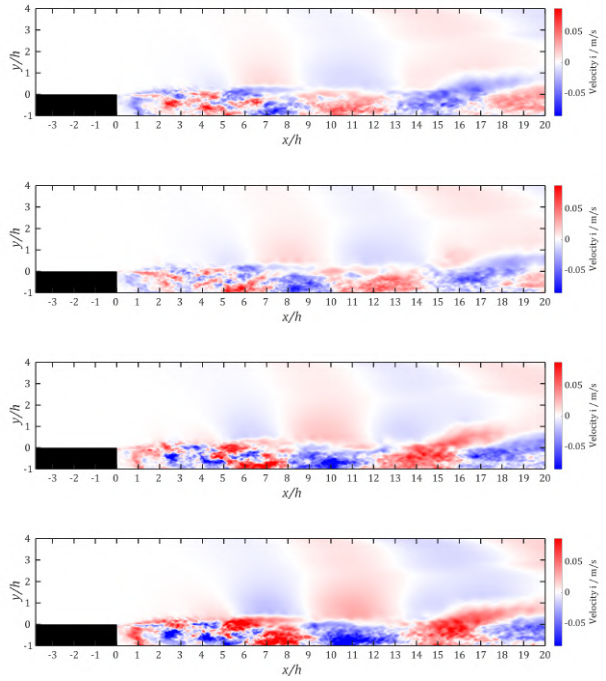

Figure B.15: Showing the vertical velocity field of the planar bisection at a filter frequency of 17.68 Hz

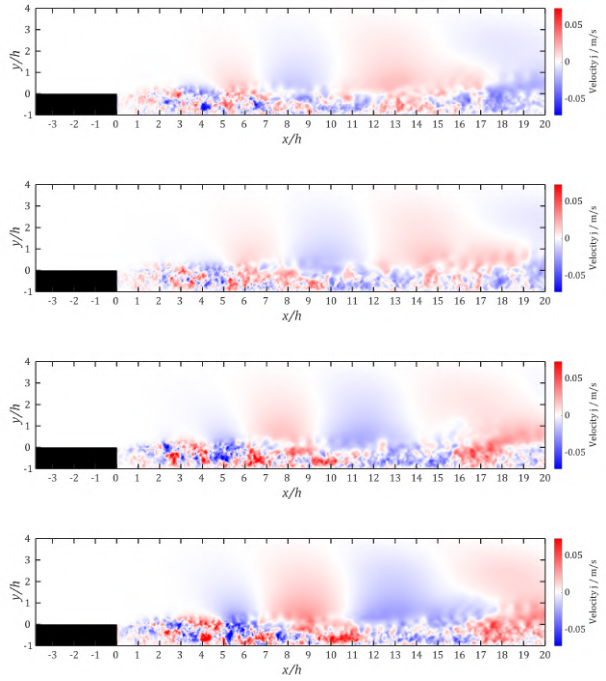

Figure B.16: Showing the horizontal velocity field of the planar bisection at a filter frequency of 17.68 Hz

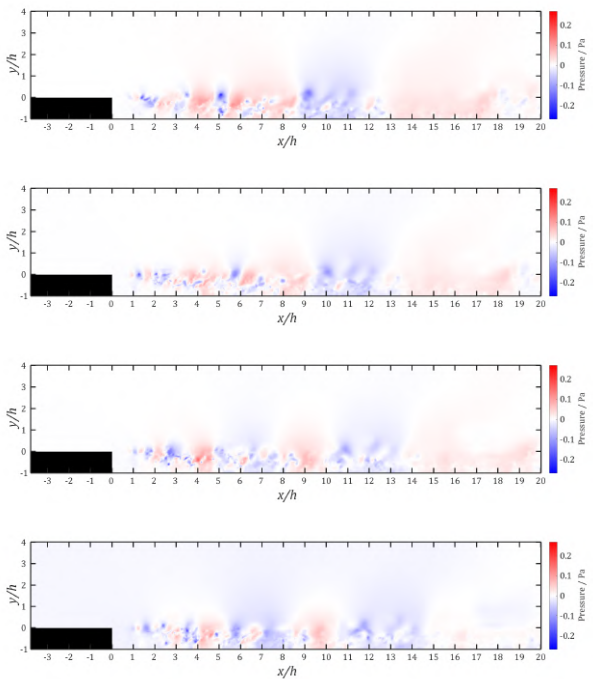

Figure B.17: Showing the pressure field of the planar bisection at a filter frequency of 26.82 Hz

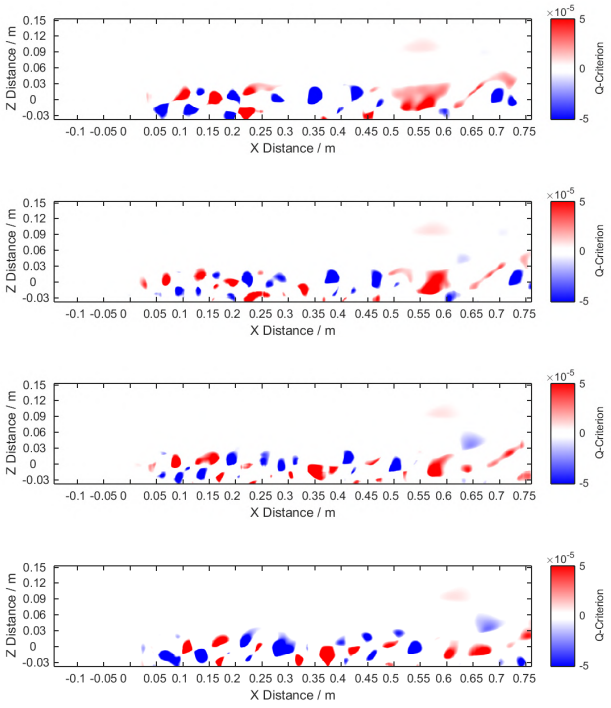

Figure B.18: Showing the rotation of vortices within the of the planar bisection at a filter frequency of 26.82 Hz

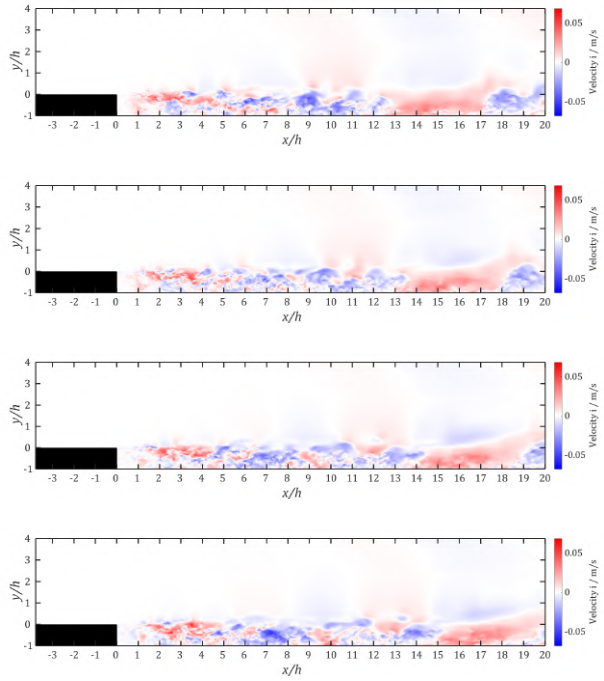

Figure B.19: Showing the vertical velocity field of the planar bisection at a filter frequency of 26.82 Hz

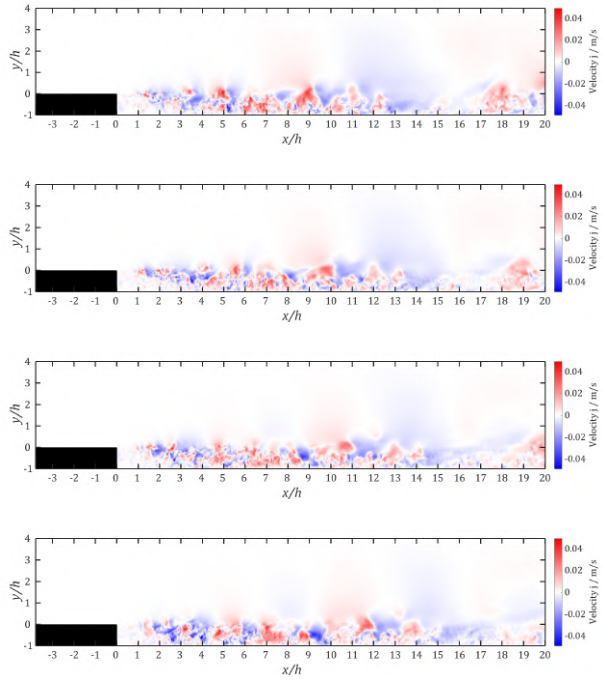

Figure B.20: Showing the horizontal velocity field of the planar bisection at a filter frequency of 26.82 Hz

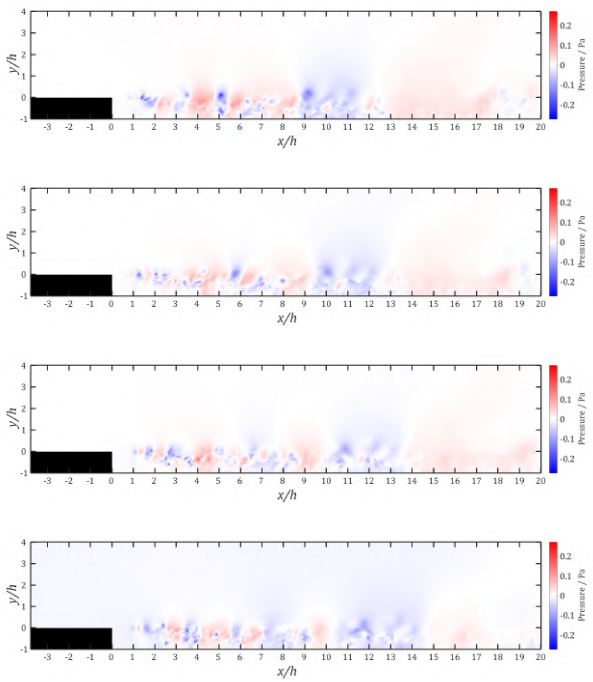

Figure B.21: Showing the pressure field of the planar bisection at a filter frequency of 30.47 Hz

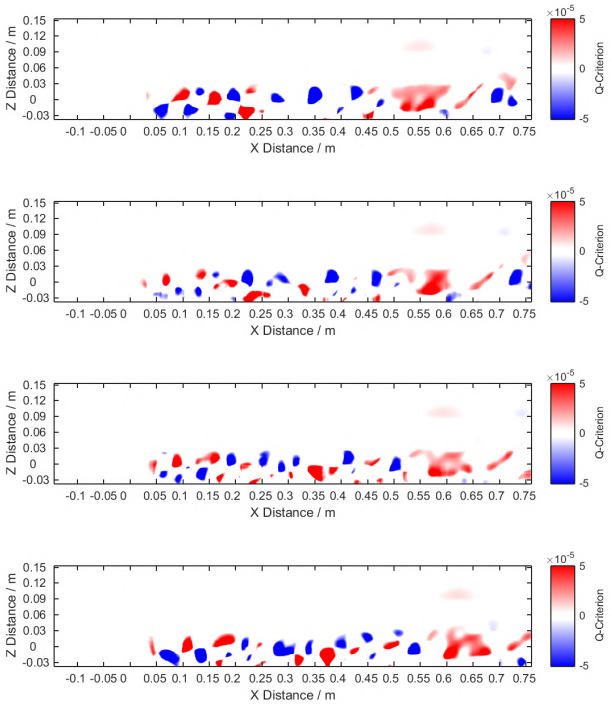

Figure B.22: Showing the rotation of vortices within the of the planar bisection at a filter frequency of 30.47 Hz

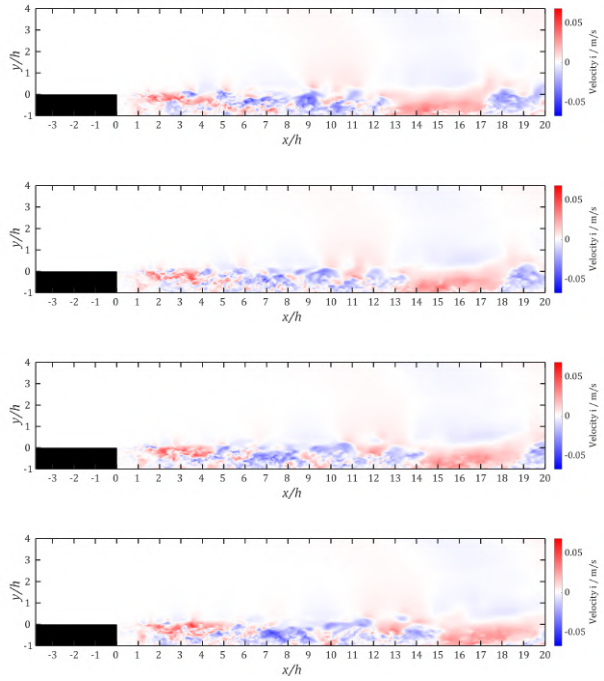

Figure B.23: Showing the vertical velocity field of the planar bisection at a filter frequency of 30.47 Hz

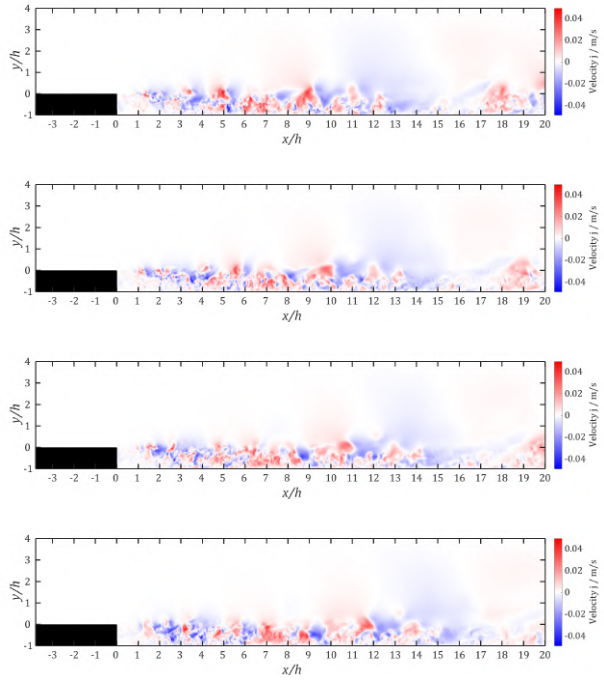

Figure B.24: Showing the horizontal velocity field of the planar bisection at a filter frequency of 30.47 Hz

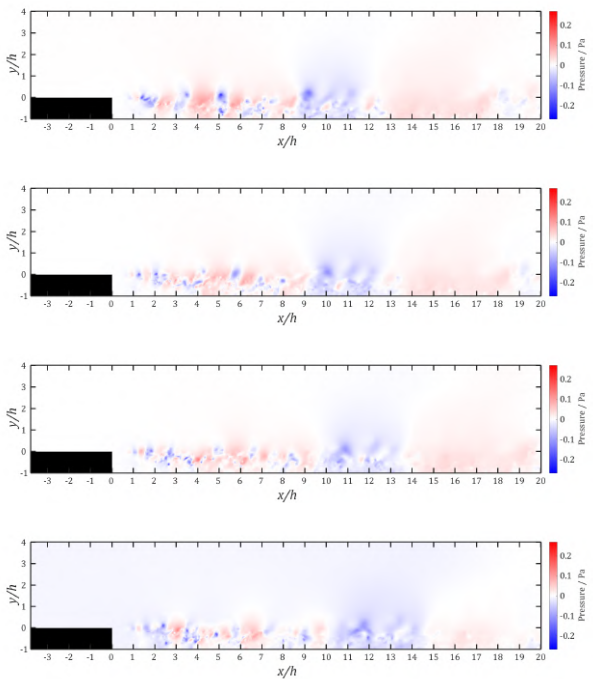

Figure B.25: Showing the pressure field of the planar bisection at a filter frequency of 40.82 Hz

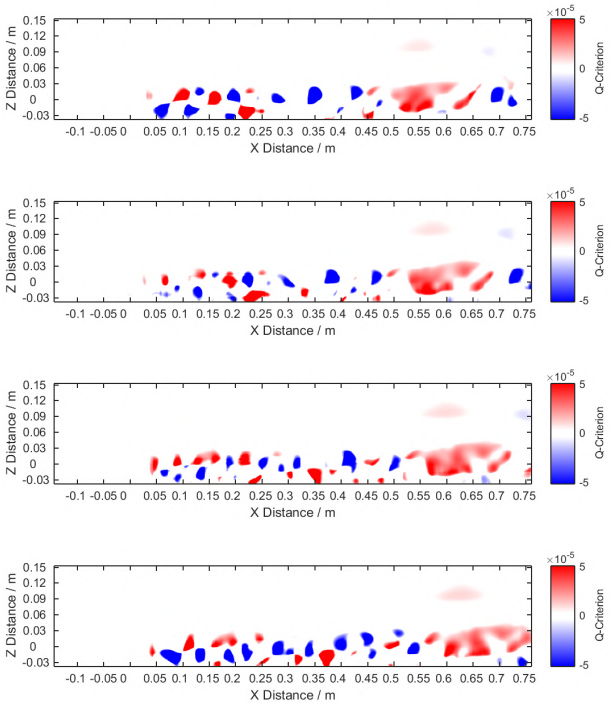

Figure B.26: Showing the rotation of vortices within the of the planar bisection at a filter frequency of 40.82 Hz

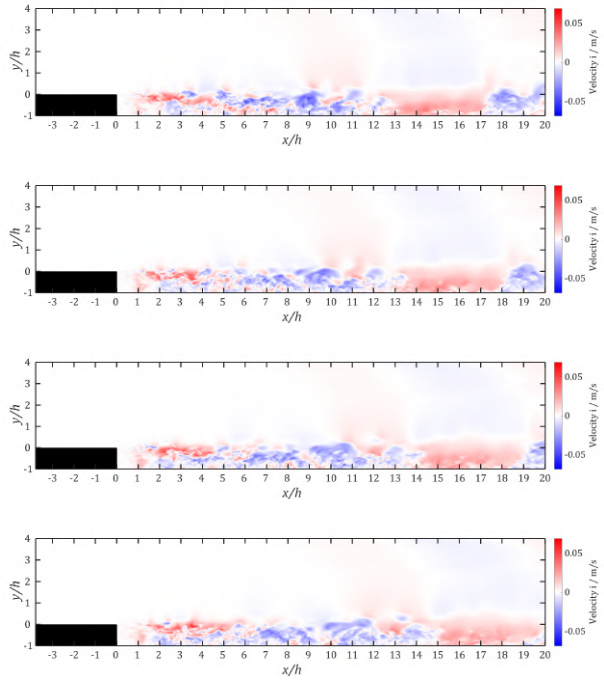

Figure B.27: Showing the vertical velocity field of the planar bisection at a filter frequency of 40.82 Hz

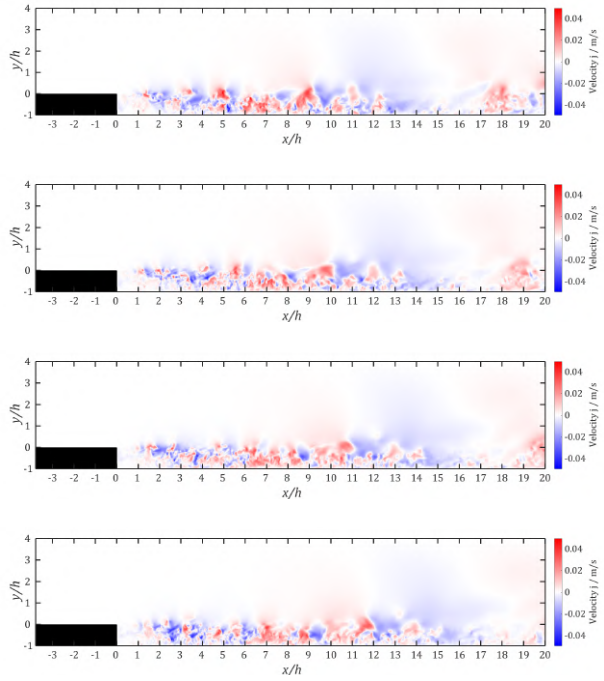

Figure B.28: Showing the horizontal velocity field of the planar bisection at a filter frequency of 40.82 Hz

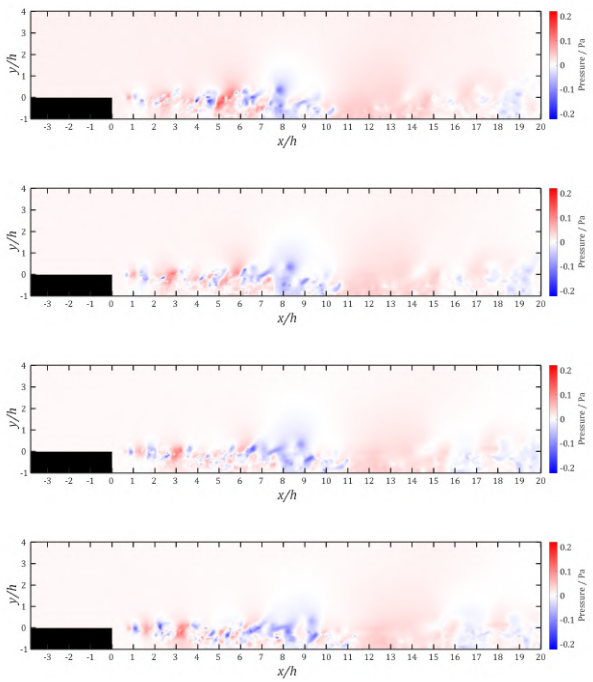

Figure B.29: Showing the pressure field of the planar bisection at a filter frequency of 50.73 Hz

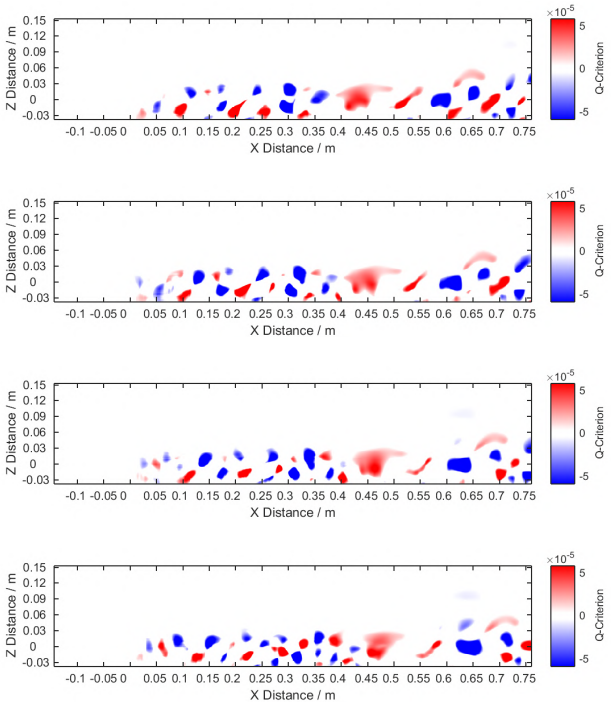

Figure B.30: Showing the rotation of vortices within the of the planar bisection at a filter frequency of 50.73 Hz

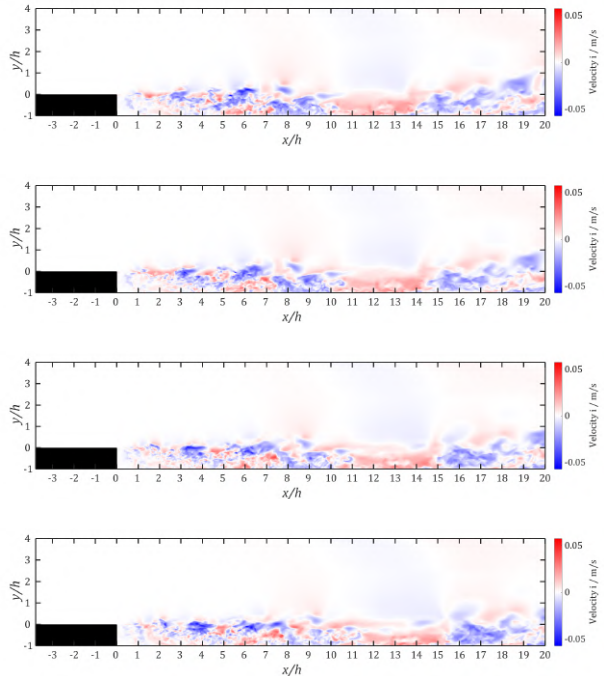

Figure B.31: Showing the vertical velocity field of the planar bisection at a filter frequency of 50.73 Hz

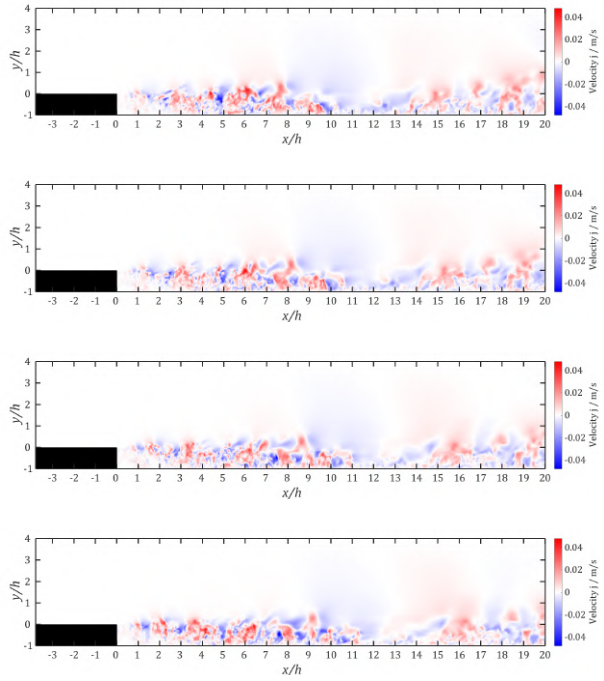

Figure B.32: Showing the horizontal velocity field of the planar bisection at a filter frequency of 50.73 Hz

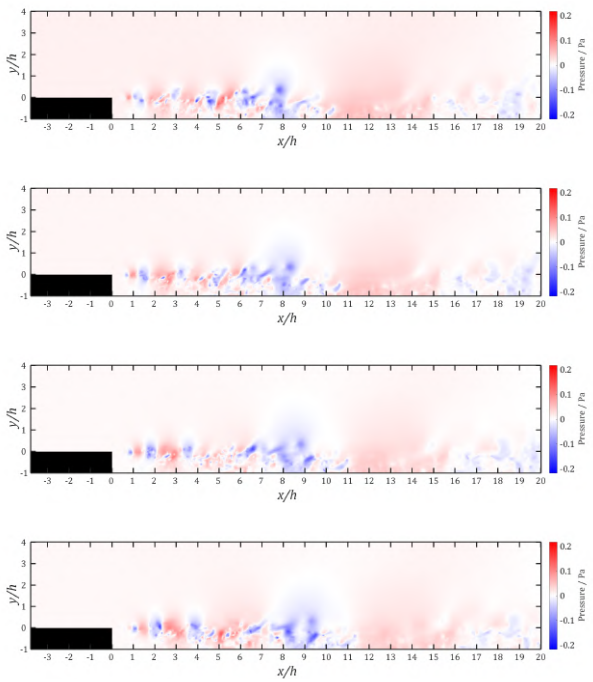

Figure B.33: Showing the pressure field of the planar bisection at a filter frequency of 68.87 Hz

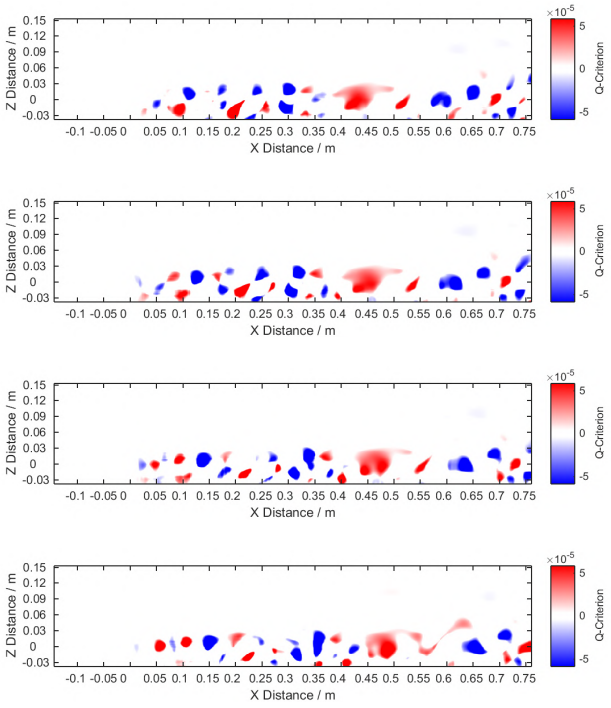

Figure B.34: Showing the rotation of vortices within the of the planar bisection at a filter frequency of 68.87 Hz

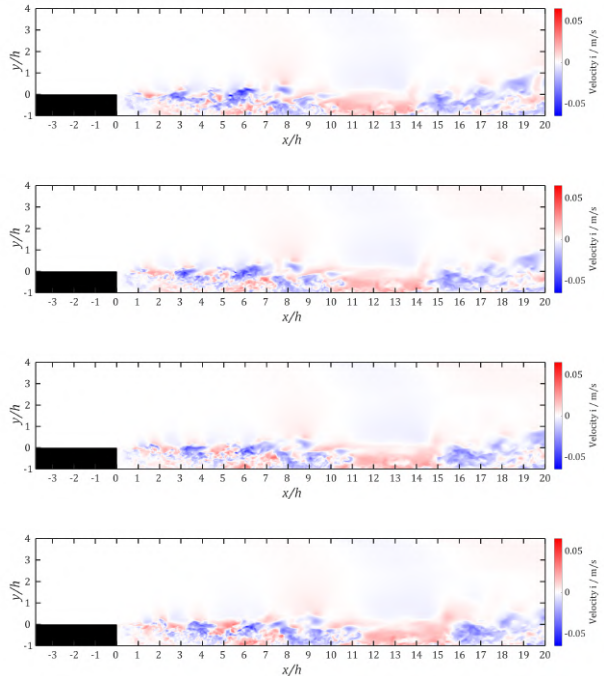

Figure B.35: Showing the vertical velocity field of the planar bisection at a filter frequency of 68.87 Hz

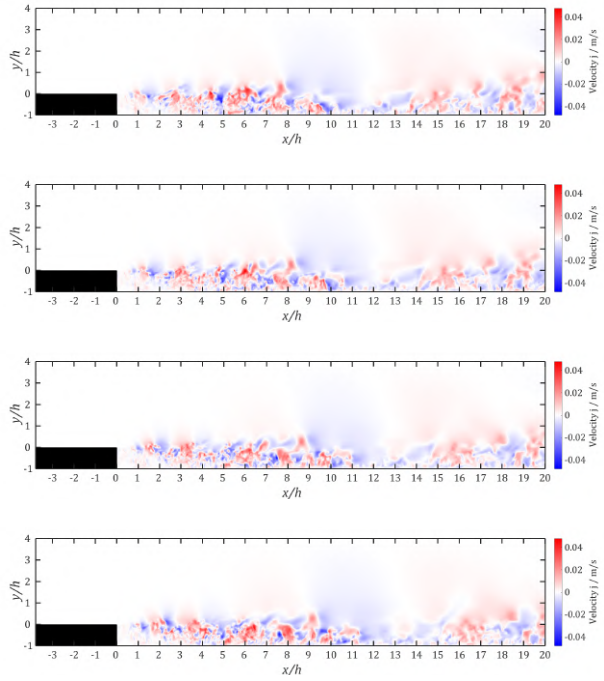

Figure B.36: Showing the horizontal velocity field of the planar bisection at a filter frequency of 68.87 Hz

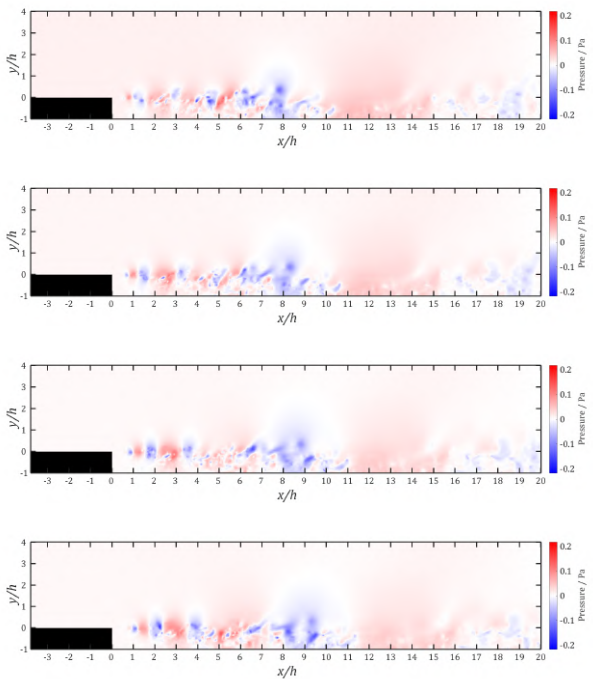

Figure B.37: Showing the pressure field of the planar bisection at a filter frequency of 73.75 Hz

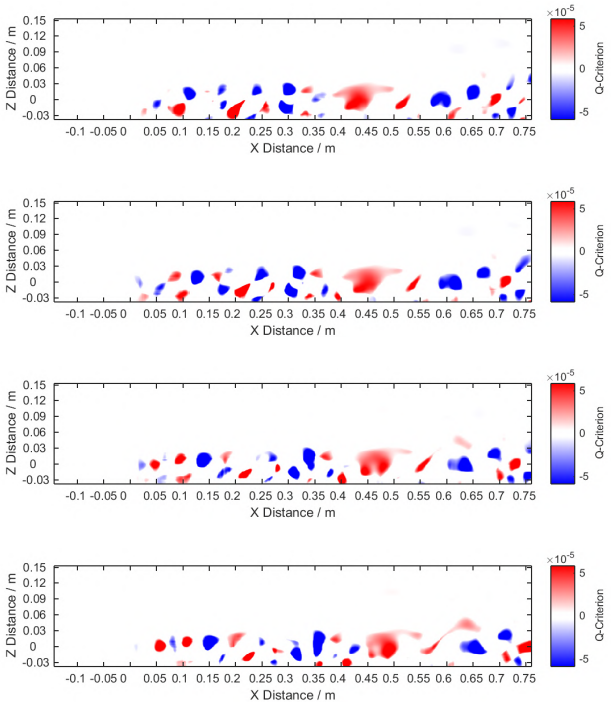

Figure B.38: Showing the rotation of vortices within the of the planar bisection at a filter frequency of 73.75 Hz

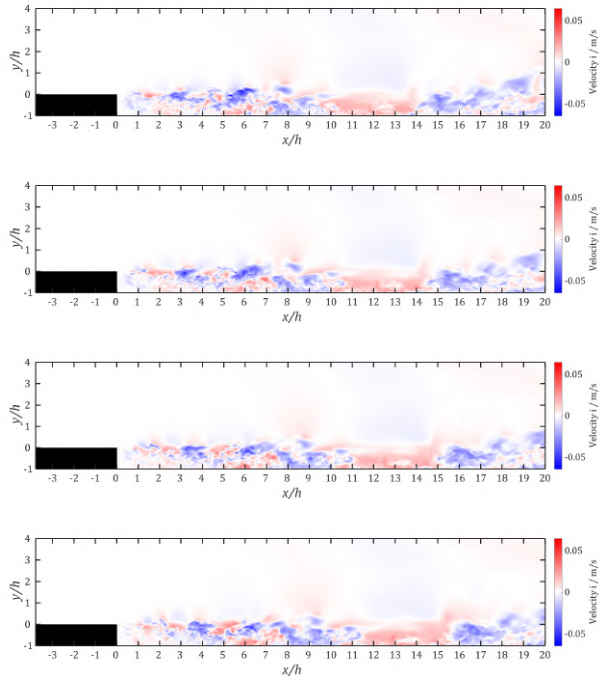

Figure B.39: Showing the vertical velocity field of the planar bisection at a filter frequency of 73.75 Hz

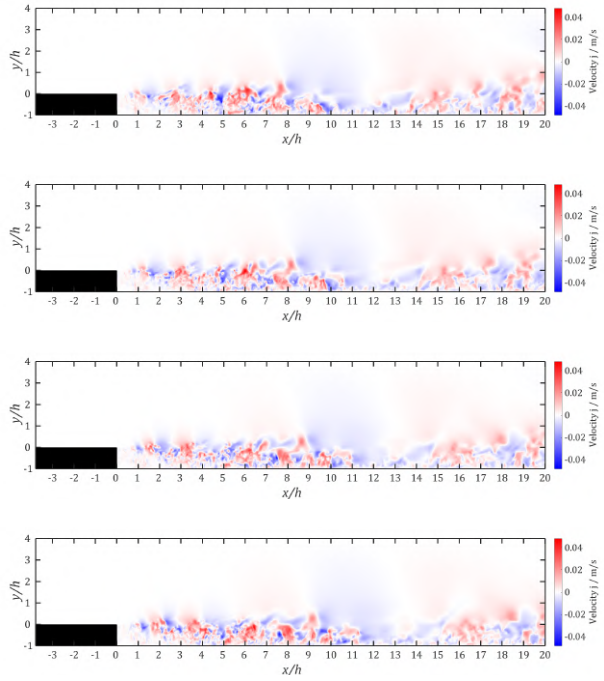

Figure B.40: Showing the horizontal velocity field of the planar bisection at a filter frequency of 73.75 Hz

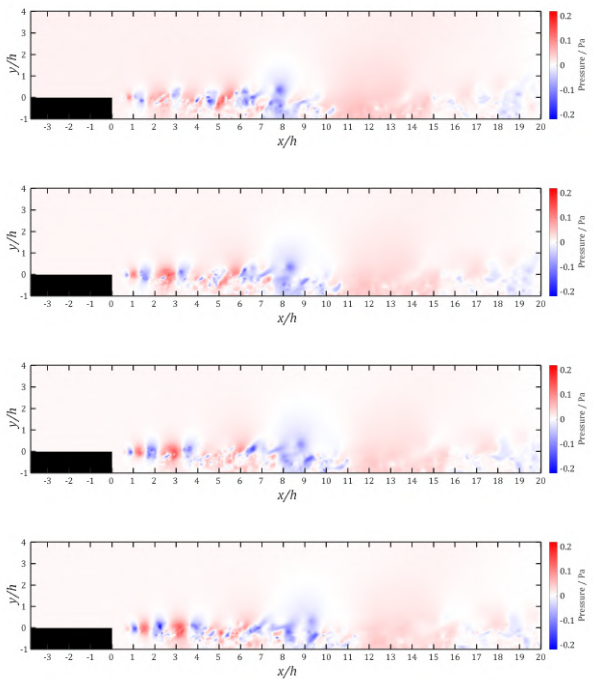

Figure B.41: Showing the pressure field of the planar bisection at a filter frequency of 91.42 Hz

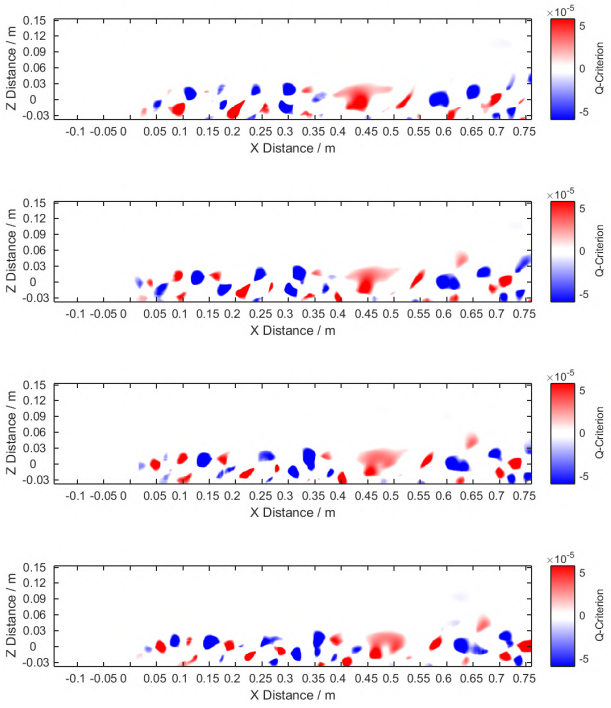

Figure B.42: Showing the rotation of vortices within the of the planar bisection at a filter frequency of 91.42 Hz

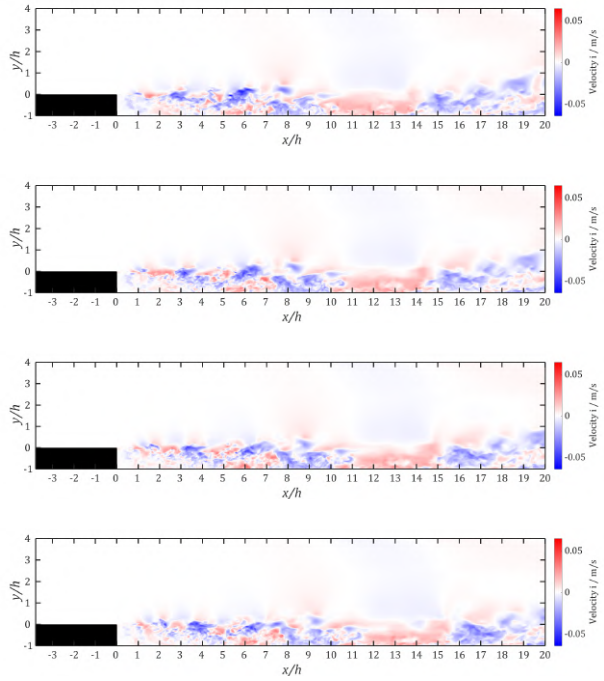

Figure B.43: Showing the vertical velocity field of the planar bisection at a filter frequency of 91.42 Hz

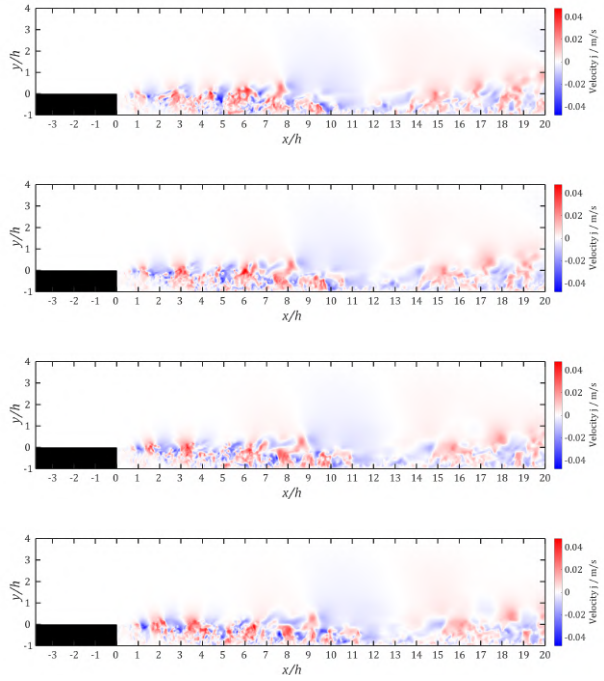

Figure B.44: Showing the horizontal velocity field of the planar bisection at a filter frequency of 91.42 Hz

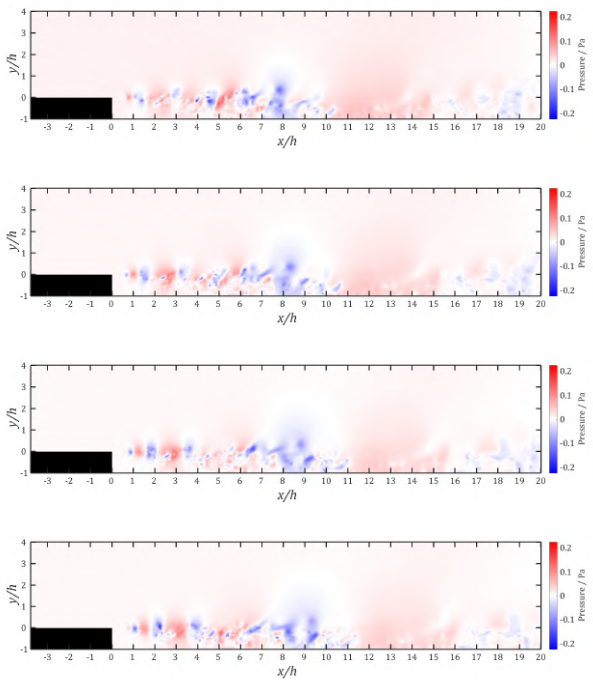

Figure B.45: Showing the pressure field of the planar bisection at a filter frequency of 103.0 Hz

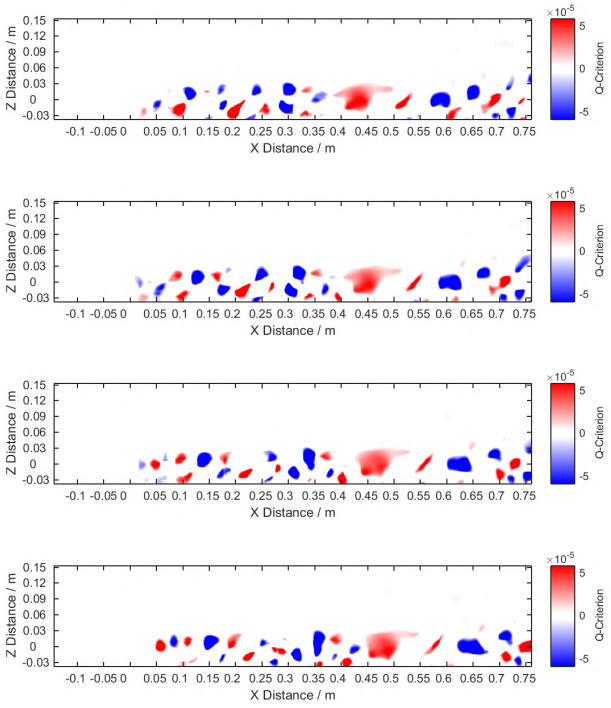

Figure B.46: Showing the rotation of vortices within the of the planar bisection at a filter frequency of 103.0 Hz

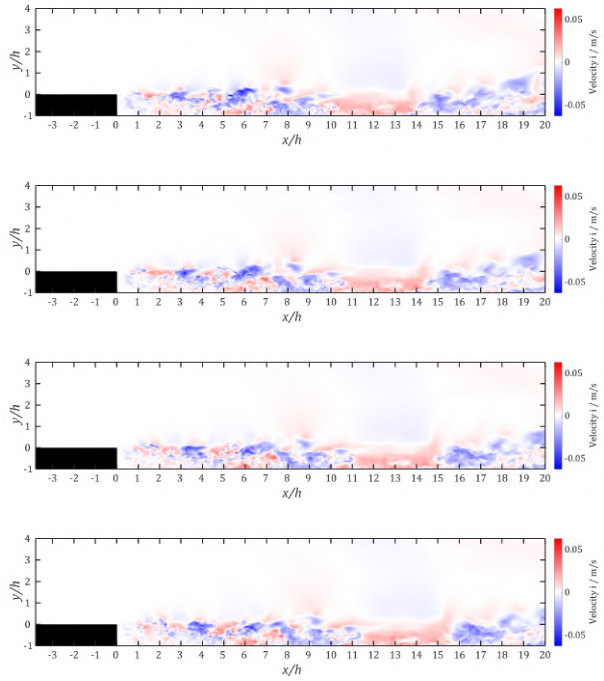

Figure B.47: Showing the vertical velocity field of the planar bisection at a filter frequency of 103.0 Hz

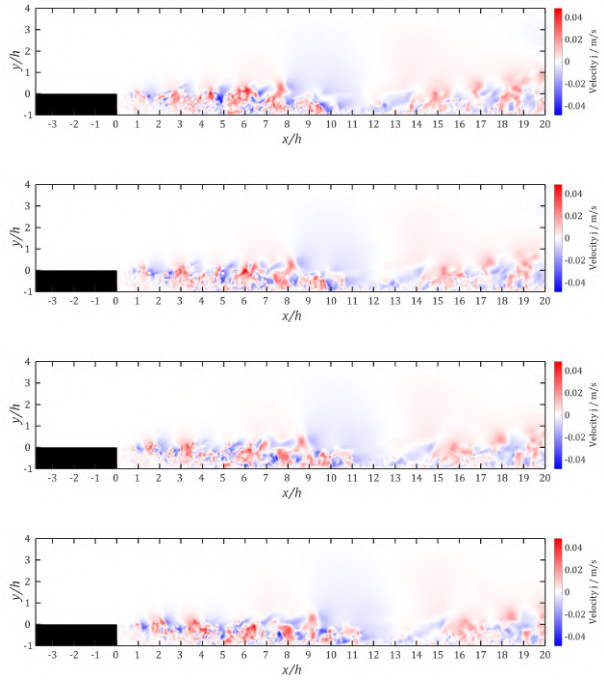

Figure B.48: Showing the horizontal velocity field of the planar bisection at a filter frequency of 103.0 Hz